FIRST-PRINCIPLES STUDY OF SOLUTE DIFFUSION MECHANISMS IN ALPHA-TI

by

Lucia Scotti

A thesis submitted to the University of Birmingham for the degree of DOCTOR OF PHILOSOPHY

School of Metallurgy and Materials

College of Engineering and Physical Sciences

University of Birmingham

March 2016

UNIVERSITY^{OF} BIRMINGHAM

University of Birmingham Research Archive

e-theses repository

Abstract

Diffusion mechanisms govern a wide range of phenomena in condensed matter including high-temperature deformation. The good influence of slow diffusers such as Si on the creep properties of α-Ti alloys is well documented, as well as the detrimental effect of fast-diffusers such as Fe, Co and Ni. The life-performance of α-Ti alloys at high temperature is also limited by light elements (O, C and N) that promote the fragile α-case phase. The study of diffusion mechanism is experimentally not trivial, since the anisotropy hcp structure of α-Ti requiring single crystal sample. The first-principles approach together with analytical models and Kinetic Monte Carlo simulations can predict the diffusivity values giving additional information on mechanism itself. This work presents the *ab initio* study of vacancy-mediated diffusion of substitutional atoms as Si, Al, Ga, Ge, In and Sn, interstitial migration of light elements, and anomalous behaviour of fast-diffusers. The findings show that the substitutional diffusion is affected by the bonding characteristic. The interstitial sites through which light elements dissolve and diffuse were updated, and they can explain the anisotropy behaviour of these solutes. The results confirm that the anomalous behaviour of fast-diffusers is a results of their ability to dissolve interstitially and substitutionally.

To my family

Acknowledgements

Table of Contents

List of Figures

VII

IX

XII

XIII

XIV

List of Tables

XVIII

XIX

XX

List of Publications

This work has already been published as

- L. Scotti and A. Mottura. Diffusion anisotropy of poor metal solute atoms in hcp-ti. *The Journal of Chemical Physics*, 142(20):204308, 2015.

- L. Scotti and A. Mottura. Interstitial diffusion of O, N, and C in α-Ti from first-principles: Analytical model and kinetic Monte Carlo simulations. *The Journal of Chemical Physics*, 144(8), 2016.

- L. Scotti and A. Mottura. Kinetic Monte Carlo study of fast-diffusers, Fe, Co and Ni migration in α-Ti . *Under review.*

Chapter 1

Introduction

Titanium alloys have a significant role in medicine and chemistry fields, aerospace and power generation industries as a result of their low density (the density of titanium is $4.52\,\mathrm{g\ cm^{-3}}$ compared to $7.8\,\mathrm{g\ cm^{-3}}$ of steel [1]), high specific strength and excellent corrosion resistance. At low temperature, the α phase is stable, which has a hexagonal close packed (hcp) crystal structure. The β phase has a body centred cubic (bcc) crystal, and stabilises at high temperature [1]. The alloying elements affect the transformation temperature and they are usually divided into α-stabilisers which extend the α field to higher temperatures (Al, O, N, C), β-stabilisers which decrease the β-transformation temperature (Mo, V, Ta, Nb, Fe, Mn, Cr, Co, Ni, Cu, Si, H) and neutral elements (Sn, Zr) [1]. The categorisation of Ti alloys is made according to the type of phases present: α alloys, α /β, and β alloys [1].

This study concentrates on the subgroup of α-Ti alloys called near-α alloys. This class of alloys shows excellent creep behaviour, and it is used in the high-pressure sections of gas turbine engines Their excellent response to creep loading is a result of the morphology and distribution of α phase, and solute additions such as Si [2–6]. As shown in the work of Bania and Hall [6], the creep properties decrease from basket-weave morphology to equiaxed α grains. Since the climb dislocation mechanism governs creep deformation behaviour [7, 8], the slow diffusion of solute and solvent atoms in α phase slows down dislocation motion, improving the high-temperature properties [1, 9, 10]. The benefits of Si addition in near-α on creep behaviour of

these alloys are well known since 1960s [3], however the actual process involved is still unclear. Some authors [11, 12] support the idea that this behaviour may be explained by precipitate strengthening through the formation of silicide particles. Others [3, 4, 13–19] suggest that Si acts as a solid solution strengthener, increasing dislocation drag. Lastly, it has suggested that both mechanisms are involved in the creep behaviour of near-α Ti alloys [20]. Nevertheless, both of these mechanisms depend on Si diffusion behaviour, which can determine the formation of solute segregation in the matrix, or the homogeneous precipitation of silicides.

Despite the excellent properties at high-temperature, the utilisation of near-α alloys in aerospace industry is limited by the high affinity of Ti with interstitial solute, such as O, N and C [1]. These elements have high solubility in α-Ti (O has maximum of 30 at.% [21, 22]) and they diffuse extremely fast in the matrix (10^3 times larger than self-diffusion [22–26]). During casting, high-temperature processing and/or serving, these elements can rapidly dissolve and diffuse in the matrix forming an embrittled phase, which is called the α-case [1]. The formation of the α-case has a severe impact upon fatigue and creep resistance of near-α alloys, and is often the initiation site for cracks [27, 28]. The loss of plasticity seems related to the crystal deformation and electronic structure of Ti-solute bonds [22, 29–31]. As a result of the rapid migration of these elements, the α-case layer grows with a quadratic law with respect to the exposure time [28]. Zhu and co-workers have also reported that the bulk diffusion behaviour in α-Ti controls the oxidation kinetics [32].

The creep properties of near-α Ti alloys are also affected by the presence of fast-diffusers such as Fe, Co and Ni [5, 33–37]. A small addition of these elements can have a severe detrimental effect upon the high-temperature properties of Ti [36]. This negative effect seems to be related to anomalous migration of these solutes within α-Ti [7, 34], which is very fast [38–40] and accelerates the substitutional solute and solvent diffusion [9, 10, 41]. This modifies the dislocation kinetics, deteriorating the mechanical properties [7, 34]. The simple migration processes such as interstitial or vacancy-mediated mechanism cannot explain this anomalous behaviour [42, 43]. Their small metallic radii allow these solutes to accommodate at both lattice and interstitial sites within the α-Ti crystal [44]. This suggests that they diffuse through

2

the dissociative diffusion mechanism proposed by Frank and Turnbull [42]. This mechanism includes interstitial and substitutional solute migration, vacancy diffusion from surface, vacancy annihilation and creation in bulk and combination-dissociation reactions [45]. In the case of metals, the vacancy flux from and to the dislocations is constant and higher than vacancy migration from the surface, leading to a constant value of the vacancy concentration. Based on this, the fast-diffusers migration depends upon their interstitial and substitutional diffusion, and the combination-dissociation process [46]. This last process consists on the annihilation of vacancy by recombination with an interstitial and the formation of vacancy as a result of substitutional atoms jumping into an interstitial site [46]. It is possibile that the anomalous fast diffusion behaviour of Fe, Co and Ni can be the result of solutes moving through interstitial sites until they encounter and annihilate with a vacancy. On the other hand, the dissociation jump may affect the vacancy concentration and consequently the self-diffusion behaviour. However, Frank and Turnbull have suggested that the rate reaction of combination-dissociation process is too small to have significant impact on the migration of fast-diffusers in α-Ti [42]. They have proposed that only few Fe, Co and Ni atoms move through interstitial jumps, while the rest of them sit at the lattice sites. This may explain the fast diffusion, but not the enhancement of solvent migration. Pasianot and co-workers have proposed that these solutes can exchange position directly with the host atoms without the need of vacancy [47]. Fe, Co and Ni atoms can jump into interstitial site from a lattice site, leaving behind a vacancy that can be occupied by the host atom nearby. Therefore, although the substitutional atoms do not participate actively in solute migration, they can speed up the solvent diffusion.

In general, solute diffusion behaviour is important for different phenomena concerning microstructural changes, such as solidification kinetics, phase equilibria, precipitation phases, and the segregation of alloying elements. In near-α alloys, the solute migration can affect positively (Si) or negatively (Fe, Co and Ni) the creep properties and promote α-case formation (O, N and C). Knowing the solute diffusion mechanisms can help understand their influence upon high-temperature properties. This is essential when designing new alloys for aerospace applications. Identifying the diffusion mechanisms through experimentation in α-Ti is not a trivial task, since

the anisotropy exhibited by the hcp crystal requires single-crystal diffusion evaluations. Such measurements are useful in calculating the bulk diffusivity of species, however it is difficult to obtain detail such as the diffusion pathways that are operating.

Recently, *ab initio* calculations have been successfully used to evaluate self- and solute diffusion in α-Mg and α-Zn [48, 49], as well as O interstitial diffusion in α-Ti [50] using an analytical model [51–53], or for complicated mechanisms involving interstitial and vacancy defects, such as O diffusion in Ni [54] using kinetic Monte Carlo (KMC) simulations [55]. The aim of this project is to calculate solute diffusion coefficients within α-Ti using first-principles, and improve upon the understanding of the diffusion mechanisms. This has been achieved through the use of analytical models ("8-frequency" [51] and Multi State Diffusion (MSD) [52, 53] methods) and KMC simulations informed by Density Functional Theory (DFT) [56, 57] calculations. The first-principles calculations in this work were performed using Vienna *ab initio* Simulation Package (VASP) [58–61] and the transition states were evaluated using the nudged elastic band method [62] with climb image [63] and improved tangent estimation [64] methods (CI-NEB). The study has focused upon three kinds of solute diffusion in α-Ti: vacancy-mediated diffusion (Si and semi-metals), interstitial diffusion (O, N and C) and fast-diffusers (Fe, Co and Ni).

The similar atomic size of Si to Ti suggests that it dissolves as a substitutional solute and diffuses by vacancy-mediated mechanism in α-Ti. The diffusion study was conducted by applying first-principles calculations to the "8-frequency" model [51] and through KMC simulations [55]. The Si behaviour was compared with the migration of elements located close to Si in the periodic table, such as Al, Ga, Ge, In and Sn. These are known as semi-metals. This investigation was performed to highlight trends that can better explain the slow diffusion behaviour of Si. Good agreement was obtained with experimental data available in the literature [9, 10], confirming the anisotropic behaviour in hcp crystal. With respect to the experimental measurements, the *ab initio* approach helped to enlighten some interesting aspects of semi-metals diffusion. For example, one of the findings is that the solute-solvent bond has a major impact upon the substitutional solute diffusion, leading to the surprisingly rapid migration of

large atoms. The cause for the severe anisotropy in certain alloying elements such as Si and Ge is attributed to the distortion of the solute-host bond which leads to the formation of a low-energy configuration at the saddle point and consequently to a lower migration barrier within the basal plane.

O, N, and C are light elements which diffuse most commonly through interstitial migration [22] and are associated with the formation of undesirable phases, such as the α-case. To control and mitigate the formation of these phases, it is important to identify the stable interstitial sites of these light elements and map the migration pathway networks that operate. This diffusion behaviour was investigated using MSD method and KMC simulations, both informed by *ab initio* calculations. The good agreement with the experimental data [23–26] shows the reliability of these two tools. The calculations have provided surprising insights into the diffusion kinetics of these alloying species. These solutes accommodate at octahedral, but not at tetrahedral sites, preferring the less traditional sites such as crowdion, basal crowdion and hexahedral. The updated transitions through these sites can explain their anisotropic diffusion behaviour, while the electronic bond of interstitial solute-host pair may explain their influence on plasticity [65].

In the last part of this work, first-principles and KMC approaches were used to investigate the anomalous fast diffusion kinetics of Fe, Co and Ni. The diffusion processes described by Frank and Turnbull [42] was assessed using KMC simulations. The interstitial and substitutional diffusion effect on the overall migration were individually evaluated. The findings confirm the fact that these two simple mechanisms cannot describe the diffusion behaviour of these three solutes [42, 43]. The interstitial diffusivity values are too large with respect to the experimental data, while the substitutional vacancy-mediated values are too small. The results also show that the effect of combination-dissociation reactions [46] on the fast-diffusers migration is minimal with respect to the interstitial mechanism. On the other hand, the effective diffusivities calculated with Frank-Turnbull formula [42] are consistent with the experiments, supporting the idea that these solutes spend only a part of their time as moving interstitials. Finally, the effect of solute-host swap [47] on the self-diffusion was qualitatively verified by the

KMC results.

Chapter 2

Literature review

2.1 Titanium and its alloys

2.1.1 Allotropic phases

Titanium has two allotropic phases: a low-temperature phase, α, and a high-temperature one, β. The transus temperature for pure Ti is 882 ± 2 °C [1]. Alpha-Ti has a hexagonal close packed structure (hcp), while β-Ti has body-centred cubic structure (bcc) (Fig. 2.1). In the case of α-Ti, the lattice parameters reported in the literature are $a = 0.295$ nm and $c = 0.468$ nm, c/a ratio is 1.587, smaller than the ideal value of 1.633 [1]. The addition of interstitial (e.g. C, N or O) or substitutional elements (e.g. Al) modifies this ratio [1, 22, 29, 30]. The lattice parameter of the β phase is equal to 0.332 nm [1]. Other parameters which describe the crystal are summarised in Table 2.1. The large variety of properties of Ti-alloy depend upon the presence, quantity and morphology of these two phases. For instance, β-Ti has superior deformability due to the higher number of slip systems and slip-plane density present in the bcc structure. The superior creep resistance of α-Ti can be attributed to relative slow solute diffusion; the atom migration is much faster in β phase than α phase [1]. Anisotropic mechanical behaviour also distinguishes the α phase. The Young's modulus perpendicular to the basal plane is 145 GPa, while it is 100 GPa when load is applied parallel to the basal plane [1].
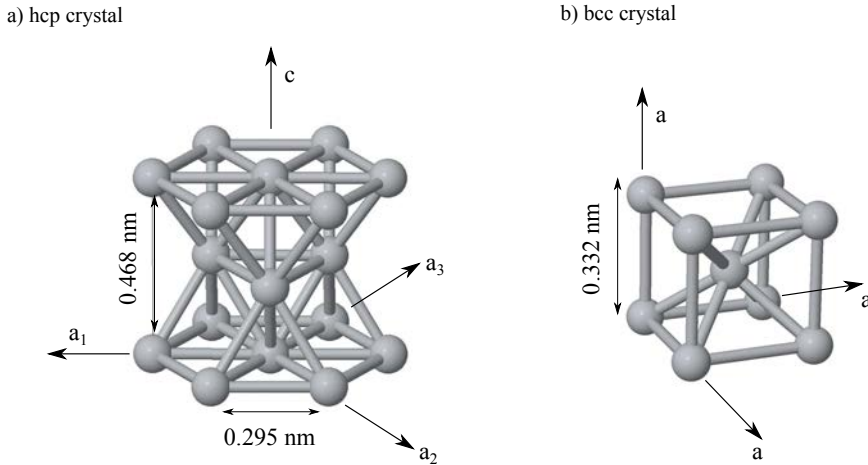
Figure 2.1: Crystal structure of a)α-Ti (hcp) and b) β-Ti (bcc) [1].

Table 2.1: Characteristic parameters of hcp and bcc structures: number of atoms per unit cell (N), coordination number(CN), packing density (P), slip system per unit cell (S), atom density of slip plane (AD) and minimal slip path (b_{min}/a) [1].

Crystal	N	CN	P	S	AD	b_{min}/a
hcp	2	12	74%	3	91%	1
bcc	1	8 (+6)	68%	12	83%	$1/2\sqrt{3} \approx 0{,}87$

2.1.2   Classification of Ti alloys

The classification of alloying elements is usually based on their influence on the β-transus temperature, as shown Fig. 2.2. Sn and Zr are neutral elements, they do not have any influence on the transformation temperature. Al, O, N and C are α-stabilising elements since they enlarge the α field. Mo, V, Ta, Nb, Fe, Mn, Cr, Co, Ni, Cu, Si and H are β-stabilising elements, decreasing the β-transus temperature [1]. Depending on the quantity of α-stabilisers and β-stabilisers, different types of alloy can be obtained, as shown in Fig. 2.3 [66]. The classification of Ti alloys depends on the predominant phase present. Three main categories are widely recognized: α alloys, α/β alloys, β alloys. These groups are presented in the following sections. The compositions of the alloys mentioned in this chapter are summarised in Table 2.3.
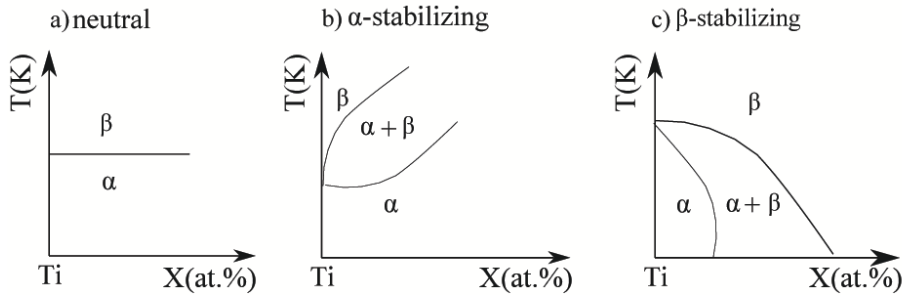
Figure 2.2: Influence of alloying elements on the phase diagram of Ti alloys [1]: a) Neutral elements (Sn, Zr), b) α-stabilizing elements (Al, O, N, C), and c) β-stabilizing elements (Mo, V, Ta, Nb, Fe, Mn, Cr, Co, Ni, Cu, Si, H).
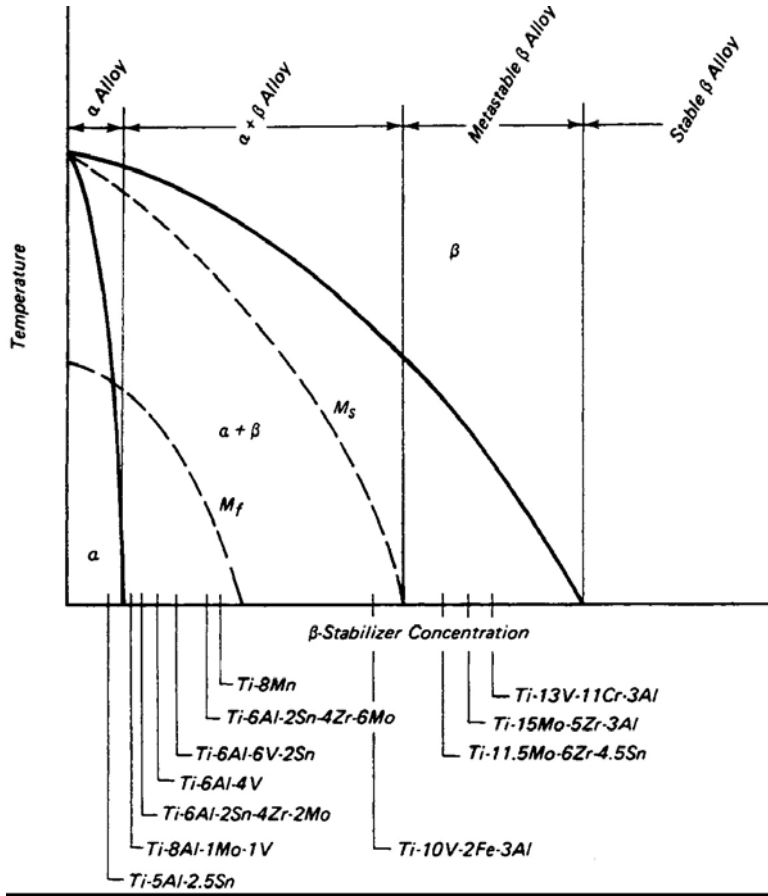
Figure 2.3: U.S. alloys mapped onto a pseudo-binary β-isomorphous phase diagram [66].

Alpha alloys

This first group of alloys is employed in chemical and process engineering industries, because of their high strength, excellent corrosion resistance and deformation behaviour. They are usually divided into three subgroups: unalloyed titanium (also known as commercially-pure or CP), α alloys and near-α alloys.

9

Characterised by very high corrosion resistance, the CP-titanium alloy microstructure is entirely composed by grains of α phase [67] (see Fig. 2.4-a). Their classification is based on the O and Fe content. Grade 1 contains 0.2 wt.% Fe and 0.18 wt.% O, and it has the lowest strength level but excellent cold deformability. It can be utilised as cladding alloy for steel or sheet metal for explosive claddings [1]. The most widely used CP-titianium is Grade 2, which has 0.3 wt.% Fe and 0.25 wt.% O, and shows a tensile strength between 390 and 540 MPa [1]. Grade 3 (0.3 wt.% Fe and 0.32 wt.% O) is less common and only used in applications requiring high strength and reduced wall thickness, such as pressure vessel applications [1]. Grade 4 (0.5 wt.% Fe and 0.4 wt.% O) has tensile strength above 740 MPa and is commonly utilised for mounting and fittings [1]. Grade 7 and Grade 12 have same O and Fe content as Grade 2, with the addition of Mo and Pb to increase corrosion resistance [1].

The second group is used in high-temperature and cryogenic applications. The addition of Al, Sn, Zr and O promotes solid solution hardening. They are not suitable for forging operations as a result of the high rate of work hardening [66]. Instead, they are suitable for welding due to of their insensitivity to heat treatment. The most common α alloy is Ti-5Al-2.5Sn which is used for the liquid hydrogen storage tanks in space vehicles [68].

Near-α alloys are obtained by introducing β-stabilizing elements, such as V and Mo in α alloys to raise their strength after heat treatment. The typical two-phase microstructure in Fig. 2.4-b is obtained by a solution heat treatment in α/β field followed by oil quench [69]. It consists in primary α (white grains) embedded in a lamellar transformed-β matrix (black grains). The design of near-α alloys started in the 1950s with TIMETAL®8-1-1 and TIMETAL®-6-2-4-2. TIMETAL®8-1-1 is more likely to corrode because of the high quantity of Al. Subsequently, Al level was reduced in TIMETAL®-6-2-4-2 and now it does not exceed the maximum of 6 wt.%. In the 1960s, Si addition started playing a central role in the development of these alloys. In 1961, IMI Titanium Ltd. (later acquired by Timet) developed the first commercial Si-containing Ti alloy, IMI679. TIMETAL®-6-2-4-2-S, containing 0.1 wt.% of silicon, was developed by Timet U.S.A. a year later. TIMETAL®685 was the first near-α alloy treated by β annealing. Nowadays, the most advanced near-α Ti alloys are TIMETAL®834

and TIMETAL®1100 used at a temperature of 600 °C. The addition of Si in these alloys has markedly improved creep properties [1].

Alpha/beta alloys

Alpha/beta alloys contain a higher fraction of β stabilisers with respect to α alloys. The most popular α/β alloy is Ti-6Al-4V developed in the United States 60 years ago and widely utilised in the aerospace industry. Its success is a result of the good balance of properties: good ductility and strength associated with good corrosion and oxidation resistance. The microstructure is constituted by α and untransformed-β grains. Ti-6Al-4V has a typical microstructure composed by acicular α and small amount of intergranular β in equiaxed α matrix [70], as shown in Fig. 2.4-c. Other α/β alloys are Ti-6-6-2 and IMI 550 developed for high-strength applications, Ti-6-2-4-6 characterized by high strength and toughness, Ti-6-2-2-2-2 and Ti-17 used in elevated-temperature applications up to 400 °C such as gas turbine engines [1].

Beta alloys

Beta alloys have high level of β-stabilising, so they retain metastable-β grain at low temperatures. The equiaxed β structure of Ti-35Nb-7Zr-5Ta-0.06O [71] is shown in Fig. 2.4-d. These alloys are more forgeable, cold-formable and they can be hardened to extremely high strength levels [66]. Unfortunately, they have a relatively high specific weight and modest weldability. Some examples of β alloys are TIMETAL 10-2-3 and Beta C, that have high strength and toughness, and TIMETAL 15-3, usually deformed at room temperature to make thin foils. A good oxidation-resistant β alloy is TIMETAL 21S, while TIMETAL LCB is a relative cheap alloy used in the automotive industry [1].

2.1.3 Microstructure, thermomechanical treatments and properties

We present in this section the thermomechanical treatments commonly applied to Ti alloys. CP-titanium and α alloys are not included since their microstructural changes are limited to grain refinement and shape.
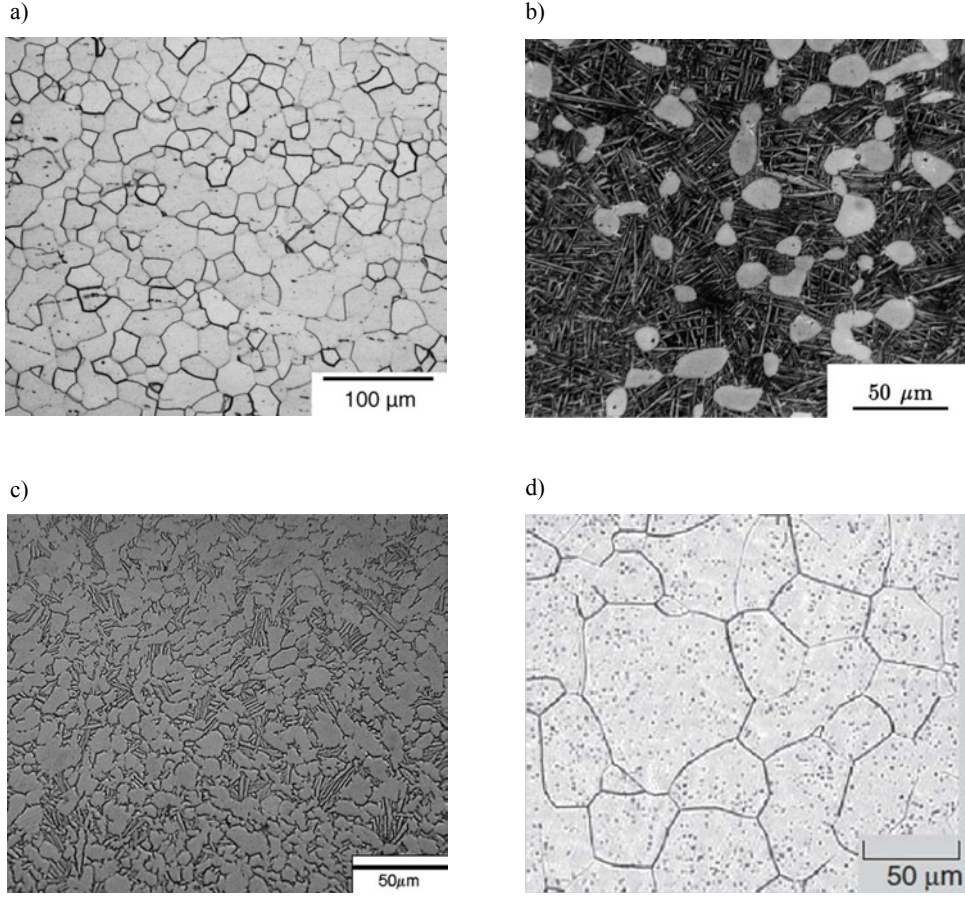
Figure 2.4: a) Equiaxed CP-titanium after annealing [67], b) two-phase TIMETAL®834 [69], c) Ti-6Al-4V alloy composed by acicular α and a small amount of intergranular β in equiaxed alpha matrix [70], and d) equiaxed β in Ti-35Nb-7Zr-5Ta-0.06O [71].

Near-alpha alloys

Near-α alloys are usually treated above β-transus curve to increase creep and fatigue crack resistance. The microstructure obtained after β-solution and slow cooling is composed of colonies of α platelets in large prior β grains with a few percent of inter-platelets β layers [72] (see Fig. 2.5-a). The basketweave morphology is obtained by cooling at 3 to 6 °C/s from β field [73], resulting in α-phase colonies intersected each other (see Fig. 2.5-b). The refining of prior-β and α platelets determines higher creep properties [72]. A finer two-phase structure (see Fig. 2.5-c) is obtained after a solution heat treatment in α/β field, and it has better ductility and elevated high-cycle fatigue strength [74].
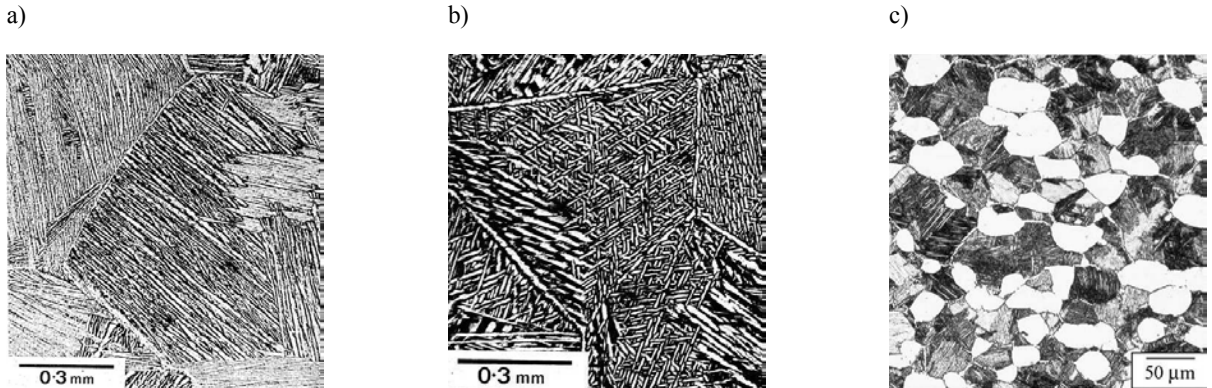
Figure 2.5: Final microstructure of TIMETAL®834: a) lamellar colony structure obtained by β solution heat treatment and relatively slow cooling [72], b) basket-weave microstructure obtained by faster cooling from β field [72], and c) two-phase microstructure obtained by solution heat treatment below the β-transus [74].

Alpha/beta alloys

Alpha/beta alloys are usually processed by a series of hot working steps followed by heat treatments. After hot working process, the microstructure is uniform and fine: globular α in a transformed matrix of α-β phase. These alloys are then subjected to cooling from β region: Fig. 2.6 schematically shows the phase changes [66]. At temperatures above the β-transus, the microstructure consists of only β grains. In the α/β field, α plates nucleate at β-grain boundaries along {110} planes. These plates grow as the temperature decreases; at room temperature, α and β plates compose the microstructure. The final heat treatment depends on the final application of the alloys. Basket-weave with fine acicular α (see Fig. 2.7-a) morphology is a result of heat treatment above transformation temperature and water quenching [75]. This structure has lower strength and higher fracture toughness than conventional α/β processed material. Lamellae colonies (see Fig 2.7-b) form after slow cooling above β-transus temperature [75]. Mechanical properties of this morphology depend upon the orientation of the lamellae. After heat treatment at low temperature in α/β field, the final microstructure is equiaxed primary α plus intergranular β [75] (see Fig. 2.7-c). Duplex structure of primary α in transformed β matrix (see Fig. 2.7-d)) is obtained after heat treatment at high temperature in α/β field [75]. These two structures are characterised by a good combination of high strength and ductility. Martensite structure forms after faster cooling. Phelps and Wood [76] have studied

13
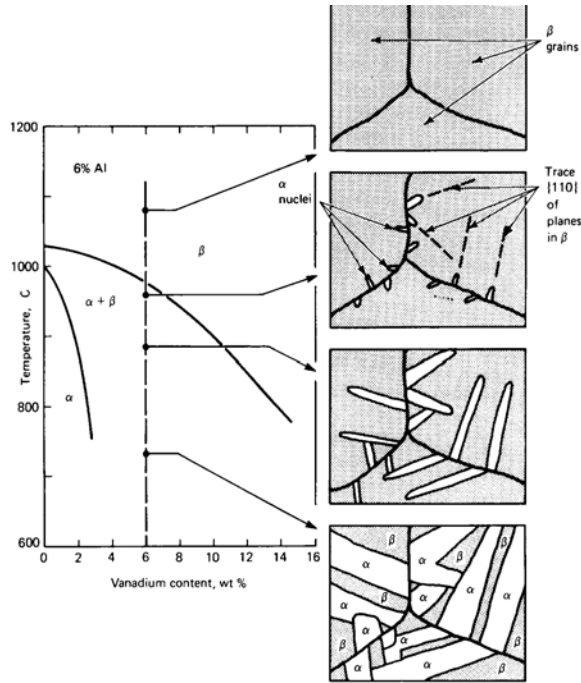
Figure 2.6: Development of Ti-6Al-4V slowly cooled from β field [66].

the correlation between the cooling rate and martensite microstructure (see Fig. 2.8). Their study shows that the width of platelets decreases with faster cooling rate, while the amount of retained β increases, raising the tensile strength.

Beta alloys

Beta alloys are usually processed by hot working followed by heat treatment, in order to transform metastable-β phase into α phase. Afterwards, they are subjected to solution heat treatment, followed by quenching and ageing. Coarse β grains form after solution heat treatment [1] (see Fig. 2.9-a). Acicular primary α phase precipitates after solution heat treatment slightly below the transformation temperature [1] (see Fig. 2.9-b). Crack nucleation is promoted by acicular and coarsing α. Globular morphology is a obtained from thermomechanical processing (see Fig. 2.9-a). The ductility depends on the size of α grains [1]. The secondary α phase precipitates after ageing treatment. The ageing temperature controls the size and distribution of the grains. Fine distribution of secondary α (see Fig. 2.9-d) precipitates after ageing at 400-600 °C improving fatigue resistance [1].
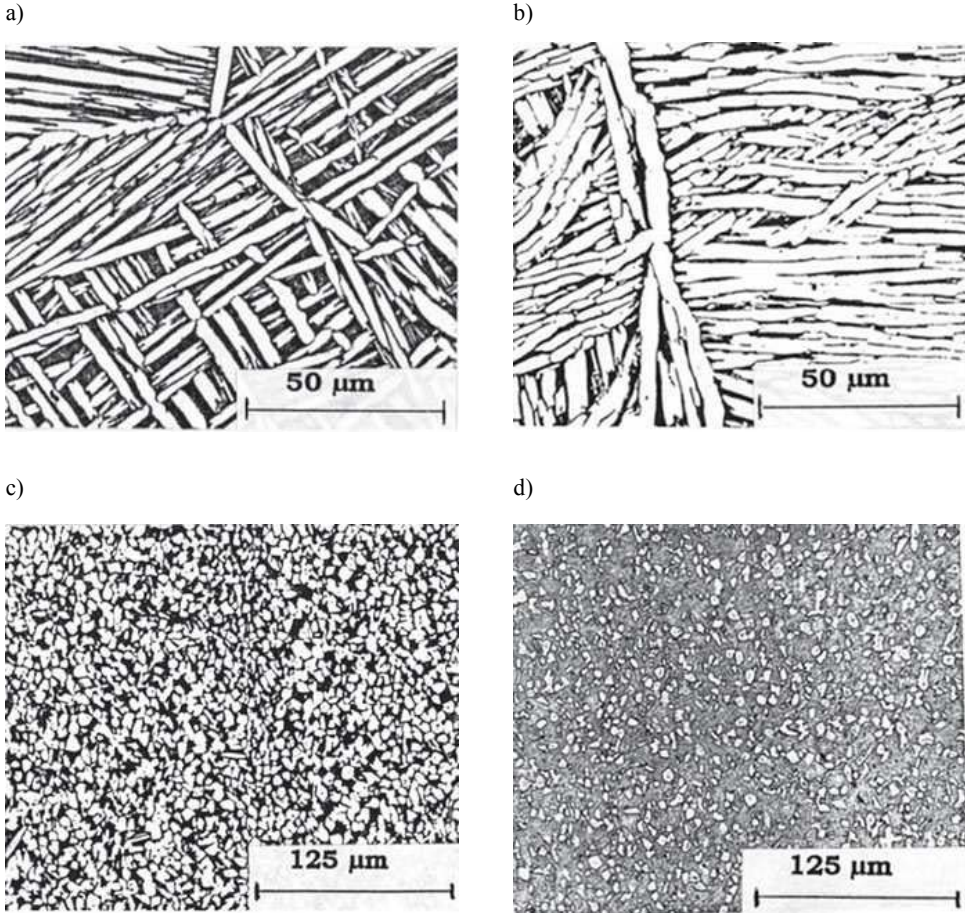
Figure 2.7: Final microstructure of Ti-6Al-2Sn-2Zr-2Cr-2Mo-Si: a) basket-weave microstructure after β solution treatment and fast cooling [75], b) lamellar colony structure after slowly cooling from β field [75], c) equiaxed structure after heat treatment at low temperature in α/β field [75], and d) duplex structure after heat treatment at high temperature in α/β region [75].

2.1.4 Alloying elements

We have already introduced the classification of alloying elements depending on their influence on the β-transus temperature: neutral elements, α stabilizers and β stabilisers. We want now to talk about their influence on Ti-alloy properties.

Al, Sn and Zr are added in almost all commercial Ti alloys, especially in α and near-α alloys. These three elements are soluble in both phases, and they have a good influence on the creep strength of α phase. In particular, Al increases the oxidation resistance, although, it deteriorates the ductility and deformation capability. It forms several intermetallic phases with Ti, as shown in Fig. 2.10: α_2-Ti$_3$Al , γTiAl, TiAl$_2$ and TiAl$_3$. α_2-Ti$_3$Al based alloys have high-temperature resistance and light weight. Additions of Zr, Si and Ga increases ductility of these
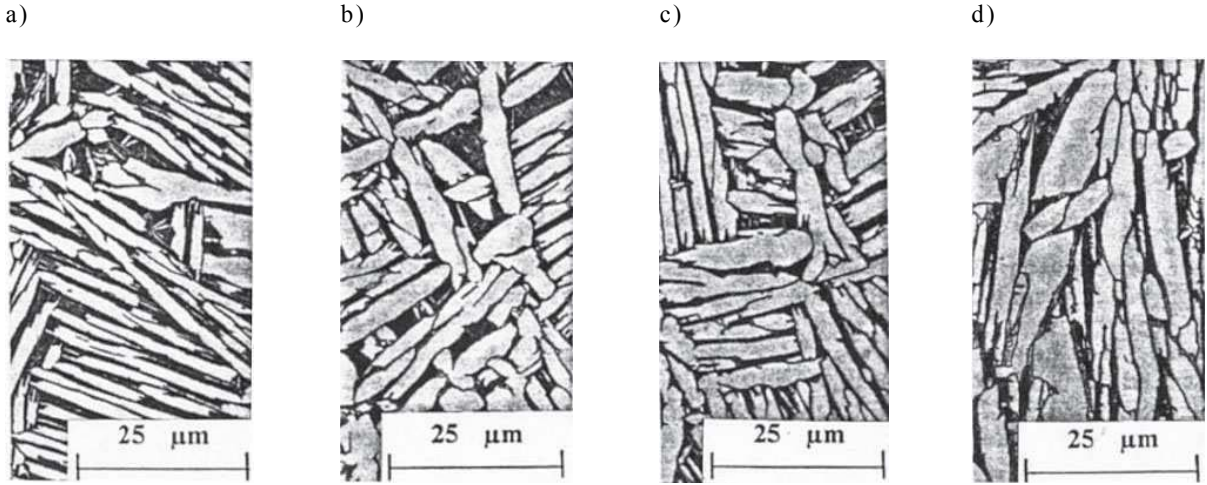
Figure 2.8: Correlation between α-platelet width, rate cooling parameterised by the time to half temperature (Th) and strength in martensite [76]: a) microstructure obtained at Th=100 s has 169 MPa strength, b) microstructure obtained at Th=1000 s has 160 MPa strength, c) microstructure obtained at Th=2000 s has 154 MPa strength, and d) microstructure obtained at Th=2880 s has 140 MPa strength.

alloys. γ-TiAl based alloys are used in aerospace and automotive industries because of their low density, high specific yield strength and specific stiffness, good oxidation resistance and creep properties. TiAl$_2$ and TiAl$_3$ phases embrittle Ti alloys, so the content of Al is usually kept under 6 wt.%. Some alloy elements promote solid-solution strengthening: Si, Sn, Zr are strengtheners of α phase, while Mo, V and Nb are solid-solution strengtheners of β phase. In particular, Si is recognised as playing a central role in the excellent high-temperature behaviour of near-α alloys [3] due to its limited diffusion and precipitation behaviour. Interstitial elements such as O, N, H and C generally improved mechanical properties of CP-titanium, but they negatively influence the ductility [22, 30, 77]. Addition of fast-diffusers, such as Cr, Co, Fe and Ni, has a negative influence on creep properties [5, 33–37].

2.2 High-temperature Ti alloys

This section is focusing on a particular group of Ti alloys: high-temperature alloys. Three new types of Ti alloys have been developed in the last few decades for high-temperature applications: dispersion strengthened alloys, aluminide alloys and near-α alloys [1].

In the first case, the improvement of creep behaviour is due to dispersoids of metalloids
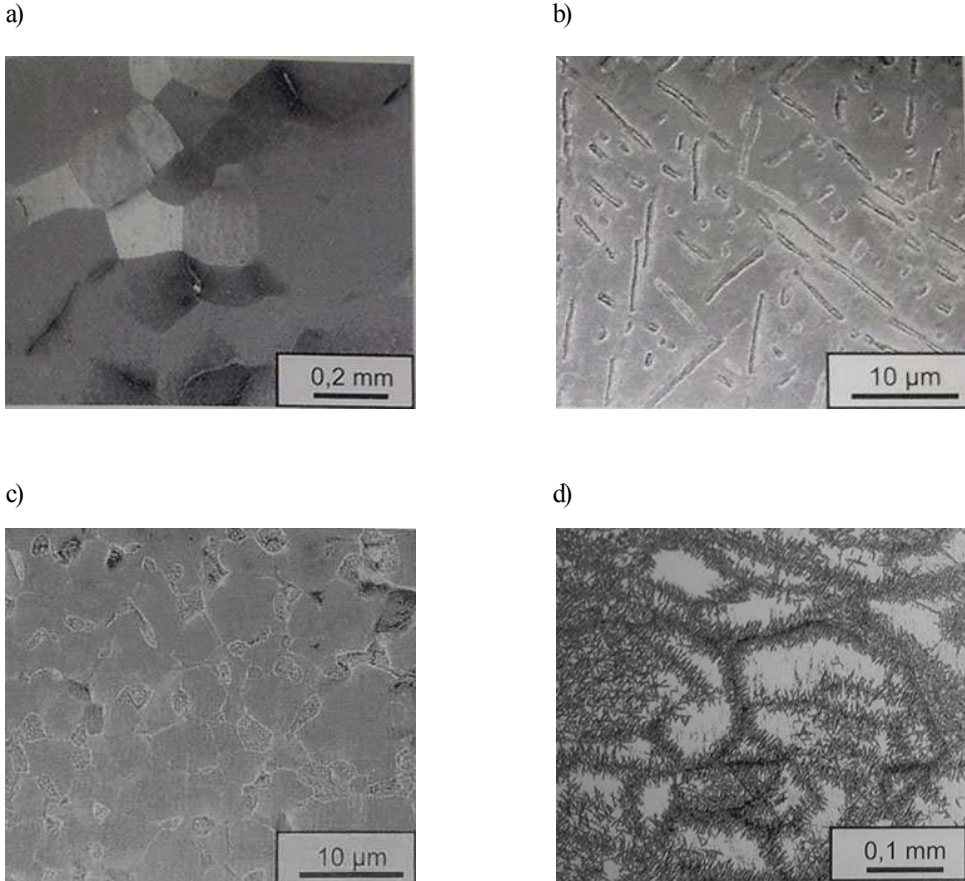
Figure 2.9: Different microstructures of β alloys: a) coarse β grains after solution heat treatment in β field of Ti-10-2-3 alloy, b) acicular structure after heat treatment in α/β field not followed by thermomechanical process of Ti-10-2-3 alloy, c) globular structure after heat treatment in α/β field followed by thermomechanical process of Ti-10-2-3 alloy, and d) fine distribution of secondary α after heat treatment and ageing of Beta-C [1].

or rare-earth metals (Er_2O_3, TiB, Y_2O_3) obtained after rapid solidification process [1]. Their high-temperature properties depend on the size and dispersion of these particles. They requires high solidification rate in order to obtain an homogenous distribution.

The second type of alloys contains a large amount of α_2-Ti_3Al and γ-TiAl [1]. These two compounds have ordered structure that increases the creep behaviour and raises the application temperature to 650-800 °C. However, they also cause brittleness and make these alloys hard to deform.

The last group, near-α alloys, has been investigated since 1975, when Seagle *et al* [3] reported that a small amount of Si (0.1 wt.%) improves the creep properties of conventional α alloys. The mechanism behind Si improvement of creep properties is still not completely clear. Several

17
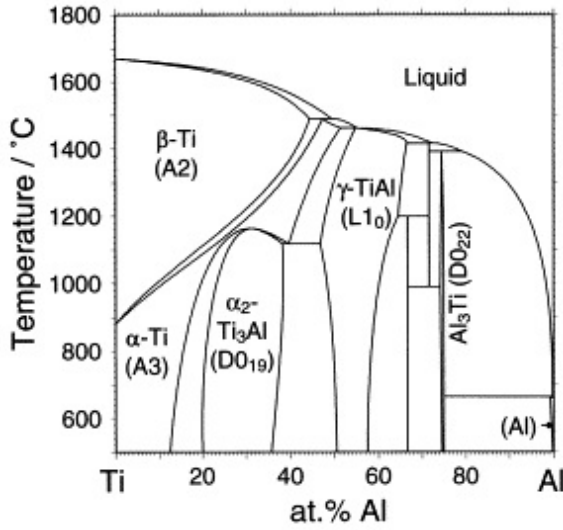
Figure 2.10: Ti-Al phase diagram (U. R. Kattner, 1992).

authors [3, 4, 13–19] have suggested that silicon diffuses to dislocation cores locking them, increasing the creep properties by a solid solution strengthening mechanism. Others [11, 12] have argued that creep improvement depends on silicide precipitation. Some researchers have suggested that the behaviour is a result of the combination of these two mechanisms [20]. Although the discussion is still open, it is clear that slow migration of Si in α-Ti plays a key role in the mechanical properties of near-α alloys. In general, the slow solute diffusion in α phase contributes to the excellent high-temperature behaviour of α-Ti alloys [1]. There is a strong dependence between creep properties, α phase content and microstructure [2, 5, 6]. The creep resistance increases with the volume fraction of α in TIMETAL®-6-2-4-2-S [5] (see Fig. 2.11). As reported by Bania and Hall [6], basket-wave morphology gives higher creep resistance with respect to equiaxed α grains. Despite their excellent behaviour at high-temperature, the use of near-α alloys in aerospace application is limited by their poor oxidation resistance and high reactivity to light elements (o, N and C) at high temperature [1]. Another negative effect on the creep properties of near-α alloys is due to the presence of fast-diffusers, such as Fe, Co, Ni [5, 33–37].
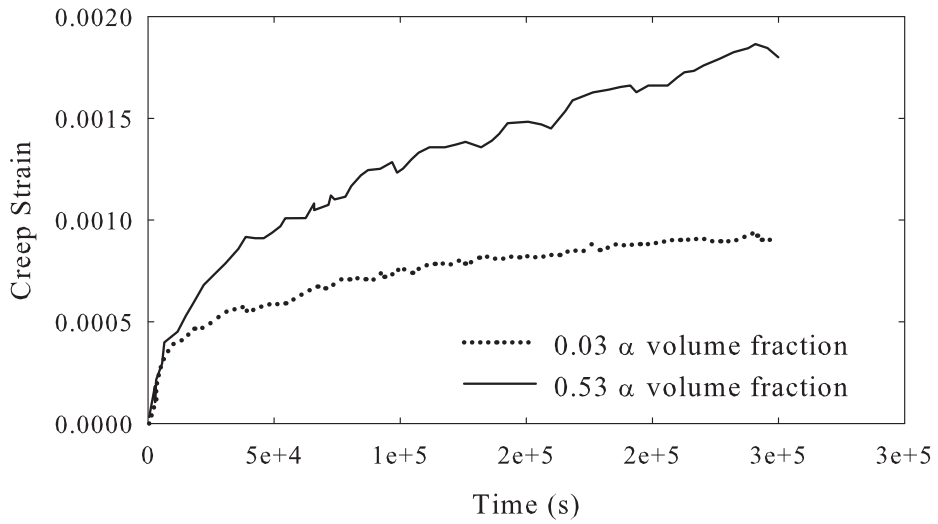
Figure 2.11: Comparison of creep curve of TIMETAL®-6-2-4-2-S with volume fraction of α equal to 0.03 and 0.53 [5]. The creep conditions are 510 °C and 241 MPa.

2.2.1 Creep mechanisms

Three regimes are usually observed during creep loading: primary and secondary creep, and failure. During primary creep, the strain rate is initially high, and then it slows down with time, while in secondary creep, the strain rate achieves a minimum and it becomes near constant. Failure happens in the last phase, when the strain rate increases exponentially with time. There are two creep mechanisms: diffusion creep and dislocation climb creep, both controlled by diffusion mechanisms. The first mechanism consists on the atom migration from one face of the grain to another, leading to the deformation of the grain. This can happen through the bulk (Nabarro-Herring creep) (see Fig. 2.12-a) or along the grain boundary (Coble creep) (see Fig. 2.12-b). These two processes are usually observed at the low stress range. The second mechanism involves dislocation motion. Dislocations can move along their glide plane until they encounter an obstacle, such as solute atoms, or precipitates. However, if the atoms at the bottom of the half-plane move away, the dislocation can climb up to a different glide plane and overcome the obstacle, as schematically shows in Fig. 2.12-c. This mechanism depends on the bulk diffusion behaviour.

In the case of α Ti alloys, it has been reported that this last mechanism governed the creep
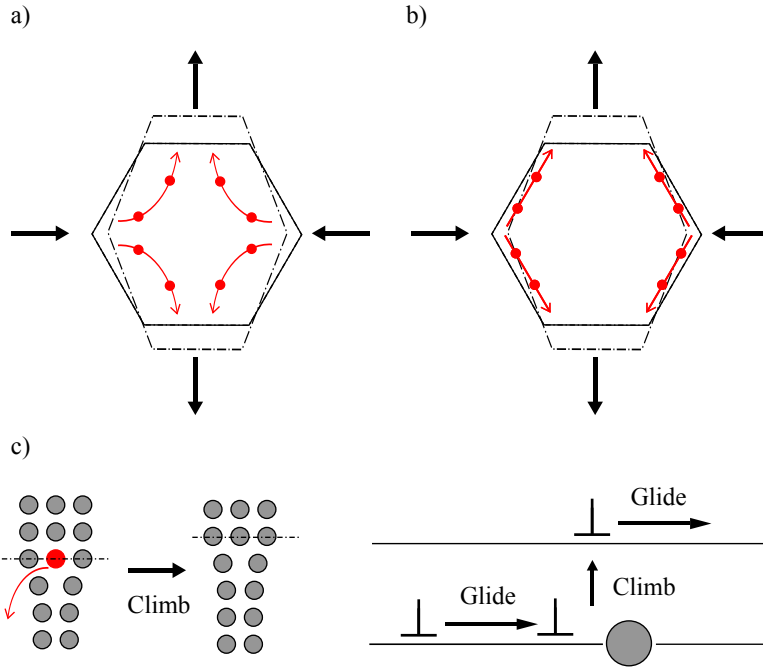
Figure 2.12: Schematic representation of creep mechanisms: in the diffusional mechanism, the deformation of the grain is due to the atom diffusion a) within the bulk (Nabarro-Herring creep), b) or along the grain boundary (Coble creep), while c) the climb dislocation creep consists of glide-climb movement of dislocations.

behaviour of these alloys [7, 8]. This is confirmed by TEM analysis of creep mechanism in near-α alloys [7, 37]. Fig. 2.13 shows $a - 1/3[11\bar{2}0]$ dislocations pinned with a jog (labelled j) at the screw segment in α phase during creep of TIMETAL®6-2-4-2-S [7]. In near-α alloys, the dislocation motion happens mostly within the α grains [7]. In his work, Es-Souni has focused on the study of the primary creep of near-α TIMETAL®6-2-4-2-S and TIMETAL®834 [78, 79]. He has reported that the grain size and morphology of α and β phases play a key role in primary creep. The primary creep resistance increases from globular to basket-weave morphology and from coarse to fine grains. He has also shown that the presence of silicides increases the creep properties by pinning dislocations. The secondary creep depends on the grain size and morphology as well, but also on the alloying elements, heat treatment and ageing time [3–6]. Three main factors have been reported as influencing the improvement of the secondary creep of these alloys: the addition of Si [3, 4], a lamellar morphology [5] and the refinement of α grains [3–5].
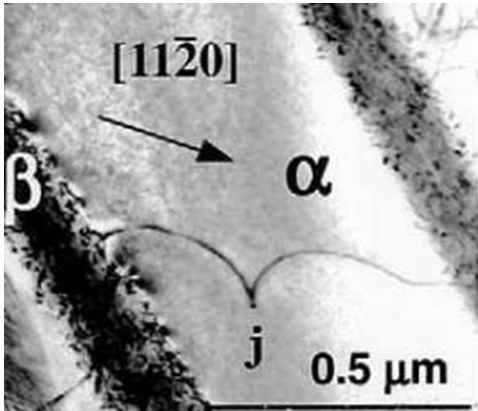
Figure 2.13: TEM images of jog (labelled j) pinning screw segments of dislocations in α phase during creep of TIMETAL®6-2-4-2-S [7].

2.2.2   Hot-corrosion and alpha-case formation

The dramatic effect of hot-corrosion limits the application of Ti alloys [1, 80]. Therefore, it has became extremely important to understand this mechanism.

In general, the oxidation mechanism in pure metals is constituted by the formation and growth of an oxide scale. Oxygen is adsorbed at the surface promoting the oxide nucleation. The nuclei grow until a compact oxide film covers all the metal surface. The growth of this layer is then controlled by mass transport mechanisms, which are grain-boundary diffusion and gas transport through micro/macro cracks and voids, at low temperature, and bulk diffusion at high temperature [1]. In the case of alloys, two possible oxidation phenomena can occur: selective oxidation and internal oxidation. The first one is usually desired and happens when alloy elements have different stabilities. At a critical concentration, the less noble element forms a stable oxide reducing the corrosion rate. Vice-versa, the internal oxidation is unwanted and occurs when O can dissolve and form oxide within the alloy. It is favoured by O solubility, diffusivity and affinity with the less noble element [1].

In the case Ti alloys, the O solubility and diffusivities are very high: solubility can reach 30 at.% [21, 22] at high temperature and diffusivity is about 10^3 times higher than self-diffusivity [22]. At room temperature, O interacts with Ti forming a thin passive layer of rutile, TiO_2. At high temperature, this layer is no longer passive and O rapidly dissolves in Ti matrix, forming a hard and brittle phase rich in oxygen known as the α-case [1] (see Fig. 2.14). Other interstitial
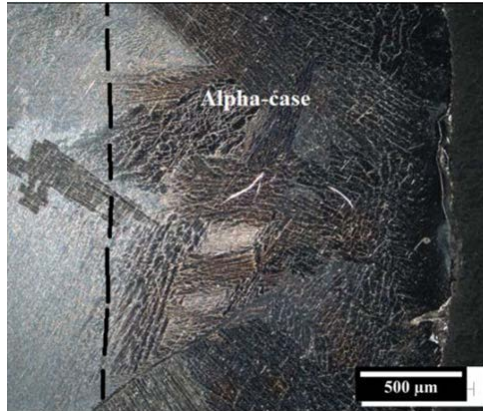
Figure 2.14: Alpha-case layer in Ti-6Al-4V [83].

elements also promote the formation of the embrittled phase: N and C [81, 82]. Similar to O, N has high solubility (19 at.% [22] at high temperature), while the highest solubility of C is 2 at.% [22]. The diffusivities of these elements are also 10^3 times higher than self-diffusion [22].

The α-case is a severe problem that affects casting, processing and high-temperature service of Ti alloys. The prevention of this phenomenon during casting and processing is quite expensive. α-case may form as a result of the reaction with liquid Ti and the mold wall, requiring the utilisation of expensive ceramic mold materials, such as CaO, ZrO_2 and Y_2O_3 [81]. During heat-treatment or forming, it is possible to reduce the α-case using anti-oxidant spray coating [84]. The machining or chemical removals are also used, but they can result in excessive loss of tool wear, because of the abrasive nature of this phase [84]. The fatigue life of Ti alloy is also affected by α-case resulting in a preferential crack initiate site for fatigue fracture [27]: Fig. 2.15 shows the crack nucleation site at the α-case layer on the surface of Ti-6Al-4V ELI [27]. The formation and propagation of this phase is also extremely dangerous during creep at high temperature. The study of Evans and co-workers [28] on creep behaviour of TIMETAL®834 shows that, for low stresses, the creep failure is due to the propagation of crack at the α-case.

2.3   Diffusion in alpha-Ti

Solid diffusion is fundamental for different topics in material science concerning solidification kinetics, phase equilibria, precipitation phases. At high temperature, solute migration is ap-
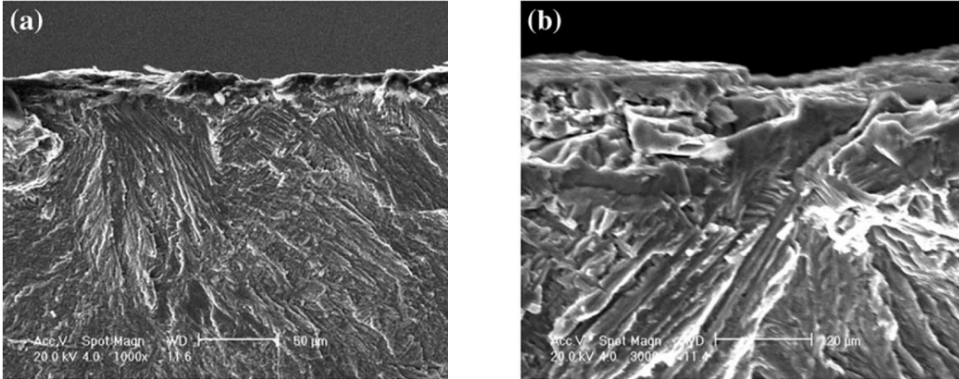
Figure 2.15: a) Crack initiation sites near the surfaces and b) fatigue facet in the α-case [27].

preciable and influences different process: creep, corrosion, solder embrittlement. Especially in the case of Ti alloy, solute diffusion can have positive (Si) or negative (Fe, Ni, Cr) influence on the dislocation climb mechanism or promote α-case (O, C, N).

2.3.1 Substitutional solutes (Si and semi-metals)

Addition of Si in α-Ti alloys has been extensively reported to improve the creep properties (see Fig 2.16) of these alloys [3, 4, 11–20] leading on the development of near-α Ti alloys. The debate on the strengthening mechanism involved is still open. Two main hypotheses have been developed: one identifies the interaction between Si atoms and dislocation cores as the source of increment of creep properties of near-α Ti alloys [3, 4, 13–19]. This theory suggests that solute atoms are attracted by dislocations, which are low-energy sites. The presence of solutes around the dislocation leads to a distortion of the lattice that can reduce the dislocation motion and enhance the creep resistance [85]. The solute atom segregation at the dislocation core depends necessarily on the solute diffusion. Therefore, it is not surprising that the supporters of this theory see as proof the small difference between the activation energies of solute diffusion and creep (see Table 2.2). On the other hand, the precipitation of silicides has been suggested as the cause of the creep behaviour of near-α alloys [11, 12]. The silicides usually formed have composition Ti_5Si_3. With the addition of Zr, the composition varies between $(TiZr)_5Si_3$ and $(TiZr)_2Si$ [20, 86]. Imbert has shown that thin silicides in IMI 684 alloy slow down the dislocation motion, increasing the creep properties [12]. Finally, Neal

Table 2.2: Comparison of activation energies of dislocation pinning process during creep (Q_{DSA}) and solute diffusion (Q) for different alloys calculated with experimental methods.

Alloys	Solute atoms involved	Q_{DSA} (eV)	Q (eV)
TIMETAL®834	Si	1.08 [19]	1.09 [14]
Inconel 718SPF7	C	1.39 [87]	1.44 [87]
3004 aluminium alloy	Mg	0.50 [88]	0.55 [88]
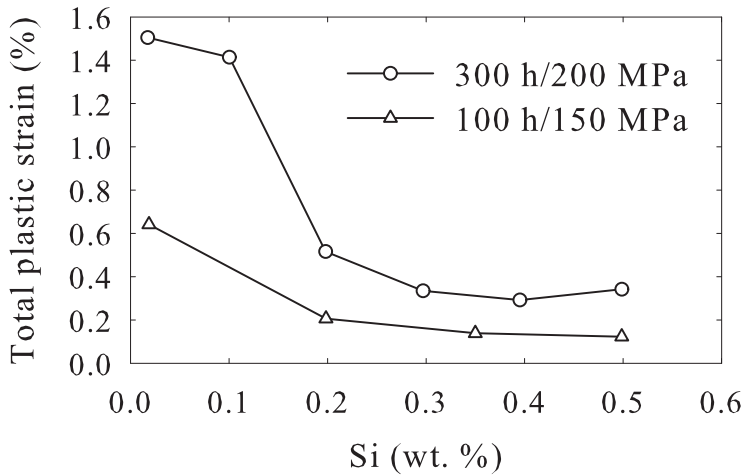
Figure 2.16: Influence of Si content on the creep properties of TIMETAL®834 at 600 °C [20].

and Fox [20] have pointed out that Si solubility in α-Ti is low (maximum of 0.8 at.%) and it is higher in β-phase. Therefore, after ageing or during service at high-temperature, the content of Si in solid solution in α phase reduces, and there is the formation of fine silicides from the transformation of β in α. Additionally, the silicides can form at the dislocations in the α phase [12, 18, 20], as shown in Fig. 2.17. It is important to notice that the nucleation, distribution and the size of silicides are also controlled by Si diffusion.

In conclusion, the good influence of Si addition on creep behaviour Ti alloys is due to its interaction with dislocation motion in α. Whether it is a result of solid solution and/or precipitation strengthening is still debated. Nevertheless, the Si diffusion controls both mechanisms and plays an important role on climb dislocation mechanism. Understanding the migration mechanism of this solute is important for the development of near-α alloys and to predict their behaviour during service.
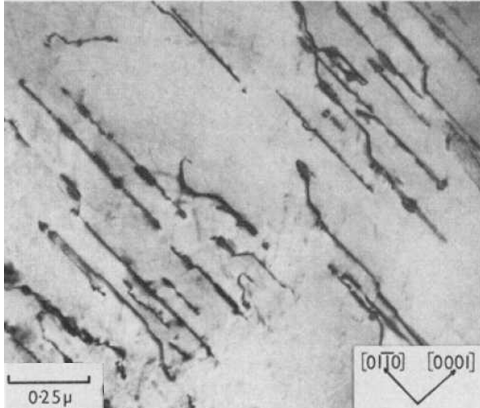
Figure 2.17: Silicides nucleated along the dislocations in Ti containing 1.7 at.% of Si and aged at 550 °C for 180 minutes [18].

Other solute atoms can have the same influence on creep properties of α-Ti. Hu and co-workers [89] have analysed the relationship between the binding energy of solute-vacancy pairs and creep properties of Ti using *ab initio* calculations. They have argued that solutes attracted by vacancy may improve the creep properties. They have suggested that vacancies can be treated as substitutional atoms with the largest size difference and a large elastic interaction with dislocations. Vacancies are attracted to dislocations and disappear in the dislocation. Therefore, a solute atom can be induced to move into the dislocation by the vacancy, promoting the solid solution or precipitation strengthening. Based on results of Hu and co-workers (see Fig. 2.18) [89], the elements sitting next to the Si on the periodic table, Al, Ga, Ge, In and Sn, known together as semi-metals, have potentially the same effect on high-temperature properties of α-Ti. Additionally, the diffusion study of these elements in Ti can give a reference for the Si diffusion behaviour itself and consequentially on its influence on the creep mechanism of near-α Ti alloys.

2.3.2 Interstitial solutes (O, N and C)

Oxygen, nitrogen and carbon are stabilizers of the α phase. As a result of their small neutral atomic radii ($R_O = 0.60$ Å, $R_N = 0.77$ Å, $R_C = 0.77$ Å [22]), they dissolve in interstitial sites. Considering the misfit-size between their radii and the hole size of the interstitial sites in α-Ti, it has been suggested that they mainly occupy the octahedral sites [22]. This determines a
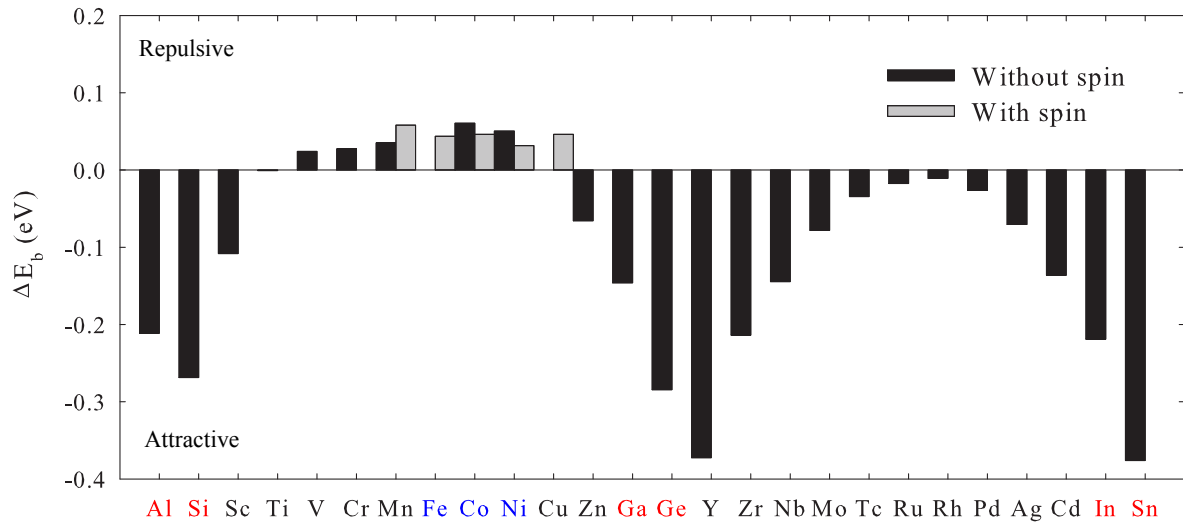
Figure 2.18: Binding energies of solute-vacancy pair in α-Ti evaluated with *ab initio* calculations [89]: red labels identify the semi-metals, while blue labels identify the fast-diffusers.

distortion of the hcp cell with a significant increment of c lattice parameter and consequently of c/a ratio [22, 29–31], as shown in Fig. 2.19. This distortion impedes the dislocation motion leading to an higher yield strength (YS), but a detrimental effect on ductility in Ti-alloys [22, 65, 90] (see Fig. 2.20). The influence of O content on the mechanical properties is confirmed by the *ab initio* study of Kwasniak *et al* [30] reported in Fig. 2.21. They have also found that negative influences of O on the plasticity of Ti does not only depend on the variation of c/a ratio but on the change of electronic structure, as well. The increase in O concentration transforms the metallic bond to a stronger covalent bond. The interaction between a O interstitial and a screw dislocation core has also been experimentally and computationally confirmed by Yu *et al* [91].

The solubility in Ti of these elements is very high, especially O and N. O solubility has a maximum of 30 at.% above 600 °C and it still is relative high at room temperature, 5 at.% [22]. N solubility is less compared to O but still significant, 19 at.% at high temperature and 2.5 at.% at room temperature [22]. On the other hand, C solubility is much smaller, the maximum is 2 at.% at high temperature and it reaches 1 at.% at room temperature [22]. This fact suggests that the atom size plays a key role on the interstitial solubility [22]. Nevertheless, Chao and
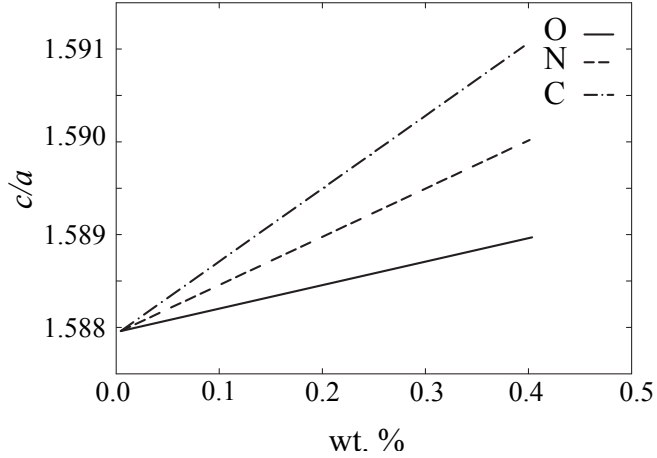
Figure 2.19: Influence of O, C, N additions on the c/a ratio of Ti [31].

Ansell [92] have showed that there is a strong relation between the solubility of interstitial elements (H and O) and the alloys' electronic structure (estimated using the electron/atom ratio). Additionally, these elements have high diffusivities relative to Ti self-diffusion values. Köpper *et al* [9] have extrapolated an activation energy for self-diffusion within the basal plane of 3.1 eV, that is 1.50, 1.58 and 1.64 times higher than Q_O, Q_N and Q_C, respectively [31]. These small Q values and the atomic radii suggest that these solutes migrate through the interstitial sites of α-Ti.

The combination of high solubility and diffusivity of O, N and C in Ti associated with the detrimental effect on the ductility has dramatic consequence on the high temperature properties of Ti alloys, promoting the α-case. Solubility governs the formation of this layer, while high diffusivity controls the rate of the penetration of this phase. At high temperature, the α-case depth increases with quadratic law with respect to the exposure time and with the temperature service, as shown in Fig. 2.22 [28]. Additionally, Zhu and co-workers [32] have studied the dynamics of oxidation in Ti with *ab initio*. They have found that the absorption of O into the bulk Ti reduces the total energy of the system of 1.6 eV leading to more stable state with respect to a layer of rutile on Ti [32]. They have evaluated the diffusion barriers for O migration in TiO_2 and have concluded that the oxidation is controlled by the O diffusion in bulk Ti. Therefore, it is important to understand the diffusion mechanisms of O, N and C in
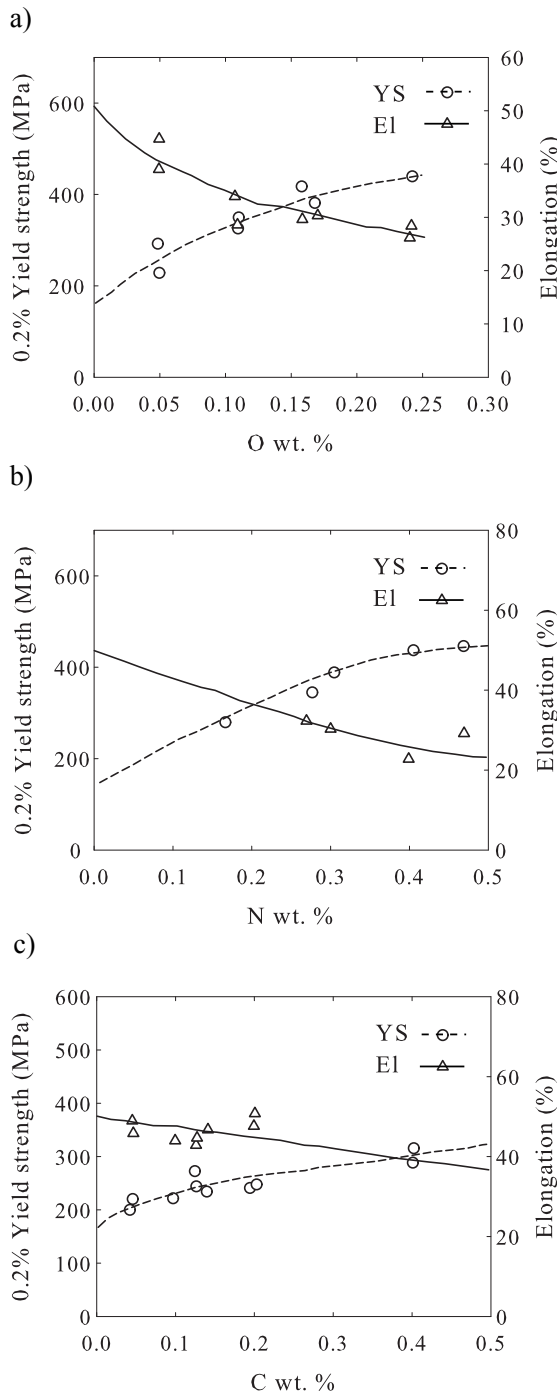
Figure 2.20: Influence of a) O, b) N and c) C additions on the yield strength (YS) and elongation (El) of α-Ti [65].

α-Ti, especially for the design of Ti alloys for aerospace applications. Mapping the transition path networks, through which the migration of these elements is developed, is fundamental for the study of prevention and/or control of α-case.
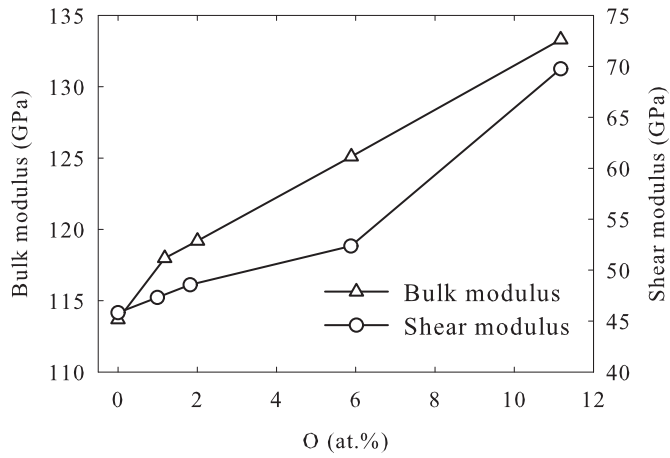
Figure 2.21: Influence of O on the bulk and shear modulus of Ti from *ab initio* calculations [30].
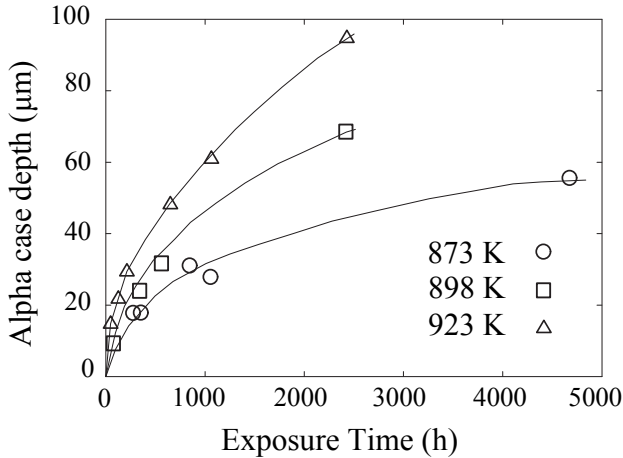
Figure 2.22: Dependence of α-case depth on exposure time at three different temperatures in TIMETAL®834 [28].

2.3.3 Fast diffusers (Fe, Co and Ni)

Titanium, Zr and Hf are known as "open" metals because of large ionic-to-atomic radii ratio compared to other metals [9]. This allows metallic atoms with small radius to dissolve interstitially and rapidly diffuse in the hcp crystal. Co, Ni and Fe have diffusivities that are 10^5 times larger than self-diffusivity [38–40]. Consistent with *ab initio* study of Hu and co-worker [89] (see Fig. 2.18), the creep properties of Ti alloys decrease due to the presence of these elements [5, 33–37]. As shown in Fig. 2.23, small additions of Fe and Ni significantly increase the creep deformation of near-α alloys, such as beta annealed TIMETAL®6-2-4-2-S [36]. Russo *et al* [36]

recommend limiting the Fe level to 0.5 wt.% and Ni level to 0.01 wt.% because of their detrimental effect on high-temperature behaviour. The researchers are still discussing the reason for this behaviour. In their work, Thiehsen and co-workers have reported the tendency of Fe and Ni to segregate in the β phase [5]. The presence of these elements enhances the self-diffusion in the bulk of β phase or at the grain boundaries affecting the creep properties. On the other hand, it has been argued that these elements can dissolve not only as substitutional but also as interstitial in α-Ti [7, 34]. This duality is confirmed experimentally by the work of Yoshida *et al* [44]. They have analysed the high temperature (472-850 °C) Mössbauer spectra of Fe in α-Ti during doping process of ^{57}Co [44]. Their findings indicates that substitutional and interstitial Fe atoms are in the equilibrium state. Because of this dual behaviour, they can form atom-vacancy pairs decreasing the self-diffusion energy barrier and consequentially have a negative effect on the creep properties. This assumption is based on the fact that a very minute addition of these elements significantly accelerates the self-diffusion [9]. Higher self-diffusion coefficients lead to more mobility of dislocation jogs increasing the strain rate [7]. This is also confirmed by the work of Gollapudi *et al* [93] who have estimated the rate of dislocation rearrangement during steady creep in TIMETAL®834 containing high and low concentrations of Fe and Ni. Their results at 873 K, 923 K and 973 K for different applied stress are summarised in Fig. 2.24. The rearrangement rate is consistently higher in the case of high contents of Ni and Fe [93], indicating more dislocation mobility. The enhancement of self-diffusivity is related to the diffusion mechanism of these elements [42, 43, 46, 47, 94]. The rapid diffusion migration of fast diffusers and the enhancement of self-diffusivity can affect the creep behaviour of near-α alloys. Therefore, a deep understanding of the diffusion mechanism of these elements in α-Ti is required for the design of near-α alloys with high creep properties.

2.3.4 Diffusion mechanisms

Diffusion consists on the transport of matter from a high-chemical potential to a low-chemical potential region, minimising the Gibbs free energy of the system. It is very fast in gases (10^{-4} m^2/s), slow in liquids (10^{-6} m^2/s), and extremely slow in solids (10^{-12}-10^{-18} m^2/s). Fick's laws

a)

b)
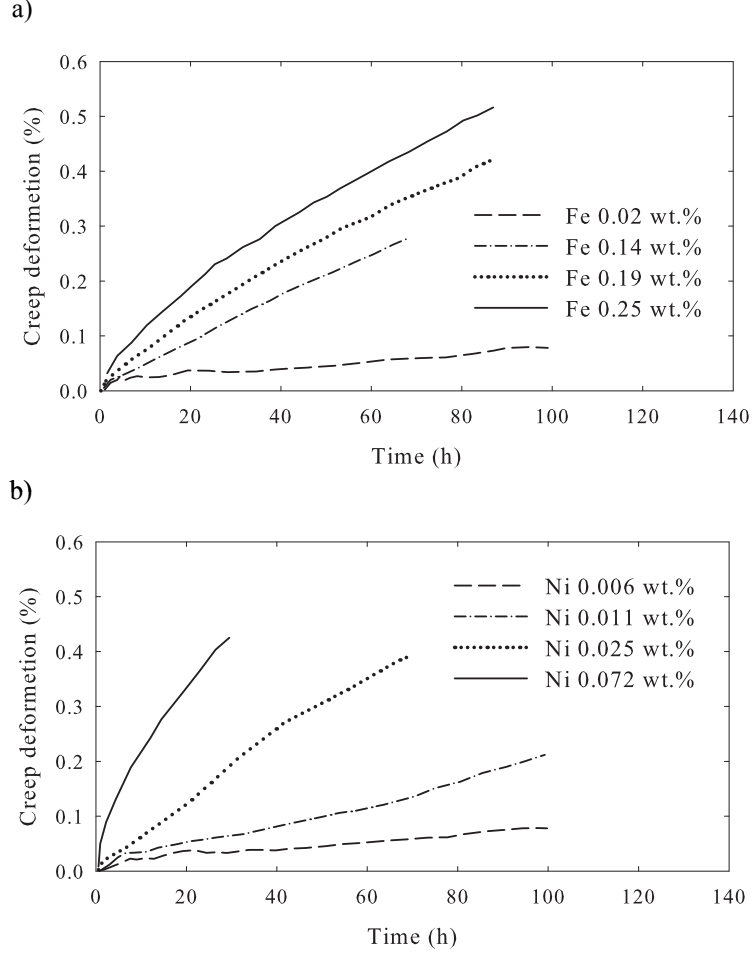
Figure 2.23: Effect of a) Fe (with 0.006-0.008 wt.% Ni) and b) Ni (with 0.02-0.03 wt.% Fe) contents on creep deformation of beta annealed TIMETAL®6-2-4-2-S [36]. In both case the creep conditions are 566 °C and 172 MPa.

phenomenally describe this mechanism,

$$J = -D\nabla C, \tag{2.1}$$

$$\frac{\delta C}{\delta t} = \nabla \cdot (D\nabla C), \tag{2.2}$$

where J is the flux of diffusion particles, C is the particle concentration and D is the proportionality factor called diffusion coefficient or diffusivity. The first equation shows the relation between J and the concentration gradient. The second describes the evolution of C in time. In the case of isotropic materials, for example cubic crystals, diffusivity is a scalar quantity, direction independent. In anisotropic materials, D depends on the direction and is a second-rank

31
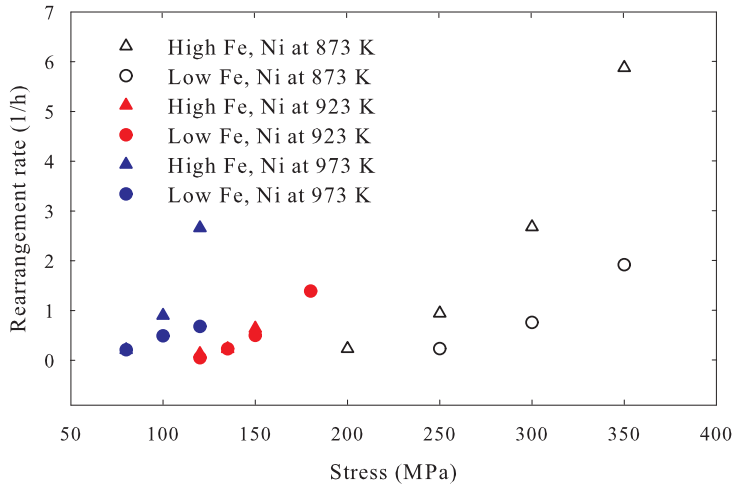
Figure 2.24: Rate of dislocation rearrangement during steady creep in TIMETAL®834 containing high (triangles) and low (circles) concentrations of Fe and Ni at 873 K (white), 923 K (red) and 973 K (blue) [93].

tensor. Diffusivity usually obeys Arrhenius' equation,

$$D = D_0 \exp\left(-\frac{Q}{k_b\,T}\right),\tag{2.3}$$

where D_0 is the pre-exponential factor, k_b is the Boltzmann constant, T is the absolute temperature, and Q is the activation energy.

Microscopically, diffusion is due to the Brownian motion of atoms and molecules. Because of the Boltzmann distribution of energy, particles are always subjected to thermal fluctuations causing stochastic motion. In solid crystals, diffusion is usually driven by atomic hops in the lattice. Point defects (vacancies, self-interstitial, interstitial) play a key role on these atomic jumps, migrating themselves or mediating atomic migration. Depending on the type of crystal defect involved, atomistic diffusion is classified as vacancy-mediated, divacancy, interstitial (solute atom migrates within the interstitial sites), interstitialcy (interstitial diffusion involving solvent atoms rather than interstitial solutes), and interstitial-substitutional exchange mechanisms such as dissociative mechanism (when the interstitial solute move into a vacancy) and kick-out mechanism (when the interstitial solutes takes the place of a the host atom at lattice site).
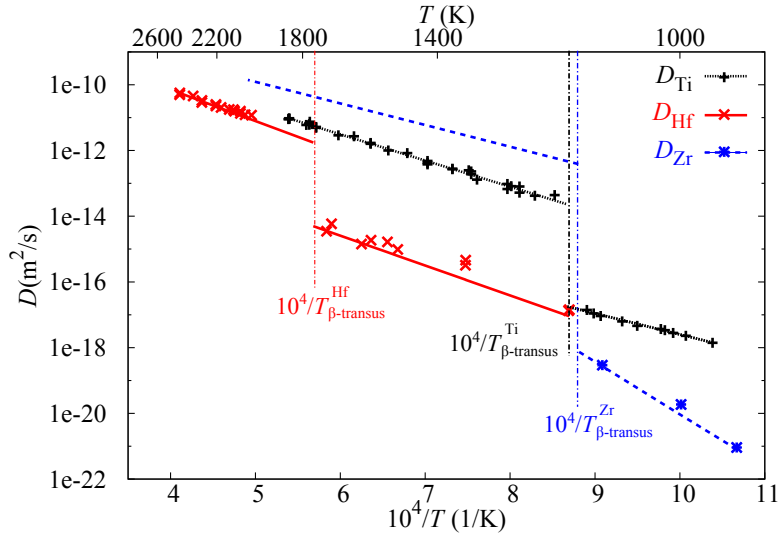
Figure 2.25: Self-diffusion coefficients of α-Ti [95], β-Ti [96], α-Hf [97], β-Hf [96], α-Zr [98] and β-Zr [99].

2.3.5 Experimental surveys on solute diffusion in alpha-Ti

The solute and self-diffusion behaviour in Ti is peculiar, due to its crystal structures. As mentioned earlier, atom diffusion in α-Ti is much lower than β phase. In particular, Ti belongs to the group of open metals such as Hf and Zr, which have the same allotropic phases of Ti. The diffusion coefficients in these metals present a discontinuity at the transition temperature, as shown in Fig. 2.25. Typically, the diffusion behaviour of allotropic metals shows a change of diffusivity slope at the transition temperature. Diffusion in α-Ti is anisotropic as a result of the hcp crystal. Usually, solute diffusion along the c-axis is slower than diffusion within the basal plane. However in the case of fast diffusers, the migration along c-axis is faster. Polycrystalline diffusivities are useful for practical purposes. For a more detailed understanding of diffusion mechanism, single crystal diffusion study is necessary. This section presents a survey of the experimental data available in the literature of semi-metals (Si, Al, Ga, Ge, In and Sn), light elements (O, N and C), and fast-diffusers (Fe, Co and Ni) migration in α-Ti.

Semi-metals dissolve as substitutional solute atoms, since they have similar radii to Ti atoms. The bulk self-diffusion has been explored using the residual activity method with ^{44}Ti [95]. The diffusion behaviour of Al [100] and Si [101] has been studied using nuclear resonance broadening (NRB) method on implanted Ti samples. Rutherford back-scattering spectrometry

(RBS) was applied to study Ga [102], Sn [103], and In [104] diffusion in polycrystalline Ti. All these data are reported in Fig. 2.26-a. At the end of the 90's, Köppers *et al* [9, 10] had studied Al, Ga, In and self-diffusion in ultrapure single crystal α-Ti along the direction parallel to the basal plane ($D_\parallel$) reported in Fig. 2.26-b. They used ^{44}Ti radiotracer and ion beam sputtering techniques for self-diffusion, and isotope of Al, Ga and In evaporated in the sample followed by Secondary ion mass spectrometry (SIMS) analysis. The diffusion coefficients of these solutes are similar to the self-diffusion confirming the hypothesis of vacancy-mediated diffusion behaviour. In the case of Al and self-diffusion, they also evaluated the perpendicular diffusivity ($D_\perp$) for two temperatures, allowing them to extrapolate the anisotropy ratios, $D_\perp/D_\parallel$, equal to 0.5 and 0.63 for self-diffusion and Al, respectively.

Light solutes, such as O, N, and C, are small atoms compared to Ti, hence they dissolve in interstitial sites and migrate through them. Oxygen and nitrogen bulk diffusion processes have been studied by Bregolin *et al* [23, 24] (see Fig. 2.26-c). They have used ion implantation and nuclear resonance techniques to study the diffusion of ^{18}O [23] and ^{15}N [24] in high-purity Ti samples (99.99%) of about 2 cm in diameter and 1 mm thickness annealed for 10 days at 1133 K in order to obtain a few big grains to avoid the effect of grain-boundary diffusion and residual stress. As shown in Fig. 2.26-c, their diffusion rates are one or two orders of magnitude higher than self-diffusion. De Barros *et al* [25] have studied the bulk diffusion coefficients of C. Their study consists of performing a diamond deposition by microwave plasma assisted with chemical vapour deposition technique on pure bulk titanium substrate. The C diffusivities are obtained from the carbon concentration profile in the diamond, titanium carbide and alpha titanium obtained by energy-dispersive X-ray analysis. A survey of C diffusivity in Ti has also been conducted by Minkwitz and Herzig in single and polycrystalline samples, using radiotracer technique with ^{14}C [26]. Carbon diffusion coefficient is higher compared to O and N migration, as shown in Fig. 2.26-c. The high values of D compared to substitutional diffusivities confirms that the migration of these elements is interstitial.

Experimental data of transition metal diffusion (Fe, Co, Ni) are reported in Fig. 2.26-d. Diffusivities have been measured by radiotracer electro-planted on a high-pure-Ti single-
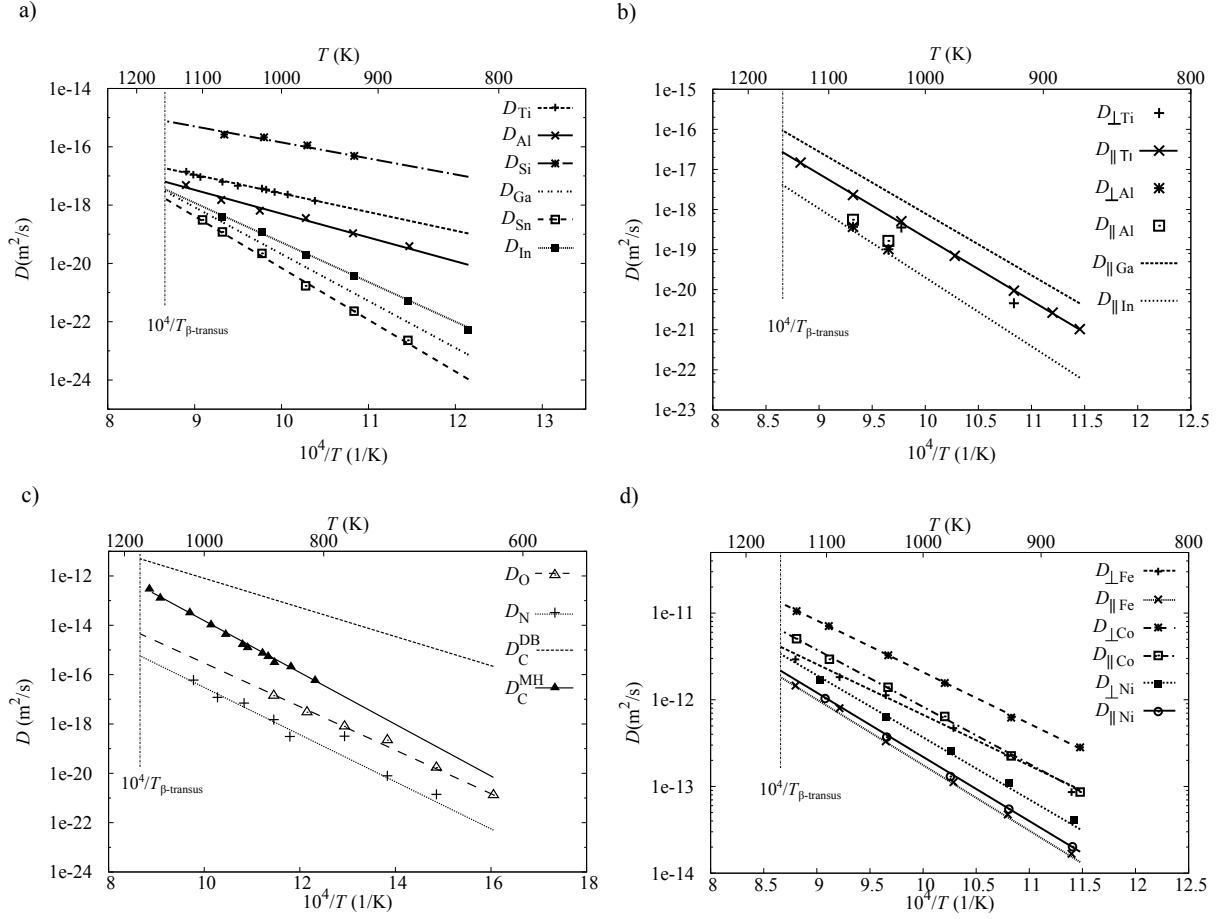
Figure 2.26: a) Self- [95], Al [100], Si [101], Ga [102], Sn [103], and In [104] diffusion coefficients in polycrystal α-Ti, b) Al, Ga, In and self-diffusivities in ultrapure single crystal α-Ti [9, 10], c) O [23], N [24] and C (D_C^{DB} [25] and D_C^{MH} [26]) diffusion coefficients in polycrystal α-Ti, and d) Fe [40], Co [39] and Ni [38] diffusivities in single crystal α-Ti.

crystal specimen [38–40]. These solutes exhibit diffusion coefficients three or five orders of magnitude higher than self-diffusion, and their anisotropy diffusion behaviour is opposite to the common trends of self- and substitutional diffusion. As mentioned earlier, these solutes can dissolve at interstitial and substitutional sites of Ti. This suggests that they migrate by the dissociative diffusion mechanism proposed by Frank and Turnbull [42], and perform combination and dissociation reactions with vacancies [46, 105] that can explain the enhancement of self-diffusion [47].

2.3.6 Computational studies of diffusion mechanisms

Performing an experimental study of diffusion behaviour is not a trivial task, especially for hcp structures that require the manufacture of single crystals. In the case of an open metal like Ti, the study is more complex because it also requires a high-purity sample to avoid the influence of fast-diffusers. Nevertheless, based on the diffusivity data, we can form only an hypothesis on the mechanisms involved. This lack of information can now be filled using analytical models implemented by quantum mechanical calculations.

Several studies have been conducted on the solute diffusion in fcc (transition metals diffusion in Ni [106]), bcc (solute diffusion in α-Fe [107]), and hcp (self and solute diffusion in Mg and Zn [48, 49]) systems using the analytical models of diffusivity in dilute alloys developed by Lidiard, Manning and Ghate [51, 108, 109] implemented with *ab initio* calculations. These studies not only show that computational data can be used to predict the diffusivity values, but they also reveal the importance of the electronic structure of the solvent-solute bond on diffusion barriers. Additionally, analytical model for interstitial diffusion was developed by Landman and Shlesinger [52, 53], and applied to O diffusion in Ti by Wu and Trinkle [50] and to O and N diffusion in α-Hf by O'Hara and Demkov [110]. Mapping the diffusion path networks of these interstitial elements is very important to discover and implement actions to prevent their deleterious effects.

A good instrument to test the accuracy of these analytical models is the Monte Carlo method [111]. This method was developed to simulate stochastic phenomena. It basically consists on determining and describing the possible processes and mechanisms that can happen in a given system and choosing randomly which one to perform. The main challenge of this approach is to recognise and list the events involved in the phenomenon considered. Nevertheless, it can be use to validate which processes actually occur in a particular mechanism. A variant of this method, called kinetic Monte Carlo (KMC), is used to study the atom diffusion in solids. It was initially developed to describe vacancy migration in ordered alloys [55] and then for more complicated process such as diffusion in non-dilute systems [112] or vacancy-modified interstitial diffusion of O in Ni [54].

Table 2.3: Composition of Ti alloys [1, 12, 14, 27, 66, 113–117].

Alloys	Si [at%]	Al [at%]	V [at%]	O [at%]	Fe [at%]	Mo [at%]	Zr [at%]	C [at%]	N [at%]	Pd [at%]	H [at%]	Sn [at%]	Nb [at%]	Cr [at%]	Ta [at%]	W [at%]
α alloys																
Grade 1				0.532	0.169			0.315	0.101		0.703					
Grade 2				0.737	0.253			0.314	0.101		0.702					
Grade 3				1.030	0.253			0.314	0.168		0.701					
Grade 4				1.176	0.421			0.313	0.168		0.700					
Grade 7				0.738	0.254			0.313	0.168	0.089	0.7					
Grade12				0.739	0.254	0.148		0.315	0.101		0.704					
Ti-5Al-2.5Sn		8.639		0.538	0.417							0.982				
TIMETAL®8-1-1		13.691	1.092	0.334	0.12	0.580		0.296	1.589		0.177					
TIMETAL®-6-2-4-2		11.296		0.440	0.210	1.075	1.850	0.312	0.167		0.581	0.869				
IMI679	0.917	4.774		0.644	0.185	0.644	3.389				0.639	4.991				
TIMETAL®-6-2-4-2-S	0.135	11.377		0.354	0.211	1.108	2.330		0.169		0.586	0.895				
TIMETAL®685	0.579	10.847		0.581	0.042	0.363	3.055	0.309	0.099		0.461					
LT26A	0.431	11.559		0.422	0.02	0.257	3.011	0.159	0.006		0.139					
TIMETAL®834	1.025	10.845		0.450	0.043	0.375	2.629	0.320	0.103		0.286	2.021	0.516			
TIMETAL®1100	0.84	11.023		0.266	0.017	0.246	2.329	0.157	0.101			1.193				
IMI684	0.759	9.24			0.004		2.732	0.127				0.639	4.991			0.980
α/β alloys																
Ti-6Al-4V		11.262	3.977	0.563	0.322			0.300	0.161		0.670					
Ti-6Al-4V ELI		10.164	3.652	0.314	0.147			0.049	0.013		0.109					
Ti-6-6-2		10.236	5.422	0.575	0.824			0.192	0.164		0.685	0.969				
IMI 550	1.176	8.740		0.398	0.169	2.458			0.455		0.585	0.993				
Ti-6-2-2-2	0.450	10.835		0.380	0.126	1.097	1.154	0.156	0.100		0.580	0.887		1.574		
Ti-17		9.799			0.258	2.255	1.317		0.137		0.596	1.012		4.160		
β alloys																
TIMETAL 10-2-3		6.185	14.975	0.387	0.213				0.170		0.710	1.406		3.209		
Beta C		7.165	8.064	0.423	0.260	2.267	2.384	0.201	0.104		0.959			6.042		
TIMETAL 21S	0.450	6.564		0.474	0.362	8.438		0.211	0.181		0.753		1.634			
TIMETAL LCB		2.706		0.456	3.922	3.449		0.203	0.174		0.724					
Ti-35Nb-7Zr-5Ta-0.06O				0.236			4.967	0.068	0.009		0.062		23.913		1.704	

37

Chapter 3

Computational Method

3.1   A very brief introduction to Quantum Mechanics

The dual nature of electrons and other particles was proposed by De Broglie in 1924. The energy of a particle in motion is a function of its mass and speed, while the energy of a wave depends on its frequency. The double nature leads to the fact that if the speed is known then the frequency can be deduced and vice-versa. In the 1926, Schrödinger formulated the fundamental equation of Quantum Mechanics, describing the particle state as wave function, Ψ, which time-independent form is,

$$-\frac{\hbar^2}{2m}\nabla^2\Psi + V\Psi = E\Psi, \qquad (3.1)$$

where $\hbar$ depends on the Planck constant, $\hbar = h/2\pi$, V is the potential energy, E is the quantum energy of the system, and Ψ is a function of the position, r_n. If V of a system is known, it is possible to solve Schrödinger's equation for all the states of the system. However, solving Schrödinger's equation and writing the wave function for a system of N particles in three dimensions is very complex. The complexity was reduced by the probabilistic Bohr interpretation of wave function. Bohr defined the probability density of finding a electron in given place and at given time as $|\Psi|^2$, which is always a real positive number. Additionally, for

a given system the electronic density, $n(r)$, is uniquely defined as normalised wave function,

$$n(r) = N \int dr_1^3 ... \int dr_N^3 \Psi(r_1...r_N) * \Psi(r_1...r_N). \tag{3.2}$$

The electron density is the key variable of the Quantum Mechanics model called Density Functional Theory (DFT).

3.2 Density Functional Theory

Density Functional Theory was developed by Hohenberg and Kohn [57] in the 1964, when they published an approach to study the properties of a homogeneous interacting electron gas. This theory is based on two fundamental theorems,

- **Theorem I**: for any system of interacting electrons in an external potential, $V_{\text{ext}}(r)$, the free energy is uniquely determined as functional of electron density, $n(r)$.

- **Theorem II**: the free energy functional is minimised by the ground state energy, E_{GS}, defined by the ground state electron density, $n_{GS}(r)$.

DFT allows one to find the ground state energy of any electron system using the Schrödinger's equation without any input from experiments. In their article, Hohenberg and Kohn successfully applied this theory to two simple cases: nearly constant density and slowly varying density. Unfortunately, an electronic system is more complicated than these two cases, and the formulation of free energy functional remains unknown. A decisive progression of this theory was the Kohn-Sham approach [56]. This approach bypasses the problem of definition of functional using an auxiliary system that can be solved more easily. The main idea is to substitute an interacting system with an non-interacting system, which is easier to solve, plus a quantity that contains all the information about the electron-electron interactions: the exchange-correlation energy, E_{xc}. The problem of the definition of the functional is still unsolved, it is just moved from E_{GS} to E_{xc}. The only way to define E_{xc} is using an approximation. The most common approximations are:

- Local Density Approximation (LDA),

- Local Spin Density Approximation (LSDA),

- Generalised-gradient Approximation (GGA).

The first one was conceived by Kohn and Sham in 1965 [56], assuming that the electron density changes very slowly. Under this statement the exchange-correlation energy can be written as,

$$E_{xc}[n] = \int n(r)\varepsilon_{xc}(n(r))dr \qquad (3.3)$$

where ε_{xc} is the exchange-correlation energy per electron of an uniform electron gas. This approximation describes exactly the properties of a system in two particular cases: slowly varying density and high density. LSDA is an extension of LDA, considering the electron density as a function of up and down spins,

$$E_{xc}[n(r,\uparrow), n(r,\downarrow)] = \int n(r)\varepsilon_{xc}(n(r,\uparrow), n(r,\downarrow))dr. \qquad (3.4)$$

The structural properties obtained by LDA or LSDA are usually good, while the calculations of band gap, binding energies can result in large errors. In order to overcoming these problems, it needs to take into account the gradient of the $n(r)$ in the formulation of ε_{xc}, the GGA approximation,

$$E_{xc}[n] = \int n(r)\varepsilon_{xc}(n(r,\uparrow), n(r,\downarrow), \bigtriangledown n(r,\uparrow), \bigtriangledown n(r,\downarrow))dr \qquad (3.5)$$

GGA is usually but not always more accurate than LDA, and improves the calculations of transition state barriers.

DFT implementation method starts by defining the atomic and electronic structures of the system. The atomic structure is described by crystal structure (e.g. bcc, fcc, hcp lattice) and presence of defects (e.g. solute atoms, vacancies, dislocations), while the electron structure is described by an approximation of the true external potential. The second step of the procedure
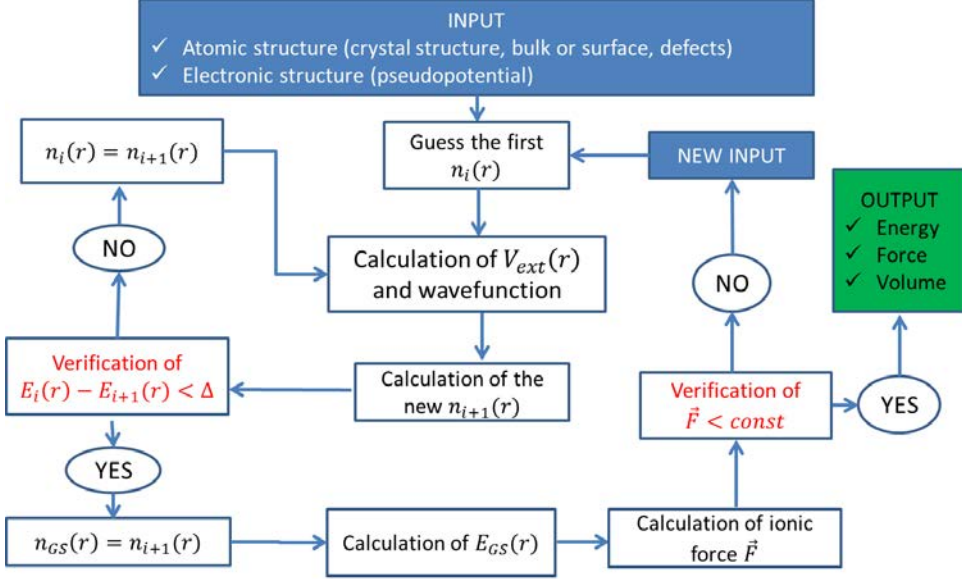
Figure 3.1: Diagram summarizing the implementation steps of DFT.

is to guess the first electron density, $n_i(r)$, and calculate the effective potential, V_{eff}, as sum of the exchange correlation potential, $\mu_{xc}(r)$, depending upon the exchange-correlation approximation, and the fixed V_{ext}. Given V_{eff}, it is possible to solve the Schrödinger's equation, and obtain Ψ and the corresponding new $n_{i+1}(r)$. At this point the free energies corresponding to $n_i(r)$ and $n_{i+1}(r)$, $E[n_i]$ and $E[n_{i+1}]$ respectively, need to satisfy,

$$E[n_{i+1}] - E[n_i] < \Delta \tag{3.6}$$

where Δ is a constant previously set. If this is not verified, it means that the accuracy of $n_i(r)$ needs to be improved, repeating all the procedure with the updated electron density. Vice versa, if the inequality 3.6 is true, the next step is the minimisation of $E[n_{i+1}]$ and the evaluation of the ground state energy, E_{GS}. The final step is to determine the ionic force, $\vec{F}$, depending on V_{ext}. Since V_{ext} is an approximation, the ionic force must be smaller than a fixed constant. If this criteria is not satisfied, it implies that the initial atomic and electronic structures are wrong, requiring a better guess of the input data. When successful, the system is described completely by the ground state energy, force, and volume. The diagram in Fig. 3.1 summarises all these steps. In recent years, different packages have been created to implement DFT. In

this work, Vienna *ab initio* simulation package (VASP) [58–61] was used.

The ground state energy is useful to understand the properties of molecular and crystal structures, and it gives information on the force acting on the nuclei at non-equilibrium states [118]. The Density Functional Theory has been successfully used for atomic and molecular problems, as well as in condensed matter studies. DFT has become an important tool in many fields such as solid-state chemistry, surface science, biochemistry, materials science, mineralogy, nuclear physics, and astrophysics. For example, DFT can predict phase transformation [119], structural properties such as geometries of molecules [120], defect structure (vacancy, grain boundary, interstitial, self-interstitial) [121–130], surface structures and adsorption kinetics [32, 131, 132], mechanical properties of materials (elastic modulus, compressibility, thermal expansion coefficients) [133–136], thermodynamic properties [137], phase diagrams [138], transport properties [48–50, 54, 121], electronic, electrical and optical properties [139], magnetic properties [140] and chemical properties [141]. Despite its success in different areas, DFT utilisation presents some restrictions and requires accurate validations of the results. This requires the careful choice of the approximation of the exchange correlation function. Additionally, the data comparison needs to be performed cautiously keeping in mind that different settings can lead to variable results.

3.2.1 Vienna *ab initio* simulation package

Vienna *ab initio* simulation package [58–61] evaluates the free energy and its ground state. The matrix diagonalisation schemes and Pulay/Broyden charge density mixing are used in VASP implementation. In this work, all the calculations were obtained using VASP 5.3.2 [58–61], where the electronic structure was described by the projector augmented wave method (PAW) [142] and the exchange-correlation functional was computed using the generalised gradient approximation (GGA) parameterised by Perdew-Burke-Ernzerhof (PBE) [143]. We chose to approximate E_{xc} with GGA with four valence electrons. GGA gives good results in terms of bulk properties, such as lattice parameters, elastic constants [144]. All the calculations were performed fully relaxation of the cell at constant pressure. The vasp parameter of energy cut-
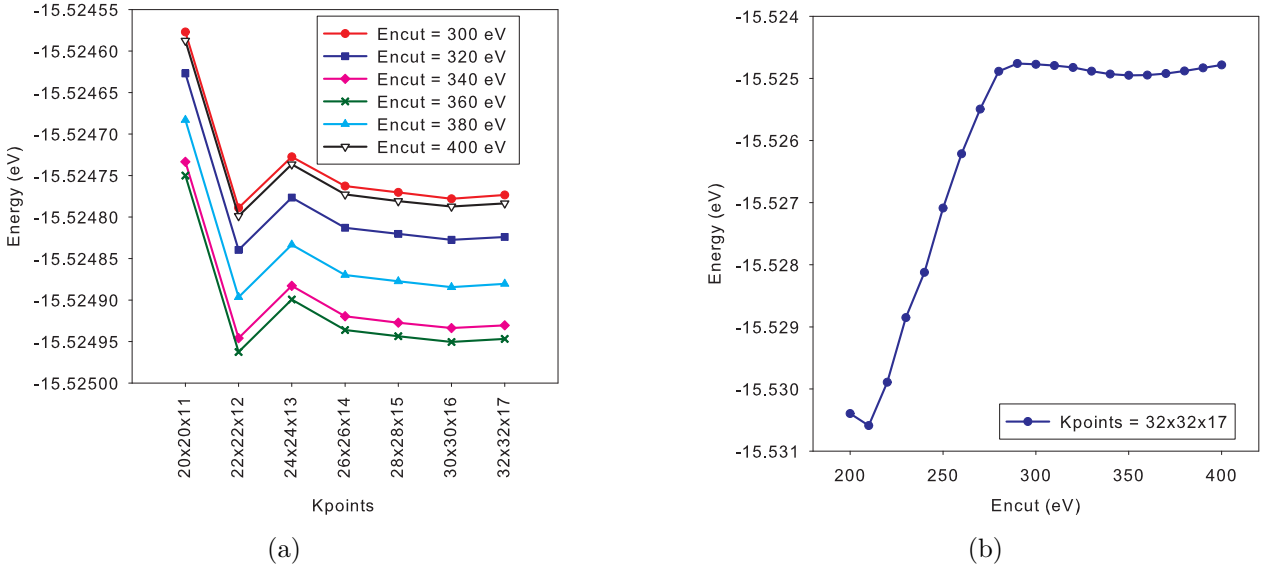
Figure 3.2: Convergence of k-points mesh and cutoff energy. A good choice to guarantee the accuracy of values in a reasonable time is 32x32x17 k-points mesh and 350 eV cutoff energy.

off and k-points mesh were obtained performing a convergence test with 2-atom unit cell. The free energy were minimised for different values of energy cut-off and k-points as reported in Figure 3.2. The calculations use a Monkhorst-Pack mesh of 32 x 32 x 17 k-points for a 2-atom cell, 54-atom supercell and an energy cut-off of 350 eV. These parameters are used to calculate the lattice constants of Ti, minimising $E[n]$ for different values of a and c/a. This minimisation of energy versus volume for different values of a is reported in Figure 3.3. The minimum energy is obtained for a equal 2.926 Å and c/a equal 1.58. A sensitivity study was performed to determine the appropriate supercell size to capture the vacancy formation energy, E_v, (for the formulation in Section 4.3.1) accurately. The 54-atom supercell size was chosen because it gives the best compromise between accuracy and computational time as shown in Figure 3.4.

3.2.2 Pseudopotentials

As mentioned earlier, the approximation of the exchange correlation functional plays a key role on the validation of DFT calculations. Different results can be obtained depending on the potential used. For example, several calculations report that the most stable phase of Ti at 0 K is the ω-phase [129, 145, 146]. This phase is not experimentally observed because of the

43
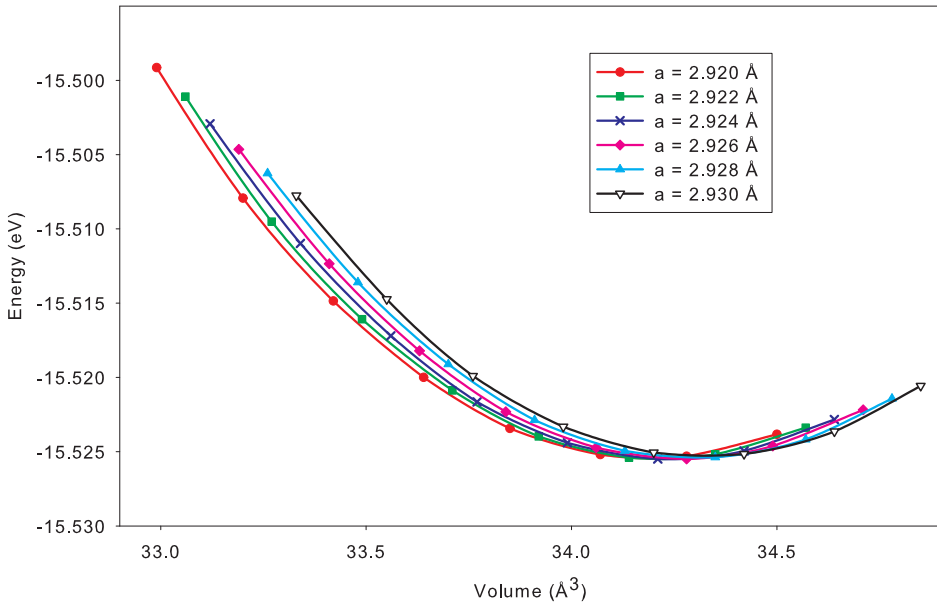
Figure 3.3: Minimisation of free energy versus volume for different values of a and c/a. The minimum is reached for a=2.926 Å and c/a =1.58.
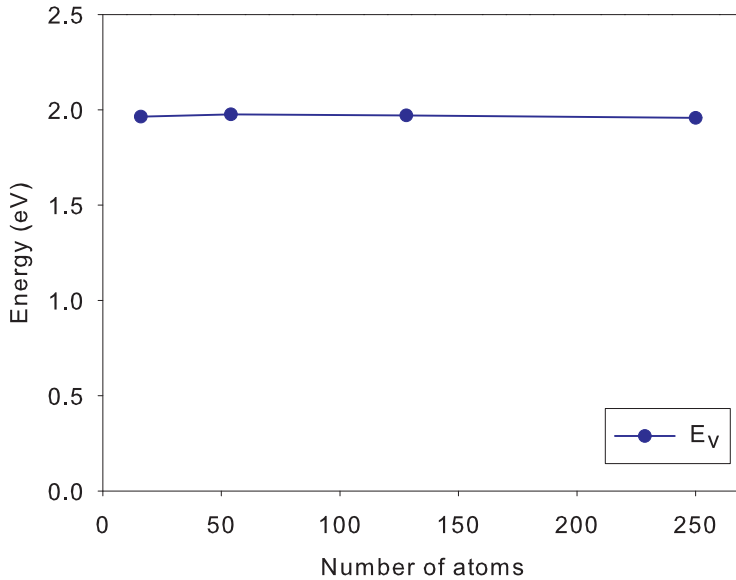
Figure 3.4: Convergence of supercell size (16, 54, 128, 250 atoms) versus defect energies in Ti hcp: vacancy formation energy, E_v.

slow formation kinetics. Nevertheless, the choice of potential can lead to other conclusions, as shown by Tegner and Ackland [147] In fact, there are three ways to treat the valence orbitals of Ti. In the standard potentials, only the electrons on the 4s and 3d orbitals are valence electrons (four valence electrons). The vasp database includes another two potentials, Ti_pv

Table 3.1: Vacancy formation energy (E_v) values calculated using Monkhorst-Pack mesh of 32 x 32 x 17 k-points for a 2-atom cell, energy cut-off of 350 eV and 54-atom supercell with LDA and GGA-PBE potentials [143] with four valence electrons (Ti), ten valence electrons (Ti_pv) and twelve valence electrons (Ti_sv_GW).

	$E_v^{\mathbf{LDA}}$ (eV)	$E_v^{\mathbf{GGA\text{-}PBE}}$ (eV)	Number of valence electrons
Ti	1.985	1.976	4
Ti_pv	2.041	2.042	10
Ti_sv_GW	2.051	2.045	12

and Ti_sv. In the case of Ti_pv, the 3p orbitals are also included in the valence state (ten valence electrons). Twelve electrons are treated as valence (3s orbitals are also included) in Ti_sv. For d-elements, it is recommended to include the semi-core p-orbitals and possibly the semi-core s-orbitals as valence state, but in the case of 3d-elements, such as Ti, the standard potentials give also reasonable results [58]. A study of the vacancy formation energy, E_v, using these different potentials has been peformed. The results using the standard version, Ti_pv and Ti_sv_GW[1] of LDA and GGA-PBE parametrisations are reported [143] in Table 3.1. The calculations were performed using Monkhorst-Pack mesh of 32 x 32 x 17 k-points for a 2-atom cell and energy cut-off of 350 eV were applied to calculate the energy of 54-atom and 53-atom supercells. Ti_pv and Ti_sv_GW potentials give very similar results. The standard potentials results are in line with higher valence-electron potentials. These results agree with previous studies that utilised different potentials, as shown in Table 3.2.

3.3 Transition State Theory

In 1935, Eyring at Princeton University developed simultaneously with Evans and Polanyi at University of Manchester a new theory known as Transition State Theory (TST) describing the chemical reaction rates or defect migration in solids [150]. The main idea is that a nucleus moves under the influence of forces due to the motion and distribution of electrons [151].

---

[1]The GW potentials are obtained by algebraic approach based on Green's function technique. They give same results of LDA and GGA for ground state calculations and they can be safely used [142].

Table 3.2: Vacancy formation energy (E_v) reported in previous studies using different potentials.

	E_v^{LDA} [143] (eV)	$E_v^{\text{GGA-PBE}}$ [143] (eV)	$E_v^{\text{GGA-PW91}}$ [148] (eV)	$E_v^{\text{GGA-PBEsol}}$ [149] (eV)	Number of valence electrons
Shang et al [121]	2.08		1.98	2.14	10
Han et al [122]			2.078		not specified
Connétable et al [124]			1.96-1.99		not specified
Le Bacq et al [125]	2.14				FP-LMTO
Raji et al [126]			1.920-2.070		12
Medesani et al [127]	2.08	2.08	1.99	2.15	not specified

Knowing these forces by quantum mechanics, the reaction rates can be estimated by kinetic theory. Since the motion of nuclei depends on the potential surface corresponding to the lowest quantum states occupied by the electrons, the kinetic energy of the system is quantized. During a chemical reaction, the compound energies correspond to the low potential surface, and the reaction itself corresponds to passing from one low-energy region to another. Eyring defined the activated state as the highest point along these lowest-energy paths known as Minimum Energy Path (MEP) [151].

Various practical techniques have been developed to determine the MEP of reaction mechanism. DIMER [152] and Nudged Elastic Band (NEB) [62–64] methods are the most famous. In the first case, the search for the saddle point does not require knowledge of the final state. It consists on a pair of images, called "dimer", is moved uphill on the potential energy surface from the initial state to find the activated state. After each displacement, the image couple is rotated by the net force acting on the two images in the direction of the lowest curvature. An effective force is introduced bringing the dimer together at the saddle point and avoiding the translational forces pushing it back to the minimum. This method requires few images but the final result depends on the orientation initially assumed. It is usually used in combination with the NEB method which can provide the initial direction for the dimer. The NEB method allows one to find the MEP knowing the initial and finale states. It consists of guessing a set of images between the initial and finale states and minimising their energy. With respect to

the DIMER method, it requires a higher number of images, but it is a very efficient tool to determine the MEP in addition to the saddle point. In this work, the MEP and saddle point calculations were performed using NEB.

3.3.1 Transition rate

According to TST [151], the rate of a chemical reaction or defect migration in the crystal is given by

$$\text{w} = \nu^* \exp\left(\frac{\Delta H_m}{k_b T}\right) \tag{3.7}$$

where ν^* is the effective frequency, ΔH_m is the energy required to move from the initial state to the saddle point, T is the absolute temperature and k_b is Boltzmann's constant. ΔH_m is equal to the energy difference of saddle point and initial state, while ν^* depends on the N normal vibrational frequencies of initial configuration, ν_i, and $N-1$ normal vibrational frequencies of activated configuration, ν'_j, [153],

$$\nu^* = \frac{\prod_{i=1}^{N} \nu_i}{\prod_{j=1}^{N-1} \nu'_j}. \tag{3.8}$$

Vineyard explained this formulation considering the jump of an atom into the nearest vacancy. A crystal of $N/3$ atoms and one vacancy has N degrees of freedom and its potential energy depends on N coordinates. When the atom jumps into the vacancy from site A to B, the potential energy of the system has two minima at these two sites, as shown in Fig. 3.5. The saddle point between A and B is defined as P, and S is an imaginary constraining hyper-surface that passes through P and divides the low-potential regions. S is always perpendicular to the potential hyper-surface, meaning that an atom at the saddle point can moves along S only by increasing energy, but if it moves along a perpendicular direction to S, it moves to one of the minima. Therefore, S has $N-1$ degrees of freedom and the potential energy in S depends on $N-1$ coordinates.
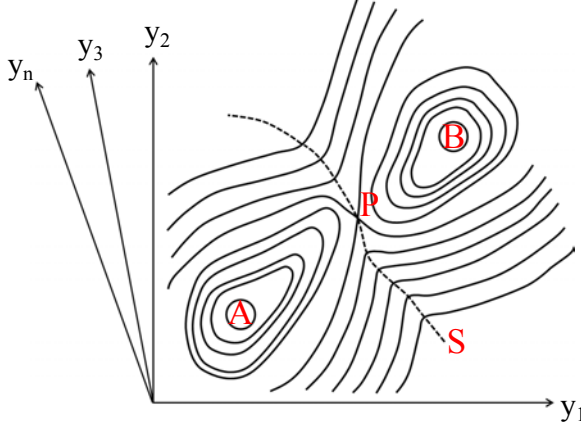
Figure 3.5: Schematic representation of the hyper-surface with constant potential energy. A and B are the minima of the system, P is the saddle point between A and B. S is the hyper-surface that divides A and B regions. S passes through the saddle point and is perpendicular to potential hyper-surface everywhere [153].

3.3.2 Nudged Elastic band method

In the classic NEB method [62], the forces of an image are decomposed into the parallel and perpendicular components to the local tangent. The first component is usually referred to as the spring force, and it affects the distribution of images within the path. The convergence of the elastic band to MEP depends on the perpendicular forces called force projections. However, the process of finding the saddle point by following the rise in the potential energy surface from the minimum-energy state using the spring forces is not trivial. In fact, an unstable state displaces to low-energy configuration if subjected to a small displacement. In 2000, Henkelman developed the Climbing Image NEB (CI-NEB) method [63], where the parallel component of the full force is due to the potential instead. As a result, the highest-energy image is driven to the exact saddle point. Another problem of the classic method NEB is that the tangent at an image is defined as the normalized line segment between the two adjacent images. However, this definition leads to formation of kinks along the path, especially, when the parallel force is large with respect to the perpendicular component [64]. The transition path towards the saddle point is smoothed by calculating the tangent from the image with higher energy rather than those neighbouring the current location [64].

3.3.3 Applications

The transition state theory is usually described as a framework to study the chemical reactions. Different versions of this theory have been successfully used to evaluate the activation energy, reaction pathway, pre-factor and rate constant of fundamental mechanisms such as CO oxidation on metal [154], hydrogen abstraction reactions [155, 156]. In biochemistry, TST has been used to study the enzymatic catalysis processes [157, 158], radical-molecule reactions such as OH-alkene reaction promoting the formation of ozone and other secondary pollutants in the troposphere [159]. TST has allowed researchers to better understand the implication of the radiative association reaction of metal ions with molecules in the chemical evolution of the interstellar cloud [160]. This theory can be also applied to study the diffusion in liquids during igneous processes in the crust or upper mantle of Earth's surface [161]. It has been also successfully used in materials science to understand diffusion behaviour in glassy polymers [162] and nano-porous materials [163].

The Nudged elastic band method has been widely used in different fields, from solid-state physics to biochemistry. This method gives important information on conformational changes in biological macromolecules such as RNA [164], reaction path of catalytic mechanisms [165]. Some examples of NEB method in materials science applications are the study on the diffusion kinetic [48–50, 121, 166], dislocation mobility [167] and phase transition [168].

3.4   Kinetic Monte Carlo

Solid diffusion is essentially a stochastic process, a result of the random atomic jumps in the matter. At the same time, the diffusion flux and temporal change of the composition are deterministic quantities, and are described by Fick's laws. In other words, it is possible to describe deterministically the average ensemble behaviours of collectively random processes. This can be achieved using theoretical and computational methods, such as Molecular Dynamic (MD), Monte Carlo (MC) methods, and Finite Element Method (FEM). MD predicts atom trajectories solving Newton's equations of motion. These trajectories are of the size of atomic

vibrations, so MD is not used to predict relative large scale phenomena. On the other hand, FEM is a powerful technique to study larger domains, such as heat transport. MC length-scale lies between MD and FEM, and it can simulate very well the atom migrations and chemical reactions.

Monte Carlo methods [111] are computational algorithms used to study a wide range of stochastic phenomena of different fields, from financial [169] to physics problems [170]. They consists of performing a large number of simulations in order to obtain a distribution of properties studied. At each step, the process is simulated by randomly choosing an event to perform from a list of stochastic events that can occur in the system.

Kinetic Monte Carlo (KMC) [55] is a particular Monte Carlo method used to describe the evolution of a system knowing the processes involved in the phenomenon under consideration. In the last fifty years, a number of different KMC methods has been developed, however the main algorithm can be summarised in the following steps,

1. set initial time $t=0$ and the initial state of the system;

2. list of all N possible events and their rates w_i;

3. for each event calculate the cumulative function R_i, defined as

$$R_i = \sum_{j=1}^{i} w_i \text{ with } i = 1, 2, ...N;$$ (3.9)

4. pick a random number $u \in (0, 1]$;

5. find and perform which event i satisfies $R_j < uR_N < R_i$;

6. pick a second random number $u' \in (0, 1]$;

7. calculate

$$\Delta t = \frac{-\ln(u')}{R_N};$$ (3.10)

8. repeat all the steps with the system occupying the new state i and $t = t + \Delta t$.

The diffusion coefficients can be obtained by simulating many random walks, and for each of them calculate the displacement, r^2, between the initial and final position of the species considered. The diffusivities are then calculated by,

$$D = \frac{1}{2\,d}\frac{<r^2>}{<t>} \tag{3.11}$$

where d is the dimension of displacement vector, $<r^2>$ and $<t>$ are respectively the average square displacement and average time.

KMC utilisations have been rapidly raised in many fields of chemistry and solid-state physics. It has been used to understand atomic physics phenomena such as surface diffusion in organic [171] and inorganic systems [172], vacancy diffusion in alloys [173], and dislocation motion [174]. KMC simulations have helped to understand the early stages of precipitation kinetics, such as the nucleation, growth and coarsening stages [175]. It is useful to model important technologies such as molecular beam epitaxy (MBE) for semiconductors [176] and chemical vapour deposition (CVD) [177]. An intensive use of KMC simulations has been done in the field of radiation effects on materials, where good results have been obtained in the study of defect mobility [178] and clustering [179].

Chapter 4

Vacancy-mediated diffusion in alpha-Ti: semi-metals

4.1 Introduction

The good influence of the slow diffusion of Si on the creep properties of near-α Ti alloys has been widely recognised [3, 4, 11–20]. The understanding of the Si diffusion mechanism is a fundamental step to determine its influence upon creep behaviour in Ti. This study assessed the diffusion of elements sitting close to Si in the periodic table (Al, Ga, Ge, In and Sn, known as semi-metals), to investigate the special behaviour of Si α-Ti. The sizes of these elements in their various ionisation states are listed in table 4.1.

Semi-metals are expected to dissolve as substitutional atoms at lattice sites in α-Ti, since they have similar atomic radii to Ti. The substitutional and self-diffusion in metals is usually mediated by vacancies. As a result of atom fluctuations, an atom can overcome the energy barrier due to the cohesive forces holding it, and jump into the neighbouring vacant site, as schematically outlined in Fig. 4.1. The diffusion is a result of several discrete atomic jumps through the lattice. These jumps are not totally independent of each other; infact an atom can swap with a given vacancy more than once, since the vacancy is still available on the neighbour site after the jump. This positional memory is taken into account by a correlation factor, f.

Table 4.1: Size of Al, Si, Ga, Ge, In and Sn in their various ionisation states [180].

Elements	ionisation state	R (Å)
Al	neutral	1.43
	3+	0.57
Si	neutral	1.17
	4+	0.26
	4-	2.71
Ga	neutral	1.22
	1+	1.13
	3+	0.62
Ge	neutral	1.23
	2+	0.90
	4-	2.72
In	neutral	1.63
	1+	1.32
	3+	0.92
Sn	neutral	1.41
	2+	0.93
	4+	0.74
	4-	2.45

This factor is defined as the diffusivity ratio of the real correlated migration and random walk. It can be expressed as,

$$f = 1 + 2 \sum_{m=1}^{\infty} \langle cos(\theta^{(m)}) \rangle \tag{4.1}$$

where $\langle cos(\theta^{(m)}) \rangle$ is the average values of the angle between the first jump and subsequent jumps of a given atom. The correlation factor depends on the type of lattice and solute, diffusion mechanism and degree of local order of the atomic components. In the case of vacancy mediated diffusion, the sum $\sum_{m=1}^{\infty} \langle cos(\theta^{(m)}) \rangle$ is less than one, therefore $f < 1$. Table 4.2 provides examples of f and $\langle cos(\theta^{(m)}) \rangle$ for self-diffusion for different types of lattice [181]. Different

Table 4.2: Calculated values of $\langle cos(\theta^{(m)}) \rangle$ and f for self diffusion vis vacancy-mediated diffusion for different types of lattice [181].

Lattice	$\langle cos(\theta^{(m)}) \rangle$	f
fcc	-0.12268	0.78146
diamond	-1/3	1/2
bcc	-0.15793	0.72722
simple cubic	-0.20984	0.65311
hcp		$f_x = f_y$=0.78121
		f_z=0.78146
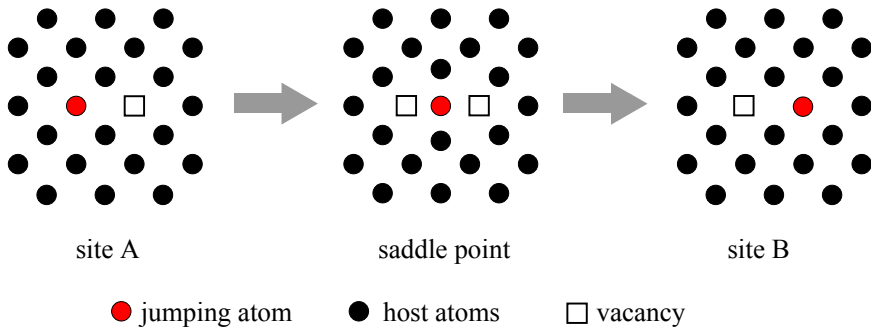
Figure 4.1: Schematic representation of substitutional diffusion via monovacancy-mediated mechanism.

analytical models have been developed to capture this behaviour depending on the type of lattice: "5-frequency" model [108] for fcc, Manning's model for bcc [109], and the "8-frequency" model [51] for hcp. If the migration mechanism involves only one vacancy at the time, it is called monovacancy diffusion. The migration is called divacancy when it involves vacancy agglomerations. The migration via divacancy is similar to the monovacancy mechanism, as shown in Fig. 4.2. The monovacancy-mediated mechanism is more relevant at temperatures of 2/3 of melting point, while the divacancy process controls the diffusion at higher-temperature range where the number of vacancies is such that the probability to find an vacancy near an other vacancy is high. The migration of Si and semi-metals diffusion in α-Ti happens via monovacancy mechanism. In this work, we refer to the monovacancy mechanism simply as vacancy-mediated diffusion.

The experimental diffusion parameters, activation energy (Q) and pre-exponential factor
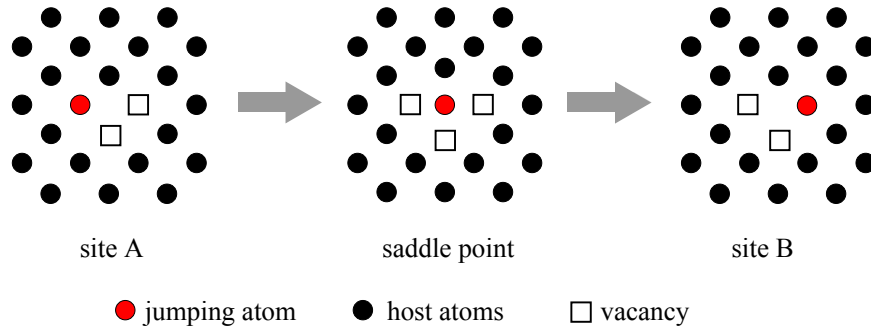
Figure 4.2: Schematic representation of substitutional diffusion via divacancy-mediated mechanism.

(D_0), available in the literature for self-, Al, Ga, In, Sn and Si diffusion in α-Ti [9, 10, 95, 100–104], are summarised in Table 4.3. Data for Ge diffusion are not presented as the author has not yet found this information in published literature. Experimental diffusion studies are not simple to conduct, since the anisotropic crystal structure of α-Ti requires a single-crystal diffusion study. Additionally, the presence of fast-diffusers in α-Ti can have a significant influence on the self- and solute diffusivity values [9], and manufacturing a high-purity single crystal is not easy. As a result, the understanding of Si and semi-metals diffusion in α-Ti is still incomplete. On the other hand, in the last few decades there has been a significant improvement in the computational analysis of diffusion based problem using DFT [56, 57]. Ganeshan *et al* [48, 49] have successfully used an analytical method called "8-frequency" model [51] (see Section 4.2) implemented with *ab initio* calculations to evaluate self- and solute diffusion in hcp elements as α-Mg and α-Zn. The purpose of this section is to use this model implemented by DFT calculations to study the semi-metals diffusion in α-Ti. KMC simulations [55] were also conducted in order to verify the predictions of the analytical model.

The results obtained in this work contradict the common belief that small atoms, such as Si, diffuse faster than large atoms such as In and Sn (see Section 4.3). This is due to the electron character of the solute-solvent bonding (see Section 4.4). In addition, the distortion of bond angle seems to have an important role on the diffusion anisotropy in α-Ti as well as the host lattice dilation. In particular, this leads to the extreme anisotropy behaviour exhibited by Ge.

Table 4.3: Experimental diffusion parameters of solvent, Al, Ga, In, Si, Sn in α-Ti. Q and D_0 are the activation energy and pre-exponential factor of bulk diffusion, $Q_{\parallel}$ and $D_{0\parallel}$ are referred to the activation energy and pre-exponential factor of the migration within the basal plane, and $D_{\perp}/D_{\parallel}$ is the diffusion anisotropy ratio.

Solute	Q (eV)	D_0 (m²/s)	
Ti [95]	1.271	6.4×10^{-12}	
Al [100]	1.62 ± 0.11	$7.4 \pm 9.8 \times 10^{-11}$	
Si [101]	1.09 ± 0.18	$4.4^{+40}_{-4.0} \times 10^{-11}$	
Ga [102]	3.19 ± 0.08	2.5×10^{-4}	
Sn [103]	3.52 ± 0.1	$4.00 \pm 2 \times 10^{-3}$	
In [104]	2.70 ± 0.42	$2.1 \pm 1.3 \times 10^{-6}$	
Solute	$Q_{\parallel}$ **(eV)**	$D_{0\parallel}$ **(m²/s)**	$D_{\perp}/D_{\parallel}$
Ti [9]	3.1 ± 0.021	$1.35^{+0.4}_{-0.3} \times 10^{-3}$	0.5
Al [9]	3.41 ± 0.021	$6.60^{+1.6}_{-1.3} \times 10^{-3}$	0.63
Ga [10]	3.06 ± 0.02	$2.1 \pm 0.6 \times 10^{-3}$	–
In [10]	3.41 ± 0.18	$3.1 \pm 2.3 \times 10^{-3}$	–

4.2   Methodology

The defect energies were calculated using VASP 5.3.2 [58–61], applying the parameters presented in Section 3.2.1. The electronic structure was described by PAW [142], and the exchange-correlation functional was computed using GGA-PBE [143]. A 54-atom supercell was used with a Monkhorst-Pack mesh of 11 x 11 x 6, corresponding to 32 x 32 x 17 k-points for a 2-atom cell, and an energy cut-off of 350 eV. The migration energies and minimum energy path were evaluated using CI-NEB [62–64] with 5 images in between the initial and final state with fully relaxed supercell, and the same set-up (supercell size, k-points mesh, and energy cut-off) for defect energy calculations.

4.2.1 Point defect

The vacancy formation energy, E_v, is obtained by

$$E_v = E\{M_{N-1}\} - \frac{N-1}{N}E\{M_N\}; \tag{4.2}$$

where $E\{M_{N-1}\}$ is the energy of a crystal containing one vacancy and $N-1$ solvent atoms, and $E\{M_N\}$ is the energy of a perfect crystal of N atoms. The binding energies of solute-vacancy pairs, ΔE_b, are defined as the energy difference of a system with the vacancy-solute pair and when the vacancy is at infinite distance from the solute,

$$\Delta E_b = E\{M_{N-2} + X_1\} - E\{M_{N-1} + X_1\} - E\{M_{N-1}\} + E\{M_N\}. \tag{4.3}$$

In this equation, M and X are the notations for solvent and solute atom respectively, and N is the total number of atoms. $E\{M_{N-1}\}$ and $E\{M_N\}$ are the same quantities in equation 4.2, $E\{M_{N-2} + X_1\}$ is the energy of crystal of $N-2$ solvent atoms with the solute sitting next to the vacancy, and $E\{M_{N-1} + X_1\}$ is the energy of crystal of $N-1$ solvent atoms and with one substitutional atom. Based on this definition, the positive values of ΔE_b indicate that the solute prefers sit away from the vacancy, whilst a negative value indicates opposite behaviour.

4.2.2 "8-frequency" model

Diffusion mediated by vacancy is not a purely random walk, but each jump conserves a position memory [182], requiring the introduction of a correlation factor, f, in the diffusion coefficients formulation. The analytical evaluation of this factor depends on the type of lattice considered. In 1955, Lidiard [108] proposed "5-frequency" model to describe the correlation effect in fcc crystals, while Manning [109] proposed a model for bcc lattices. Mullen was the first to study anisotropic systems in 1961 [183]. His formulation for correlation factors of hcp crystal was resumed three years later by Ghate in the "8-frequency" model (8FM) [51] to describe the impurity diffusion in Zn. Ganeshan *et al* [48, 49] have applied this model to study diffusion

in Mg and Zn systems with DFT implementation. Mantina [166] has also explored vacancy-mediated diffusion mechanism in α-Mg, α-Zn, and α-Ti . The "8-frequency" model has also been used by Shang *et al* [121] to study self-diffusion in α-Ti .

In the case of diffusion in hcp crystal, there are two solute jumps: out-of-plane and in-plane jumps, as displayed in Fig. 4.3. In this work, $\parallel$ and $\perp$ notations are used to identify diffusion within the basal plane and along the c-axis respectively. In 8FM, these two diffusivities are defined as functions of the two impurity jump frequencies, $w_\parallel$ and $w_\perp$, and six solvent jump frequencies, w_a, w_b, w_c, w_a', w_b', w_c' [51] (see Fig. 4.3). They have the following definitions,

- $w_\parallel$ is the jump frequency of solute-vacancy exchange within the basal plane;

- $w_\perp$ is the jump frequency of solute-vacancy exchange between adjacent basal planes;

- w_a is the jump frequency of vacancy-solvent exchange between adjacent basal planes rearranging the solute-vacancy pair from in-plane to out-of-plane configuration;

- w_b is the jump frequency of solvent-vacancy exchange within the basal plane rearranging the in-plane solute-vacancy pair;

- w_c is the jump frequency of solvent-vacancy exchange resulting in the separation of the in-plane solute-vacancy pair;

- w_a' is the jump frequency of vacancy-solvent exchange in the adjacent basal plane rearranging the solute-vacancy pair from out-of-plane to in-plane configuration;

- w_b' is the jump frequency of solvent-vacancy exchange within the basal plane rearranging the out-of-plane solute-vacancy pair;

- w_c' is the jump frequency of solvent-vacancy exchange resulting in the separation of the out-of-plane solute-vacancy pair.

$D_\parallel$ and $D_\perp$ are defined as [51],

$$D_\parallel = \frac{1}{2} \, C \, a^2 (3 f_{\parallel x} w_\parallel + f_{\perp x} w_\perp) \tag{4.4}$$

$$D_\perp = \frac{3}{4} C \ c^2 f_{\perp z} \mathrm{w}_\perp, \tag{4.5}$$

where a and c are the lattice parameters, C is the vacancy concentration, $f_{\|x}$, $f_{\perp x}$ and $f_{\perp z}$ are the partial correlation factors. The vacancy concentration is defined as an exponential function of the formation energy of a vacancy next to the solute, ΔH_v,

$$C = \exp\left(-\frac{\Delta H_v}{k_b T}\right), \tag{4.6}$$

where k_b is the Boltzmann's constant and T is the absolute temperature. The binding energies share similar definitions as presented in Section 4.2.1. ΔH_v is the sum of E_v and ΔE_b. The correlation factors, $f_{\|x}$, $f_{\perp x}$ and $f_{\perp z}$ are,

$$f_{\|x} = 1 + \frac{2S_{\|x}}{\lambda_\|} \tag{4.7}$$

$$f_{\perp x} = 1 + \frac{2S_{\perp x}}{\lambda_{\perp B}} \tag{4.8}$$

$$f_{\perp z} = \frac{2\mathrm{w}_a' + 7F\mathrm{w}_c'}{2\mathrm{w}_a' + 2\mathrm{w}_\perp + 7F\mathrm{w}_c'}, \tag{4.9}$$

where $\lambda_\|$ is the jump distance within the basal plane, $\lambda_{\perp B}$ is the projection of $\mathrm{w}_\perp$ jump distance on the basal plane. $S_{\|x}$ and $S_{\perp x}$ represent the average final displacement of the solute in the direction x after in-plane and out-of-plane jump. They are calculated as follows,

$$S_{\|x} = \frac{2\mathrm{w}_a\left(\frac{\sqrt{3}}{2}\right)S_{\perp x} + 2\mathrm{w}_b\left(\frac{1}{2}\right)S_{\|x} - \mathrm{w}_\|(\lambda_\| + S_{\|x})}{2\mathrm{w}_a + 2\mathrm{w}_b + 7F\mathrm{w}_c + \mathrm{w}_\|} \tag{4.10}$$

$$S_{\perp x} = \frac{2\mathrm{w}_a'\left[\frac{\sqrt{3}}{2}S_{\|x} + \frac{1}{2}S_{\|y}\right] + 2\mathrm{w}_b'\left(\frac{1}{2}\right)S_{\perp x} - \mathrm{w}_\perp\left(\lambda_{\perp B} + S_{\perp x}\right)}{2\mathrm{w}_a' + 2\mathrm{w}_b' + 7F\mathrm{w}_c' + \mathrm{w}_\perp} \tag{4.11}$$

$$S_{\|y} = \frac{2\mathrm{w}_a\left(\frac{1}{2}\right)S_{\perp x} + 2\mathrm{w}_b\left(-\frac{1}{2}\right)S_{\|y}}{2\mathrm{w}_a + 2\mathrm{w}_b + 7F\mathrm{w}_c + \mathrm{w}_\|}, \tag{4.12}$$

where F has a value of 0.736 [51] and is a ratio descriptive of the effect of the vacancy returning back to the nearest-neighbour position. Each jump frequency depends on the migration energy,
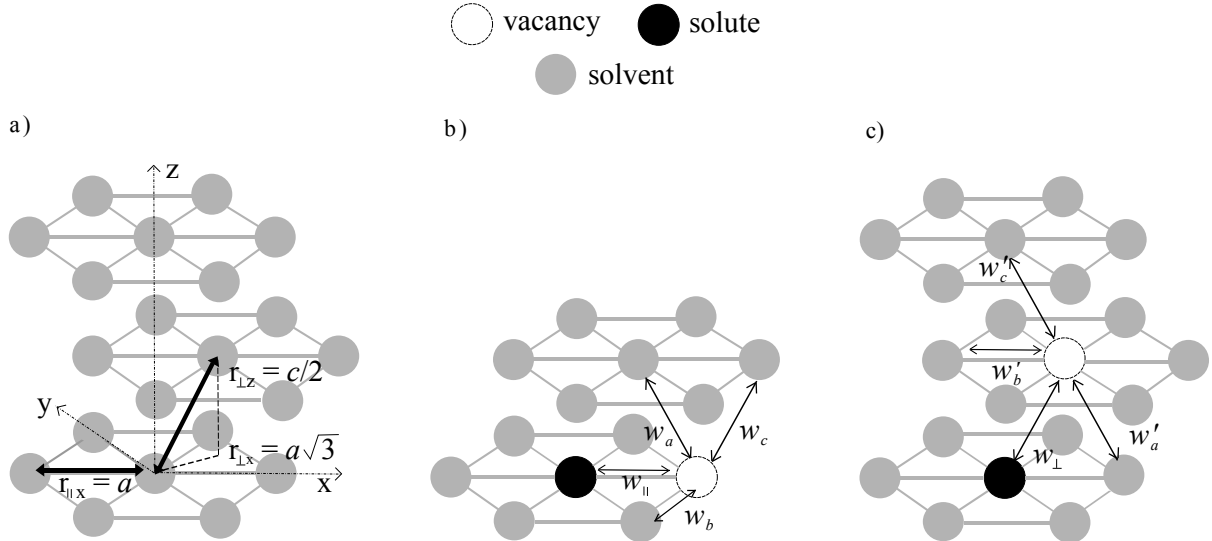
Figure 4.3: a) Schematic representation of out-of-plane ($\perp$) and in-plane ($\parallel$) jumps of the solute atom in hcp crystal. The jump frequencies when solute and vacancy are b) in the same basal plane and c) in adjacent basal planes.

ΔH_m, and effective frequency, ν^*,

$$\mathrm{w} = \nu^* \exp\left(-\frac{\Delta H_m}{k_b T}\right). \tag{4.13}$$

ΔH_m is defined as the energy difference of the activated state, E_{TS}, and the initial state, E_{IS}, along the energy pathway. The effective frequency was calculated following the Vineyard definition [153] (see equation 3.8 in Section 3.3.1). In the case of self-diffusion, w_a, w'_a, w_c and w'_c are equal to $\mathrm{w}_\perp$, while w_b and w'_b are equal to $\mathrm{w}_\parallel$, and ΔH_v is equal to E_v. Therefore, only these two jump frequencies are required to calculate the self-diffusivities.

4.2.3 KMC simulations

Kinetic Monte Carlo simulations were used to study the diffusion of semi-metals in α-Ti and verify the analytical model. The main algorithm of KMC is reported in Section 3.4. In the case of vacancy-mediated mechanism the diffusion is simulated in a rigid lattice with fixed sites, repeated infinite times to simulate the real lattice. This introduces an error due to the fact that the concentration of vacancy sites in this small box is much higher than real values. Therefore,

it is necessary to scale the time with equivalent concentration of vacancy, C_{eq},

$$D = \frac{1}{2} \frac{1}{d} \frac{<r^2>}{<t>} \frac{1}{C_{eq}},$$ (4.14)

$$C_{eq} = \frac{N_v}{N_s} \frac{1}{C},$$ (4.15)

where N_v and N_s are respectively the number of vacancies and lattice sites in the simulation box, and C is the vacancy concentration.

The KMC simulations were informed with the eight jump frequencies of the analytical model, and the addition of the two reverse jumps of w_c and w'_c, and in-plane and out-of-plane solvent-vacancy swaps when the vacancy is far away from the solute atom. The diffusion coefficients were calculated after 100 simulations. Each of these simulations was terminated after 10^6 solute jumps or 10^9 vacancy jumps.

4.3 Results

4.3.1 Point defect

The vacancy formation energy, E_v, and the binding energy of solute-vacancy pair, ΔE_b, were calculated using equations 4.2 and 4.3, respectively. E_v was evaluated with 54-atom supercell equal to 1.976 eV, very similar to 1.971 eV obtained using 128-atom supercell. These results confirm the previous first-principles studies where E_v was evaluated between 1.97 eV and 2.18 eV [121, 122, 124–126]. However, they overestimate the experimental values of 1.27±0.05 eV [184] and 1.55 eV [185]. Nevertheless, these experimental values compared to the diffusion activation energy, 3.1 eV. In fact, the migration energy would be around 1.55 eV. on the other hand, E_v estimated from the melting temperature of Ti using the empirical relation $E_v = T_m(K) \, 10^{-3}$ provides a value of 1.95 eV.

The binding energy values of Al, Si, Ga, Ge, In and Sn in α-Ti are shown in Fig. 4.4. The energies of a vacancy-solute pair in adjacent basal planes are displayed in black bars ($\Delta E_{b_\perp}$). The grey bars display the binding energy of a vacancy-solute pair sitting in the same basal
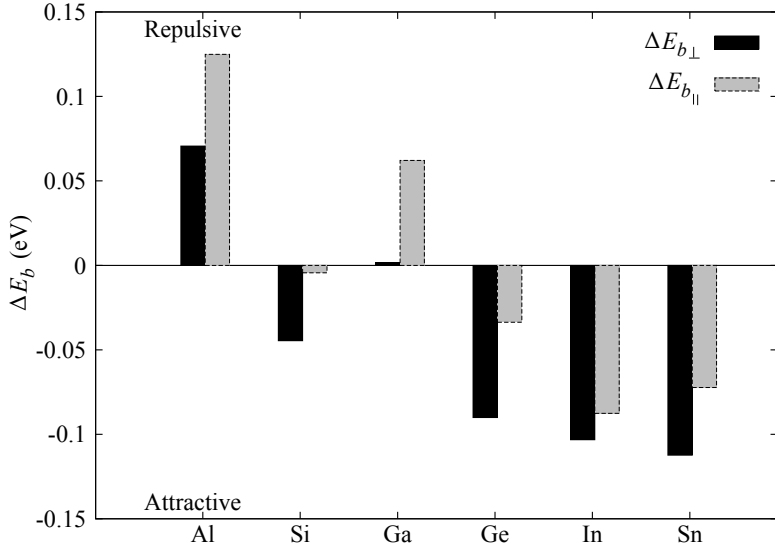
Figure 4.4: Calculated binding energies of solute-vacancy pairs (ΔE_b) when the solute and vacancy are in adjacent basal planes (black bars) and in the same basal plane (grey bars) for Al, Ga, Ge, In, Si, Sn in α-Ti. Positive values of ΔE_b indicate that the solute atom is repulsed by the vacancy, while negative values indicate attraction between the vacancy and solute.

plane ($\Delta E_{b_{\parallel}}$). The vacancy is attracted by Si, Ge, In and Sn, while Ga and Al have a repulsive behaviour.

4.3.2 Self-diffusion

The minimum energy paths and vacancy migration energies of in-plane, $w_{\parallel}$, and out-of-plane, $w_{\perp}$, solvent-vacancy swaps were evaluated by CI-NEB using five images. In the case of $w_{\perp}$, the path is rectilinear and there is only one saddle point, as shown in Fig. 4.5, with a migration energy of 0.427 eV. On the contrary, the path of $w_{\parallel}$ diverges from the rectilinear walk to the one illustrated in Fig. 4.6 with two saddle points instead of one (see Fig. 4.5). Similar pathways have been found in the case of self-diffusion in Zr and Ti in previous *ab initio* works [121, 186, 187]. This may be a result of the presence of the host atoms in the above and below basal planes, as suggested by Shang *et al* [121]. The parallel migration energy is 0.413 eV, which is similar to the value found for the out-of-plane jump. The diffusion coefficients data evaluated using 8FM and KMC are in good agreement, as shown in Fig. 4.7. The diffusion activation energies along the two directions are similar, $Q_{\parallel}$ is equal to 2.393 eV and $Q_{\perp}$ to 2.399 eV. Also, the pre-exponential factors do not significantly differ. $D_{0\parallel}$ was estimated equal to 0.978×10^{-6}
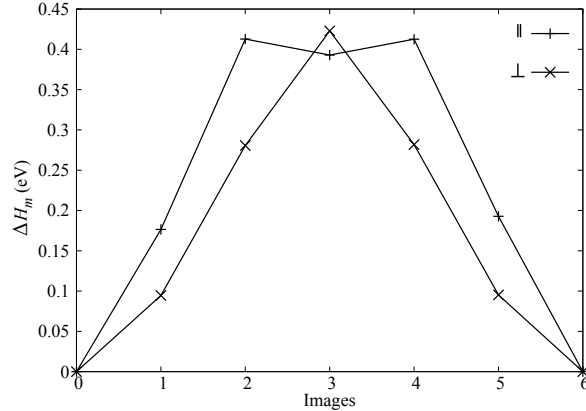
Figure 4.5: Migration energies (ΔH_m) of out-of-plane ($\perp$) and in-plane ($\parallel$) solvent jumps in α-Ti evaluated with five images between the initial and final states.
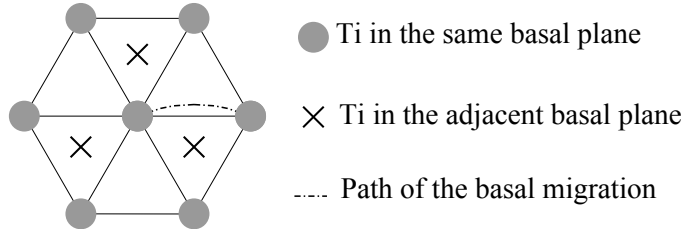
Figure 4.6: Schematic path of the in-plane jump. The path is diverged from the straight line by the presence of Ti atoms in the two adjacent basal planes.

m^2/s, while $D_{0\perp}$ to 0.934x10^{-6} m^2/s. These results confirm the anisotropy diffusion behaviour observed experimentally. In fact, the migration is faster within the basal plane with respect to the direction along c-axis, and the anisotropic ratio, $D_\perp/D_\parallel$, is equal to $\simeq$0.89, confirming the trend $D_\perp/D_\parallel < 1$ observed experimentally by Köpper and co-workers for Ti [9] and for other hcp elements with c/a ratio smaller than 1.633, such as Zr [98, 188].

The DFT diffusivity results were compared with previous DFT [121] and experimental [9] studies (see Fig. 4.7). In their work, Shang *et al* [121] have estimated self-diffusivity using GGA-PBEsol approximation [149] and PAW method with k-points mesh of 11 x 11 x 11 for 36-atom cell and energy cut-off equal to 500 eV in MedeA. The experimental data have been obtained using radio-tracer ^{44}Ti in ultra-pure single crystal [9]. Our calculated diffusivities are consistent with Shang *et al* study [121]. However, they have estimated higher Ev, $Q_\perp$ and $Q_\parallel$ equal to 2.14 eV, 2.65 eV and 2.57 eV respectively, and pre-exponential, $D_{0\perp}$ and $D_{0\parallel}$, equal to 1.20x10^{-5} m^2/s and 1.07x10^{-5} m^2/s). The difference can be attributed to the choice of approximation for the exchange and correlation functional. In fact, E_v values obtained with GGA-PBEsol are usually

higher than GGA-PBE results [127]. On the other hand, the different supercell size, k-point mesh, and energy cut-off have less influence. Our findings show that ΔH_m values increase only 0.05-0.06 eV when using 4x4x4 supercells, and by 1 meV with higher energy cut-off (500 eV) and density k-point mesh. Both first-principles surveys overestimate the experimental diffusivities of Köpper and co-workers [9]. This may be due to error on the evaluation of E_v. Many researchers have tried to improve the calculation of this quantity, suggesting new exchange and correlation energy approximations or correcting them *a posteriori* [128]. In fact, a vacancy can be treated as an internal surface [128] since it locally introduces a change of the electron density. However, the GGA approximation do not describe very well surface behaviour introducing the problem of "internal surface error correction" in the calculation of E_v. In an attempt to overcome this, new GGA approximations have been proposed (GGA-PBEsol [149], LAG [189], AM05 [190]) which correct for this error. Medesani and co-worker have compared the formation energy of several elements, including Ti, obtained with different approximations of exchange and correlation energies, and with or without the *a posteriori* correction. Their results shows that GGA-PBE generally underestimate the vacancy formation energy with respect to the experimental data. In the case of Ti, E_v values vary between 1.95 eV to 2.18 eV, which are much larger than the experimental values reported in the literature, 1.27 eV [184] and 1.55 eV [**?**]. However, these experimental data seem too small compared to the activation energy $Q_\parallel$ of 3.1 eV extrapolated by Köpper *et al* [9]. In fact, supposing a $\Delta H_{m\parallel}$ of 0.5 eV, E_v is expected to be equal to 2.6 eV. This value is more consistent with the DFT calculations than experimental values. In addition, the vacancy formation energy empirically calculated from the melting temperature is 1.95 eV, similar to the value obtained in this work. It is clear that the evaluation of vacancy formation energy requires further computational and experimental investigations in order to overcome this gap between predictions and experiment.

The high diffusion barriers indicate that at very low temperature (i.e. less than 200 °C) the migration of Ti atoms is very slow. However, the study of Zhang and co-workers [191] on the cold dwell fatigue indicates that Ti atoms still diffuse at room temperature. The activation energy of this migration is supposed to be around 0.62 eV [191]. This value is remarkably lower
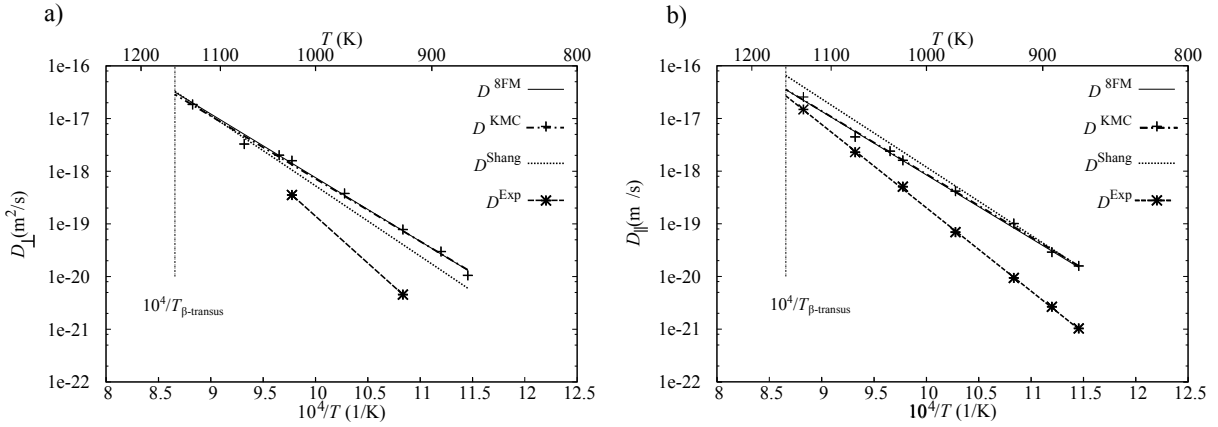
Figure 4.7: Comparison of a) $D_\perp$ and b) $D_\parallel$ data obtained in this work by 8-frequency method (D^{8FM}) and KMC method (D^{KMC}), with previous DFT (D^{Shang}) [121] and experimental studies (D^{Exp}) [9].

than the activation energy of vacancy-mediated mechanism, suggesting that self-interstitial migration may be involved. A brief investigation on self-interstitials in α-Ti is reported in Appendix A.

4.3.3 Semi-metals diffusion

The "8-frequency" model and KMC simulations are now applied to the evaluation of solute diffusion coefficients of Al, Si, Ga, Ge, In and Sn in α-Ti. The jump pathways were obtained following the procedure described earlier in Section 4.3.2. The MEPs are plotted in Fig. 4.8, and the values of ΔH_v and ΔH_m are presented in Table 4.4. The CI-NEB results indicate that $\parallel$ jump is energetically more favourable than $\perp$ jump. The solute-vacancy pair formation energy of in-plane and out-of-plane configurations are comparable, while migration energies can be considerably different between the two transitions. In the case of Ge particularly, $\Delta H_{m\perp}$ is two times higher than migration energy of in-plane jump. In the case of Si and Ga, the energy difference between $\Delta H_{m\perp}$ and $\Delta H_{m\parallel}$ is 0.2-0.3 eV. On the other hand, the energy difference in the case of Al, Sn and In is around 0.1 eV or less.

The Al-diffusivity values calculated in this work were compared with previous computational [166] and experimental [9] works in Fig. 4.9. Mantina [166] has studied Al diffusion coefficients with 8FM informed with *ab initio* data. The jump frequencies have been obtained using VASP

Table 4.4: First-principles evaluation of the formation energy of vacancy adjacent to the impurity (ΔH_v) and migration energy (ΔH_m) of semi-metals in the case of out-of-plane ($\perp$) and in-plane ($\parallel$) configurations in α-Ti. The calculations were performed at constatn pressure and fully relaxation of the cell.

Solute	$\Delta H_{v\perp}$ (eV)	$\Delta H_{m\perp}$ (eV)	$\Delta H_{v\parallel}$ (eV)	$\Delta H_{m\parallel}$ (eV)
Al	2.047	0.696	2.101	0.603
Si	1.932	1.290	1.972	0.938
Ga	1.978	0.753	2.038	0.546
Ge	1.886	1.018	1.942	0.526
In	1.873	0.314	1.889	0.270
Sn	1.868	0.477	1.904	0.320
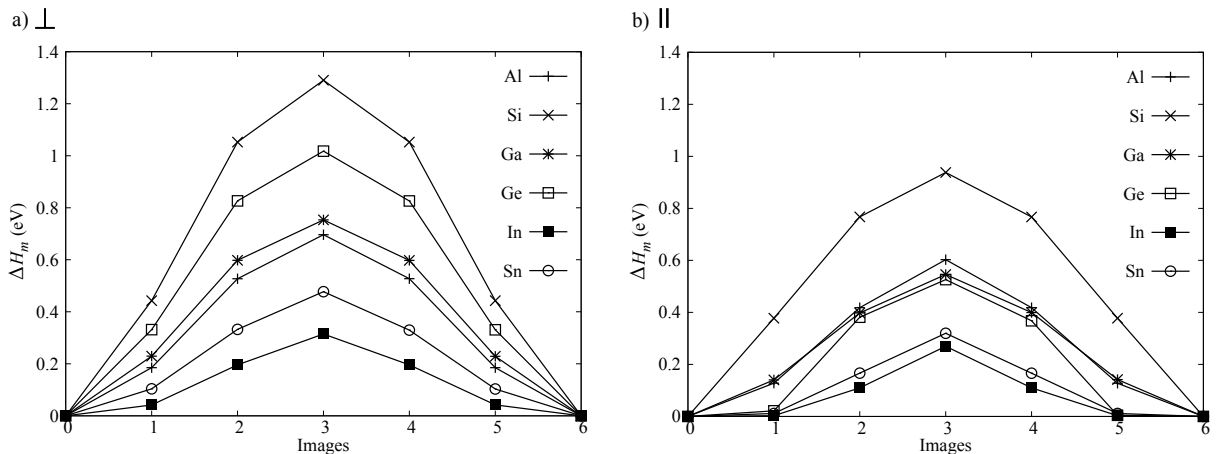
Figure 4.8: Minimum energy paths of a) out-of-plane ($\perp$) and b) in-plane ($\parallel$) transitions of semi-metals in α-Ti.

with LDA approximation, PAW method, energy cut-off of 300 eV, and kpoint mesh of 7 x 7 x 6 for 36-atom supercell. MEPs have been estimated using NEB without climb image method. Köppers *et al* [9] have studied diffusivity of Al in high-pure single crystal sample using SIMS . The large difference between the current work and Mantina's work is probably due to the fact the CI-NEB is more accurate method to estimate the saddle point than NEB. Additionally, our results are more consistent with experimental data than Mantina's values.

The perpendicular and parallel diffusivities of semi-metals evaluated using 8FM are presented and compared with self-diffusivities in Fig. 4.10, while the diffusion parameters are
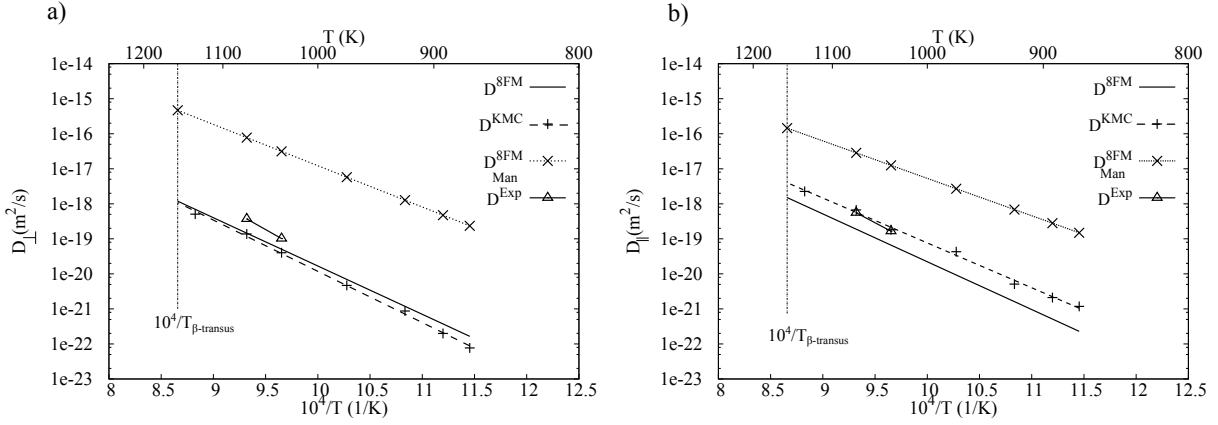
Figure 4.9: Comparison of a) $D_\perp$ and b) $D_\parallel$ data of Al migration obtained in this work by using "8-frequency" model, (D^{8FM}), and KMC simulations (D^{KMC}), with previous DFT data ($D^{\text{8FM}}_{\text{Man}}$) [166], and experimental data obtained (D^{Exp}) [9].
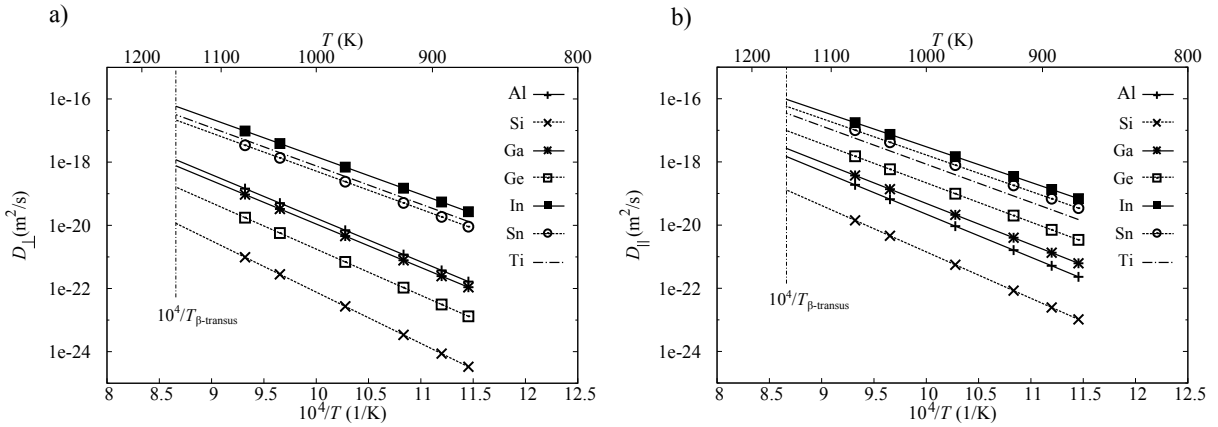
Figure 4.10: Comparison of self-diffusion coefficients with semi-metals diffusivities a) along the c-axis ($D_\perp$), and b) within the basal plane ($D_\parallel$) obtained by 8FM.

summarised in Table 4.5 and 4.6. The activation energies follow the order $Q^{\text{Si}}_\perp > Q^{\text{Ge}}_\perp > Q^{\text{Al}}_\perp > Q^{\text{Ga}}_\perp > Q^{\text{Sn}}_\perp > Q^{\text{In}}_\perp$ in the case of perpendicular diffusion, and $Q^{\text{Si}}_\parallel > Q^{\text{Al}}_\parallel > Q^{\text{Ga}}_\parallel > Q^{\text{Ge}}_\parallel > Q^{\text{Sn}}_\parallel > Q^{\text{In}}_\parallel$ in the case of parallel migration. In both directions, Si is the slowest diffuser of the semi-metals, while In is the fastest, followed by Sn. Ge is the second slowest diffuser along the c-axis, slower than Ga and Al. However, Ge diffuses faster than Al and Ga within the basal plane. The semi-metals diffusion along the c-axis is slower than the migration within the basal plane, respecting the trend $D_\perp/D_\parallel < 1$ of self-diffusivity. $D_\perp/D_\parallel$ of In, Sn and Ga ratio are equal to $\simeq 0.53$, $\simeq 0.31$ and $\simeq 0.22$, smaller than solvent and Al ratio, respectively, equal to $\simeq 0.89$ and $\simeq 0.8$. In the case of Si and Ge, $D_\parallel$ is two/three orders of magnitude higher than $D_\perp$ leading to a very low $D_\perp/D_\parallel$ values, equal to $\simeq 0.053$ and $\simeq 0.008$ respectively.

In order to verify the accuracy of 8FM results, KMC simulations were performed, the diffusivity values are compared in Fig. 4.11 in the case of perpendicular diffusion and Fig. 4.12 for parallel migration. The activation energies and pre-exponential factors are compared in Table 4.5 and 4.6. Our results show consistency between the analytical and KMC approaches.
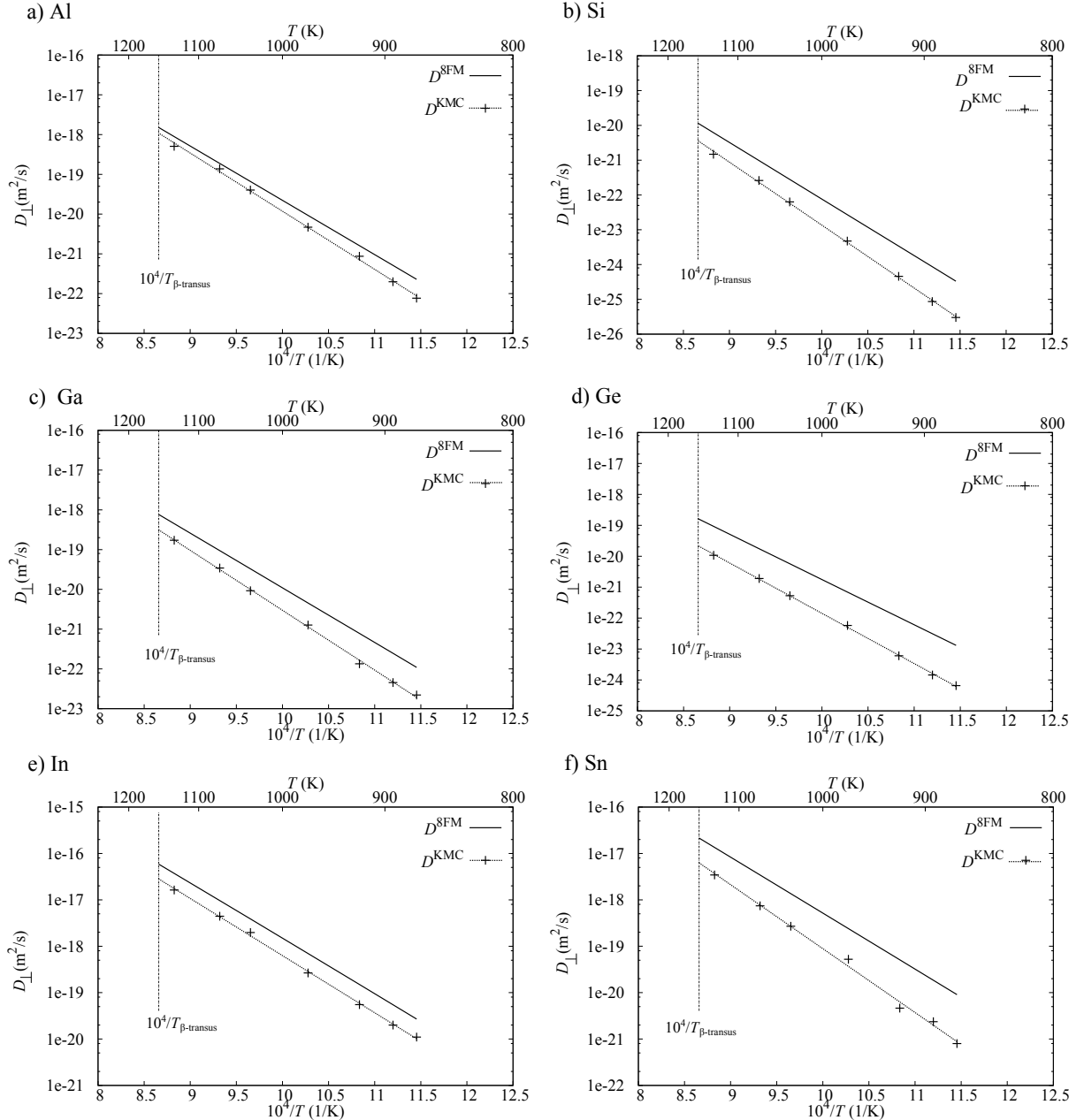
Figure 4.11: Comparison of perpendicular diffusivities ($D_\perp$) obtained by 8FM (D^{8FM}) and KMC simulations (D^{KMC}) of a) Al, b) Si, c) Ga, d) Ge, e) In and f) Sn.
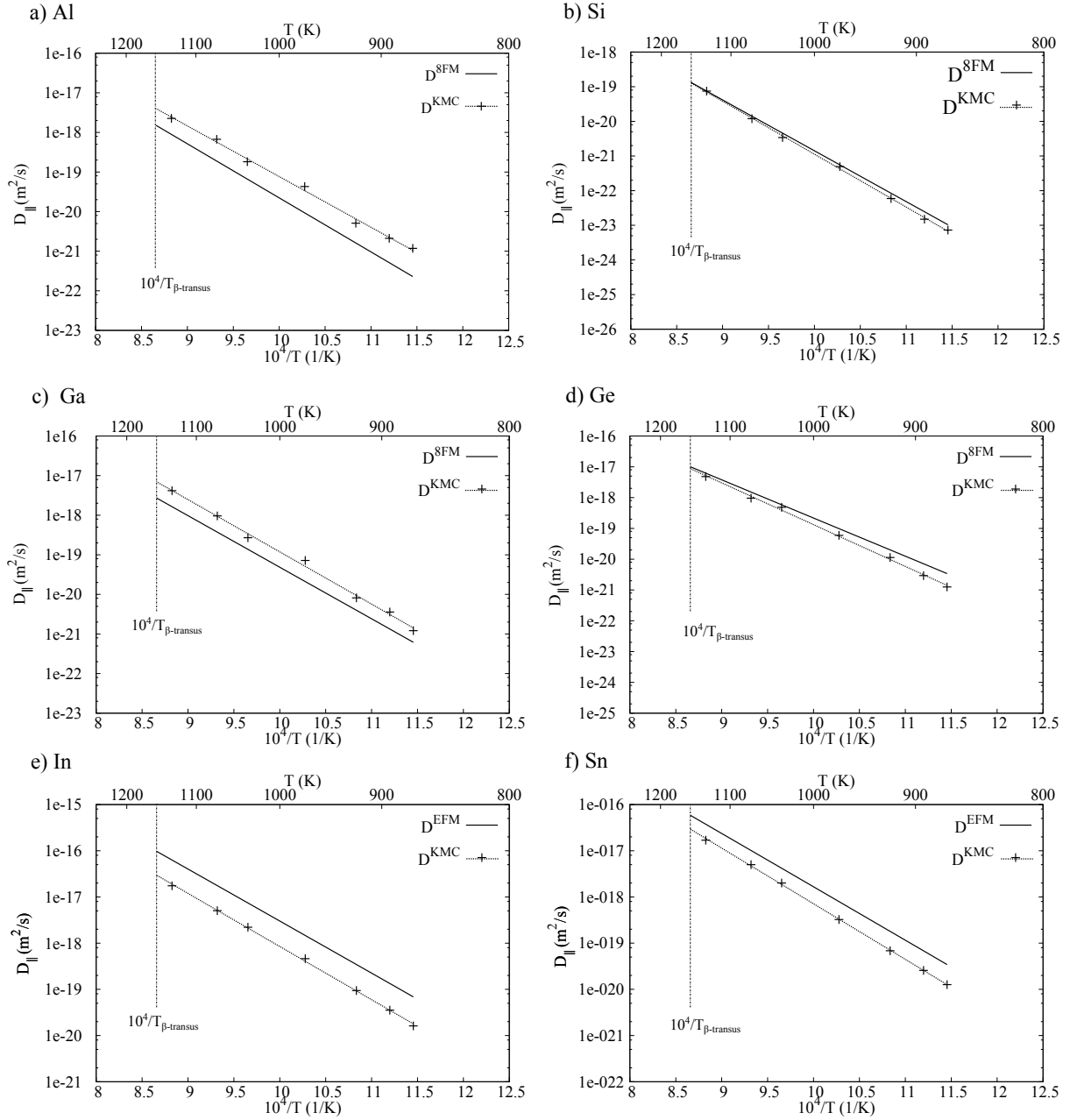
Figure 4.12: Comparison of parallel diffusivities ($D_\parallel$) obtained by 8FM (D^{8FM}) and KMC simulations (D^{KMC}) of a) Al, b) Si, c) Ga, d) Ge, e) In and f) Sn.

4.4   Discussion and Conclusions

We have obtained the values of the semi-metals diffusivities in α-Ti using "8-frequency" model implemented by *ab initio* calculations. Our results agree with KMC values, and in the case of solvent and Al diffusion also agree with previous first-principles and experimental data.

One interesting finding is that large atoms move faster than small atoms. Large solute

Table 4.5: Activation energies (Q) of semi-metals diffusion perpendicular ($\perp$) and parallel ($\parallel$) to the basal plane in α-Ti obtained by using 8FM model and KMC approach.

Solute	$Q_\perp^{\text{8FM}}$ (eV)	$Q_\perp^{\text{KMC}}$ (eV)	$Q_\parallel^{\text{8FM}}$ (eV)	$Q_\parallel^{\text{KMC}}$ (eV)
Al	2.736	2.902	2.709	2.541
Si	3.222	3.584	2.912	3.032
Ga	2.728	2.988	2.585	2.620
Ge	2.903	3.224	2.461	2.692
In	2.369	2.444	2.236	2.283
Sn	2.395	2.734	2.293	2.389

Table 4.6: Pre-exponential factors (D_0) of semi-metals diffusion perpendicular ($\perp$) and parallel ($\parallel$) to the basal plane in α-Ti obtained by using 8FM and KMC approach.

Solute	$D_{0\perp}^{\text{8FM}}$ (m²/s)	$D_{0\perp}^{\text{KMC}}$ (m²/s)	$D_{0\parallel}^{\text{8FM}}$ (m²/s)	$D_{0\parallel}^{\text{KMC}}$ (m²/s)
Al	1.034×10^{-6}	4.990×10^{-6}	9.290×10^{-7}	4.894×10^{-7}
Si	1.319×10^{-6}	1.574×10^{-5}	6.740×10^{-7}	2.154×10^{-6}
Ga	6.100×10^{-7}	3.417×10^{-6}	5.160×10^{-7}	1.896×10^{-6}
Ge	7.580×10^{-7}	2.529×10^{-6}	5.470×10^{-7}	4.885×10^{-6}
In	1.127×10^{-6}	1.304×10^{-6}	5.520×10^{-7}	2.707×10^{-7}
Sn	6.080×10^{-7}	5.335×10^{-6}	5.940×10^{-7}	7.816×10^{-7}

such as In has smaller migration energy than Si, as shown in Fig. 4.13, where the out-of-plane and in-plane ΔH_m energies are plotted against the solute radius. Although Si has smaller atomic radius (1.11 Å) than In (1.54 Å), In has migration energies three times smaller than Si. This seems to be related to the electronic character of solute-solvent bond as described in Section 4.4.1. The second result offers an explanation for the anisotropic behaviour of the solute diffusion in α-Ti. The migration energies of out-of-plane jump are larger than $\Delta H_{m\parallel}$, as shown in Fig. 4.13, leading to anisotropy ratio lower than one (see Fig. 4.14). Ge is a special case, since $D_\parallel^{\text{Ge}}$ is 10^3 times higher than $D_\perp^{\text{Ge}}$, and $\Delta H_{m\parallel}$ is half of $\Delta H_{m\perp}$ value. The bond angle of solute-solvent pair seems to play a key role on the diffusion anisotropy behaviour, as reported in Section 4.4.2.
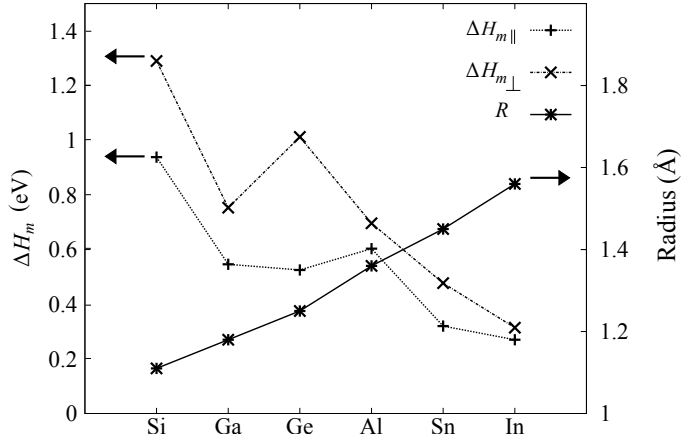
Figure 4.13: Comparison of migration energies (ΔH_m) and atomic radius (Radius) trends of semi-metals in α-Ti.
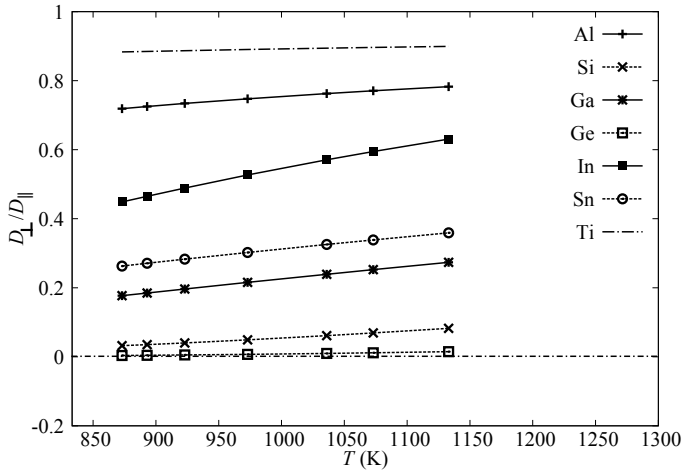
Figure 4.14: Comparison of anisotropic ratio ($D_\perp/D_\parallel$) of solvent, Al, Si, Ga, Ge, In and Sn diffusion obtained by 8FM method.

4.4.1 Atomic size and solute diffusion

The results obtained in this work contradict the common opinion that small atoms diffuse faster than large atoms. This fact has already been observed by Krcmar *et al* [106] on the diffusion of transition metals in Ni, where the solute migration is governed by the electronic characteristics of solute-solvent bonds, and the size effect has only a minor role. This observation can be also applied to semi-metals diffusion in Ti, especially when we compare Si and In diffusion. Using DFT calculations, the charge density of a crystal with Si and In sitting next to the vacancy are compared with the charge density at the saddle point of the out-of-plane jump in Fig. 4.15. The charge accumulation around Si is orientated along the directions [0001] and [$1\bar{1}00$], as the
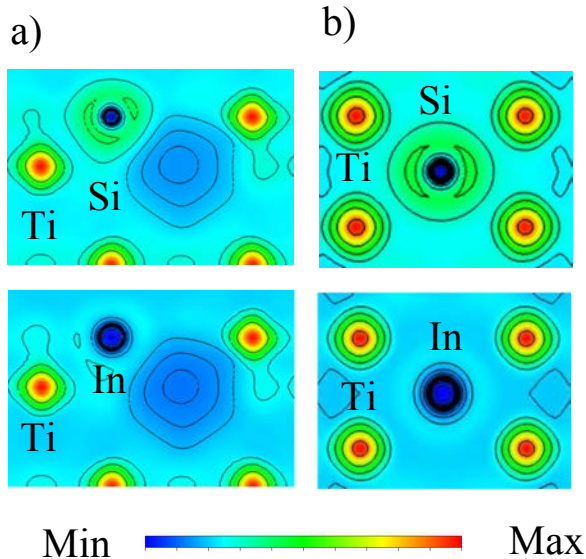
Figure 4.15: Electronic charge density of a) Si and In next to a vacancy, and b) Si and In at the saddle point in the plane normal to the migration direction.

solute creates directional bonds with the nearest Ti. The behaviour displayed by In differs as the charge density is spherically-symmetrical around the In atom indicating no directional bond. Therefore, Si requires higher energy to jump than In. The density of state (DOS) curves were also calculated. The DOS of the first-nearest neighbour Ti atom to the Si and In atom at initial and transition states during $\perp$ jump are presented in Fig. 4.16. In general, the 0 eV energy value corresponds to the Fermi energy. This is the highest level of energy occupied by the electrons. The energy levels below 0 eV correspond to the valence band, while the covalent band is identified on the region over the Fermi energy. In the case of In, the area under the curve in the covalent region is larger than Si case, indicating a weak solute-solvent bond that can be easily broken. Si has smaller covalent region both at the initial and transition state, indicating that the Si-Ti bond requires a large energy to be broken. In conclusion, the diffusion behaviour of semi-metals in α-Ti is not only controlled by the atomic size, but also by the solute-solvent bond.

4.4.2 Diffusion anisotropy

Our results show that semi-metals diffusion in α-Ti is characterised by anisotropic behaviour which is extreme in the case of Ge (see Fig. 4.14). The electronic structure of solute-host bond

is not sufficient to explain this anisotropy diffusion.

We apply the model proposed by Swalin to describe the diffusion in fcc crystal [192] to hcp α-Ti in order to investigate such behaviour. Swalin considers the migration energy as a result of two components. The energy due to the dilation of the "host window" surrounding the solute at the saddle point, and the energy due to the compression of solute in order to squeeze through this window. When the solute jumps, it passes through the window formed by the nearest solvent atoms at the saddle point. These solvent atoms can move closer or further away from the jumping atom. If the host displacement is small, the dilation component of activation energy is high and vice-versa. The dilation energy is proportional to the circumferential circle radius, R, of the host window. The solvent windows for in-plane and out-of-plane jumps are schematically shown in Fig. 4.17. The red dashed line indicates the circumferential circle to the host window. In Table 4.7, R and ΔH_m values of out-of-plane and in-plane solute jumps are compared. While the migration energies are quite different, the $R_\parallel/R_\perp$ is close to 1, indicating that dilation is similar for the two transitions, and therefore it has no relevant effect on the anisotropy. The second term of Swalin's model is proportional to the compressibility of the solute atoms. An estimation of solute compressibility can be obtained by calculating the migration energy with unrelaxed host window. These values are reported in Table 4.8, and they suggest that the compressibility also has a small effect on the anisotropy behaviour in α-Ti, since the $\left(\Delta H_{m\parallel}/\Delta H_{m\perp}\right)^{\mathrm{unrelaxed}}$ ratios are circa 1.

A third term is needed when considering a hcp crystal, as the angle of solute-solvent bond at the transition state differs between the in-plane and out-plane jumps. In this work, this angle is denoted as γ, and it is highlighted in Fig. 4.17. In the ideal case, γ is equal to 71.1º for out-of-plane jump and to 68.8º for in-plane jump. During the solute migration, these two values change as reported in Table 4.9. Both $\gamma_\perp$ and $\gamma_\parallel$ decrease with respect to the ideal values. The reduction of $\gamma_\perp$ is around 6.2-7.5 %, while $\gamma_\parallel$ is reduced by 9.5-10.5 %. The effect of γ can be qualitatively measured by calculating the migration energy, allowing for the dilation, but without bond angle distortion. The migration energy calculated when the bond angle are not distorted ($\Delta H_m^{\gamma\mathrm{ideal}}$) are reported in Table 4.9. As expected, both $\Delta H_{m\perp}^{\gamma\mathrm{ideal}}$ and $\Delta H_{m\parallel}^{\gamma\mathrm{ideal}}$ values

Table 4.7: Values and ratios of semi-metals circumferential radii (R) and migration energies (ΔH_m) of in-plane ($\parallel$) and out-of-plane ($\perp$) jumps after full relaxation. The circumferential radius quantifies the dilation component of migration energy.

Solute	$R_\perp$ (Å)	$R_\parallel$ (Å)	$R_\parallel/R_\perp$	$\Delta H_{m\perp}$ (eV)	$\Delta H_{m\parallel}$ (eV)	$\Delta H_{m\parallel}/\Delta H_{m\perp}$
Al	2.758	2.734	0.991	0.696	0.603	0.866
Si	2.661	2.633	0.990	1.290	0.938	0.727
Ga	2.725	2.710	0.985	0.753	0.546	0.725
Ge	2.690	2.674	0.994	1.018	0.526	0.514
In	2.844	2.825	0.993	0.314	0.270	0.859
Sn	2.826	2.810	0.994	0.477	0.320	0.671

Table 4.8: Values and ratios of semi-metals migration energies of in-plane ($\parallel$) and out-of-plane ($\perp$) jumps calculated with unrelaxed solvent-window ($\Delta H_m^{\text{unrelaxed}}$). These migration energies qualitatively measure the solute compressibility.

Solute	$\Delta H_{m\perp}^{\text{unrelaxed}}$ (eV)	$\Delta H_{m\parallel}^{\text{unrelaxed}}$ (eV)	$\left(\Delta H_{m\parallel}/\Delta H_{m\perp}\right)^{\text{unrelaxed}}$
Al	1.748	1.781	1.019
Si	1.655	1.810	1.094
Ga	1.340	1.659	1.238
Ge	2.269	2.444	1.077
In	1.696	1.888	1.113
Sn	1.675	2.069	1.235

increase with respect to the fully relaxed data reported in Table 4.7. However, in the case of in-plane jump, the migration energies without bond angle distortion are higher than fully relaxed case, while in case of out-of-plane jumps the migration energies are similar to the fully relaxed case. In particular, the ratio $\left(\Delta H_{m\parallel}/\Delta H_{m\perp}\right)^{\gamma\text{ideal}}$ is close to 1. This suggests that the distortion of bond angle after full relaxation leads to a low-energy configuration at the saddle point in the case of in-plane jump. As a result, the solute diffusion in α-Ti has an anisotropic character, which is extreme in the case of Ge. The $\Delta H_{m\perp}^{\text{Ge}}$ energy does not significantly change between conditions with and without bond angle distortion. On the contrary, the $\left(\Delta H_{m\parallel}\right)_{\gamma ideal}^{\text{Ge}}$ energy doubles the complete relaxation values. Si shows similar behaviour to Ge, with the migration

Table 4.9: Values of semi-metals bond angles (γ) after full relaxation, and the values and ratios of migration energies evaluated with ideal angle ($\Delta H^{\gamma\mathrm{ideal}}$) of in-plane ($\parallel$) and out-of-plane ($\perp$) jumps. These migration energies quantify the effect of bond distortion.

Solute	$\gamma_\perp$	$\gamma_\parallel$	$\Delta H_{m\perp}^{\gamma\mathrm{ideal}}$ (eV)	$\Delta H_{m\parallel}^{\gamma\mathrm{ideal}}$ (eV)	$\left(\Delta H_{m\parallel}/\Delta H_{m\perp}\right)^{\gamma\mathrm{ideal}}$
Al	66.7º	62.0º	0.829	0.680	0.820
Si	66.6º	62.0º	1.329	1.349	1.015
Ga	66.6º	62.1º	0.842	0.975	1.157
Ge	66.6º	62.2º	1.062	1.121	1.055
In	66.0º	61.9º	0.566	0.814	1.437
Sn	65.8º	61.6º	0.711	0.914	1.285

energies of ideal γ having ratio of $\left(\Delta H_{m\parallel}/\Delta H_{m\perp}\right)^{\gamma\mathrm{ideal}}$ close to 1. However, the $\Delta H_{m\parallel}^{\mathrm{Si}}$ energy decreases by 0.411 eV when the symmetry is relaxed. In the case of perpendicular jumps, the reduction is only of 39 meV. The migration energies of In and Sn atoms also reduce from ideal to fully relaxed symmetry cases. In the of case of Al, the $\Delta H_{m\parallel}/\Delta H_{m\perp}$ ratio is not significantly influenced by γ. This is consistent with the fact that the anisotropy ratio of Al is close to 1. In general, the relaxed bond angle leads to a low-energy configuration at the activated state in the case of parallel jump. As a result, the substitutional solute requires larger energy to perform the $w_\perp$ than $w_\parallel$ jump.

(a)

(b)
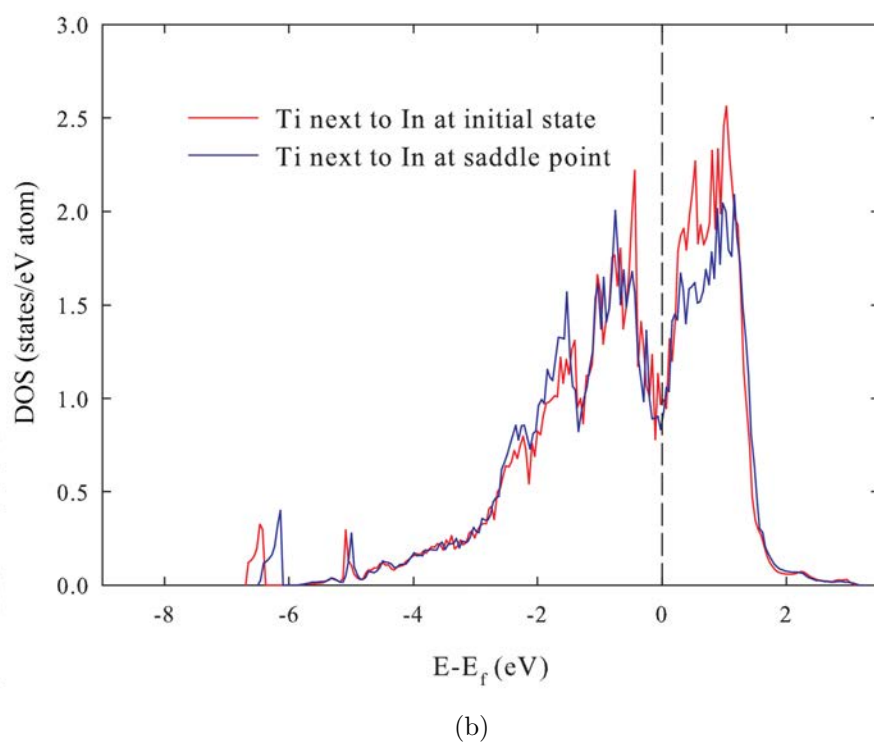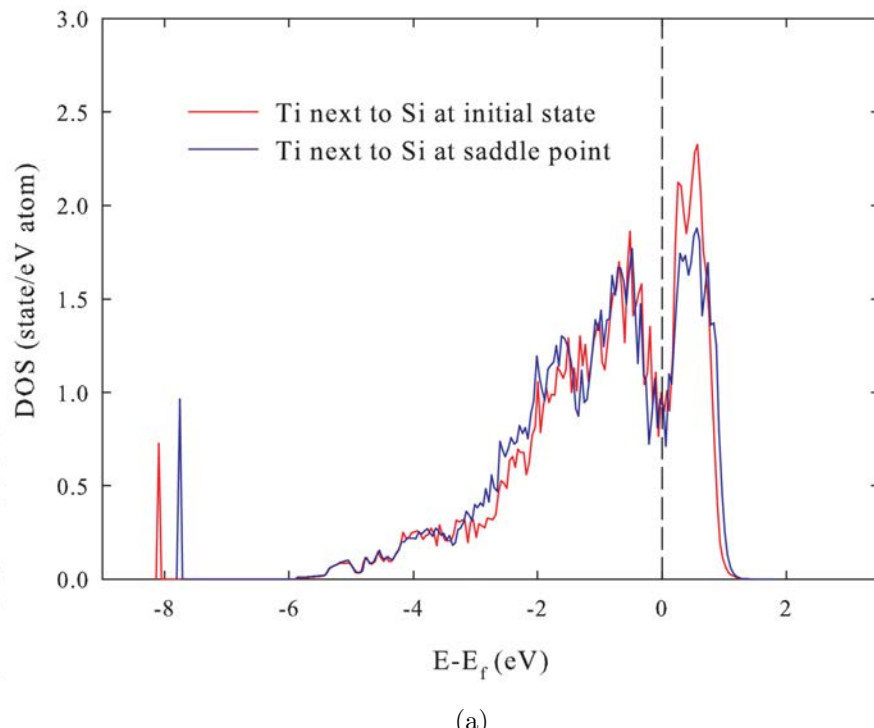
Figure 4.16: Comparison of DOS curves of Ti atom sitting next to a) Si and b) In at initial state and saddle point in the case of out-of-plane jump.
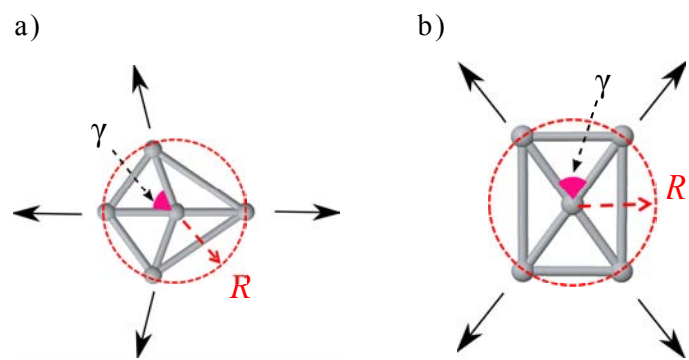
Figure 4.17: Window formed by the nearest-Ti atoms surrounding the solute at the saddle point of a) $\parallel$ and b) $\perp$ jumps. The circumferential circles are displayed in red dashed line, the corresponding radii are defined as R, and the bond angles are referred as γ.

Chapter 5

Interstitial diffusion in alpha-Ti: O, N and C

5.1 Introduction

Oxygen, Nitrogen and Carbon have severe detrimental effect on the creep properties of near-α Ti alloys, forming the fragile α-case phase [1, 28]. Due to the poor ductility of the phase, the α-case acts as source for fracture initiation [28]. The large concentration of these elements leads to a loss of plasticity in Ti [22, 65, 90]. At high temperature, these elements dissolve in the interstitial sites, and the α-case phase rapidly spreads in the Ti bulk, as a result of their fast diffusion rates [28]. The study of Zhu *et al* [32] on the dynamics of Ti oxidation shows that O is thermally more stable in the bulk than in TiO$_2$. Additionally, Zhu and co-workers have established that the oxidation process is controlled by the O bulk diffusion barrier [32]. Understanding the O, N and C diffusion mechanism is important for the prevention and mitigation of α-case phase formation when designing high-temperature alloys and their thermo-mechanical processing. Knowing which interstitial sites they occupy and through which transition pathways they move is fundamental for the control of oxide growth in Ti.

The diffusion of O, N and C is governed by interstitial transitions, given the small radius of these three solute. In the interstitial diffusion, the host lattice shows no displacement before and
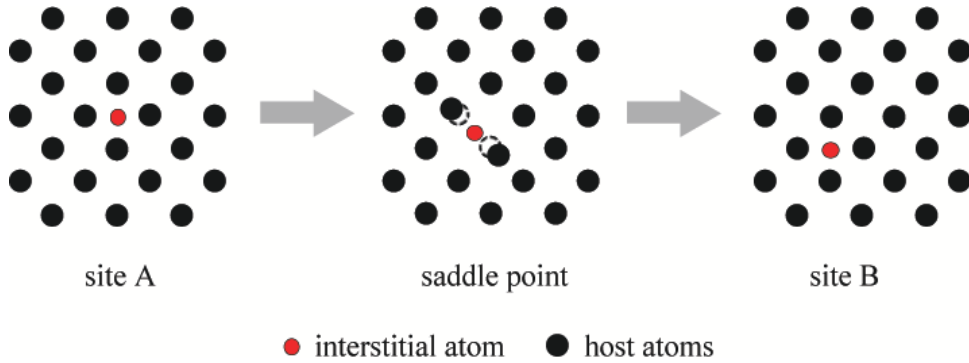
Figure 5.1: Schematic representation of solute interstitial migration.

after the solute jump (see Fig. 5.1). The shift of solvent atoms happens only at the activated state to allow the solute jump. All the jumps are equally probable and independent, at least in dilute alloys. The solute walk can be considered random and it is not required to introduce the correlation factor in the diffusion coefficients formulation. When the interstitial concentration is higher, more interstitial sites are occupied, blocking some jumps. In this case, the migration can not be considered completely random any more. A particular case of interstitial diffusion is the interstitialcy migration which involves self-interstitials instead of solute atoms. This mechanism consists on the self-interstitial atom jumping into an occupied lattice site, pushing away the solvent atom, as shown in Fig. 5.2. In this scenario, the jump from lattice to a self-interstitial site can not be considered independent, since one of the interstitial sites is already occupied. Therefore, the interstitialcy mechanism needs to be considered as correlated migration. The self-interstitial formation energy is high, two or three times higher than vacancy formation energy, so the self-interstitial concentration is usually neglected considering the magnitude of the vacancy concentration. The thermal diffusion is usually not significantly influenced by interstitialcy mechanism, but the migration of these defects becomes important in the case of energetic particle radiation, hence in radiation-induced diffusion.

The experimental bulk diffusivities of O [23], N [24], C [25, 26] have already been presented in Fig. 2.26 in Section 2.3.5, the corresponding diffusion parameters are summarised in Table 5.1. N and O have similar diffusion behaviour, with O migration energetically more favourable with respect to N diffusion. In the case of C, there is a discrepancy between the two experimental studies found in the literature [25, 26]. Nevertheless, C diffusivities are higher than O and
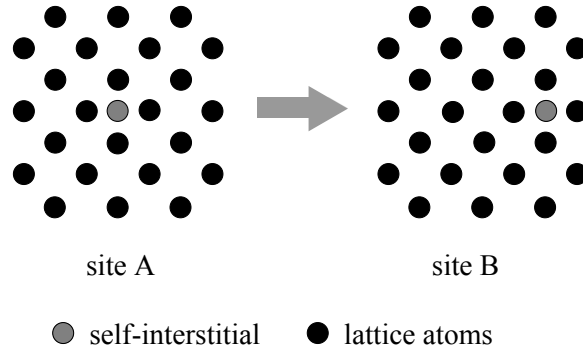
Figure 5.2: Schematic representation of interstitialcy migration.

N values in α-Ti. These three solutes present larger diffusivity values with respect to the solvent diffusion, suggesting that they move through interstitial transitions. However, these experimental studies do not give informations on the mechanism itself. For example, the O and C diffusions follow the same $D_\perp/D_\parallel < 1$ trend of self-diffusion and substitutional solute diffusion [26, 193], contradicting the predictions of the model proposed by Bertin and co-workers[194]. In their model, Bertin *et at* have suggested that O, C and N dissolve in and move through octahedral and tetrahedral sites. On the other, *ab intio* method has been shown capable of predicting the interstitial diffusion [50, 110], using an analytical method called Multi-State Diffusion (MSD). The MSD method was developed by Landman and Shlesinger [52, 53] to describe the random walk when the atom moves through internal sites (see Section 5.2). It has been used by Wu and Trinkle [50] to study O interstitial diffusion in α-Ti and by O'Hara and Demkov for O and N diffusion in α-Hf [110], obtaining good results with respect to the experimental data. These works also show that the interstitial migration can happen through less traditional interstitial sites than octahedral and tetrahedral sites. The aim of this chapter is to investigate the diffusion mechanism of O, N and C using MSD and KMC simulations informed by DFT calculations.

Our results confirm the fact that O, N and C preferentially occupy octahedral sites, however tetrahedral sites are unstable and relax to hexahedral site (see Section 5.3). As established by Wu and Trinkle [50], less traditional interstitial sites were found to be stable such as hexahedral, crowdion and basal crowdion. Nevertheless, when these solutes sit at octahedral sites, they form strong bond with Ti atoms. The covalent nature of these bonds can explain the loss of plasticity

Table 5.1: Experimental diffusion parameters of O, N, and C in α-Ti. Q and D_0 are the activation energy and pre-exponential factor of bulk diffusion.

Solute	Q (eV)	D_0 (m²/s)
O [23]	1.752±0.5	2±1x10⁻⁷
N [24]	1.897±0.02	1.1±0.8x10⁻⁷
C [25]	1.171±0.03	6.4±0.2x10⁻⁷
C [26]	2.083	4.85x10⁻⁴

in Ti. A review of the common migration pathways through which these elements were believed to migrate [22] is also required. The updated MEPs can explain the diffusion anisotropy in α-Ti of these atoms (see Section 5.4).

5.2 Methodology

The interstitial energies were calculated using VASP 5.3.2 [58–61] and with electronic structure described by PAW [142], the exchange-correlation functional was computed using GGA-PBE [143], and used a 54-atom supercell, with a Monkhorst-Pack mesh of 32 x 32 x 17 k-points for a 2-atom cell and an energy cut-off of 350 eV. The migration energies and minimum energy path were evaluated using CI-NEB [62–64] with five images using the same set-up of interstitial energy calculations (supercell size, k-points mesh, and energy cut-off).

5.2.1 Interstitial site in hcp crystal

In a hcp crystal, there are eight possible interstitial sites, as shown schematically in Fig. 5.3. In this work, octahedral site is indicated as OC, tetrahedral as TE, crowdion as CR, split dumbbells along the c-axis as SP, basal octahedral as BO, hexahedral as HE, basal crowdion as BC and split dumbbells in the basal plane as BS. OC and TE sites have trigonal symmetry, and there are two octahedral and four tetrahedral sites in the unit cell. OC is surrounded by six Ti atoms, while TE has four nearest solvent atoms. CR has monoclinic symmetry and has two 1st-nearest-neighbour and four 2nd-nearest-neighbour Ti atoms. There are six equivalent
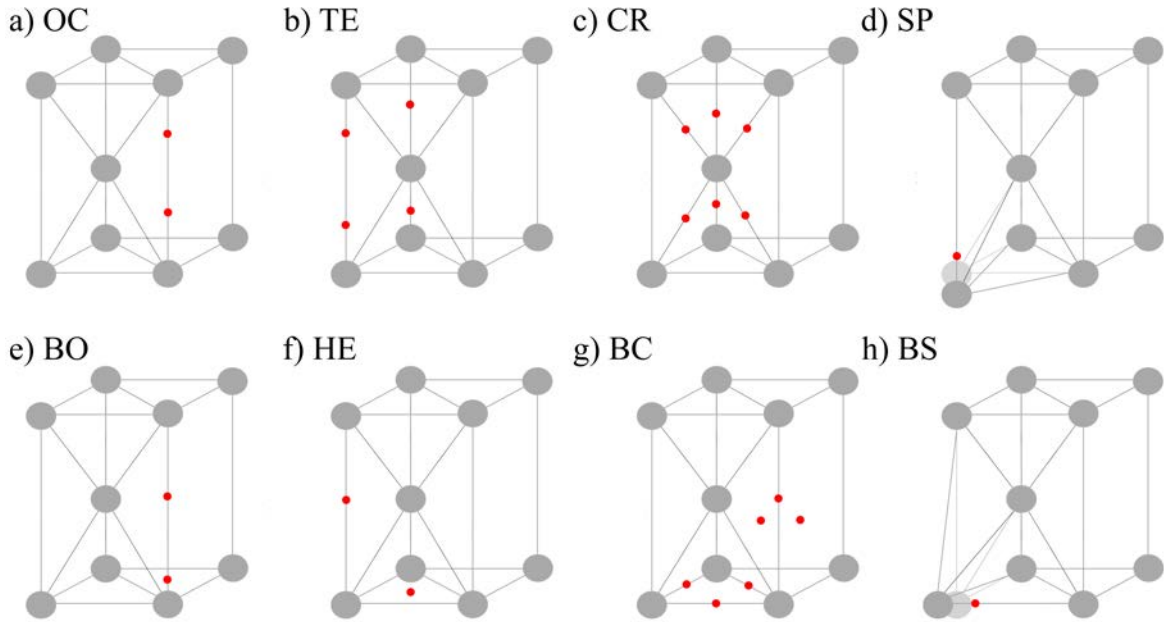
Figure 5.3: Schematic representation of the possible stable interstitial sites in hcp crystal: octahedral (OC), tetrahedral (TE), crowdion (CR), split dumbbells along the c-axis (SP), basal octahedral (BS), hexahedral (HE), basal crowdion (BC) and split dumbbell in the basal plane (BS).

crowdion sites in the unit cell. SP, BS and BC sites have orthorhombic symmetry. BS and SP configurations are obtained by substituting the solvent atom by solute-host pair at the lattice position. BC site has two 1st-nearest-neighbour and four 2nd-nearest-neighbour solvent atoms. In the unit cell, it is possible to count four SP, six BS and four BC sites. HE and BO have hexagonal geometry and they are surrounded by three solvent atoms. There are two HE and two BO equivalent sites in hcp unit cell. The geometries and symmetries of these sites are summarised in Table 5.2, where the reduced coordinates are given for lattice sites at (0,0,0) and (1/3,1/3,1/2).

The interstitial energy, E_i, was evaluated using,

$$E_i = E\{M_N + I\} - E\{M_{N-1} + X_1\} - \frac{N+1}{N} E\{M_N\}; \qquad (5.1)$$

where N is the total number of solvent atoms, $E\{M_N + I\}$ is the energy of system where solute occupies the interstitial site, $E\{M_{N-1} + X_1\}$ is the energy of system with substitutional solute and $E\{M_N\}$ is the energy of the perfect site. Negative values of E_i indicate that solute tends

Table 5.2: Geometry, symmetry and number of equivalent sites of the eight interstitial sites in hcp unit cell. The reduced coordinates are given for lattice sites at (0,0,0) and (1/3,1/3,1/2). In the case of SP and BS, the solvent atom in the origin moves to a new position reported in the second line.

Site	Symmetry system	Symmetry group	Reduced coordinates	Number of equivalent sites
OC	Trigonal	$\bar{3}m1$	(2/3,2/3,1/4)	2
TE	Trigonal	$3m$	(0,0,3/8)	4
CR	Monoclinic	$2/m$	(1/6,1/6,1/4)	6
SP	Orthorhombic	$\bar{6}m2$	(0,0,1/4)	4
			(0,0,-1/4)	
BO	Hexagonal	$\bar{6}m2$	(2/3,2/3,0)	2
HE	Hexagonal	$\bar{6}m2$	(0,0,1/2)	2
BC	Orthorhombic	$mm2$	(1/2,0,0)	4
BS	Orthorhombic	$mm2$	(1/3,0,0)	6
			(-1/3,0,0)	

to dissolve as interstitial and vice-versa.

5.2.2 Multi State Diffusion method

Landman and Shlesinger have developed the Multi-State Diffusion method technique to generalize the continuous-time random walk to systems where the atom transitions occur between internal states [52, 53]. This method can be applied to study the interstitial diffusion [50, 110]. In practice, it consists on defining the stable interstitial sites occupied by the solute in the crystals. The second step is to identify and map the possible transitions occurring from each stable interstitial site. Once the map is complete, the average displacement and waiting-time distribution function, $\underline{\psi}_{ij}(t)$, of each jump is calculated. This function governs the temporal dependence of the $i \to j$ jump, and it depends on the sum of n jump frequencies from site j,

Λ_j, and jump frequency from j to i site, w_{ij},

$$\underline{\psi}_{ij}(t) = n_{ij} \; \mathrm{w}_{ij} \exp\left(-\Lambda_j t\right) \tag{5.2}$$

where n_{ij} is the total number of $i \to j$ jump from site i,

$$\Lambda_j = \sum_i \mathrm{w}_{ij}. \tag{5.3}$$

The next step is to build the Laplace transform matrix of waiting-time function, $\overrightarrow{\psi}(u)$, and Fourier transform matrix of the average displacement, $\underline{\tilde{p}^*}\left(\overrightarrow{k}\right)$. The probability to perform transition states is described by propagator matrix, $\underline{R}\left(\overrightarrow{k}, u\right)$, defined as,

$$\underline{R}\left(\overrightarrow{k}, u\right) = \left[I - \underline{\tilde{p}^*}\left(\overrightarrow{k}\right) \cdot \overrightarrow{\psi}(u)\right], \tag{5.4}$$

where I is the identity matrix. Finally, the diffusion coefficient along a generic r direction is defined as,

$$D_r = \frac{\sigma_r^2(t)}{2t}, \tag{5.5}$$

where $\sigma_r^2(t)$ is the variance of diffusion depending on determinant of $\underline{R}\left(\overrightarrow{k}, u\right)$, $\Delta\left(\overrightarrow{k}, u\right)$,

$$\sigma_r^2(t) = \lim_{\overrightarrow{k} \to 0} t \frac{1}{\Delta_0} \frac{\delta^2 \Delta}{\delta k_r^2}\Big|_{u \to 0}, \tag{5.6}$$

with

$$\Delta_0 = \lim_{u \to 0} \frac{\Delta\left(\overrightarrow{k}, u\right)}{u}. \tag{5.7}$$

In this work, the possible transition pathways are presented in Section 5.3.2, while the Laplace transform matrices of waiting time and the Fourier transform matrices of displacement obtained following the procedure explained in [53] are presented in Appendix B.

Table 5.3: Interstitial formation energies (E_i) of O, N and C in α-Ti. If the interstitial site results unstable, the solute can displace to an other configuration or be a saddle point, as reported in bracket.

Site	E_i^O (eV)	E_i^N (eV)	E_i^C (eV)
OC	**-5.612**	**-5.931**	**-3.862**
TE	(HE)	(HE)	(HE)
CR	**-4.304**	**-4.554**	**-2.554**
SP	(HE)	HE)	(HE)
BO	(Saddle point)	(Saddle point)	(Saddle point)
HE	**-4.384**	**-4.182**	(Saddle point)
BC	(HE)	**-4.610**	**-2.547**
BS	(HE)	(BC)	(BC)

5.2.3 KMC simulations

KMC simulations were also performed in order to verify the results of the analytical method. The diffusion coefficients were calculate using the equation 3.11 in Section 3.4. Since the vacancies are not involved and the migration can be considered random, there is no need to introduce the C_{eq} correction in the diffusivity equation. The diffusivities are obtained after 100 simulations of 10^6 solute jumps each.

5.3 Results

5.3.1 Interstitial sites

The O, N and C interstitial energies and their stability at each interstitial site in α-Ti were evaluated using DFT and they are reported in Table 5.3.

Oxygen has three stable interstitial sites, OC, CR and HE. TE, SP, BC and BS sites are unstable, and O moves to HE configuration after relaxation. BO configuration is metastable since it has one imaginary vibrational frequency. The values of E_i indicate that O preferentially dissolves at octahedral site, where it is surrounded by six solvents at distance of 2.085 Å. HE

is the second energetically favourable site to be occupied by O, followed by CR site. In the HE site, O has three 1st-nearest solvents at 1.949 Å in the same basal plane and two 2nd-nearest neighbours at 2.163 Å along c-axis. When O is at CR position, there are two 1st-nearest-neighbour and four 2nd-nearest-neighbour Ti atoms in the adjacent basal planes at 2.036 Å and 2.139 Å, respectively. In the unit cell, there are two OC, two HE and six CR sites as shows schematically in Fig. 5.4-a.

Nitrogen occupies OC, BC, CR and HE sites. Similar to oxygen, BO is metastable with one imaginary vibrational frequency. The calculations of TE and SP sites show that these sites are unstable and atomic forces drive N to HE site, while in the case of BS, they drive it to BC. Nitrogen at OC is the most favourable configuration followed by BC, CR and HE. At OC site, the distance between N and one of the six 1st-nearest solvent is 2.070 Å. At CR site, the two 1st-nearest and four 2nd-nearest Ti atoms are respectively at 2.027 Å and 2.116 Å. At HE site, there are three 1st-nearest solvents at 1.937 Å in the same basal planes of N and two 2nd-nearest neighbours at 2.142 Å along c-axis. When N occupies BC position, it has two 1st-nearest host atoms at 1.970 Å, one 2nd-nearest solvent atoms at 2.066 Å, and two 3rd-nearest Ti atoms at 2.129 Å. All these four sites and their equivalent sites in the unit cell are schematically shown in Fig. 5.4-b.

Carbon occupies preferentially OC site followed by CR and BC sites. BO and HE sites have one imaginary vibrational frequency, hence they are metastable. After relaxation, C moves from TE and SP to HE sites and from BS to BC sites. At OC site, the six nearest solvents distance 2.097 Å from C. The distance between the two 1st-nearest Ti atoms and C at CR is 2.049 Å, while the four 2nd-nearest Ti atoms are at 2.168 Å. When C is at BC site, there are two 1st-nearest solvent atoms at 2.000 Å, one 2nd-nearest solvent atom at 2.107 Å and two 3rd-nearest solvent atoms at 2.156 Å. These three interstitial sites and their equivalent in the unit cell are schematically shown in Fig. 5.4-c.
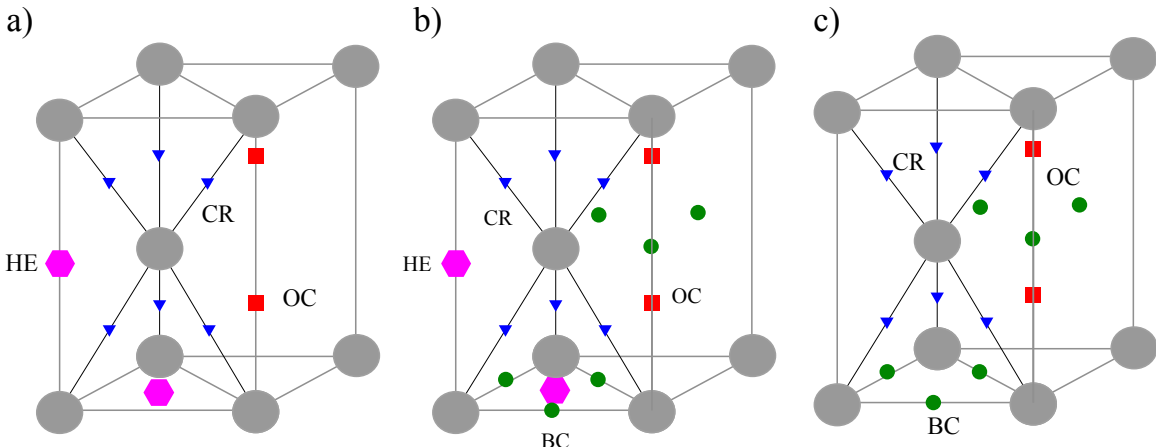
Figure 5.4: Schematic representation of a) O, b) N and c) C stable interstitial sites in α-Ti.

5.3.2 Transition Pathways

In this section, the map of all possible transitions and the jump frequencies calculated using CI-NEB method of O, N and C stable in α-Ti are reported.

Octahedral, hexahedral and crowdion are O stable interstitial sites in α-Ti. The transitions from these three sites are shown in Fig. 5.5. From the OC sites, O can perform two OC→OC transitions along c-axis, six OC→CR transitions within the basal plane and two OC→HE transitions. When O sits at CR sites, it can move to one of the two OC sites on the same basal plane (CR→OC), or to one of the two HE sites on the adjacent basal plane (CR→HE). There are six possible jumps from HE to CR sites (HE→CR) and six jumps from HE to OC sites (HE→OC). The MEPs of these transitions were evaluated using CI-NEB with fives images between the initial and final states (see Fig. 5.6). The corresponding migration energies, ΔH_m, and effective frequencies, ν^*, are summarised in Table 5.4.

The pathway networks of N are shown in Fig. 5.7. The jumps are similar to the ones described for O with the addition of the jumps from and to BC sites. From OC site, N can perform the same jumps described for O plus six OC→BC transitions in the adjacent basal planes. The CR site is surrounded by two OC sites in the same basal plane, two HE sites and four BC sites in the adjacent basal planes, corresponding to two CR→OC, two CR→HE and four CR→BC jumps. Nitrogen can move from HE sites to one of the six CR sites (HE→CR) or to one of the six OC sites (HE→OC). BC sites are surrounded by four CR and two OC
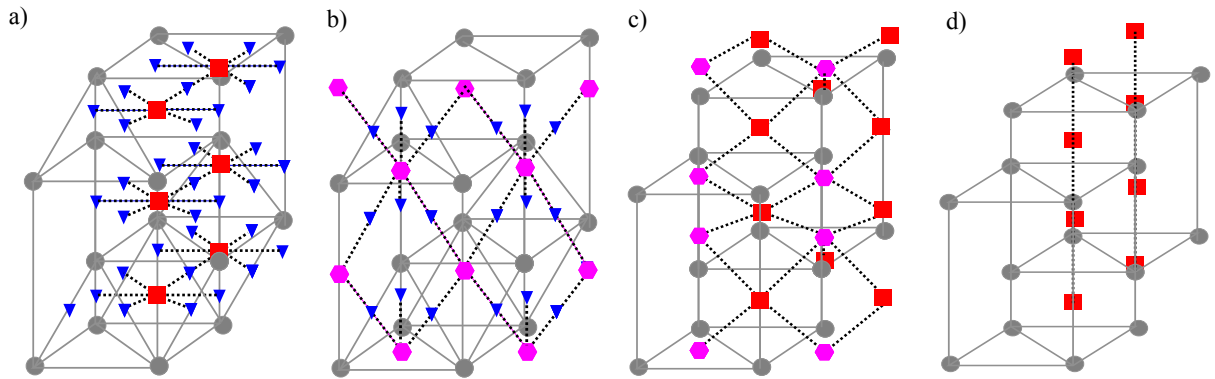
Figure 5.5: Schematic representation of transition pathways of O in α-Ti: a) OC$\leftrightarrow$CR, b) HE$\leftrightarrow$CR, c) OC$\leftrightarrow$HE and d) OC$\leftrightarrow$OC along c-axis.

Table 5.4: Migration energy (ΔH_m) and effective frequency (ν^*) of O interstitial jumps in α-Ti.

	ΔH_m (eV)	ν^* (THz)
OC$\rightarrow$OC	3.850	13.67
OC$\rightarrow$CR	1.883	27.92
OC$\rightarrow$HE	2.061	12.24
CR$\rightarrow$OC	0.575	11.19
CR$\rightarrow$HE	0.596	3.60
HE$\rightarrow$OC	0.833	10.45
HE$\rightarrow$CR	0.676	5.70
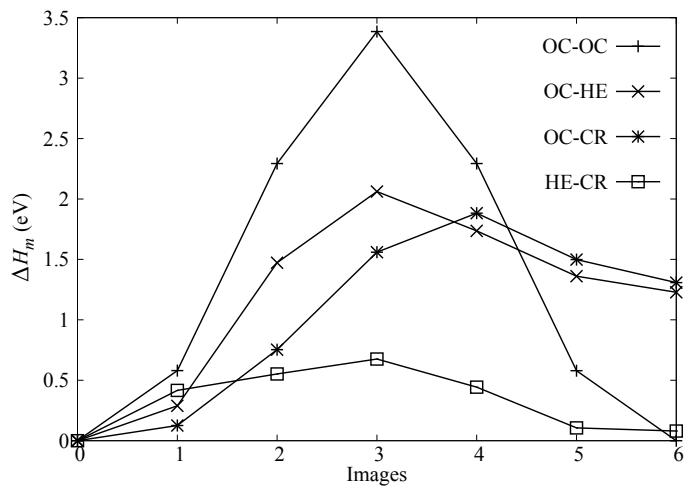
Figure 5.6: MEPs of O interstitial jumps in α-Ti: OC$\leftrightarrow$OC, OC$\leftrightarrow$HE, OC$\leftrightarrow$CR and HE$\leftrightarrow$CR transitions.
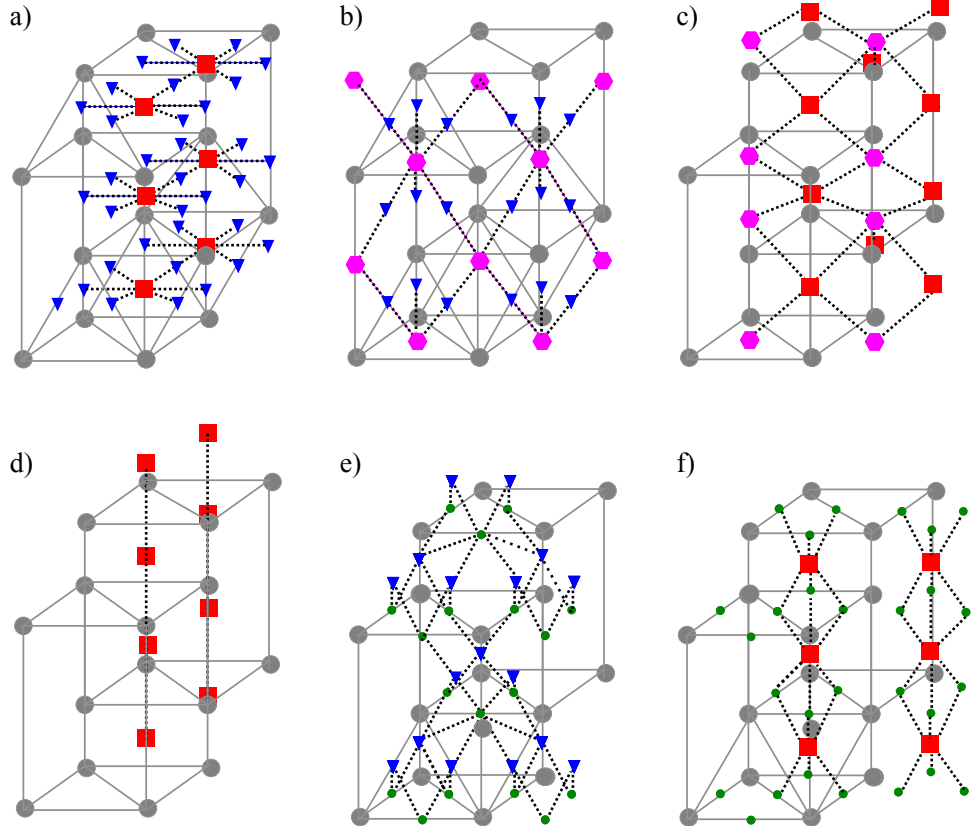
Figure 5.7: Schematic representation of transition pathways of N in α-Ti: a) OC$\leftrightarrow$CR, b) HE$\leftrightarrow$CR, c) OC$\leftrightarrow$HE, d) OC$\leftrightarrow$OC along c-axis, e) BC$\leftrightarrow$CR and f) BC$\leftrightarrow$OC.
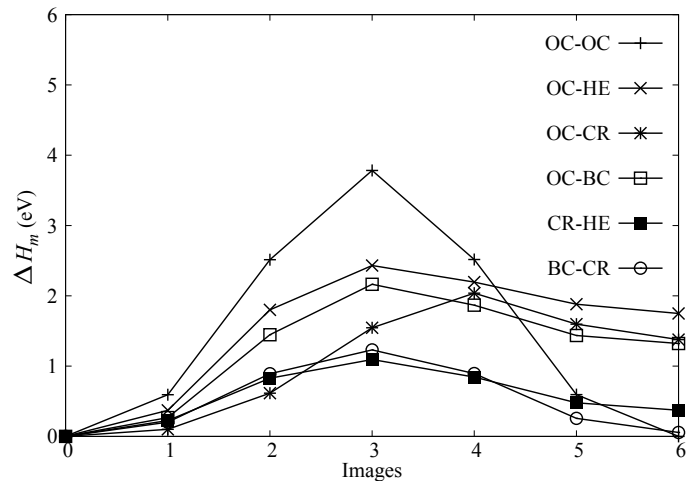
Figure 5.8: MEPs of N interstitial transitions in α-Ti: OC$\leftrightarrow$OC, OC$\leftrightarrow$HE, OC$\leftrightarrow$CR, OC$\leftrightarrow$BC , CR$\leftrightarrow$HE and BC$\leftrightarrow$CR transitions.

sites leading to four BC$\rightarrow$CR and two BC$\rightarrow$OC jumps. The BC$\leftrightarrow$HE swap is not considered because it occurs within the CR site. The MEPs of these transitions are displayed in Fig. 5.8 and their ΔH_m and ν^* values are summarised in Table 5.5.

Table 5.5: Migration energy (ΔH_m) and effective frequency (ν^*) of N interstitial jumps in α-Ti.

	ΔH_m (eV)	ν^* (THz)
OC→OC	3.784	18.858
OC→CR	2.038	23.217
OC→HE	2.430	10.566
OC→BC	2.164	18.181
CR→OC	0.661	20.100
CR→HE	1.093	15.098
CR→BC	1.175	12.719
HE→OC	0.682	13.237
HE→CR	0.722	9.503
BC→OC	0.842	17.367
BC→CR	1.230	35.113
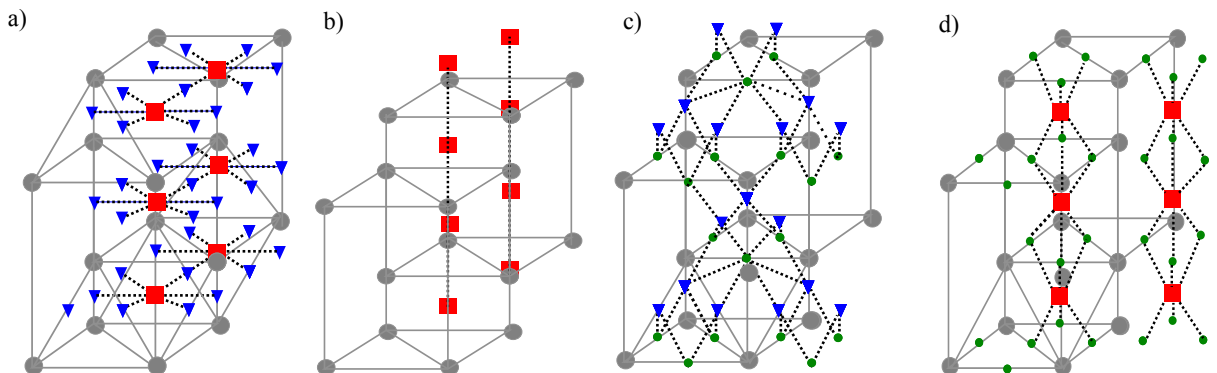
Figure 5.9: Schematic representation of transition pathways of C in α-Ti: a) OC↔CR, b) OC↔OC along c-axis, c) BC↔OC and d) OC↔CR .

Finally, the interstitial jumps for C are displayed in Fig.5.9. From the OC site, there are two OC→OC transitions along the c-axis, six OC→CR transitions within the basal plane and six OC→BC transitions. In the case of CR site, there are two CR→OC transitions in the same basal plane and four CR→BC transitions. From the BC site, there are two BC→OC and four BC→CR transitions. The MEPs of these jumps are displayed in Fig. 5.10, and the corresponding ΔH_m and ν^* values are summarised in Table 5.6.

Table 5.6: Migration energy (ΔH_m) and effective frequency (ν^*) of C interstitial jumps in α-Ti.

	ΔH_m (eV)	ν^* (THz)
OC→OC	3.396	16.701
OC→CR	1.424	94.570
OC→BC	1.694	70.874
CR→OC	0.116	3.210
CR→BC	0.848	10.85
BC→OC	0.379	17.599
BC→CR	0.841	33.68
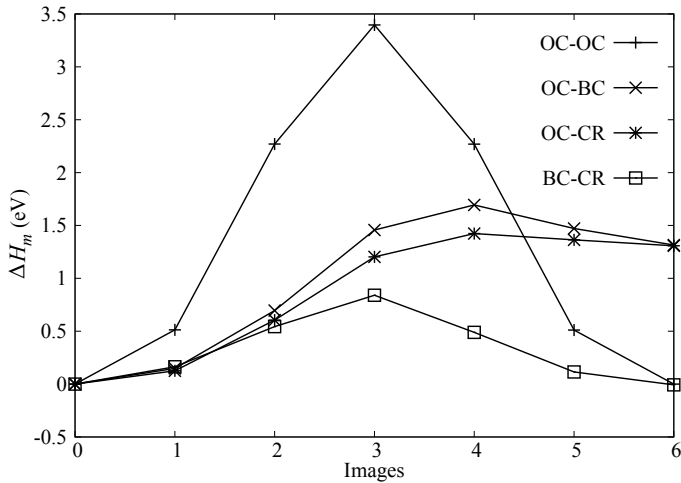
Figure 5.10: MEPs of C interstitial transitions in α-Ti: OC↔OC, OC↔CR, OC↔BC and BC↔CR transitions.

5.3.3 Diffusion coefficients

Knowing the stable interstitial sites and transition pathways, it is possible to evaluate the diffusion coefficients of O, N and C in α-Ti using the MSD and KMC methods. The perpendicular and parallel diffusivities of O, N and C evaluated in this work are displayed respectively in Fig. 5.11, Fig. 5.12 and Fig. 5.13. The diffusion parameters, Q and D_0, are compared in Table 5.7 and Table 5.8, respectively. There is a good agreement between the results of these two approaches.

The O diffusion coefficients evaluated in this work were compared with previous first-principles study [50] (see Fig. 5.11). Wu and Trinkle have applied the MDS method, informed
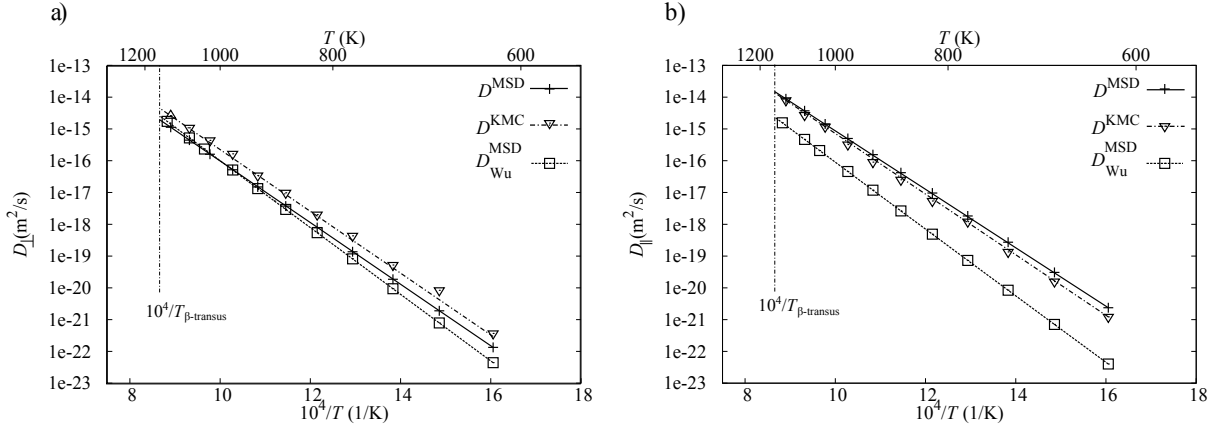
Figure 5.11: Oxygen diffusion coefficients along a) perpendicular ($\perp$) and b) parallel ($\parallel$) directions to the basal plane evaluated by MSD (D^{MSD}) and KMC method (D^{KMC}) and compared with previous first-principles study [50] ($D^{\mathrm{MSD}}_{\mathrm{Wu}}$).
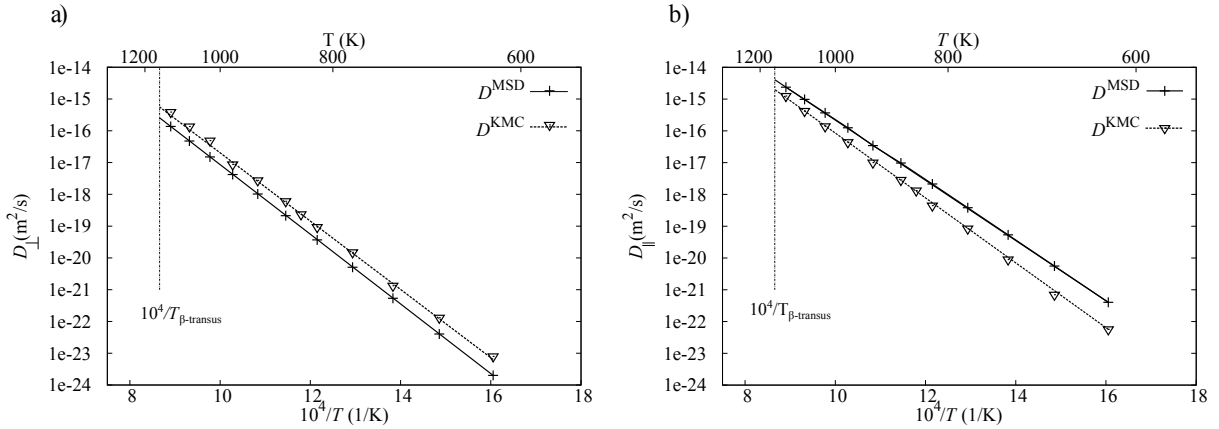
Figure 5.12: Nitrogen diffusion coefficients along a) perpendicular ($\perp$) and b) parallel ($\parallel$) directions to the basal plane evaluated by MSD (D^{MSD}) and KMC method (D^{KMC}).
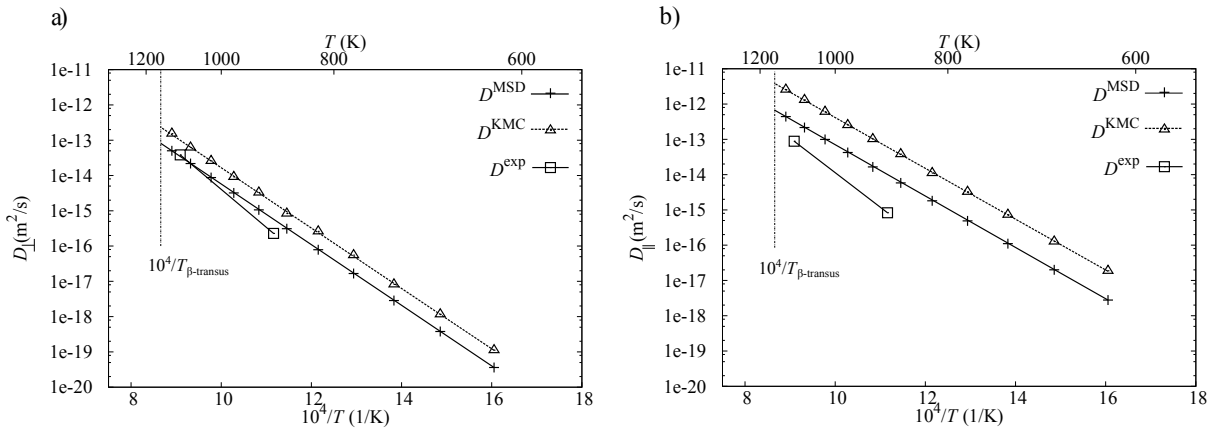
Figure 5.13: Carbon diffusion coefficients along a) perpendicular ($\perp$) and b) parallel ($\parallel$) directions to the basal plane evaluated by MSD (D^{MSD}) and KMC method (D^{KMC}) compared with experimental data (D^{Exp})[26].

Table 5.7: Activation energies of O, N and C diffusion along perpendicular ($Q_\perp$) and parallel ($Q_\parallel$) directions obtained by using MSD and KMC methods, and bulk migration evaluated by KMC (Q^{KMC}).

Solute	$Q_\perp^{\text{MSD}}$ (eV)	$Q_\parallel^{\text{MSD}}$ (eV)	$Q_\perp^{\text{KMC}}$ (eV)	$Q_\parallel^{\text{KMC}}$ (eV)	Q^{KMC} (eV)
O	1.923	1.825	1.930	1.899	1.903
N	2.175	1.880	2.179	2.038	2.049
C	1.705	1.444	1.697	1.428	1.431

Table 5.8: Pre-factor diffusion coefficients of O, N and C diffusion along perpendicular ($D_{0\perp}$) and parallel ($D_{0\parallel}$) directions obtained by using MSD and KMC methods, and bulk migration evaluated by KMC (D_0^{KMC}).

Solute	$D_{0\perp}^{\text{MSD}}$ (m²/s)	$D_{0\parallel}^{\text{MSD}}$ (m²/s)	$D_{0\perp}^{\text{KMC}}$ (m²/s)	$D_{0\parallel}^{\text{KMC}}$ (m²/s)	D_0^{KMC} (m²/s)
O	4.829x10⁻⁷	1.374x10⁻⁶	1.205x10⁻⁶	2.485x10⁻⁶	2.036x10⁻⁶
N	7.914x10⁻⁷	6.485x10⁻⁷	1.838x10⁻⁶	1.530x10⁻⁶	1.295x10⁻⁶
C	2.246x10⁻⁶	1.336x10⁻⁶	5.905x10⁻⁶	6.489x10⁻⁶	4.575x10⁻⁶

by *ab initio* calculations, to study O diffusion in Ti. They have estimated the defect energies and jump frequencies using VASP with ultrasoft-pseudopotentials [195, 196] and generalized-gradient approximation of Perdew and Wang [197] (USPP). They have used 400 eV energy cut-off, 2 x 2 x 2 k-points mesh for 96-atom supercell and CI-NEB method with constant-shape supercell [50]. The values of $Q_\perp$ and $Q_\parallel$ obtained by Wu and Trinkle are 2.086 eV and 2.085 eV, respectively [50]. Their $D_{0\perp}$ and $D_{0\parallel}$ are 3.257x10⁻⁶ m²/s and 2.912x10⁻⁶ m²/s [50]. Our results confirm the prediction of Wu and Trinkle in the case of perpendicular diffusion coefficients. In the case of parallel migration, our results overestimate the results of Wu and Trinkle. With respect to the current work, Wu and Trinkle have calculated the MEPs using constant-shape supercells, higher energy cut-off (400 eV), larger supercell size (96-atoms), and different electronic structure including the 3p orbitals in the valence. In order to investigate such discrepancy, further calculations were performed to test each of these conditions. The migration energies of O transitions were calculated using i) constant-shape supercell and the

set-up is reported in Section 5.2 (ΔH_m^{cs}), as well as using ii) 400 eV energy cut-off, 96-atoms supercells and fully-relaxed supercell with four-electron PAW ($\Delta H_m^{\text{400-96}}$) and iii) ten-electron PAW ($\Delta H_m^{\text{400-96-pv}}$). These energies are compared in Table 5.9 with the values of Wu and Trinkle [50]. The supercell size and energy cut-off values seem to have minor impact on the migration energies, since the values of $\Delta H_m^{\text{400-96}}$ are similar to the data obtained with smaller supercell reported in Table 5.4. The migration energy values evaluated with 3p PAW ($\Delta H_m^{\text{400-96-pv}}$) are closer to the data of Wu and Trinkle. However, the best match is obtained with constant-shape supercell calculations (ΔH_m^{cs}). In particular, there is a good agreement between the results of this work and the values of Wu and Trinkle in the case of CR→HE and CR→OC transitions. In addition, the energy difference between OC site and the HE and CR sites calculated with 4s PAW are 1.24 eV and 1.40 eV, respectively. This is similar to results obtained with the 3p PAW calculations, which are 1.18 eV and 1.57 eV, respectively. Since Wu and Trinkle have obtained very small values of CR→OC and CR→HE, they have assumed that CR sites thermalise at high temperature, resulting in OC→OC and HE→HE jumps, and a simplified equation for $D_\perp$ and $D_\parallel$. This mainly affects the parallel diffusion of O. We have tested the formula of Wu and Trinkle by replacing OC→CR→OC paths with OC→OC paths and HE→CR→HE paths with HE→HE paths in the KMC simulations. The obtained diffusivities are closer to those using the formula of Wu and Trinkle [50] if informed by the same jump frequency data (see Fig. 5.14). Finally, our KMC results of O bulk diffusion are compared with the experimental data obtained by Bregolin [23] in Fig. 5.15. Bregolin *et al* have studied the O bulk diffusion using ion implantation and nuclear resonance technique in high-purity Ti sample (99.99%) annealed for ten days at 1133 K so that the grain-boundary diffusion can be neglected [23]. They have extrapolated bulk diffusion parameters of Q equal to 1.752±0.5 eV and D_0 to 2±1 x10^{-7} m^2/s. The KMC values agree with the experimental data as shown in Fig. 5.15.

The bulk diffusivity values of N obtained with KMC simulations were compared with the experimental data of Bregolin *et al* [24]. Like the case of O, they have used ion implantation and nuclear resonance techniques, extrapolating Q equal to 1.897±0.02 eV and D_0 equal to 1.1±0.8x10^{-7} m^2/s [24]. Our KMC simulation results well predict the experimental data as

94

Table 5.9: Comparison of migration energies of O interstitial transitions in α-Ti computed with (i) 54-atom supercells, 350 eV cut-off energy, and constant-shape relaxation (ΔH_m^{cs}), (ii) 96-atom supercells, 400 eV cut-off energy, and fully-relaxed supercells ($\Delta H_m^{400\text{-}96}$), and (iii) 96-atom supercells, 400 eV cut-off energy, fully-relaxed supercells, and 3p PAW potentials ($\Delta H_m^{400\text{-}96\text{-pv}}$), with the results of Wu and Trinkle [50] ($\Delta H_m^{\text{Wu-USPP}}$ and $\Delta H_m^{\text{Wu-PAW}}$).

	ΔH_m^{cs} (eV)	$\Delta H_m^{400\text{-}96}$ (eV)	$\Delta H_m^{400\text{-}96\text{-pv}}$ (eV)	$\Delta H_m^{\text{Wu-USPP}}$ (eV)	$\Delta H_m^{\text{Wu-PAW}}$ (eV)
OC→OC	3.430	3.306	3.238	3.25	3.27
OC→CR	2.052	1.971	2.034	2.16	2.09
OC→HE	2.086	2.047	2.021	2.04	2.02
CR→OC	0.287	0.566	0.459	0.28	0.32
CR→HE	0.367	0.498	0.399	0.24	0.30
HE→OC	0.805	0.837	0.890	0.85	0.84
HE→CR	0.851	0.666	0.790	0.94	0.89
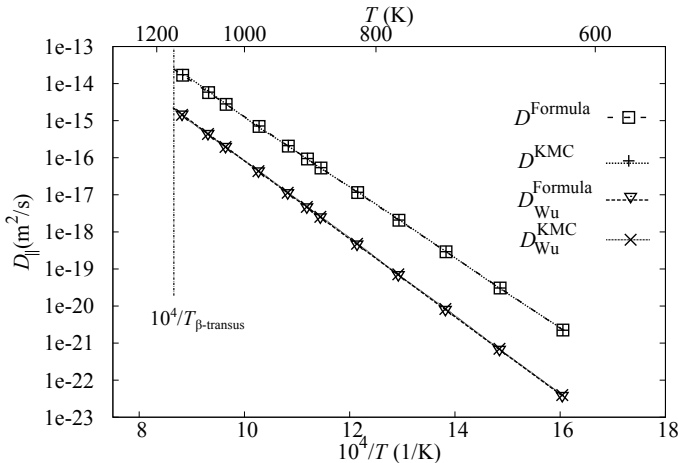
Figure 5.14: Parallel diffusivities of O evaluated by using formulation of Wu and Trinkle (D^{Formula}) and KMC simulations (D^{KMC}), neglecting the CR→OC and CR→HE jumps, both informed by the jump frequency values evaluated in this work, and with jump frequency data of Wu and Trinkle ($D_{\text{Wu}}^{\text{Formula}}$ and $D_{\text{Wu}}^{\text{KMC}}$) [50].

shown in Fig. 5.16.

The calculated perpendicular and parallel diffusivities of C are compared with the experimental survey of Minkwitz and Herzig [26] in Fig. 5.13. They have measured diffusion coefficients at 896 K and 1100 K with radiotracer serial sectioning technique with ^{14}C on high-purity single crystal samples annealed in high vacuum (p<10^{-5} Pa) at 1130 K for 6 days [26]. Our
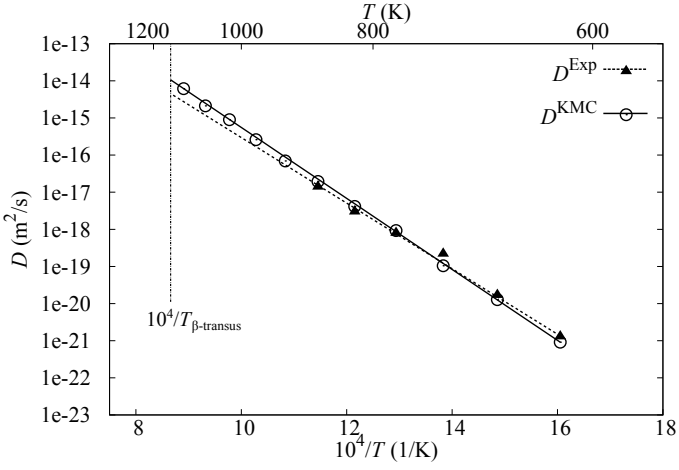
Figure 5.15: Bulk diffusion coefficients of O evaluated by KMC simulations (D^{KMC}) and compared with experimental data (D^{Exp}) [23].
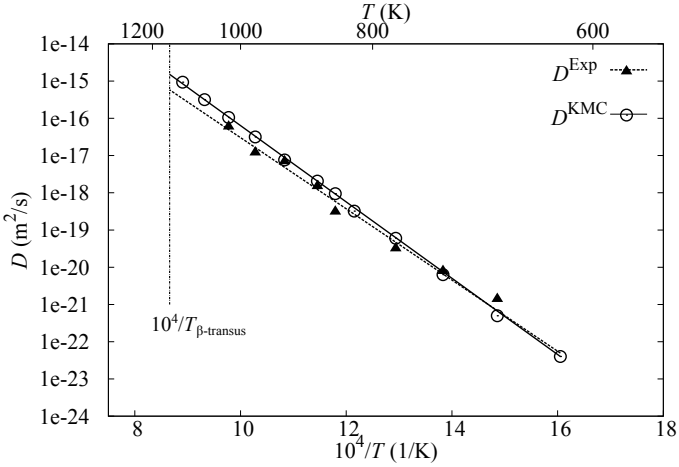
Figure 5.16: Bulk diffusion coefficients of N evaluated by KMC simulations (D^{KMC}) and compared with experimental data (D^{Exp}) [24].

results are consistent with these experimental data, especially in the case of perpendicular diffusivity. Both MSD and KMC methods overestimate the experimental diffusivities. In Fig. 5.17, the bulk diffusivity of C in α-Ti obtained with KMC simulations is compared with De Barros *et al* study [25] and the survey of Minkwitz and Herzig [26]. De Barros and co-workers have determined the diffusion coefficient by performing a diamond deposition by microwave plasma assisted chemical vapour on pure bulk titanium substrate [25]. They have extrapolated Q equal to 1.171 $\pm$0.03 eV and D_0 equivalent to 6.4$\pm$0.2x10^{-7} m^2/s [25]. Minkwitz and Herzig have measured diffusion on polycrystalline samples with different level of purity [26]. Their results shows that the C diffusion is not influenced by the presence of fast-diffusers. They have de-
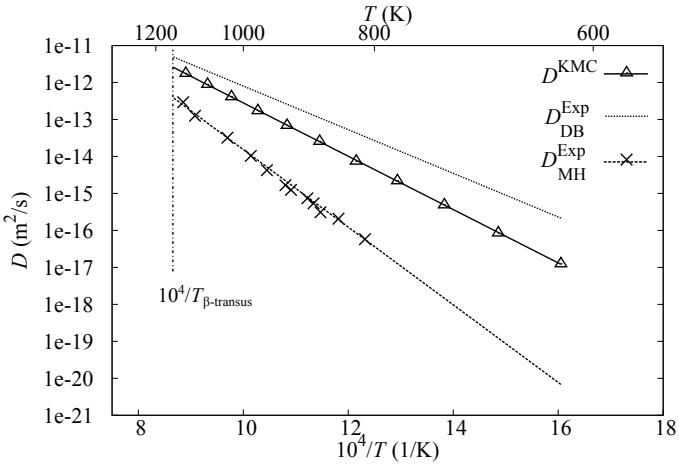
Figure 5.17: Bulk diffusivity of C evaluated by KMC simulations (D^{KMC}) and compared with experimental data of De Barros *et al* ($D_{\text{DB}}^{\text{Exp}}$) [25], and the study of Minkwitz and Herzig ($D_{\text{MH}}^{\text{Exp}}$) [26].

termined higher activation energy with respect to Barros *et al* study, equal to 2.083 eV, and pre-factor coefficient equal to 4.85×10^{-4} m^2/s [26]. Our results underestimate the data of De Barro *et al* and overestimate the values of Minkwitz and Herzig, as shown in Fig. 5.17. Since the experimental findings are so different, it is hard to comment on these results and additional investigations are required.

Oxygen and Nitrogen have similar diffusion behaviour, while C diffusivity values are 10^2-10^3 times higher (see Fig. 5.18). The diffusion barriers follow the order $Q^{\text{N}} < Q^{\text{O}} < Q^{\text{C}}$ (see Table 5.7). The diffusion of these three elements is slower along $\perp$ direction than diffusion within the basal plane. The anisotropy ratio of O evaluated by KMC is around 0.3. Nitrogen has anisotropy ratio varying from 0.108 to 0.257. Carbon has the lower anisotropy ratio equal to 0.006-0.058 (see Fig. 5.19).

5.4 Discussion and Conclusions

The diffusivities along the perpendicular and parallel directions to the basal plane of O, N, and C in α-Ti were calculated using MSD and KMC methods, both informed by *ab initio* calculations. The results show that both methods are valid tools to estimate the diffusion behaviour of interstitial solutes. Additionally, the KMC simulations allow us to extrapolate

97
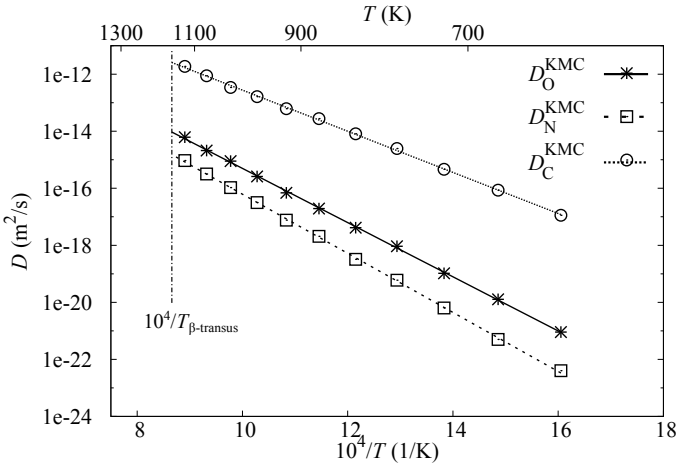
Figure 5.18: Comparison of O, N and C diffusion coefficients obtained by KMC simulations.
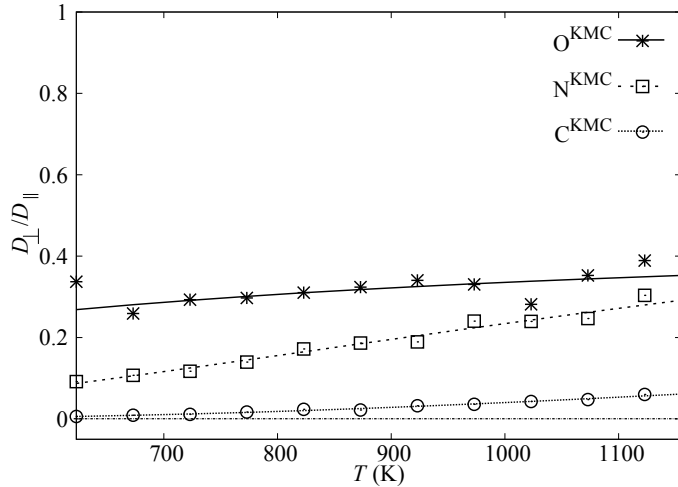
Figure 5.19: Anisotropy ratio of O, N and C in α-Ti evaluated by KMC simulations.

the bulk diffusion coefficients which can be compared with the experimental studies. In the case of O and N, KMC values of bulk diffusivity completely match the experimental data (see Fig. 5.15 and 5.16). In the case of C, the KMC results sit between the experimental data obtained by De Barro et al [25] and the data of Minkwitz and Herzig [26] (see Fig. 5.17). Since the gap between the experimental data is significant, it is hard to comment on the C diffusivities obtained in this work.

The DFT calculations of the interstitial energy confirm previous ab $initio$ studies [50, 129] that O, N and C tend to occupy octahedral sites, while the tetrahedral sites are unstable. Instead, less traditional interstitial sites are stable: crowdion, basal crowdion, hexahedral sites. Therefore, updated maps of the transition pathways are needed. The new networks obtained

can explain the anisotropy behaviour of these elements (see Fig. 5.19) and the fast migration of C with respect to O and N (see Fig. 5.18). In fact, the OC-CR-OC jumps parallel to the basal plane are energetically favourable with respect the other jumps, especially in case of C.

5.4.1 Electronic structure of O, N and C at interstitial sites in alpha-Ti

The findings of this work show that O, N and C have a preference for dissolving at octahedral sites, confirming the common belief [22]. However, the tetrahedral sites are unstable configurations, and O, N and C prefer to sit at less traditional interstitial sites such as crowdion, basal crowdion and hexahedral sites. The electronic structures of these configurations were studied analysing the DOS curves of the Ti atom sitting next to the interstitial.

The *ab initio* results show that O stably occupies octahedral, hexahedral and crowdion sites. The electronic structures of the first nearest neighbouring Ti atoms to the O atom at OC and HE sites are similar (see Fig. 5.20). The anti-bonding regions (above 0 eV) in the case of OC and HE sites are smaller compared to the CR site. The pseudo-gap is deeper in the case of O at octahedral site with respect to HE and CR sites. This indicates that the Ti-O bond at the OC site is stronger compared to O at the HE and CR sites which show more metallic nature.

Nitrogen shows similar behaviour to O; the Ti-N bond is stronger when N occupies OC and HE sites, whilst it is weaker in the case of CR and BC sites as shown by the DOS curves of the first-nearest neighbour solvent atoms next to the interstitial N in Fig. 5.21. When N sits at the OC and HE sites, the DOS curves has a smaller anti-bonding region with respect to the CR and BC cases. The pseudo-gap is deeper in the case of OC and HE sites, while it moves up when N occupies CR or BC sites.

Carbon also displays similar behaviour, the solvent-interstitial solute bond is stronger when C occupies the OC sites rather than CR and BC sites, as shown by the DOS curves of the first-nearest neighbour Ti to the interstitials in Fig. 5.22. In fact, the pseudo-gap in the cases of OC and BC is deeper than CR site. In the case of C at the octahedral site, the area occupied in anti-region is narrower with respect to CR and BC cases. The difference in the DOS curves
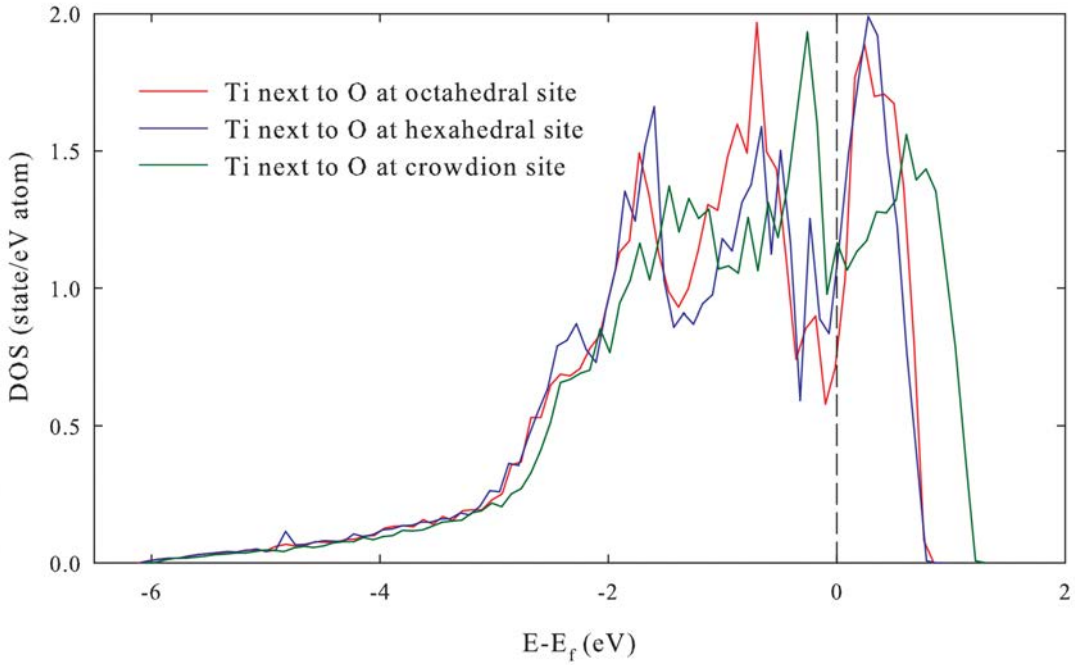
Figure 5.20: The DOS curve of the first-nearest neighbour Ti atom to O at the different stable sites, OC, HE, and CR.

for C positioned at the OC and CR sites is not as great as the difference calculated when considering O or N at these locations. This indicates that the bonds formed by C with Ti at OC and CR sites are similar, which contrasts to the behaviour exhibited by O and N.

Interstitial O and N form similar bonds with Ti atoms. The solute-solvent bond is strong when these two elements are sitting at octahedral sites, while it is weaker and easier to break at crowdion sites. As a result, the values of O and N diffusion barriers are very similar (see Table 5.7). On the other hand, the Ti-C bond at OC site is similar to the CR case, which may lead to a smaller activation energy for the OC↔CR jumps, resulting in a faster migration. The electronic structure of solvent-solute bond can also explain the loss of ductility due to O, N and C atoms in α-Ti. Kwasniak et al [30] have reported that the plasticity loss in Ti increases with the O concentration as a result of the more covalent nature of Ti-O bond. Similar investigations can be applied to N and C highlighting trends and giving more information about the α-case phenomena. These kinds of studies can also explain why C addition has a more restrained effect on the plasticity with respect to O and N additions [65].
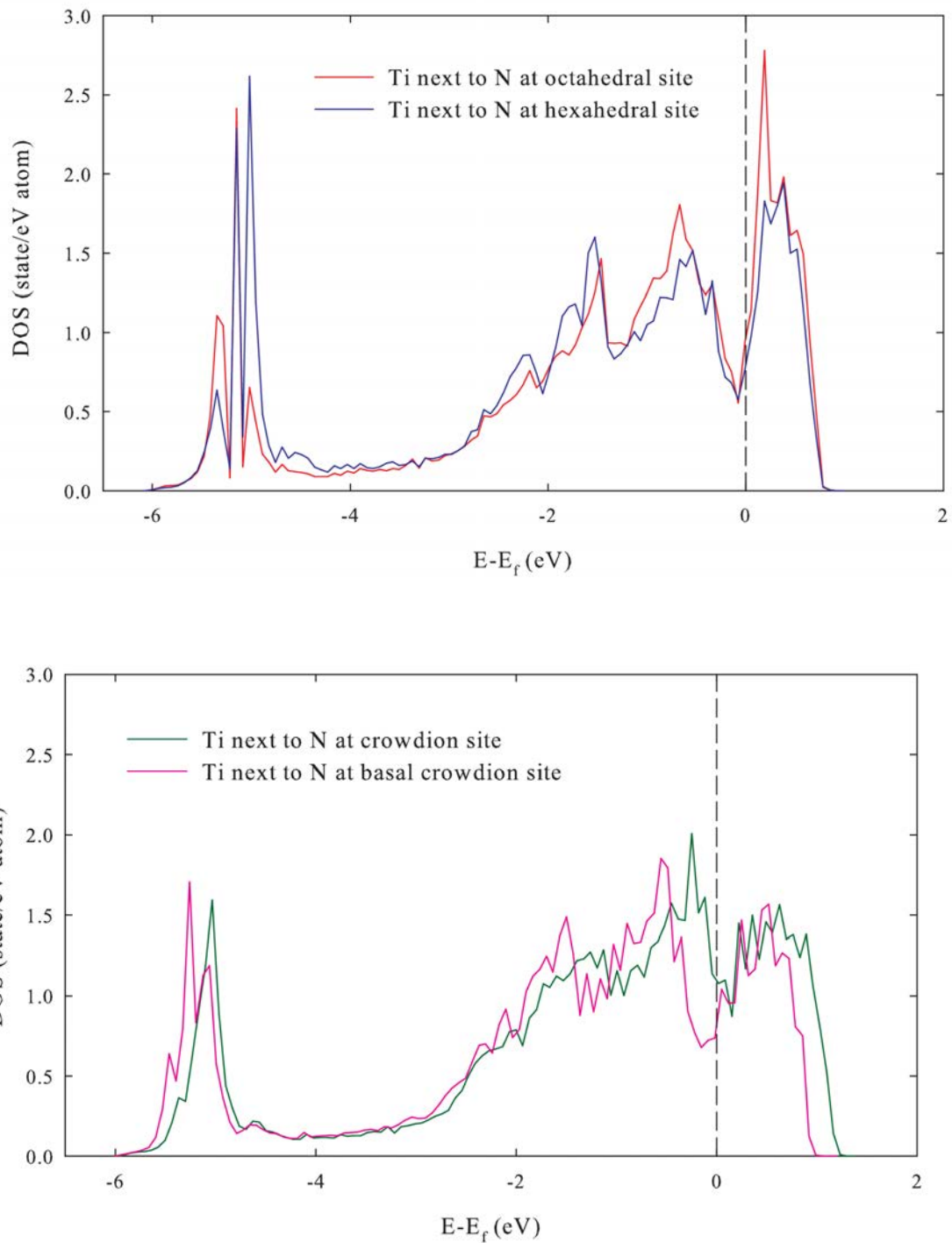
Figure 5.21: The DOS curve of the first-nearest neighbour Ti atom to N at the different stable sites, a) OC, HE, b) CR, and BC.

5.4.2 Transition pathways network and anisotropy behaviour

The diffusivity calculations of this work along the perpendicular and parallel directions to the basal plane confirm the trend of $D_\perp / D_\parallel < 1$ for O and C reported by Vykhodets *et al* [193] and
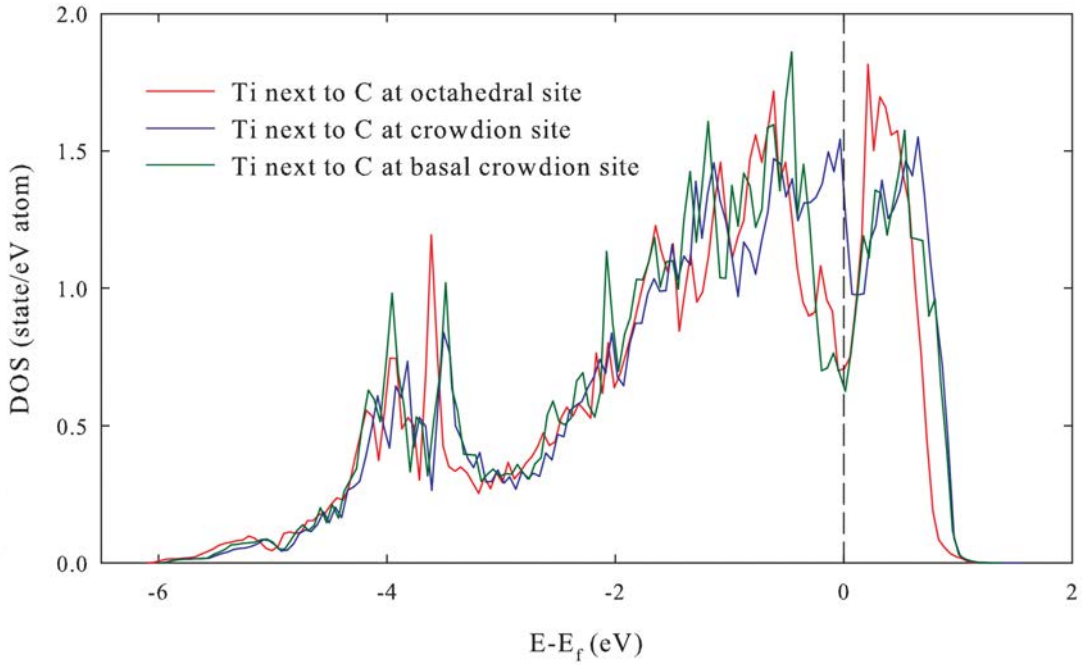
Figure 5.22: The DOS curve of the first-nearest neighbour Ti atom to C at the different stable sites, OC, CR, and BC.

Minkwitz and Herzig [26], respectively. The calculations suggest similar anisotropic behaviour in the migration of N, however experimental data has not yet been found to verify this finding. Vykhodets and co-workers [193] have evaluated the anisotropy of O in α-Ti to be equal to 0.87 ± 0.01 at 581.9 °C, using nuclear reaction method with $^{18}O(p,\alpha)^{15}N$ and $^{16}O(d,p_I)^{17}O$ on single crystal. The anisotropy of C in α-Ti has been experimentally evaluated equal to 0.28 at 896 K and 0.43 at 1100 K [26]. These findings contradict the values estimated by the model of Bertin and co-workers [194]. Bertin *et al* [194] have assumed that O dissolves at octahedral and tetrahedral sites, and that it performs OC↔OC transitions along c-axis, OC→TE→OC transitions along the basal plane and OC→TE→TE→OC transitions. Based on these jumps, the estimated $D_\perp/D_\parallel$ ratio of O is between 1.53 and 1.32 at 700-1000 K temperature range [194]. As a consequence of these assumptions, the values of $D_\perp/D_\parallel$ evaluated for C would vary from 1.30 to 1.24 at 896-1100 K temperature range [26]. This confirms the fact that the transitions between octahedral and tetrahedral sites cannot describe the migration of O, C and N in α-Ti. Our findings show that diffusion of these solutes happens through different interstitial sites.

In particular, the crowdion stability plays a key role on the anisotropy diffusion behaviour of these three elements, allowing the OC→CR→OC transition along the three directions $[2\bar{1}\bar{1}0]$, $[\bar{1}2\bar{1}0]$ and $[\bar{1}\bar{1}20]$. This jump requires smaller activation energy with respect to the OC→OC transition along c-axis direction. At the same time, the number of transition pathways along c-axis is reduced by the instability of tetrahedral site. These facts lead to high anisotropy behaviour as shown in Fig. 5.19, especially in the case of C.

Chapter 6

Fast-diffusers migration in alpha-Ti

6.1 Introduction

It has been reported that the presence of Fe, Co and Ni significantly decreases the creep properties of Ti alloys [5, 33–37]. Russo and co-workers [36] have found that even small additions have a drastic detrimental effect on the high-temperature behaviour of these alloys. Two theories have been developed to describe this phenomenon. The first was formulated by Thiehsen and co-workers [5] and it is based on Fe and Ni tendency to segregate at the β phase, accelerating the self-diffusion in this phase and/or at the grain boundaries with a decrease of the high-temperature properties. In the second theory, the detrimental effect is due to self-diffusion enhancement in the presence of these solutes in α-Ti, accelerating the dislocation motion and decreasing the mechanical properties [7, 34]. This enhancement has been quantified by the research group of Herzig [9, 198] as shown in Fig. 6.1. These elements are also characterised by high diffusivity values as reported in the works of Nakajima and Koiwa [38–40]. The diffusion coefficients of Fe, Co and Ni are 10^5 times higher than self-diffusion values, therefore they are usually called fast-diffusers. The migration of fast-diffusers is also characterised by inverse anisotropy trend, $D_\perp/D_\| > 1$, with respect to the solvent diffusion [38–40]. Their diffusion parameters, Q an D_0, are reported in Table 6.2. The diffusion behaviour of Fe, Co and Ni is very interesting and it has attracted the attention of many [38–40, 42, 43, 46, 94]. The investigation
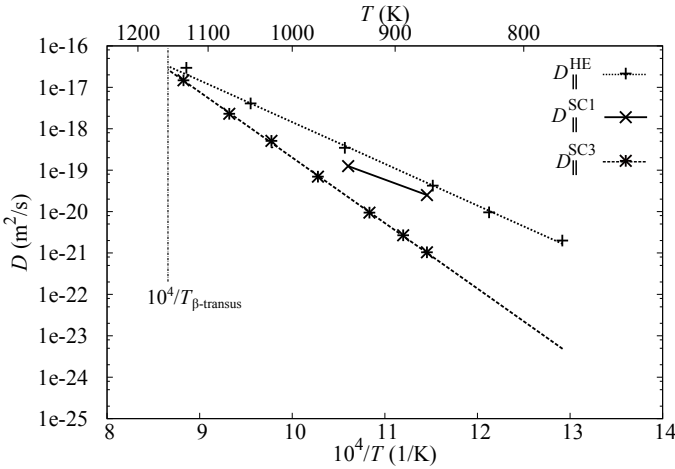
Figure 6.1: Influence of fast-diffusers on the self-diffusivities in α-Ti: self-diffusivity values evaluated by i) Herzig and co-workers [198] (D^{HE}) on nominally pure single crystal, ii) Koppers et al [9] on nominally pure single crystal (D^{SC1}) and ultra-pure crystal (D^{SC3}) along the parallel direction to the basal plane. The Fe, Ni and Co concentrations are reported in Table 6.1.

Table 6.1: Fast-diffusers concentrations in the samples used by Herzig et al [198] (HE), and by Koppers et al [9] (SC1, SC3) to study the self-diffusion in α-Ti.

	Fe (wt ppm)	Co (wt ppm)	Ni (wt ppm)
HE [198]	40	-	40
SC1 [9]	50	10	<0.44
SC3 [9]	0.02	0.007	<0.015

Table 6.2: Experimental diffusion parameters of Fe, Co, and Ni in α-Ti evaluated using radiotracer technique. Q and D_0 are referred to the activation energy and pre-exponential factor of diffusion along the c-axis ($\perp$) and within the basal plane ($\parallel$), while $D_\perp/D_\parallel$ is the diffusion anisotropy ratio at 1073 K.

Solute	$Q_\perp$ (eV)	$D_{0\perp}$ (m²/s)	$Q_\parallel$ (eV)	$D_{0\parallel}$ (m²/s)	$D_\perp/D_\parallel$ at 1073 K
Fe [40]	1.164±0.03	$4.7^{+1.7}_{-1.2} \times 10^{-7}$	1.495±0.01	$6.4^{+1.0}_{-0.9} \times 10^{-6}$	2.6
Co [39]	1.183±0.01	$1.9 \pm 0.2 \times 10^{-6}$	1.307±0.01	$3.2^{+0.5}_{-0.4} \times 10^{-6}$	3.6
Ni [38]	1.422±0.02	$5.6^{+1.1}_{-0.9} \times 10^{-6}$	1.470±0.02	$5.4^{+1.1}_{-0.9} \times 10^{-6}$	1.7

of the migration processes involved can give important information on fast-diffusers effect on

the creep phenomena in α-Ti.

Many authors have argued that the diffusion behaviour of these atoms cannot be justified

by a simple substitutional vacancy-mediated diffusion (D_s) or interstitial migration (D_i) [42, 43]. The fast diffusion has been associated with dissociative solubility, namely the ability to accommodate at both interstitial and substitutional sites [42]. In the case of Fe α-Ti, the hight-temperature Mössbauer spectra obtained by Yoshida and co-workers [44] confirm the presence of substitutional and interstitial Fe atoms at equilibrium. This suggests the possibility for these solutes to migrate through interstitial-substitutional exchange mechanisms [42] (see Fig. 6.2). If the process involves interstitial solutes and vacancy defects, it is usually called dissociative diffusion mechanism [42]. Some examples of this diffusion mechanism are Cu diffusion in Ge [42], as well as noble metals (Au [199], Hg [105], Ag [200]) and Zn [201] diffusion in lead. If the interstitial solute takes the place of the host atom at the lattice site creating a self-interstitial, the mechanism is called kick-out [202]. This is the case of Au and Pt diffusion in Si [203]. The anomalous diffusion of Fe, Co and Ni in α-Ti, and other open metals such as α-Zr and α-Hf, has been associated with the dissociative diffusion mechanism [42] (see Section 6.2). Five processes are involved in the dissociative diffusion mechanism [45],

- Interstitial solute diffusion;

- Substitutional solute diffusion;

- Vacancy diffusion from surface;

- Mechanisms of annihilation and creation of vacancy in the bulk;

- Combination-dissociation reaction of interstitial solute-vacancy pair [46].

The complexity of the problem can be reduced by analysing each of these processes and their impact on the overall diffusion. For example, in the case of metals the production and annihilation of vacancy by dislocations is such that the vacancy concentration can be considered constant and equal to the equilibrium value [42, 45]. Frank and Turnbull have suggested that in the case of fast-diffusers in Ti, the impact on the overall migration of the combination-dissociation reaction is small [42]. The majority of solute atoms sit stationary at lattice sites, and the anomalous migration mainly depends on the relative few interstitial solutes which move
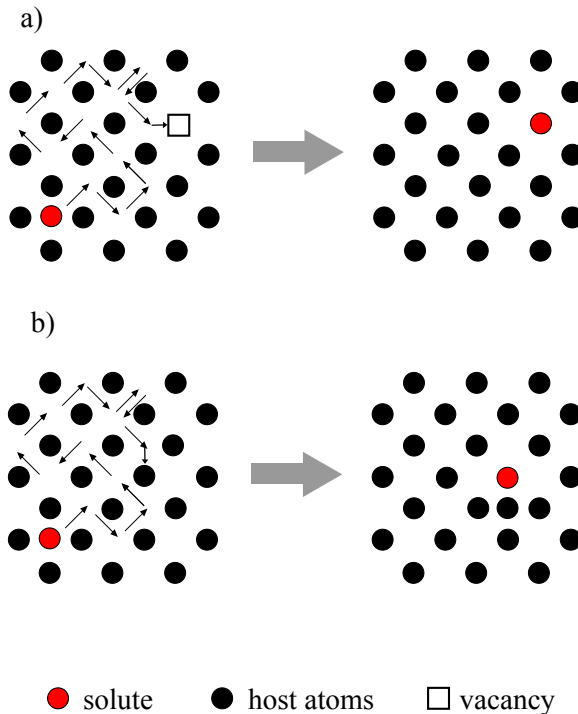
Figure 6.2: Schematic representation of interstitial-substitutional exchange mechanisms [42]: a) dissociative diffusion mechanism, b) kick-out mechanism.

through interstitial sites [42]. The Frank-Turnbull model can well describe the fast migration of Fe, Co and Ni solutes in Ti. However, it is not sufficient to explain the enhancement of self-diffusion. Pasianot and co-workers [47] have suggested another mechanism to explain the acceleration of solvent migration: the solute-host swap without the presence of vacancy (see Fig. 6.3).

This chapter aims to understand and explain the diffusion mechanism of fast-diffusers, Fe, Co, and Ni in α-Ti using DFT calculations and KMC simulations (see Section 6.3). A first-principles approach was used to understand the substitutional and interstitial behaviour of these solutes and map the possible solute jumps. The KMC simulations informed by *ab initio* data were used to verify that simple mechanisms, such as interstitial and substitutional vacancy-mediated diffusion, cannot explain the fast migration of these solutes in Ti. The validity of dissociative diffusion mechanism proposed by Frank and Turnbull for fast-diffusers [42] was investigated. In particular, the impact of combination-dissociation reaction of interstitial solute-vacancy pair [46] was simulated by KMC method. The effect of solute-host swap [47, 94] on the self-diffusion was tested as well.
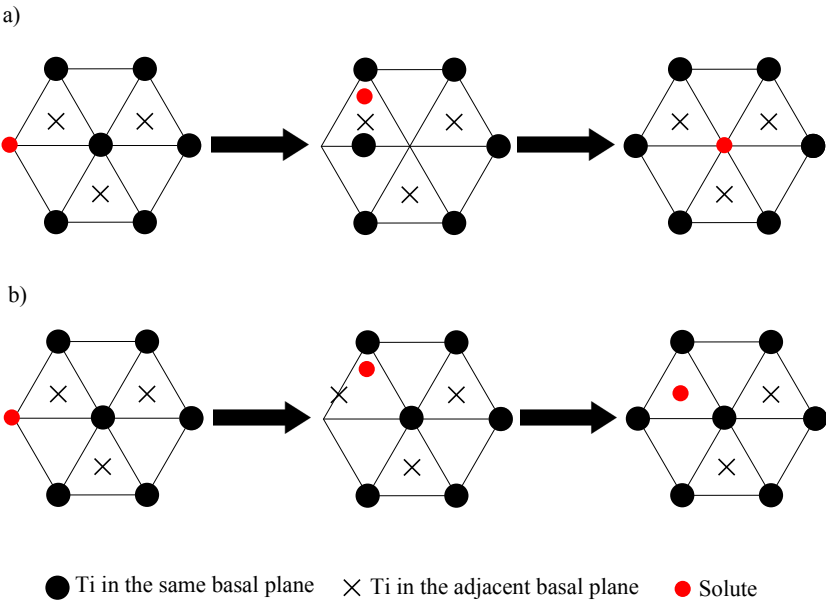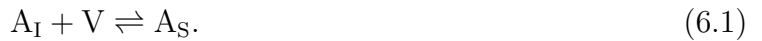
Figure 6.3: Scheme of a) in-plane and b) out-of-plane solute-host swaps without the presence of vacancy.

The results show that Co and Fe prefer to occupy off-lattice configurations instead of lattice sites (see Section 6.4.1). On the other hand, Ni does not have any off-lattice configurations, but it sits at lattice sites. The analysis of interstitial defects shows that any of the eight interstitial sites are stable but distorted configurations are preferred (see Section 6.4.2). The KMC results confirm that simple vacancy-mediated and interstitial mechanism cannot describe the migration of these atoms in α-Ti (see Section 6.4.4). The combination-dissociative process [46] has no effect on the migration of Fe, Co and Ni, confirming the formula proposed by Frank and Turnbull [42]. Finally, the effect of solute-host swap mechanism [47, 94] on the self-diffusivity in Ti was proved qualitatively.

6.2 Theory

The fast migration of Fe, Co and Ni in α-Ti cannot be explained by simple interstitial or vacancy-mediated mechanism [42, 43]. The diffusivity would be too high in the first case and too low in the second one. These solutes have small metallic radii (R_{Fe}=1.26 Å, R_{Co}=1.25 Å,

R_{Ni}=1.24 Å [204]) relative to Ti (1.47 Å). This allows them to dissolve both substitutionally and interstitially, and to migrate via the dissociative diffusion mechanism [42]. In the general case, the interstitial solutes can move through the crystal by interstitial jumps until eventually they encounter and combine with a vacancy, as shown in Fig. 6.2. As substitutional solute, they can move via a vacancy-mediated mechanism or jump to the interstitial site creating a vacancy and moving away via interstitial transitions. This process is called combination-dissociation and it can be described by,

$$A_{\mathrm{I}} + V \rightleftharpoons A_{\mathrm{S}}. \tag{6.1}$$

where V identifies the vacancy, A_{I} and A_{S} are the interstitial and substitutional solute, respectively. This mechanism can in theory explain the anomalous diffusion of fast-diffusers, since the interstitial migration is slowed down by vacancy annihilation. The opposite mechanism (dissociative) can affect the solvent diffusion altering the vacancy concentration. However, Frank and Turnbull have indicated that the reaction rate of combination-dissociation process is very small and such mechanism has no influence on the migration of fast-diffusers in Ti [42]. The anomalous fast diffusion of Fe, Co and Ni solutes is a result of few atoms moving interstitially, while the majority are steady at lattice sites [42]. Nevertheless, the Frank-Turnbull model cannot explain the acceleration of self-diffusion in Ti due to the presence of fast-diffusers. Pasianot *et al* [47] have suggested that the enhancement is due to substitutional solute-host swap without the presence of a vacancy This process would not affect the migration rate of fast-diffusers since it is reasonable to assume that it requires similar activation energy to the vacancy-mediated mechanism, but it can speed up the solvent migration.

6.2.1 Combination-dissociation process

The combination-dissociation process was described by Miller in 1969 [46] for the simple case of fcc crystal (see Fig. 6.4). This mechanism is based on the formation of interstitial solute-vacancy pair defects. This can happen as a result of the interstitial encountering a vacancy or substitutional solute moving to interstitial site (v_1). After the formation of this defect, the
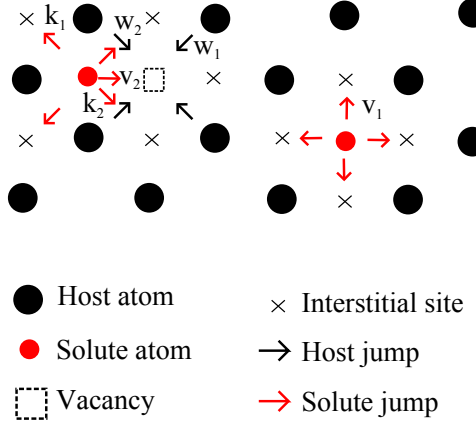
Figure 6.4: Schematic representation of solute (red arrows) and host (black arrows) jumps in the case of interstitial-vacancy pair in fcc crystal [46]: v_1 is the solute-vacancy dissociation jump, v_2 is the interstitial-vacancy combination jump, k_1 is the interstitial jump with dissociation of the pair, k_2 is the interstitial jump with reorientation of the pair, w_1 is the host-vacancy exchange with dissociation of the pair, and w_2 is the host-vacancy exchange with reorientation of the pair.

solute and vacancy can combine (v_2), or the interstitial can move away from the vacancy (k_1) or maintain the couple reorienting the pair (k_2). The host-vacancy exchanges are also allowed with (w_1) or without dissociation of the pair (w_2).

The activation energy of interstitial-vacancy combination can be presumed to be much smaller than the energy required for the dissociative jump. Therefore, the vacancy defect can be seen as a trap for the interstitial solute slowing down its migration. At the same time, the creation of a vacancy as a result of a dissociative jump can influence the solvent migration, increasing the number of vacancies.

6.2.2 Frank-Turnbull theory

The diffusion mechanism of fast-diffusers involved three species: vacancies, interstitials and substitutional solutes as highlighted by the reaction 6.1. At each temperature, their concentrations must satisfy the mass law,

$$\frac{C_I C_V}{C_S} = \frac{C_I^{eq} C_V^{eq}}{C_S^{eq}} \tag{6.2}$$

where C_V, C_I and C_S are respectively the concentration of vacancies, interstitial and substitutional solutes, and eq indicates the thermal equilibrium values. In the case of metals, the

vacancy concentration does not change from the equilibrium value as a result of vacancy anni-hilation and creation mechanisms in the bulk, and the mass law can be rewritten as,

$$\frac{C_{\mathrm{I}}}{C_{\mathrm{S}}} = \frac{C_{\mathrm{I}}^{eq}}{C_{\mathrm{S}}^{eq}} \tag{6.3}$$

The solute diffusion along a direction x can be described as,

$$\frac{\delta(C_{\mathrm{S}} + C_{\mathrm{I}})}{\delta t} = D_{\mathrm{i}}\frac{\delta^2 C_{\mathrm{I}}}{\delta x^2} + D_{\mathrm{s}}\frac{\delta^2 C_{\mathrm{S}}}{\delta x^2} \tag{6.4}$$

where D_{i} and D_{s} are the interstitial and substitutional diffusivities. Frank and Turnbull have also supposed that the reaction rate of combination-dissociation is very small and it can be neglected [42]. Based on this, Frank and Turnbull have extrapolated the effective diffusivity from equations 6.4 and 6.3,

$$D^{eff} = \frac{D_{\mathrm{s}}C_{\mathrm{S}}^{eq}}{C_{\mathrm{I}}^{eq} + C_{\mathrm{S}}^{eq}} + \frac{D_{\mathrm{i}}C_{\mathrm{I}}^{eq}}{C_{\mathrm{I}}^{eq} + C_{\mathrm{S}}^{eq}}, \tag{6.5}$$

In the particular case of Fe, Co and Ni in α-Ti, the values of D_{i} are much higher than D_{s}, and at the same time $C_{\mathrm{S}}^{eq} > C_{\mathrm{I}}^{eq}$. Therefore, the equation 6.5 can be rewritten as,

$$D^{eff} \approx D_{\mathrm{i}}\frac{C_{\mathrm{I}}^{eq}}{C_{\mathrm{S}}^{eq}}, \tag{6.6}$$

with

$$\frac{C_{\mathrm{I}}^{eq}}{C_{\mathrm{S}}^{eq}} = \exp\left(-\frac{G_{IS}}{k_b\,T}\right), \tag{6.7}$$

where G_{IS} is the Gibbs free energy difference of interstitial and substitutional configurations, T is the absolute temperature and k_b is the Boltzmann's constant.

Equation 6.6 indicates that two phenomena are involved in the migration of fast-diffusers. These solutes can rapidly move via the interstitial mechanism, but at the same time it is more likely that they sit stationary at lattice sites. The overall mass transportation is a result of these two processes. In other words, the effective diffusivity is obtained by correcting the interstitial
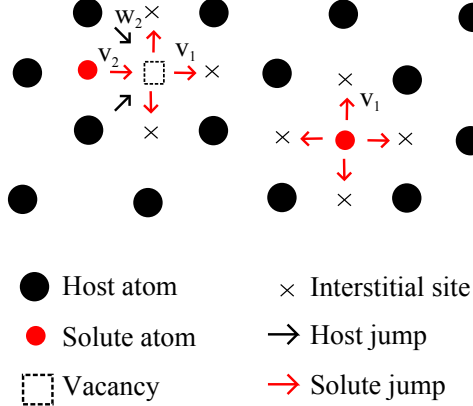
Figure 6.5: Schematic representation of solute (red arrows) and host (black arrows) jumps in the modified interstitial-vacancy pair model [94] in fcc crystal: v_1 is the solute-vacancy dissociation jump, v_2 is the interstitial-vacancy combination jump, w_2 is the host-vacancy exchange with reorientation of the pair.

diffusion coefficient by the $C_{\mathrm{I}}^{eq}/C_{\mathrm{S}}^{eq}$ factor.

6.2.3 Solute-host swap

The solute-host swap [47] is based on the model proposed by Warburton [94] which is a modification of the interstitial-vacancy pair diffusion model [46]. In his model, Warburton has assumed that after the formation of an interstitial-vacancy pair, the solute cannot be dissociated by the vacancy or reoriented by interstitial jumps. The orientation can only happen through host-vacancy jumps or a sequence of combination-dissociation solute jumps (see Fig. 6.5). Therefore, returning to the Miller's model, only v_1, v_2 and w_2 jumps are permitted. This allows for the solute to exchange position with the host atom without requiring the aid of a vacancy, but by forming an interstitial-vacancy couple. The relatively small radius allows Fe, Co and Ni to occupy the nearest interstitial site from substitutional positions (v_1 jump), leaving a vacant lattice site that the solvent atom can occupy (w_2 jump), and finally the solute can recombine with the vacancy (v_2 jump). Two examples of possible solute-host swap in hcp crystal are illustrated in Fig. 6.3.

6.3   Methodology

The defect energies were evaluated using VASP 5.3.2 [58–61], applying PAW [142] to describe electronic structure, GGA-PBE [143] for the exchange-correlation functional. The calculations were performed with 54-atom supercell, Monkhorst-Pack mesh of 32 x 32 x 17 k-points for a 2-atom cells and an energy cut-off of 350 eV, as described in Section 3.2.1. The migration energies and minimum energy path were evaluated using CI-NEB [62–64] using the same set-up (supercell size, k-points mesh, and energy cut-off) of defect energy calculations.

6.3.1   Defect energies

The binding energy of substitutional solute-vacancy pairs (ΔE_b^s) was studied by using equation 4.3 in Section 4.2.1. Following the definitions of binding energies given in Section 4.2.1, the formation energy of the vacancy next to the substitutional solute (ΔH_v^s) is the sum of E_v and ΔE_b^s. In order to verify possible off-lattice configurations, a supercell containing one interstitial solute and one vacancy at the first-nearest neighbour lattice site was relaxed. Such solute-vacancy pairs are unstable, and the interstitial is expected to displace to the lattice site. However, for the fast-diffusers, this is not always the case. If the solute atom occupies off-lattice positions, the binding energies were evaluated using the following configuration,

- supercell containing the solute at the off-lattice site $(E^{\text{Off}}\{M_{N-1} + X_1\})$;

- supercell containing the solute at the off-lattice site and the vacancy at nearest neighbour lattice site in the adjacent basal plane $(E^{\text{Off}}\{M_{N-2} + X_1\}_\perp)$;

- supercell containing the solute at the off-lattice site and the vacancy at nearest neighbour lattice site in the same basal plane $(E^{\text{Off}}\{M_{N-2} + X_1\}_\parallel)$.

The interstitial behaviour of Fe, Co, and Ni in α-Ti was investigated with the same approach presented in Section 5.2.1 using equation 5.1. Additionally, the binding energy of the second nearest-neighbour interstitial-vacancy pair (ΔE_b^i) was evaluated as

$$\Delta E_b^i = E\{M_{N-1} + I\} - E\{M_N + I\} - E\{M_{N-1}\} + E\{M_N\} \qquad (6.8)$$

where $E\{M_{N-1} + I\}$ is the energy of system with interstitial-vacancy pair, $E\{M_{N-1} + I\}$ is the energy of a system with solute at the same interstitial site and no vacancy, $E\{M_{N-1}\}$ is the energy of system with one vacancy and $E\{M_N\}$ is the energy of the perfect site. The formation energy of the vacancy next to the interstitial solute (ΔH_v^i) is the sum of E_v and ΔE_b^s.

6.3.2 KMC simulations

KMC simulations were used to verify which diffusion mechanism is involved in the migration of fast-diffusers in α-Ti.

The solute vacancy-mediated mechanism was tested using the same procedure explained in Section 4.2.3. The KMC simulations were informed by the solute jumps $w_{\parallel}$, $w'_{\perp}$, host-vacancy exchange jumps, w_a, w'_a, w_b, w'_b, w_c, w'_c, w_d, w'_d, in the case of substitutional solute-vacancy pair (bounded situation), and the host-vacancy exchanges within and in the adjacent plane when the substitutional solute and vacancy are apart (unbounded situation). These jumps were evaluated using CI-NEB with one image between initial and final states. Diffusivity values converged after 100 simulations of 10^6 solute jumps each. Additionally, the self-diffusivity values were extrapolated, tracking the host migrations. The interstitial jumps obtained with CI-NEB with five images were used to informed interstitial KMC simulations following the procedure in Section 5.2.3. In order to guarantee a good approximation, 500 simulations were performed which contained 10^9 solute jumps each. These results were then used to verify the Frank and Turnbull theory [42] using the equations 6.6 and 6.7. The G_{IS} value was approximated with the interstitial formation energy,

$$\frac{C_I^{eq}}{C_S^{eq}} = \exp\left(-\frac{E_i}{k_b\,T}\right). \tag{6.9}$$

The E_i values were evaluated with the equation 5.1 in Section 5.2.1.

The kinetic Monte Carlo simulations were used to verify the effect of the combination-dissociation process upon fast-diffusers migration [46]. This is not a simple task since three species (vacancy, substitutional and interstitial solute) are involved in this process and the

migration is not random. It is reasonable to believe that the correlation factor mostly depends upon the solute-vacancy dissociation reaction. After the dissociation jump, the presence of a vacancy endeavours to restore the initial configuration. On the other hand, the interstitial jumps and vacancy annihilation process can be considered an uncorrelated mechanism, since in both cases, each interstitial site has the same probability of being occupied. Since our investigation focuses on establishing the impact of combination-dissociation process on the overall migration, the vacancy and substitutional solute migration were omitted, and the mass transportation was considered only affected by random interstitial transitions with the addition of combination and dissociation jumps. The first hypothesis is not far from the real behaviour since both diffusions are much slower than interstitial migration. If the combination-dissociation process is found to be important, the mechanism may be modelled in more detail including the correlation factor. Therefore, the diffusion study was conducted including the interstitial transitions leading to the formation or separation of interstitial-vacancy pairs, the combination and dissociation solute jumps in the KMC code simulating the interstitial diffusion. Since this mechanism depends upon the presence of vacancies, all these jumps were multiplied by the probability of the interstitial to encounter a vacancy,

$$P = \exp\left(-\frac{(\Delta H_v^i)}{k_b\ T}\right),\tag{6.10}$$

Where ΔH_v^i is the formation energy of vacancy-interstitial pair. The diffusivities were calculated performing 500 simulations of 10^9 solute jumps. The effect of the solute-host swap mechanism [47] on the self-diffusivities was tested by including in-plane and out-of-plane solute-host swaps in the KMC code when simulating vacancy-mediated diffusion. This is illustrated in Fig. 6.3. One hundred simulations of 10^6 solute jumps each were performed and the self-diffusivities were obtained as an average of all host atom migrations.

Table 6.3: Calculated energies of supercells containing Fe, Co and Ni solute at lattice ($E\{M_{N-1} + X_1\}$) and off-lattice site ($E^{\text{Off}}\{M_{N-1} + X_1\}$).

Solute	$E\{M_{N-1} + X_1\}$ (eV)	$E^{\text{Off}}\{M_{N-1} + X_1\}$ (eV)
Fe	-418.999	-419.313
Co	-418.164	-418.346
Ni	-417.007	-

6.4 Results

6.4.1 Substitutional sites

The energies of crystals containing one solute atom at a lattice site ($E\{M_{N-1} + X_1\}$) and the off-lattice configuration ($E^{\text{Off}}\{M_{N-1} + X_1\}$) are reported in Table 6.3. Fe and Co have off-lattice configurations that are more stable than simple substitutional sites, while Ni sits at lattice sites. Referring to the site (0,0,0) and the primitive lattice defined as [$a_1 = (a; 0; 0)$; $a_2 = (a/2; \sqrt{3}a/2; 0)$; $a_3 = (0; 0; c)$], the off-site position of Fe is $(0.28, -0.14, 0)$ and for Co is $(0.26, -0.13, 0)$. This may be due to the fact the Ni has a smaller atomic radius than Fe and Co, introducing fewer distortions into the lattice. As a result of their small radii, at the lattice sites, these atoms cause a contraction of the Ti lattice, which is smaller than the constriction due to a vacancy. In the case of Ni, the volume difference relative to a vacancy is $|0.05|\%$, while it is $|0.12|\%$ for Fe and $|0.14|\%$ for Co. The relative volume differences of Fe and Co are smaller when they occupy the off-lattice configurations, respectively $|0.06|\%$ and $|0.03|\%$.

The binding energies of out-of-plane and in-plane configurations were evaluated using equation 4.3 and are presented in Fig. 6.6. The data shows the attraction between the vacancy and the substitutional Fe, Co and Ni. CI-NEB method was used to evaluate the migration energy of $\perp$ and $\parallel$ solute jumps of Fe, Co and Ni in α-Ti (see Fig. 6.7). ΔE_b^s, ΔH_v and ΔH_m energies of substitutional solute-vacancy pairs are summarised in Table 6.4.
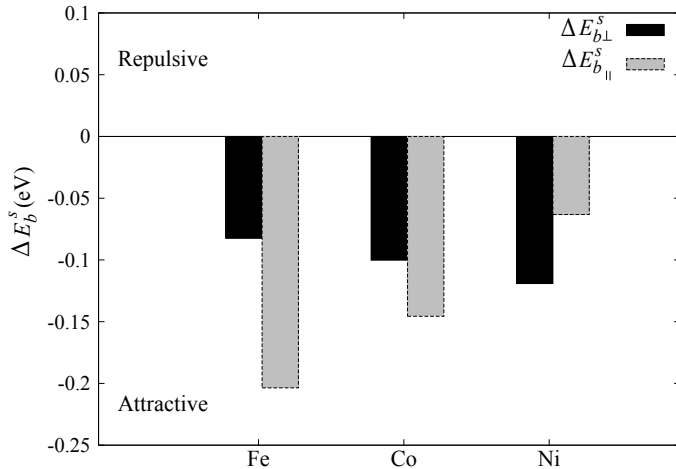
Figure 6.6: Calculated binding energy of out-of-plane (black bar) and in-plane (grey bar) substitutional solute-vacancy pairs (ΔE_b^s) of Fe, Co, and Ni in α-Ti. Positive values of ΔE_b^s indicate that the substitutional solute atom is repulsed by the vacancy, while negative values indicate attraction between vacancy and solute.
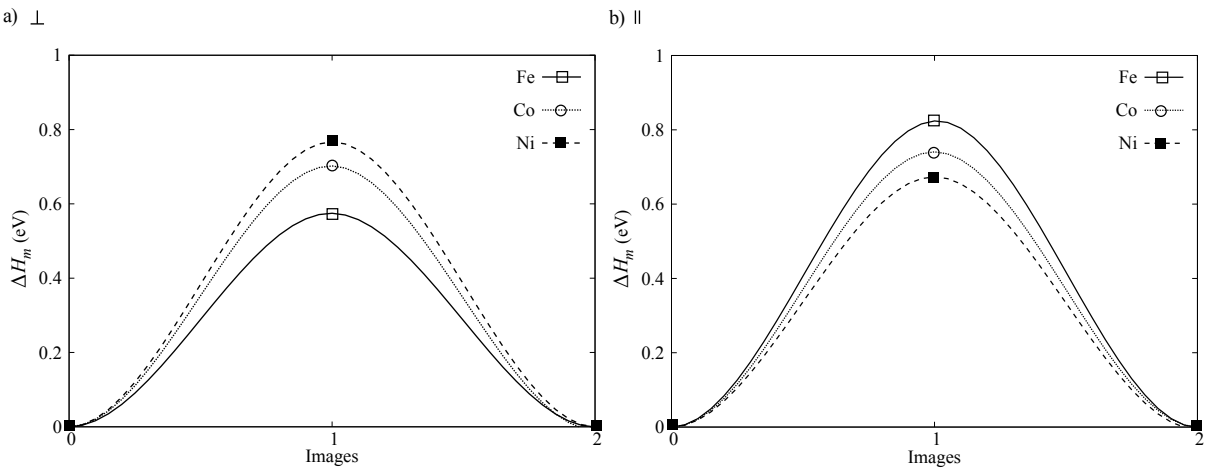
Figure 6.7: MEPs of a) out-of-plane and b) in-plane jumps of substitutional Fe, Co, and Ni in α-Ti, calculated with CI-NEB with one image.

Table 6.4: First-principles evaluation of the binding energies (ΔE_b^s), formation energies of substitutional solute-vacancy pair (ΔH_v^s), and migration energies (ΔH_m) of fast-diffusers, Fe, Co and Ni, of out-of-plane ($\perp$) and in-plane ($\parallel$) configurations in α-Ti.

Solute	$\Delta E_{b\perp}^s$ (eV)	$\Delta H_{v\perp}^s$ (eV)	$\Delta H_{m\perp}$ (eV)	$\Delta E_{b\parallel}^s$ (eV)	$\Delta H_{v\parallel}^s$ (eV)	$\Delta H_{m\parallel}$ (eV)
Fe	-0.083	1.894	0.575	-0.204	1.773	0.824
Co	-0.100	1.876	0.702	-0.146	1.831	0.741
Ni	-0.191	1.857	0.767	-0.063	1.913	0.674

117

Table 6.5: Interstitial energy (E_i) of Fe, Co and Ni in α-Ti. The notation in brackets indicates the interstitial position occupied after the relaxation.

Site	E_i^{Fe} (eV)	E_i^{Co} (eV)	E_i^{Ni} (eV)
OC	0.777	1.046	1.524
TE	(SP)	(SP)	(SP)
CR	0.482	0.597	1.213
SP	0.960	1.046	1.465
BO	0.990	1.127	1.555
HE	1.806	1.797	2.196
BC	0.692	0.860	1.322
BS	0.575	0.731	1.162

6.4.2 Interstitial sites

The interstitial energies of Fe, Co and Ni of the eight traditional interstitial sites (see Section 5.2.1) were studied using equation 5.1 and they are reported in Table 6.5. For each site, the possible transition pathways were mapped using CI-NEB calculations with five images in between the initial and final states. The results show that the traditional interstitial sites are not always the minima, as in the case of the OC→CR transition in Fig. 6.8. The OC and CR sites are not minima for any of the fast-diffusers. This indicates that these elements occupy distorted interstitial sites instead of the traditional configurations. After an accurate analysis of all the MEPs (CR↔BS, CR↔SP, CR↔OC, CR↔BO, BS↔OC, BS↔BO, SP↔SP, SP↔OC, OC↔OC, OC↔BO), the distorted interstitial site of Fe, Co and Ni were catalogued, and they are schematically displayed in Fig. 6.9.

Iron dissolves in three distorted interstitial sites identified in this work as distorted octahedral (DO), distorted crowdion (DC) and distorted basal octahedral (DBO). In the unit-cell, there are six DO, six DC and six DBO sites, as shown in Fig. 6.9-a. The reduced coordinates and E_i energies are summarised in Table 6.6 along with the coordinates of the nearest Ti atoms. The positive signs of interstitial energy indicate that Fe prefers to occupy the off-lattice site over the interstitial sites. Note, however, that these energies are relatively small. The transition
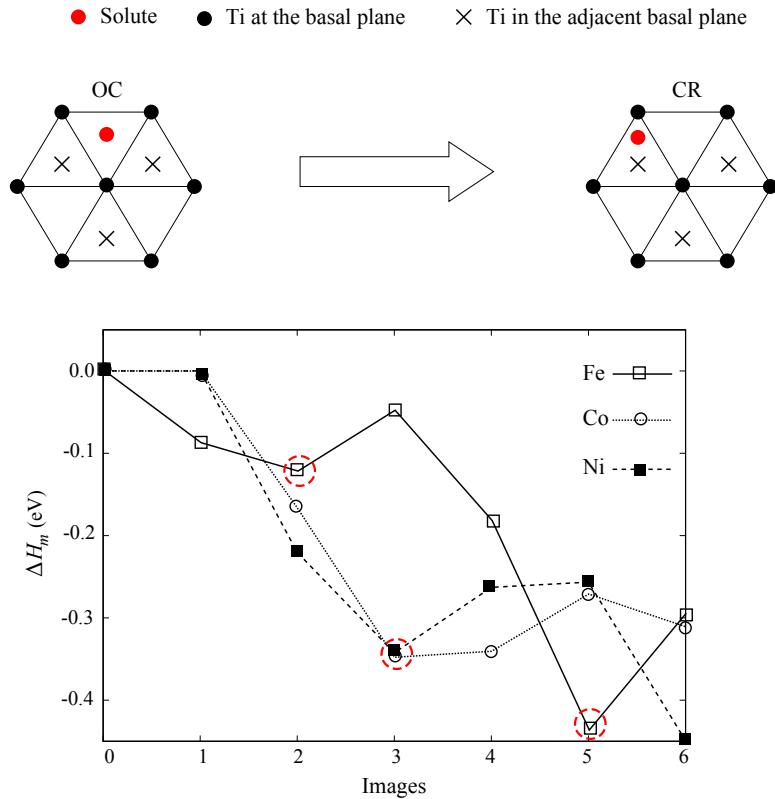
Figure 6.8: MEPs of Fe, Co and Ni OC→CR jump. The migration energy is calculated with respect to octahedral sites. The minima are indicated by dashed red circle line.
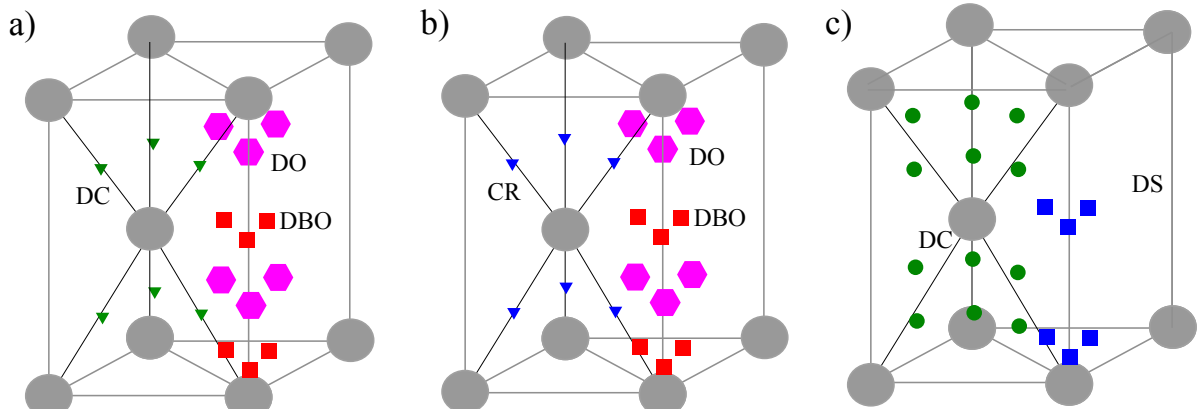
Figure 6.9: Schematic representation of a) Fe, b) Co and c) Ni stable interstitial sites in α-Ti.

pathways were mapped and displayed in Fig. 6.10. DO sites are surrounded by two DC, two DO in the same basal plane, and two DBO sites along the c-axis, leading to as many jumps. From DC sites, Fe can jump to one of the two distorted octahedral site, while from DBO, it can perform six DBO→DO jumps along the c-axis, and two DBO→DBO jumps within the basal plane. The DBO↔DC jumps happen through DO sites. The migration energies and

Table 6.6: The reduced coordinates with respect to lattice sites $(0,0,0)$ and $(1/3,1/3,1/2)$ with primitive lattice $[a_1 = (a;0;0); a_2 = (a/2; \sqrt{3}a/2;0); a_3 = (0;0;c)]$ and interstitial energy (E_i) of Fe distorted interstitial sites in α-Ti. The position of the nearest Ti atoms are also reported.

	Reduced coordinates	E_i (eV)
DO	Fe (0.51,0.75,0.22)	0.575
	Ti (-0.17,1.08,-0.11)	
	Ti (0.36,1.36,0.55)	
DC	Fe (0.17,0.17,0.25)	0.252
	Ti (-0.10,-0.10,-0.10)	
	Ti (0.44,0.44,0.59)	
DBO	Fe (0.5,0.78,0.04)	0.311
	Ti (-0.26,1.03,-0.10)	
	Ti (0.33,1.35,0.51)	
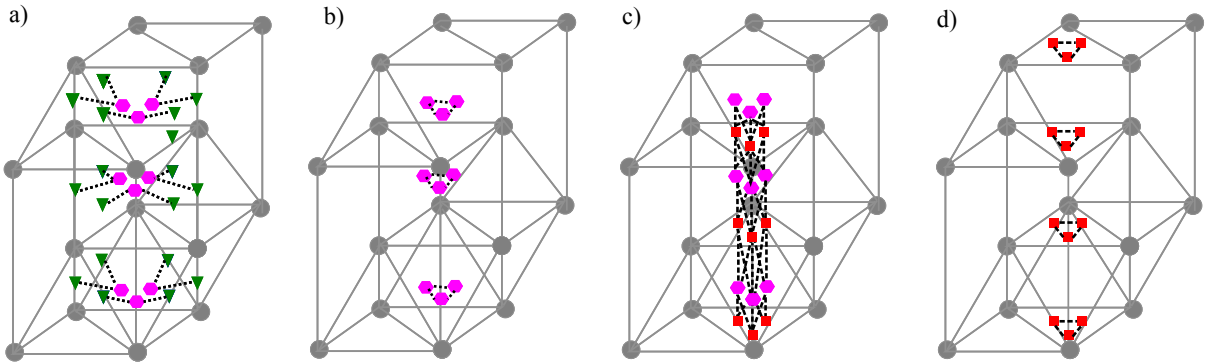
Figure 6.10: Schematic representation of transition pathways of Fe interstitial jumps in α-Ti: a) DC↔DO, b) DO↔DO, c) DBO↔DO and d) DBO↔DBO transitions.

effective frequencies of these jumps are summarised in Table 6.7, and their MEPs with five images between initial and final states are shown in Fig. 6.11.

Similar to Fe, Co has three stable interstitial sites: distorted octahedral (DO), crowdion (CR) and distorted basal octahedral (DBO) (see Fig. 6.9-b). The reduced coordinates and E_i energies are collected in Table 6.8. The distorted octahedral site is surrounded by two DO and two CR sites in the basal plane, and two DBO sites along the c-axis. Therefore, from DO sites there are two DO→DO, two DO→CR and two DO→DBO jumps. From CR sites, Co can perform two CR→CR and four CR→DBO jumps. There are four DBO→CR, two

Table 6.7: Migration energy (ΔH_m) and effective frequency (ν^*) of Fe interstitial jumps in α-Ti.

	ΔH_m (eV)	ν^* (THz)
DO→DC	0.137	8.00
DO→DO	0.203	12.18
DO→DBO	0.188	6.53
DC→DO	0.460	9.11
DBO→DO	0.264	8.78
DBO→DBO	0.193	18.081
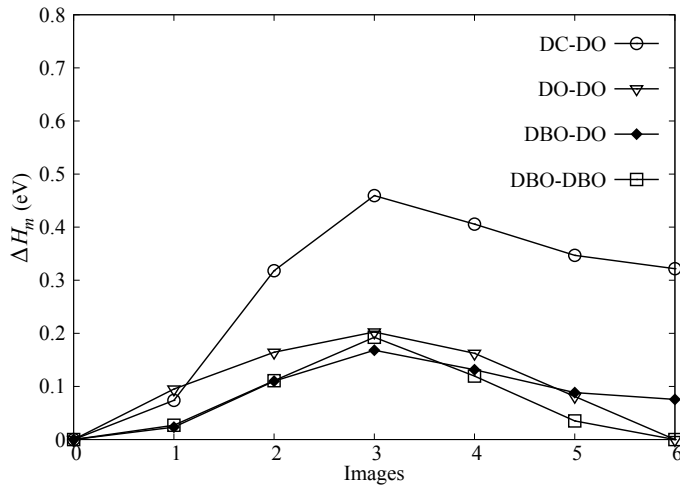
Figure 6.11: MEPs of Fe interstitial transitions in α-Ti: DC↔DO, DO↔DO, DBO↔DO and DBO↔DBO transitions.

DBO→DBO and six DBO→DO jumps from DBO sites, as displayed in Fig. 6.12. For each of these jumps, the ΔH_m and ν^* were evaluated and summarised in Table 6.9 along with the MEPs (see Fig. 6.13).

The DFT calculations show that in the case of Ni, two types of distorted interstitial sites are minima: distorted split dumbbell (DS) and distorted crowdion (DC). In the unit cell, there are twelve DC and six DS sites, as shown in Fig. 6.9-c, their reduced coordinates and E_i are reported in Table 6.10. Ni can perform six DS→DS and four DS→DC jumps, when it occupies DS site. From DC sites, Ni can reach one of the two nearest DS sites or one of the nearest DC sites, as shown in Fig. 6.14. The migration energies, effective frequencies and MEPs are

Table 6.8: The reduced coordinates with respect to lattice sites (0,0,0) and (1/3,1/3,1/2) with primitive lattice $[a_1 = (a;0;0); a_2 = (a/2;\sqrt{3}a/2;0); a_3 = (0;0;c)]$ and interstitial energy (E_i) of Co distorted interstitial in α-Ti. The position of the nearest Ti atoms are also reported.

	Reduced coordinates	E_i (eV)
DO	Co (0.47,0.78,0.21)	0.879
	Ti (-0.19,1.09,-0.11)	
	Ti (0.37,1.36,0.56)	
CR	Co (1/6,1/6,1/4)	0.597
DBO	Co (0.49,0.79,0.05)	0.621
	Ti (-0.28,1.03,-0.11)	
	Ti (0.33,1.35,0.51)	
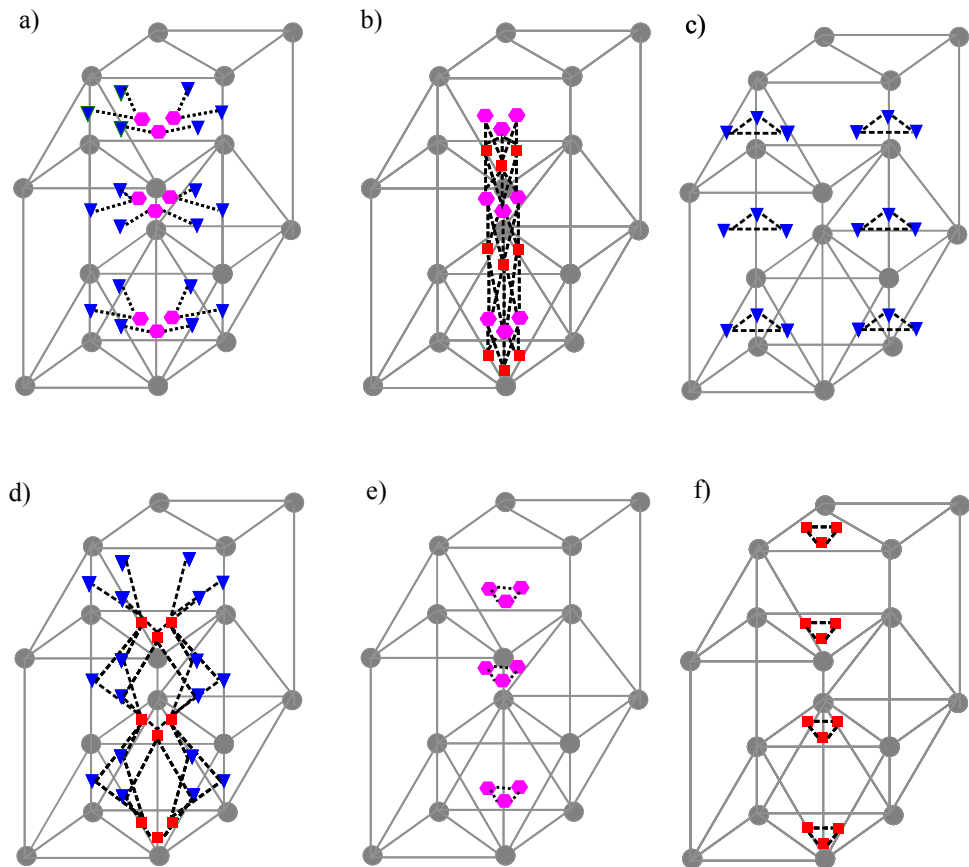
Figure 6.12: Schematic representation of transition pathways of Co interstitial jumps in α-Ti: a) CR↔DO, b) DBO↔DO, c) CR↔CR, d) DBO↔CR, e) DO↔DO and f) DBO↔DBO transitions.

Table 6.9: Migration energy (ΔH_m) and effective frequency (ν^*) of Co interstitial jumps in α-Ti.

	ΔH_m (eV)	ν^* (THz)
DO→CR	0.123	4.174
DO→DO	0.098	4.718
DO→DBO	0.023	3.499
CR→DO	0.221	5.985
CR→CR	0.279	9.529
CR→DBO	0.193	7.236
DBO→DO	0.138	32.642
DBO→CR	0.159	13.055
DBO→DBO	0.281	95.793
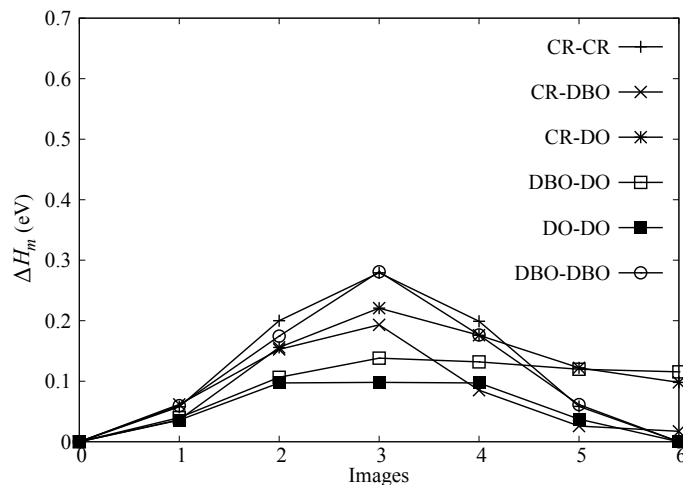
Figure 6.13: MEPs of Co interstitial transitions in α-Ti: CR↔CR, CR↔DBO, CR↔DO, DBO↔DO, DO↔DO, and DBO↔DBO transitions.

summarised in Table 6.11 and Fig. 6.15.

6.4.3 Interstitial solute-vacancy pair

In order to investigate the combination-dissociation process, the interstitial solute-vacancy pair were studied. It is reasonable to assume that the first-nearest neighbour interstitial sites to the vacancy are unstable. Therefore, the stability of the next-nearest-neighbour pairs were

Table 6.10: The reduced coordinates with respect to lattice sites $(0,0,0)$ and $(1/3,1/3,1/2)$ with primitive lattice $[a_1 = (a; 0; 0); a_2 = (a/2; \sqrt{3}a/2; 0); a_3 = (0; 0; c)]$ and interstitial energy (E_i) of Ni distorted interstitial in α-Ti. The position of the nearest Ti atoms are also reported.

	Reduced coordinates	E_i (eV)
DS	Ni (0.44, 0.83, 0.13)	1.036
	Ti (-0.27, 1.01, -0.13)	
	Ti (0.37, 1.37, 0.54)	
DC	Ni (0.22, 0.20, 0.16)	1.088
	Ti (-0.13, -0.15, -0.12)	
	Ti (0.39, 0.40, 0.60)	
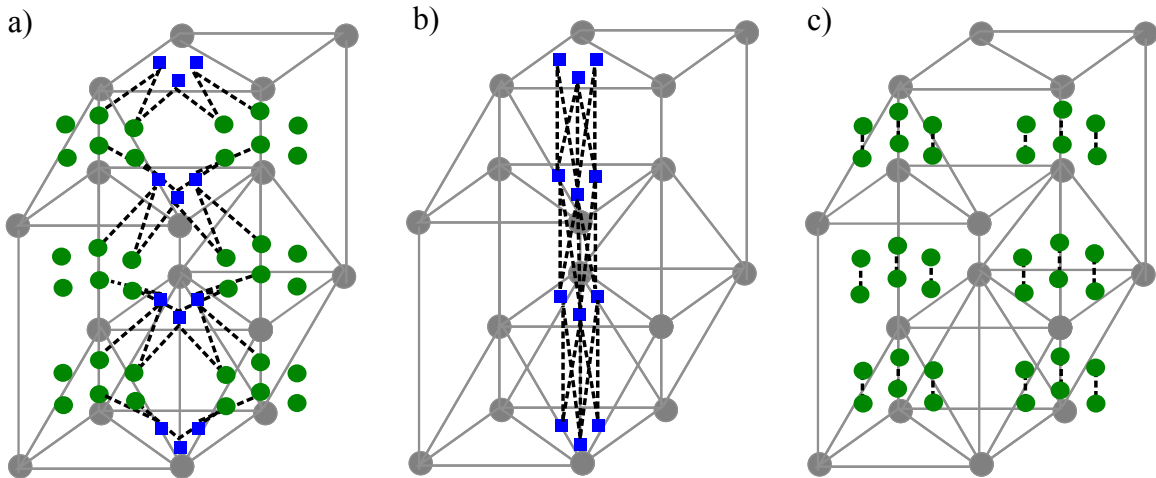
Figure 6.14: Schematic representation of transition pathways of Ni interstitial jumps in α-Ti: a) DC↔DS, b) DS↔DS and c) DC↔DC transitions.

Table 6.11: Migration energy (ΔH_m) and effective frequency (ν^*) of Ni interstitial jumps in α-Ti.

	ΔH_m (eV)	ν^* (THz)
DS→DC	0.081	1.040
DS→DS	0.126	3.125
DC→DS	0.028	2.076
DC→DC	0.126	11.336
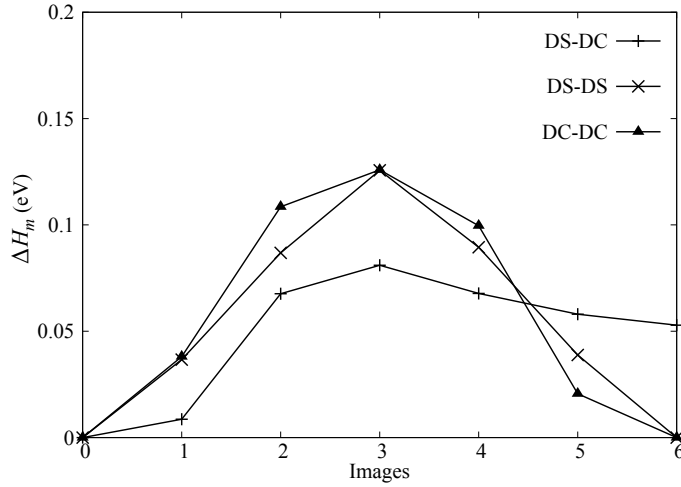
Figure 6.15: MEPs of Ni interstitial transitions in α-Ti: DS$\leftrightarrow$DC, DS$\leftrightarrow$DS and DC$\leftrightarrow$DC transitions.
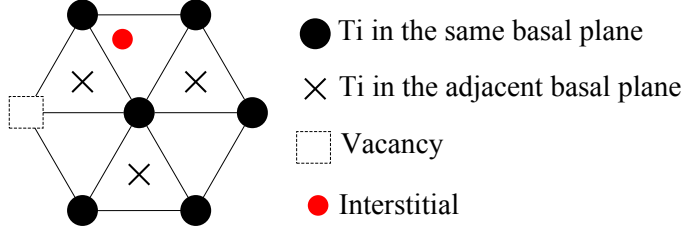
Figure 6.16: Projection on the basal plane of interstitial-vacancy pairs when the interstitial is at the next-nearest neighbour site.

investigated using *ab initio* calculations. DFT results show that the next-nearest-neighbour DBO site to the vacancy is stable for Fe and Co. In the case of Ni, the vacancy forms a stable pair with the next-nearest-neighbour DS site. These three configurations are schematically shown in Fig. 6.16 and their binding energies are reported in Fig. 6.17. The interstitial Fe and Ni are attracted by the vacancy, while Co is repulsed by the vacancy.

CI-NEB method was employed to map the solute jumps in the case of next-nearest-neighbour interstitial-vacancy pair configurations. The annihilation jump is shown schematically in Fig. 6.18, as well as the reverse jump.

In the case of Fe, there are two possible annihilation jumps from the DBO site, DBO $\rightarrow$ L. When Fe is at the substitutional site, it can jump to one of six next-neighbour interstitial DBO sites, L $\rightarrow$ DBO. After the formation of interstitial-vacancy pair, the interstitial solute can jump away to one of the six DBO sites in the above or under unit cell along c-axis, DBO$_I$ $\rightarrow$ DBO$_{NI}$.
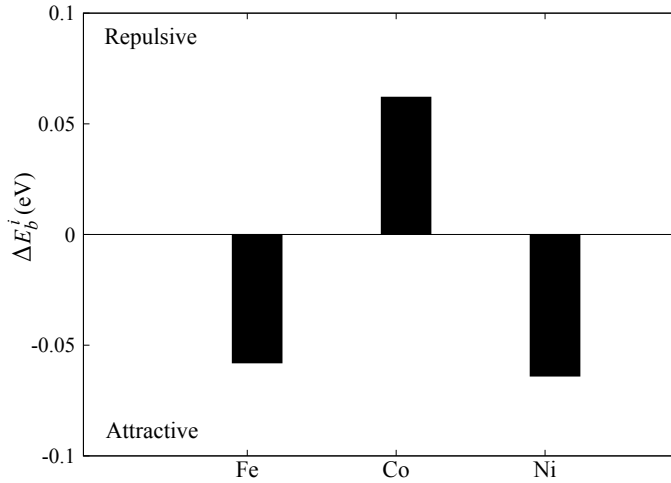
Figure 6.17: Calculated binding energy of interstitial-vacancy pair (ΔE_b^i) of Fe and Co at the next-nearest neighbour DBO site, and Ni at the next-nearest neighbour DS site. Negative sign indicates attraction between interstitial solute and vacancy and vice-versa.
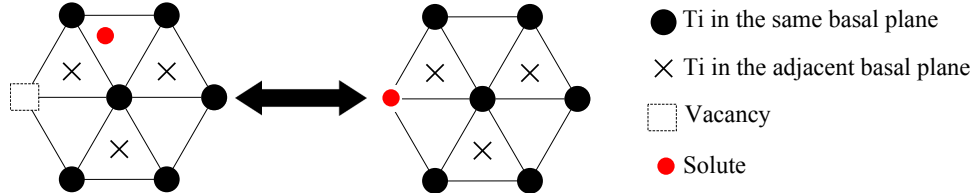
Figure 6.18: Scheme of combination-dissociation processes of the interstitial solute-vacancy pair in hcp crystal.

Table 6.12: Migration energy (ΔH_m) and effective frequency (ν^*) of Fe jumps in the case of interstitial solute-vacancy pair configuration. The binding (ΔE_b^i) and formation (ΔH_v^i) energies of interstitial-vacancy pairs are also reported.

	ΔH_m (eV)	ν^* (THz)	ΔE_b^i (eV)	ΔH_v^i (eV)
DBO → L	1.025	24.070	-0.053	1.924
L → DBO	3.254	7.299	-	-
DBO_I → DBO_{NI}	0.515	47.345	-0.053	1.924
DBO_{NI} → DBO_I	0.233	8.350	0.223	2.200

Vice-versa, the vacancy-interstitial pair can be obtained by six DBO_{NI} → DBO_I jumps. The effective frequencies, migration and formation energies, interstitial-vacancy binding energy of these jumps are reported in Table 6.12.

The vacancy annihilation and creation jumps of Co are similar to Fe transitions, since they form similar interstitial-vacancy pairs. Co can interstitially move away through one DBO_I →

Table 6.13: Migration energy (ΔH_m) and effective frequency (ν^*) of Co jumps in the case of interstitial-vacancy pair configuration. The binding (ΔE_b^i) and formation (ΔH_v^i) energies of interstitial-vacancy pairs are also reported.

	ΔH_m (eV)	ν^* (THz)	ΔE_b^i (eV)	ΔH_v^i (eV)
DBO → L	0.869	7.017	0.062	2.038
L → DBO	3.527	2.983	-	-
DBO_I → CR_{NI}	0.067	34.473	0.062	2.038
CR_{NI} → DBO_I	0.368	1.010	-0.239	1.737

Table 6.14: Migration energy (ΔH_m) and effective frequency (ν^*) of Ni jumps in the case of interstitial-vacancy pair configuration. The binding (ΔE_b^i) and formation (ΔH_v^i) energies of interstitial-vacancy pairs are also reported.

	ΔH_m (eV)	ν^* (THz)	ΔE_b^i (eV)	ΔH_v^i (eV)
DS → L	0.189	4.241	-0.064	1.912
L → DS	3.254	7.299	-	-

CR_{NI} jump. Vice-versa, the vacancy-interstitial pair can be formed by two CR_{NI} → DBO_I transitions. The energies and effective frequencies of these jumps are reported in Table 6.13.

Nickel can combine in two ways with the vacancy, DS → L transition. From the substitutional configurations, Ni can create a vacancy in six ways, L → DS transition. In this case, it was not possible to calculate any interstitial solute jump with dissociation of interstitial-vacancy pair, since the nearest sites to the couple are not stable. Therefore, only the combination and dissociation jumps are included in the KMC simulations. The energies and effective frequencies related to these jumps are reported in Table 6.14.

Finally, the MEPs and kinetic reactions of solute-host swaps were evaluated with CI-NEB. Since the distorted crowdion (Fe, Ni) or traditional crowdion (Co) are stable sites, the solute-host swaps were hypothesised to happen through these sites. The swaps within the basal plane (L → $H_\parallel$) and in the adjacent basal plane (L → $H_\perp$) are shown in Fig. 6.3. The solute can exchange position with one of the twelve nearest host atoms, six in the basal plane and six in the two adjacent basal planes. The corresponding migration energies and effective frequencies

Table 6.15: Migration energy (ΔH_m) and effective frequency (ν^*) of Fe, Co and Ni in-plane ($\parallel$) and out-of-plane ($\perp$) solute-host swaps in Ti.

	$\Delta H_{m\perp}$ (eV)	$\nu^*_{\perp}$ (THz)	$\Delta H_{m\parallel}$ (eV)	$\nu^*_{\parallel}$ (THz)
Fe	2.723	0.414	2.563	2.492
Co	2.816	4.880	2.656	1.830
Ni	2.513	3.294	3.012	0.295

are reported in Table 6.15.

6.4.4 Diffusion behaviour

KMC simulations were used to investigate the behaviour of fast-diffusers. Simple vacancy-mediated and interstitial mechanisms were initially tested and compared with the experimental data. The dissociative diffusion mechanism proposed by Frank-Turnbull for fast-diffusers was also investigated using equation 6.6 [42], and KMC simulations were used to verify the impact of the combination-dissociation process [46]. To conclude, the KMC code modified to include the solute-host swaps [47, 94] was used to study the impact of this mechanism on the solvent diffusivity values.

Simple mechanisms

The hypothesis of substitutional vacancy-mediated (s) and interstitial (i) diffusions were verified using the KMC codes described respectively in Sections 4.2.3 and 5.2.3. The *ab initio* calculations of the solute jumps for these codes were presented in Sections 6.4.1 and 6.4.2. The comparison of these results and experimental values are reported in Fig. 6.19 for Fe, Fig. 6.20 for Co and Fig. 6.21 for Ni. The activation diffusion barriers and the pre-exponential factors are reported in Tables 6.16 and 6.17. The results confirm that these two simple mechanisms cannot explain the anomalous behaviour of these solute atoms. In particular, in the case of solute vacancy-mediated diffusion, the calculated diffusivities are 10^{11}-10^6 times smaller than the experimental data, and the activation energies are double the experimental values. This is not

Table 6.16: Values of Fe, Co and Ni diffusion barriers along the perpendicular ($\perp$) and parallel ($\parallel$) directions to the basal plane evaluated by KMC simulations supposing substitutional vacancy-mediated (Q^s) and interstitial (Q^i) migrations.

Solute	$Q^s_\perp$ (eV)	$Q^i_\perp$ (eV)	$Q^s_\parallel$ (eV)	$Q^i_\parallel$ (eV)
Fe	2.396	0.488	2.632	0.458
Co	2.679	0.087	2.635	0.152
Ni	3.070	0.083	2.931	0.029

Table 6.17: Values of Fe, Co and Ni pre-exponential diffusion factor along the perpendicular ($\perp$) and parallel ($\parallel$) directions to the basal plane evaluated with KMC simulations supposing only vacancy-mediated (D^s_0) and interstitial (D^i_0) migrations.

Solute	$D^s_{0\perp}$ (m²/s)	$D^i_{0\perp}$ (m²/s)	$D^s_{0\parallel}$ (m²/s)	$D^i_{0\parallel}$ (m²/s)
Fe	1.557×10^{-7}	4.327×10^{-7}	7.140×10^{-7}	1.289×10^{-7}
Co	1.339×10^{-6}	3.050×10^{-7}	1.027×10^{-6}	1.131×10^{-7}
Ni	2.163×10^{-6}	1.514×10^{-7}	1.133×10^{-6}	1.071×10^{-8}

surprising as the activation energy of vacancy-mediated diffusion depends on the high vacancy formation energy (see Table 6.4). Therefore, the substitutional migration of fast-diffusers is negligible. On the other hand, the pure interstitial mechanism overestimates the experimental values, as a result of the very small interstitial migration energies. The diffusivities in this case are 10^4 faster times than the experimental data. The interstitial mechanism cannot be neglected, but these results indicate that different processes are involved.

Combination-dissociation process

The KMC code simulating the interstitial mechanism was modified to include the combination-dissociation process [46] with the jump frequencies presented in Table 6.12 for Fe, Table 6.13 for Co, and Table 6.14 for Ni. Where required, the jump rates were multiplied by the probability of having a vacancy near the interstitial solute (see equation 6.10). The diffusivities obtained (D^{KMC}_{cd}) are presented in Fig. 6.22 for Fe, Fig. 6.23 for Co and Fig. 6.24 for Ni, and compared with experimental data (D^{Exp}) and simple interstitial KMC results (D^{KMC}_i).
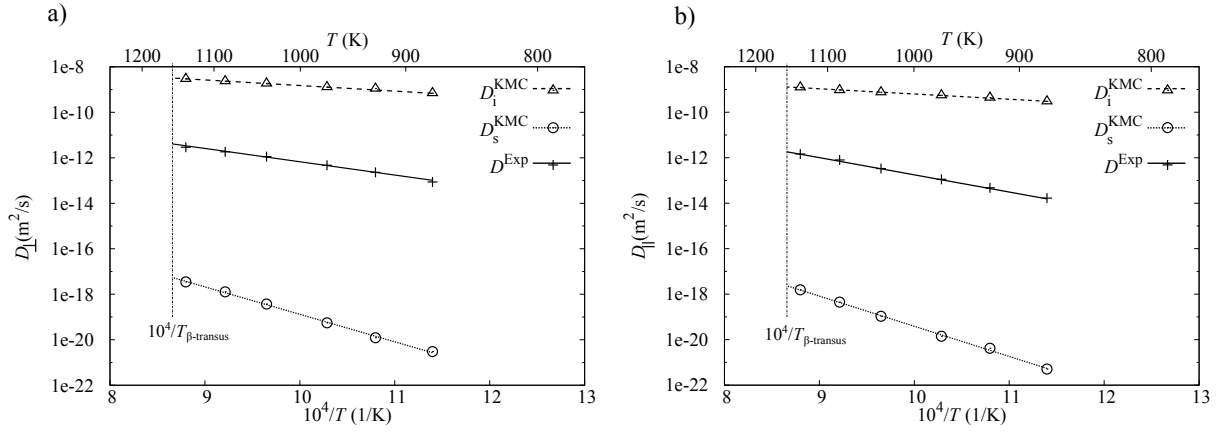
Figure 6.19: a) Perpendicular ($\perp$) and b) parallel ($\parallel$) diffusivities of Fe in the case of interstitial ($D_{\mathrm{i}}^{\mathrm{KMC}}$) and substitutional vacancy-mediated mechanism ($D_{\mathrm{s}}^{\mathrm{KMC}}$) calculated by KMC simulations, and compared with experimental data (D^{Exp}) [40].
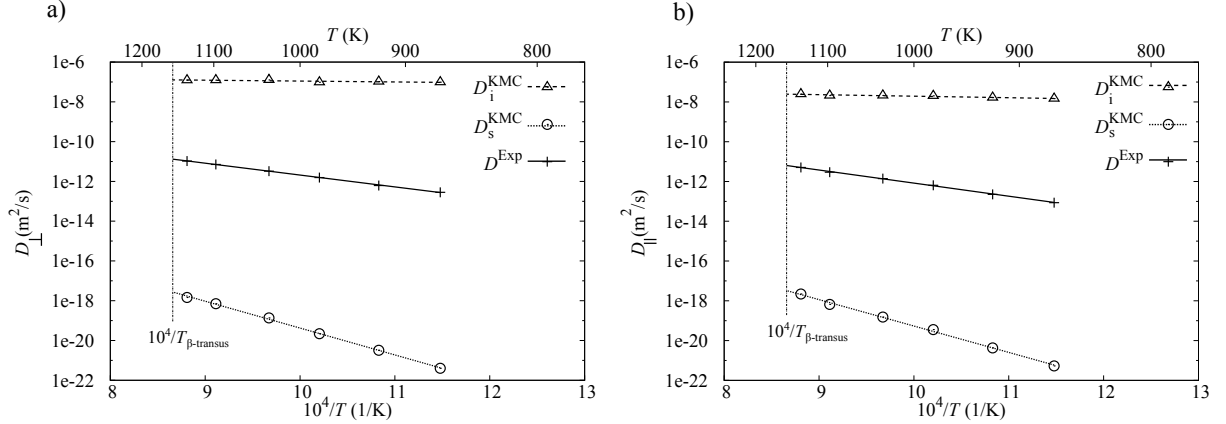
Figure 6.20: a) Perpendicular ($\perp$) and b) parallel ($\parallel$) diffusivities of Co in the case of interstitial ($D_{\mathrm{i}}^{\mathrm{KMC}}$) and substitutional vacancy-mediated mechanism ($D_{\mathrm{s}}^{\mathrm{KMC}}$) calculated by KMC simulations, and compared with experimental data (D^{Exp}) [39].
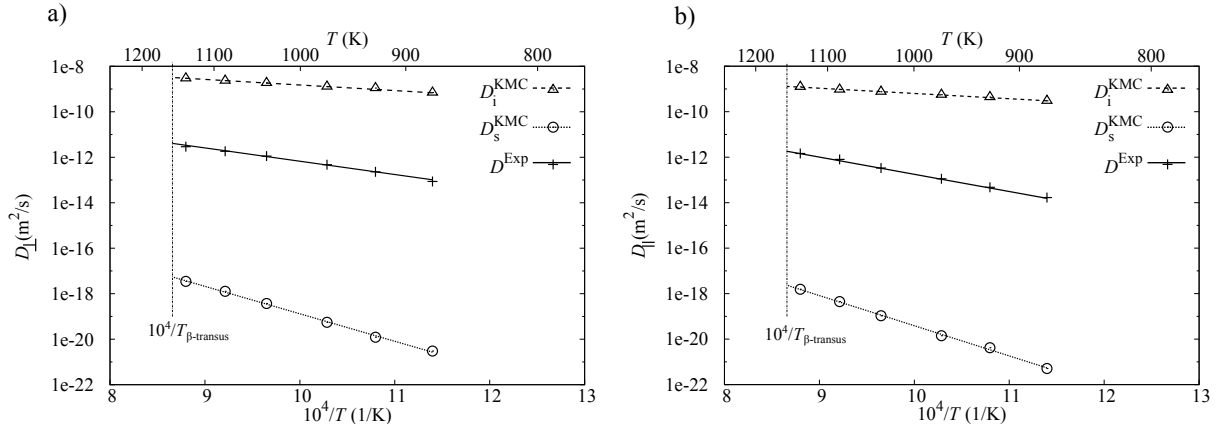
Figure 6.21: a) Perpendicular ($\perp$) and b) parallel ($\parallel$) diffusivities of Ni in the case of interstitial ($D_{\mathrm{i}}^{\mathrm{KMC}}$) and substitutional vacancy-mediated mechanism ($D_{\mathrm{s}}^{\mathrm{KMC}}$) calculated by KMC simulations, and compared with experimental data (D^{Exp}) [38].

Table 6.18: Values of Fe, Co and Ni diffusion parameters (Q^{Eff} and D_0^{Eff}) along the perpendicular ($\perp$) and parallel ($\parallel$) directions to the basal plane calculated by Frank-Turnbull equation [42].

Solute	$Q_\perp^{\text{Eff}}$ (eV)	$D_{0\perp}^{\text{Eff}}$ (m²/s)	$Q_\parallel^{\text{Eff}}$ (eV)	$D_{0\parallel}^{\text{Eff}}$ (m²/s)
Fe	1.063	4.327x10⁻⁷	1.032	1.289x10⁻⁷
Co	0.966	3.050x10⁻⁷	1.031	1.131x10⁻⁷
Ni	1.171	1.514x10⁻⁷	1.117	1.071x10⁻⁸

The $D_{\text{cd}}^{\text{KMC}}$ values match with simple interstitial mechanism diffusivities, indicating that the combination-dissociation process has an insignificant impact on the fast-diffusers migration.

Frank-Turnbull theory

The effective diffusivities (D^{Eff}) of fast-diffusers was calculated by using equation 6.6 [42], and compared with experimental values (D^{Exp}) and interstitial diffusivities ($D_{\text{i}}^{\text{KMC}}$) in Fig. 6.25 for Fe, Fig. 6.26 for Co, and Fig 6.27 for Ni. The interstitial-substitutional Gibbs free energy is approximated by the interstitial formation energies, E_i. The $C_{\text{I}}^{eq}/C_{\text{S}}^{eq}$ ratio is then approximated with the probability of finding the solute at the substitutional position rather than the interstitial site. The highest values of E_i were chosen because they correspond to the highest probability of finding the solute at the lattice site. In the case of Fe and Co, the highest value is E_i^{DO}, while in the case of Ni, it is E_i^{DC}. The values of D^{Eff} calculated are consistent with the experimental data, especially in the case of Co. In the case of Fe, our results overestimate the experimental data of Nakajima *et al* (1983) [40], while they underestimate the experimental data of Nakajima *et al* (1984) [38] in the case of Ni. This may be due to the approximation of ΔG_{IS}, which is taken to be the highest interstitial formation energy for Fe, Co, and Ni. Iron has the smallest values of E_i between the fast-diffusers, while Ni shows the highest energies. The diffusion activation energies and pre-exponential factors obtained are summarised in Table 6.18.

The effective diffusion coefficients of Fe, Co and Ni along the two directions are compared in Fig. 6.28. Ni is the slowest of the fast-diffusers, while Co and Fe diffuse $\simeq 10^2$ times faster.
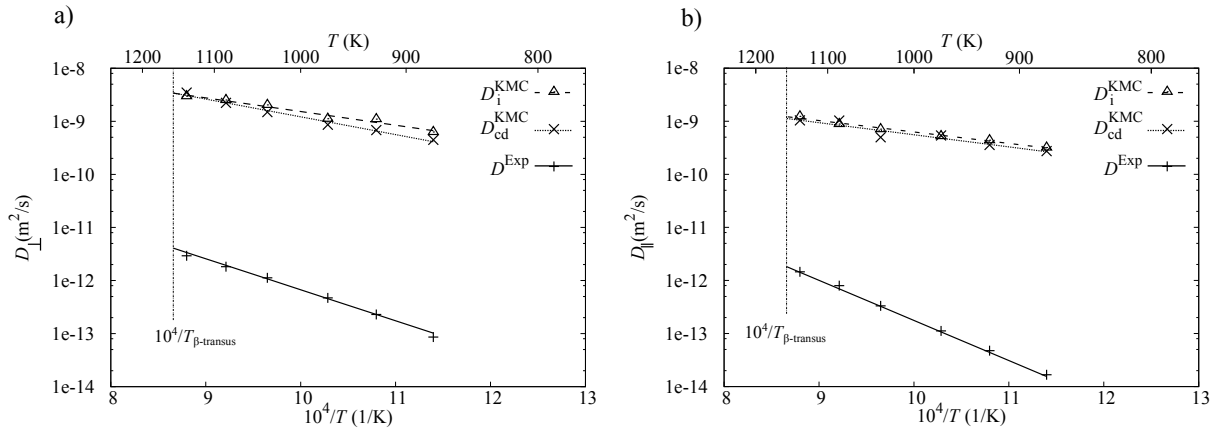
Figure 6.22: a) Perpendicular ($\perp$) and b) parallel ($\parallel$) diffusivities of Fe calculated by including the combination and dissociation jumps ($D_{\mathrm{cd}}^{\mathrm{KMC}}$), and compared with simple interstitial diffusivities ($D_{\mathrm{i}}^{\mathrm{KMC}}$), and experimental data (D^{Exp}) [40].
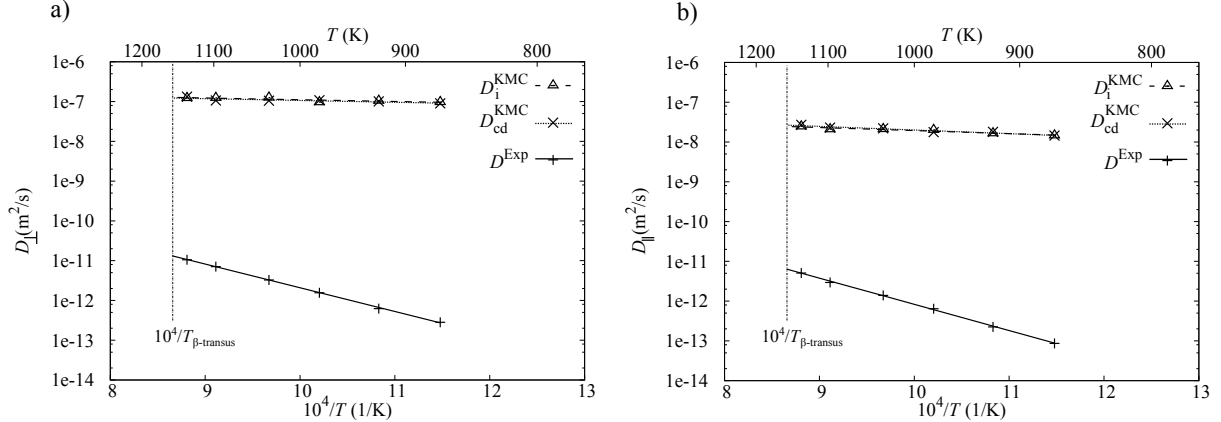
Figure 6.23: a) Perpendicular ($\perp$) and b) parallel ($\parallel$) diffusivities of Co calculated by including the combination and dissociation jumps ($D_{\mathrm{cd}}^{\mathrm{KMC}}$), and compared with simple interstitial diffusivities ($D_{\mathrm{i}}^{\mathrm{KMC}}$), and experimental data (D^{Exp}) [39].
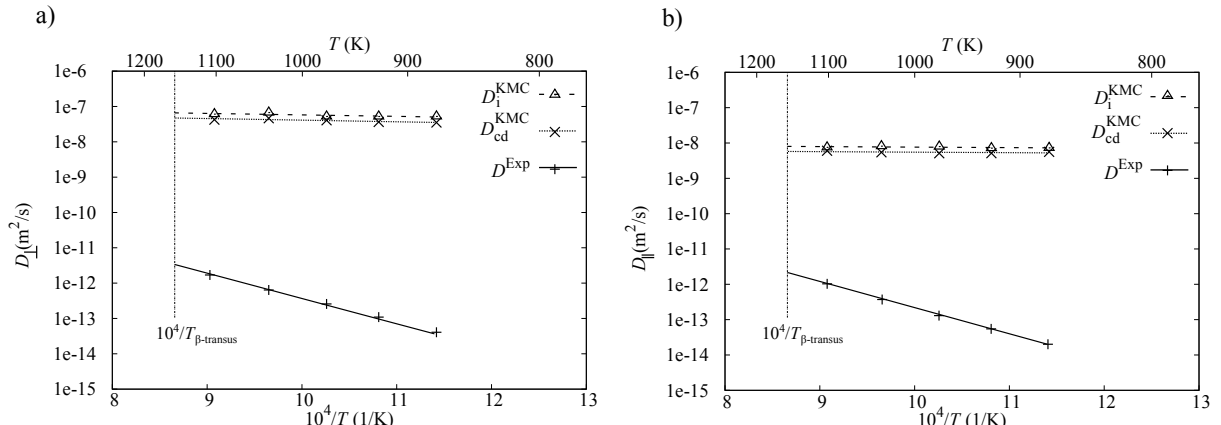
Figure 6.24: a) Perpendicular ($\perp$) and b) parallel ($\parallel$) diffusivities of Ni calculated including the combination and dissociation jumps ($D_{\mathrm{cd}}^{\mathrm{KMC}}$) and compared with no-corrected interstitial diffusivities ($D_{\mathrm{i}}^{\mathrm{KMC}}$), and experimental data (D^{Exp}) [38].

132
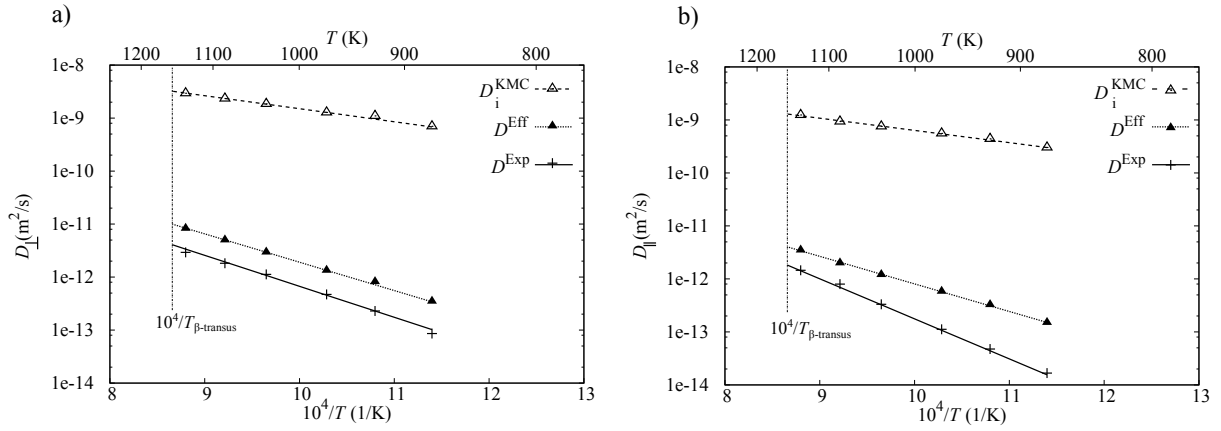
Figure 6.25: Effective a) perpendicular ($\perp$) and b) parallel ($\parallel$) diffusivities of Fe calculated by Frank-Turnbull equation [42] (D^{Eff}), and compared with simple interstitial diffusivities (D_i^{KMC}), and experimental data (D^{Exp}) [40].
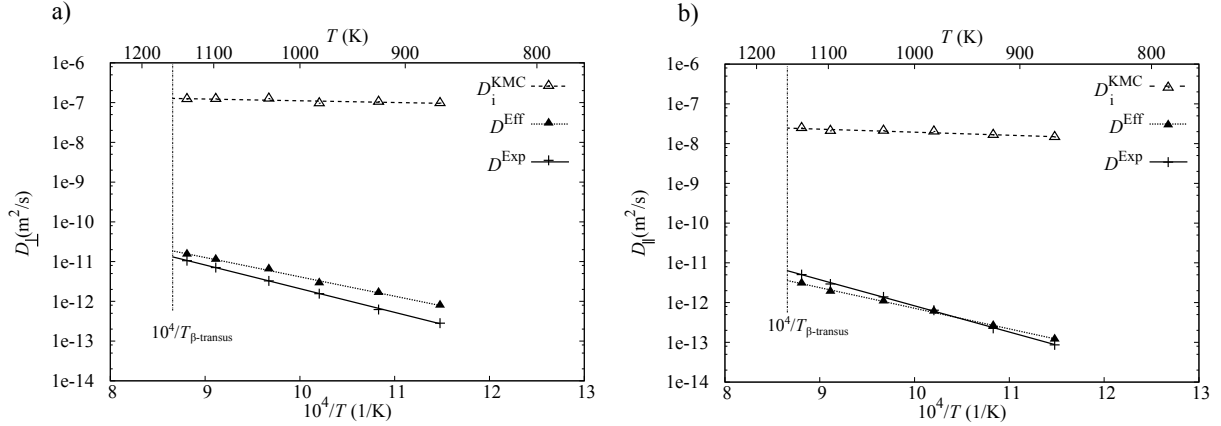
Figure 6.26: Effective a) perpendicular ($\perp$) and b) parallel ($\parallel$) diffusivities of Co calculated by Frank-Turnbull equation [42] (D^{Eff}), and compared with simple interstitial diffusivities (D_i^{KMC}), and experimental data (D^{Exp}) [39].
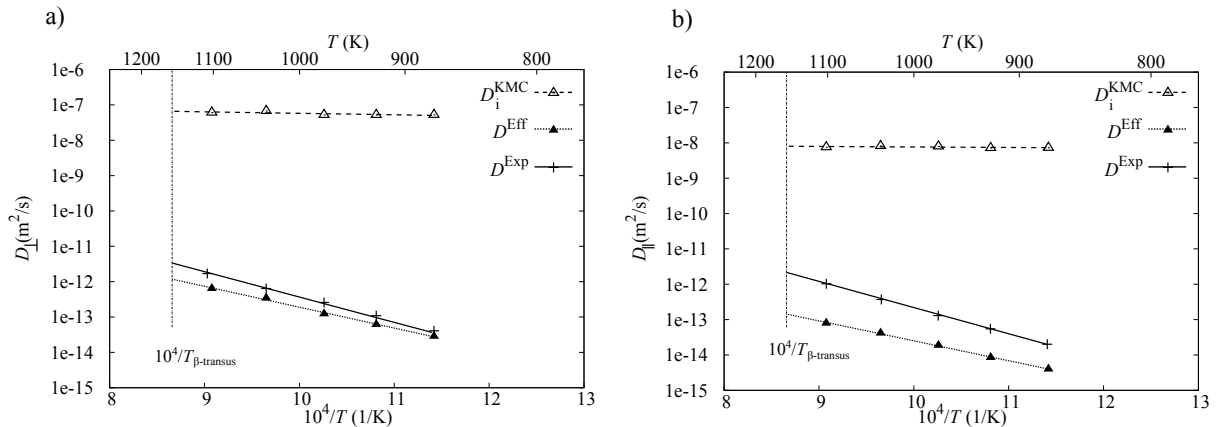
Figure 6.27: Effective a) perpendicular ($\perp$) and b) parallel ($\parallel$) diffusivities of Ni calculated by Frank-Turnbull equation [42] (D^{Eff}), and compared with simple interstitial diffusivities (D_i^{KMC}), and experimental data (D^{Exp}) [38].

133
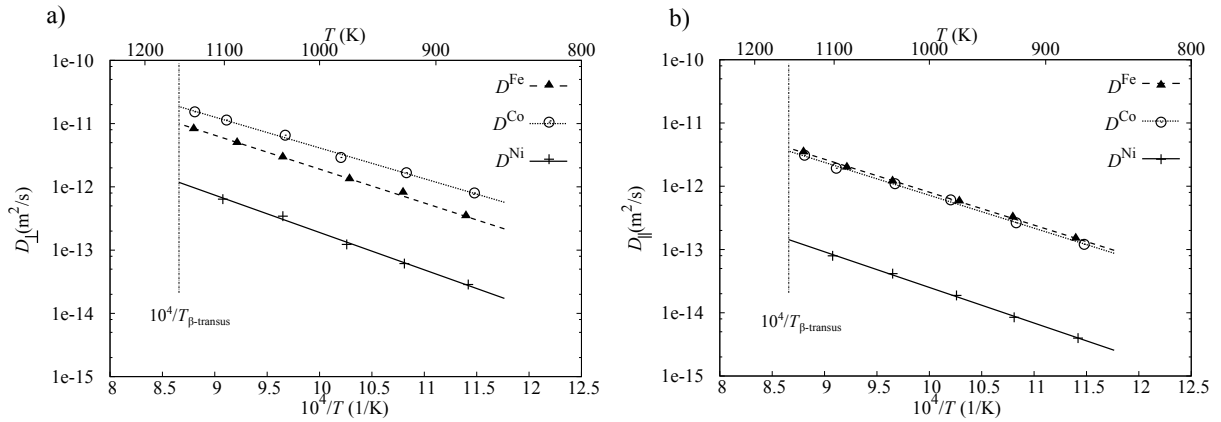
Figure 6.28: Comparison of a) perpendicular ($\perp$) and b) parallel ($\parallel$) diffusivities of Fe (D^{Fe}), Co (D^{Co}) and Ni (D^{Ni}) calculated by Frank-Turnbull formula [42].
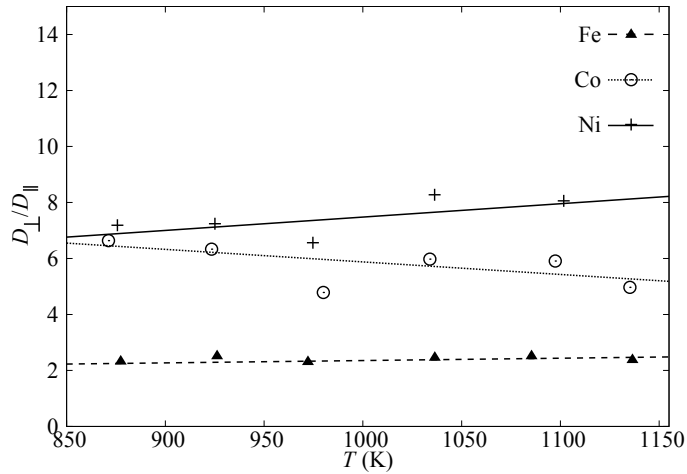
Figure 6.29: Comparison of calculated $D_\perp/D_\parallel$ ratio of Fe, Co and Ni in α-Ti.

The diffusion coefficients along the c-axis are larger than parallel diffusion data. This trend of the anisotropy ratio ($D_\perp/D_\parallel > 1$) has also been experimentally observed by Nakajima and co-workers [38–40].

Solute-host swap

Finally, the influence of the solute-host swap without vacancy [47, 94] on the self-diffusivity was examined. The KMC code simulating the vacancy-mediated migration was modified to include the two solute-host swaps shown in Fig. 6.3. The simulations were running for 54-atoms cell with one vacancy and one solute atom, corresponding to solute concentration of 1.85 %, and the self-diffusivity values were obtained as average of all host atoms migration. These solvent

Table 6.19: Values of activation energy of self-diffusion along the perpendicular ($\perp$) and parallel ($\parallel$) directions to the basal plane in presence of Fe, Co and Ni evaluated by KMC simulations including only vacancy-mediated mechanism (Q^{vm}), and also solute-host swaps (Q^{sh}) migration.

Solute	$Q_{\perp}^{\mathrm{vm}}$ (eV)	$Q_{\perp}^{\mathrm{sh}}$ (eV)	$Q_{\parallel}^{\mathrm{vm}}$ (eV)	$Q_{\parallel}^{\mathrm{sh}}$ (eV)
Fe	2.498	2.510	2.437	2.252
Co	2.606	2.573	2.374	2.405
Ni	2.677	2.571	2.566	2.495

diffusivities ($D_{\mathrm{sh}}^{\mathrm{KMC}}$) are displayed in Fig. 6.30 for Fe, Fig. 6.31 for Co and Fig. 6.32 for Ni, and compared with the previous results of vacancy-mediated KMC code ($D_{\mathrm{vm}}^{\mathrm{KMC}}$). The diffusion activation energy and pre-factors values of solvent migration are reported in Table 6.19 and Table 6.20. The self-diffusivity enhancement is evident in the case of Ni in both directions, the updated self-diffusion coefficients are 2.25-3.0 times higher than $D_{\mathrm{vm}}^{\mathrm{KMC}}$. In the case of Fe, the solute-host swaps mainly affect the parallel diffusion, the $D_{\mathrm{sh}}^{\mathrm{KMC}}/D_{\mathrm{vm}}^{\mathrm{KMC}}$ ratio ranges from 2.25 to 4.23. In the case of Co, the self-diffusivity values do not change significantly with respect to the vacancy-mediated mechanism. When the solute and vacancy are apart, the solvent diffusion happens via vacancy-host or solute-host exchanges. In the first case, the activation energy of vacancy-host swaps is equal to the sum of formation and migration energies of the vacancy. In the case of Ti, this value is equal $\simeq 2.4$ eV for in-plane and out-of-plane jumps, as shown in Section 4.3.2. The migration energies of Fe-Ti swap within the basal plane and Ni-Ti swap in the adjacent plane are respectively 2.563 eV and 2.513 eV (see Table 6.15), close to 2.4 eV. Therefore, these swaps compete with the vacancy-host exchanges, accelerating the self-diffusion. In the case of Fe, this results in an acceleration of Ti migration parallel to the basal plane, while in the case of Ni, the enhancement affects both directions since the displacement of Ti atoms occurs in both directions during the out-of-plane solute-host swap. On the other hand, the migration energy of Co-Ti swaps are higher than 2.4 eV, resulting in jump rates two orders of magnitude lower than vacancy-Ti exchanges. Therefore, these jumps are less likely to happen, and they do not influence the solvent diffusion. These findings may be limited by the fact that only two solute-host swaps are considered.
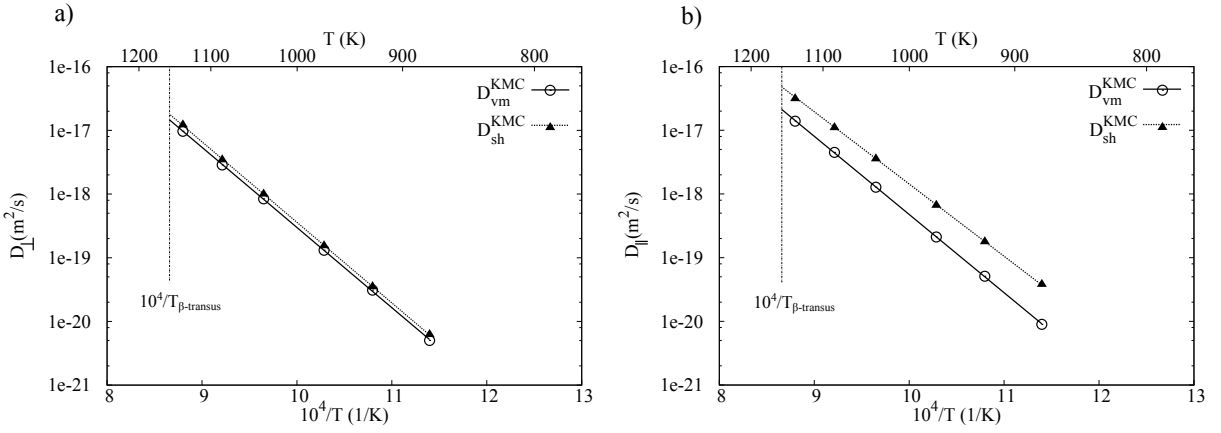
Figure 6.30: Solvent a) perpendicular ($\perp$) and b) parallel ($\parallel$) diffusivities in presence of Fe calculated by KMC simulations including only simple vacancy-mediated migration ($D_{\text{vm}}^{\text{KMC}}$), and also solute-host swaps [47, 94] ($D_{\text{sh}}^{\text{KMC}}$).
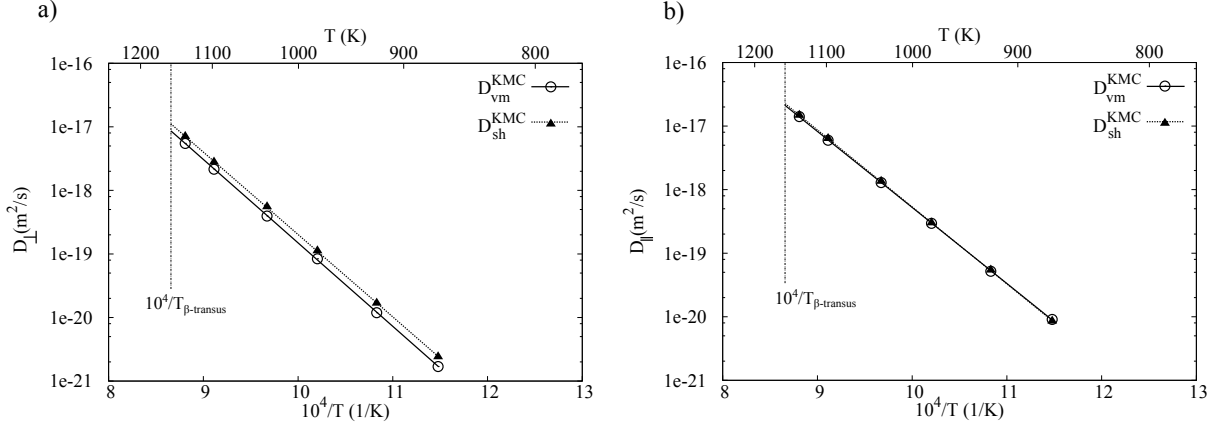
Figure 6.31: Solvent a) perpendicular ($\perp$) and b) parallel ($\parallel$) diffusivities in presence of Co calculated by KMC simulations including only simple vacancy-mediated migration ($D_{\text{vm}}^{\text{KMC}}$), and also solute-host swaps [47, 94] ($D_{\text{sh}}^{\text{KMC}}$).
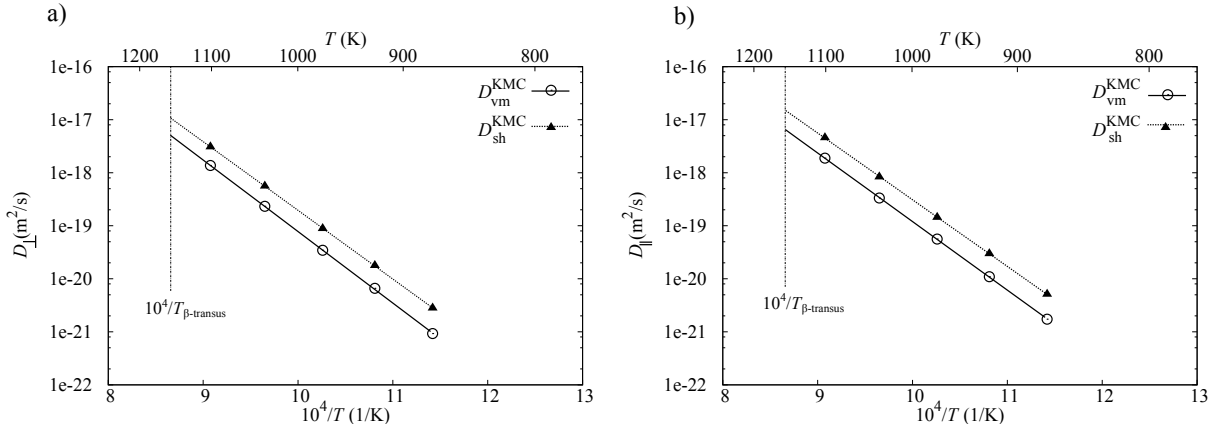
Figure 6.32: Solvent a) perpendicular ($\perp$) and b) parallel ($\parallel$) diffusivities in presence of Ni calculated by KMC simulations including only simple vacancy-mediated migration ($D_{\text{vm}}^{\text{KMC}}$), and also solute-host swaps [47, 94] ($D_{\text{sh}}^{\text{KMC}}$).

Table 6.20: Values of pre-exponential factor of self-diffusion along ($\perp$) and parallel ($\parallel$) directions to the basal plane in presence of Fe, Co and Ni evaluated by KMC simulations including only vacancy-mediated mechanism (D_0^{vm}), and also solute-host swaps (D_0^{sh}) migration.

Solute	$D_{0\perp}^{\mathrm{vm}}$ (m²/s)	$D_{0\perp}^{\mathrm{sh}}$ (m²/s)	$D_{0\parallel}^{\mathrm{vm}}$ (m²/s)	$D_{0\parallel}^{\mathrm{sh}}$ (m²/s)
Fe	1.159×10^{-6}	1.606×10^{-6}	9.114×10^{-7}	3.206×10^{-7}
Co	2.030×10^{-6}	1.875×10^{-6}	4.828×10^{-7}	7.063×10^{-7}
Ni	2.412×10^{-6}	1.777×10^{-6}	1.026×10^{-6}	1.163×10^{-6}

6.5 Discussion and Conclusions

In this work, the first-principles techniques and KMC simulations were used to understand the particular diffusion behaviour of fast-diffusers, Fe, Co and Ni in α-Ti. The analysis of the interstitial and substitutional configurations confirms the fact that these solutes can dissolve both interstitially and substitutionally [44]. In the case of substitutional positions, Fe and Co are more stable at off-lattice configurations, while Ni substitutes one Ti atom at the lattice site. In addition, distorted interstitial sites are preferred to the eight traditional sites.

The KMC results demonstrate that vacancy-mediated migration does not affect the mass transportation of these elements. Nevertheless, the interstitial mechanism alone is insufficient to explain their diffusion behaviour. The effective diffusivities calculated using Frank-Turnbull formula [42] are very similar to the experimental data. The effect of combination-dissociation process [46] on the overall migration is limited, since the interstitial-vacancy pairs are unlikely to form. The self-diffusivity values support the hypothesis that the enhancement of self-diffusion is due to solute-host swap without vacancy-mediation [47, 94].

6.5.1 Substitutional and interstitial configurations

Titanium and other hcp-elements such as Zr and Hf are characterised by large ionic-to-atomic radii ratios. This allows elements with relatively small radii such as Fe, Co, and Ni to occupy both interstitial and substitutional sites [7, 34]. Experimental evidence of this has been reported by Yoshida and co-workers [44, 205] using Mössbauer technique for Fe atoms in α-Ti and α-Zr.

This dissociative solubility leads to anomalous fast diffusion behaviour and acceleration of the self-diffusion. *Ab initio* calculations were used to determine the stability of substitutional and interstitial Fe, Co and Ni, and the respective biding energies of solute-vacancy pairs in α-Ti. The findings indicate that Ni is stable at lattice sites, while Co and Fe tend to occupy off-lattice configurations. This is not surprising, since off-site positions have also been reported in the *ab initio* works of Pérez group research [47, 206, 207] and Burr and co-workers [208] in the case of fast-diffuser Fe and Cr in α-Zr and α-Ti. This may be due to the fact that Ni is the smallest atom and it introduces smaller distortions in the Ti lattice with respect to Co and Fe.

The study of interstitial sites reveals that Fe, Co and Ni do not occupy the eight traditional interstitial sites. Instead, they prefer to occupy distorted configurations of octahedral, basal octahedral, crowdion, and split dumbbell. The *ab initio* work of Burr and co-workers [208] has shown similar behaviour in the case of Fe in α-Zr. The interstitial formation energies reported in this work indicate that these solutes energetically prefer to dissolve at substitutional sites, however these energies are relatively small. Similar behaviour has been reported in the case of Fe in α-Zr by previous first-principles studies [207], and by Mössbauer spectra which show that 30 % iron atoms dissolve at interstitial sites in Zr at 24 K [205]. Our E_i values are similar to the *ab initio* data obtained by Bernstein and co-workers [204].

6.5.2 Diffusion behaviour

The KMC results confirm the hypothesis that simple vacancy-mediated and interstitial mechanisms cannot describe the anomalous diffusion behaviour of fast-diffusers in α-Ti [42]. In the first case, the activation energies are too high as a result of the vacancy formation energy, leading to small migration rates. The substitutional diffusion of Fe, Co and Ni have minimal impact on the overall solute migration. On the other hand, the interstitial mechanism is characterised by very small jump energies leading to larger diffusion coefficients which overestimate the experimental data. This suggests that the interstitial solute migration is not the only process involved in the anomalous behaviour of these solutes, but other processes occur.

In the dissociative diffusion mechanism proposed by Frank and Turnbull [42], the migration

is due to the interstitial and substitutional solute diffusion, vacancy migration from the surface, vacancy production in the bulk, and combination-dissociation reactions [45]. In metals, the production of vacancy from the surface (through migration) and in the bulk (from dislocations) is such that the vacancy concentration reaches a constant magnitude as vacancy source and sink rates balance [42]. In addition, the substitutional solute diffusion can also be neglected as suggested by the KMC simulations reported in this study. Frank and Turnbull have also assumed that the combination-dissociation process [46] has no appreciable effect on the fast-diffusers migration in α-Ti [42]. The comparison of KMC simulations with and without combination-dissociation processes [46] confirm their intuition. In fact, the probability of the interstitial to encounter a vacancy is very low, hence the contribution of combination and dissociation jumps is negligible with respect to interstitial migration. However, the diffusivities calculated with Frank-Turnbull formula are consistent with the experimental data. The discrepancy in the case of Fe and Ni may be due to the approximation of free energy difference between interstitial and substitutional atoms with 0 Kelvin calculations of E_i energies. In addition, the C_I^{eq}/C_S^{eq} ratio is approximated using only the highest value of E_i, while there are different interstitial sites that Fe and Ni can occupied. Nevertheless, the anomalous fast migration of these solutes is due to the fact that a small number of these atoms move though interstitial sites, while the majority of them sit at lattice sites [42]. In other words, the solute effective diffusion coefficients are equal to the interstitial diffusivities corrected by the C_I^{eq}/C_S^{eq} ratio [42]. An indirect confirmation of the dissociative diffusion mechanism is given by the comparison of channelling experiments conducted on Pd [209] and Au [210] in α-Ti. Both elements show small solubility values in Ti, but Pd diffuses two orders of magnitude faster than Ti [209], while the diffusivity data of Au are similar to solvent diffusion coefficients [210]. The channelling experiment shows that 30% of Pd atoms sit at interstitial sites at 673-973 K [209], while only substitutional solutes have been found in the case of Au [210]. This suggests that anomalous migration of Pd is due to the presence of 30% interstitial atoms which diffuse very fast. As mentioned earlier, the dissociative solubility in interstitial and substitutional sites seems due to the small metallic radius, and an empirical relation has been found between the atomic size and interstitial diffusivity [38].

The interstitial migration can explain the opposite anisotropy behaviour of fast-diffusers with respect to self- and substitutional diffusion [38]. Although, all the interstitial transitions require similar migration energy, there is an higher number of jumps along the c-axis than within basal plane. For example, from distorted basal octahedral sites, Fe has six possible jumps along c-axis and only two in-plane jumps. In the case of Co, there are six DBO→DO transitions along the c-axis, four out-of-plane DBO→DC transitions and only two DBO→DBO transitions within the basal plane. Ni diffuses mainly along the c-axis with only two DC→DS and four DS→DC jumps contributing significantly to the parallel diffusion.

The Frank-Turnbull model describes well the fast migration of Fe, Co and Ni, but it cannot explain the enhancement of self-diffusivity values. This study shows that the acceleration of solvent migration can be attributed to the solute-host swap mechanism proposed by Pasianot et al [47]. The dissociative solubility of fast-diffusers allows the substitutional solute to exchange position with host atoms without vacancy mediation. This transition is schematically described by the model proposed by Warburton [94]. When the interstitial-vacancy pair is formed after a dissociation jump (v_1), only combination solute-vacancy jumps (v_2) and host-vacancy reorienting (w_2) jumps are allowed [94]. The solute-host swap is a result of the sequence of dissociation, reorienting host-vacancy and combination transitions. For simplicity, in this work only two solute-host swap jumps, involving the crowdion site in the case of Co and distorted crowdion site for Fe and Ni, are considered for the simulations (in-plane and out-of-plane swaps). The KMC results show that the solvent diffusivities which include the solute-host swap mechanism are larger than the simple vacancy-mediated process in the case of Ni and Fe, while the enhancement is minimal for Co. This may be due to the fact that, in the case of Fe and Ni, the migration energies of solute-host swaps are close to 2.4 eV corresponding to the sum of E_v and ΔH_m of vacancy-solvent exchange. In the case of Ni, the enhancement occurs along both directions because the Ni-Ti swap in the adjacent basal plane are more likely to happen, while the Fe-Ti swap within the basal plane increases the self-diffusivity along the parallel direction. On the other hand, in the case of Co, the migration energies of solute-host swaps are higher than vacancy-host exchange, resulting in no significant enhancement of the self-diffusion. The

solute can exchange position with the solvent atom through other transitions, and requires further investigations of the pathway networks. These results need to be interpreted as a qualitative description rather than a quantitative measure of this mechanism. It is important to bear in mind that the migration of fast-diffusers is a very complex phenomenon with different processes involved, while the KMC simulations here presented focus only on one aspect of their behaviour. Additionally, there are no systematic studies of the individual effect of fast-diffusers on Ti migration in the literature, making it hard to interpret and validate these results. Nevertheless, our findings support the idea that solute-host swap of Fe, Co and Ni can have an appreciable impact on solvent migration, and therefore on the creep properties of Ti [7, 34, 36].

Chapter 7

Conclusions and Future work

7.1   Conclusions

This work presents the findings from a study on solute and self-diffusion in α-Ti, focusing on three migration mechanisms: vacancy-mediated, interstitial, and fast-diffuser diffusion. The aim of this project was to determine the diffusivities of different species in Ti and also to understand the migration mechanisms involved. This investigation was conducted with *ab initio* techniques, using both analytical methods and kinetic Monte Carlo simulations.

Given the importance of Si and its slow diffusion which influence high-temperature proper-ties of α-Ti alloys, the research started with an investigation of its vacancy-mediated diffusion and compared the behaviour with other semi-metals, Al, Ga, Ge, In and Sn. The next phase was to better understand the interstitial migration of the light elements, O, N and C. These interstitials have dramatic influence on the creep and fatigue resistance of Ti, limiting the utilisation of α alloys at high temperature. The large diffusion coefficients of these elements contribute to the decline of Ti properties. The research finishes with an investigation of the fast-diffusers (Fe, Co and Ni) which are important when considering creep behaviour. These alloying elements may be linked to the reduction in creep properties through their fast migra-tion and to their role in enhancing the of self-diffusion in Ti. The following sections summarise our findings on diffusion of these solutes and possible ideas of further investigations.

7.1.1 Vacancy-mediated diffusion in alpha-Ti: semi-metals

The semi-metals and self-diffusion coefficients in α-Ti along the perpendicular and parallel direction to the basal plane were calculated using an analytical model ("8-frequency" model [51]) and kinetic Monte Carlo simulations informed by *ab initio* calculations. The results are consistent with the experimental data and previous DFT works available in the literature, showing the accuracy of these two methods.

The study shows that the atomic size plays a minor role in the solute migration, while the electronic structure of the solute-solvent bond has a major impact on the diffusion. In fact, the DFT results show that a smaller atom such as Si diffuses many times slower than a large one such as In. The charge density analysis indicates the formation of a strong Si-Ti bond that requires high energy to be broken. Vice-versa, the bond created between In and Ti is easier to break leading to a small diffusion activation energy. The slow migration of Si may positively influence the creep behaviour affecting the dislocation climb. The addition of solutes in the matrix changes the vacancy formation and migration energies. This may effect the speed of dislocation climb mechanism as suggested by Yu and Wang [211]. However the work of Goswani and Mottura [212] shows that the addition of slow-diffusers such as Re in Ni does not reduce the vacancy diffusion appreciably to explain the good influence of Re addition on the creep properties of Ni. Further investigations are required to better address these phenomena.

The first-principles calculations have been shown to be an excellent tool to study the anisotropic diffusion that characterises α-Ti. The calculations confirm the trend $D_\perp/D_\parallel < 1$ reported for hcp elements with $c/a < 1.633$ [9]. In particular, the behaviour of Ge and Si stands out with respect to the other solutes. The anisotropy is a result of the difference between in-plane and out-of-plane jump migration energies. In the case of Si and semi-metals, the out-of-plane jump is more energetically favourable. For hcp crystals, this energy depends on three terms. The first one is the energy necessary to dilate the "window" of host atoms around the solute at the saddle point. The second term is the energy required to compress the solute in order to squeeze through this window. The last term depends upon the distortion of the solute-solvent bond that can lead to a low-energy configuration at the saddle point. *Ab initio* studies

allow for the evaluation and comparison of these terms for the semi-metals showing that the last term can significantly decrease the migration energy for the in-plane jump, promoting the parallel diffusion over the perpendicular migration, which has an especially large contribution in the case of Ge.

7.1.2   Interstitial diffusion in alpha-Ti: O, N and C

The diffusion behaviour of O, N and C was studied using the analytical model proposed by Landaman and Shlesinger [52, 53]. The findings obtained are in good agreement with the KMC simulations informed by the same jump frequencies, as well as by previous experimental values and first-principles studies.

The *ab initio* study shows that these elements prefer to dissolve as interstitials in α-Ti. In particular, the calculations confirm that they occupy octahedral sites. However, the tetrahedral sites are unstable for these elements, while less traditional sites such as crowdion, hexahedral and basal crowdion are stable. The electronic structure of the solute-Ti bond of these stable sites were evaluated. The findings show that when these solutes occupy octahedral sites, they form a very strong bond with Ti, while in the case of the other interstitial sites, this bond is more metallic. The effect of these elements on the Ti plasticity can be related to this more covalent bond [30]. In particular, O and N show similar electronic behaviour, while the Ti-C bond is weaker. This may be why C reduces ductility less than O or N in α-Ti.

With this new information, the transition networks through which these solutes migrate in the hcp crystal of Ti was updated. The new pathway networks explain the anisotropic diffusion behaviour of these solute, $D_\perp/D_\parallel < 1$. In fact, the migration is strongly dependent on the octahedral↔crowdion swap which occurs on the directions parallel to the basal plane. The energy required to perform octahedral↔crowdion transition is very low, especially compared to the octahedral↔octahedral jump along c-axis. The diffusion behaviour of O and N is similar, while C diffusivities are faster. This can be attributed to the lower energy migration of C with respect to O and N, and can be explained by the weaker Ti-C bond.

7.1.3 Fast-diffusers migration in alpha-Ti

The diffusion behaviour of fast-diffusers in α-Ti was investigated using KMC simulations informed by *ab initio* calculations. First-principles results show that Fe, Co and Ni can be accommodated at interstitial sites in addition to substitutional configurations in Ti as experimentally observed by Yoshida *et al* [44]. As substitutional atoms, Co and Fe occupy off-lattice sites, while Ni replaces the host atom at the lattice site. Off-site configurations have been reported for Fe in α-Zr in previous first-principles studies [47, 207] and experimentally [205]. This behaviour may be due to volumetric factors. As interstitial atoms, Fe, Co and Ni tend to accommodate at distorted interstitial sites rather than the traditional configurations. Fe shows similar behaviour in α-Zr as reported experimentally by Yoshida *et al* [205], and computationally by Pérez *et al* [207] and Burr *et al* [208]. The interstitial formation energies are in good agreement with the values reported by Bernstein and co-workers [204]. These solutes show a tendency to occupy the lattice sites rather than interstitial sites. This is not surprising, since Yoshida *et al* have reported that only 30% of Fe atoms sit at interstitial sites in Ti [44].

The anomalous fast migration depends on the dissociative solubility in interstitial and substitutional sites, as suggested by Frank and Turnbull [42]. Since Fe, Co and Ni can be found both at interstitial and lattice sites, both mechanisms of interstitial and vacancy-mediated diffusion are possible. However, in the case of the interstitial process, the diffusivity values are too high with respect to the experimental data, while the substitutional solute diffusion makes no significant contribution to the overall migration of these solutes. Our findings suggest that the anomalous diffusion of fast-diffusers is due to the fast migration of the relatively few atoms at interstitial sites, while the majority of solutes are stationary at lattice sites. In fact, the effective diffusivities calculated by Frank-Turnbull formula [42] are consistent with experimental data of Fe [40], Co [39] and Ni [38] migration in Ti. On the other hand, the combination and dissociation jumps [46] are very rare and they do not significantly influence the migration of fast-diffusers. The interstitial transitions through which these solutes move can explain the anisotropic diffusion behaviour. The trend $D_\perp/D_\parallel > 1$ is a result of the higher number of interstitial jumps along c-axis.

The acceleration of solvent atom migration in the presence of fast-diffusers seems to be related to the substitutional solute-host swap without vacancy assistance [47]. The solute-host swap is based on the interstitial-vacancy pair model proposed by Warburton [94]. With respect to Miller's model [46], only the dissociation and combination solute reactions, and the reorientation of the pair through vacancy-host exchange transitions can occur [94]. A sequence of dissociation, reorienting vacancy-host, and combination jumps allows the fast-diffusers to exchange position with solvent atoms. The KMC investigation on this mechanism qualitatively shows that the solvent diffusion is promoted by this type of transition.

7.2 Future work

This work has shown the potential of DFT and KMC methods as a tool to understand different diffusion mechanisms in dilute binary Ti alloys. In terms of directions for future research, a few areas could yield interesting results:

1. The calculation of vacancy-mediated diffusion of semi-metals and Ti can be improved by including the vibrational entropy term in the vacancy formation energy. The vibrational entropy can be obtained using quasi-harmonic approximation from phonon or Debye model, using respectively the supercell [213] and Debye-Grüneisen methods [214].

2. The substitutional solute and self-diffusivities in non-dilute binary alloys can be achieved using statistical methods such as cluster expansion [215] and KMC techniques to predict the thermodynamic properties of binary alloys [216].

3. The DFT calculations can be used to study the impact of composition upon the stacking fault energy. This information is important as it can be used to assess dislocation climb [211]. Yasi and co-workers [217] have performed similar studies mapping the solute/dislocations interaction energy in Mg. It would be interesting to apply their methods to Ti.

4. A study of O, C and N effect on the structural stability, lattice constant and elastic

constants and electronic structure mechanical properties of Ti can aid understanding their effect on the α-Ti plasticity [30]. A better understanding of the diffusivity of light elements effects upon the mechanical properties in Ti can also be achieved by studying their interaction with dislocations [77, 91], and deformation slip modes [218].

5. The gap between fast-diffusers diffusivity values calculated in this work and the experimental data could be addressed by calculating the temperature dependence of the interstitial formation energy. The free energy can be obtained by vibrational entropy, using frozen phonon calculations [219].

6. A more detailed investigation of self-diffusion enhancement due to fast-diffusers can be achieved by an accurate map of all solute-host swaps. A comparative study of the effect of these elements can give important information on their influence on creep properties of α-Ti. It has been reported that very small additions of Ni have a 7-11 times higher detrimental effect on the Ti properties than Fe [36].

7. The addition of fast-diffusers in Ti does not only affect the solvent atom migration, but it accelerates the diffusion of some substitutional atoms, such as Ta [41] and Al [10]. In other cases, the fast-diffusers have no effect on the substitutional migration (Zr diffusion [220]). A study on the substitutional solute migration in the presence of Fe, Co and Ni can give more information on these phenomena. Understanding the impact of substitutional elements on the formation of vacancy-interstitial defects is also fundamental for the design of α-Ti alloys and their mechanical properties.

Appendix A

Self-interstitial diffusion

In this section, we report on a brief investigation of self-interstitials in α-Ti in order to address the inquiries advanced by the article of Zhang *et al* [191] on the cold dwell fatigue mechanism and self-diffusion at low temperature. In their work, Zhang and co-workers have estimated that dwell fatigue mechanism in Ti has an activation energy of 0.62 eV. They have assumed that this energy is due the fact that Ti atoms can migrate at low temperature via self-interstitial mechanism.

The self-interstitial defects were studied using electronic structure described by PAW [142], exchange-correlation functional computed using GGA-PBE [143] treating the 3p-orbitals as valence. We used 54-atom supercell, Monkhorst-Pack mesh of 32 x 32 x 17 k-points for a 2-atom cell and an energy cut-off of 350 eV. The formation energy of self-interstitial were computed using,

$$E_{si} = E\{M_{N+1}\} - \frac{N+1}{N}E\{M_N\}; \tag{A.1}$$

where N is the total number of solvent atoms, $E\{M_{N+1}\}$ is the energy of a system with one self-interstitial, and $E\{M_N\}$ is the energy of the perfect site. These energies are presented in Table A.1. The stable self-interstitial sites of Ti are octahedral (OC), basal octahedral (BO) and split dumbbell along c-axis (SP). Our result are in good agreement with the work of Vérité [186] (see Table A.1). In the hcp unit cell, there are two equivalent OC sites, two equivalent BO sites, and two equivalent couple of SP sites, as displayed in Fig. A.1. For simplicity, each

Table A.1: Calculated self-interstitial energies (E_{si}) in α-Ti compared with previous *ab initio* data (E_{si}^{V}) [186].

Site	E_{si} (eV)	E_{si}^{V} (eV)[186]
OC	2.654	2.63
TE	(SP)	(SP)
CR	(saddle point)	2.92
SP	2.722	2.74
BO	2.641	2.54
HE	(saddle point)	(BO)
BC	(BO)	(BS)
BS	(saddle point)	2.76
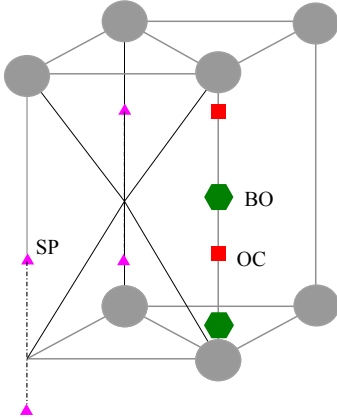
Figure A.1: Schematic representation of stable self-interstitial sites in hcp unit cell of α-Ti.

atom of the SP couple is considered separately, therefore there are four SP self-interstitial in the unit cell.

The self-diffusion coefficients were calculated using 100 KMC simulations of 10^9 events each. The migration energies and minimum energy path were evaluated using CI-NEB [62–64] with a constant-shape supercell, and the same set-up (supercell size, k-points mesh, and energy cut-off) of the defect energy calculations. From the BO sites, two BO→OC along c-axis and six BO→SP transitions are possible. There are twelve OC→SP jumps within the basal plane, and two OC→BO transitions along c-axis from OC sites. From the SP, self-interstitial Ti can move within the basal plane to one of the three OC sites (SP→OC), to one of the six BO site in the

Table A.2: Migration energy (ΔH_m) and effective frequency (ν^*) of self-interstitial jumps in α-Ti.

	ΔH_m (eV)	ν^* (THz)
BO→OC	0.370	15.975
BO→SP	0.397	17.007
OC→BO	0.346	59.724
OC→SP	0.373	62.553
SP→BO	0.280	14.865
SP→OC	0.280	14.624
SP→SP	1.359	44.273
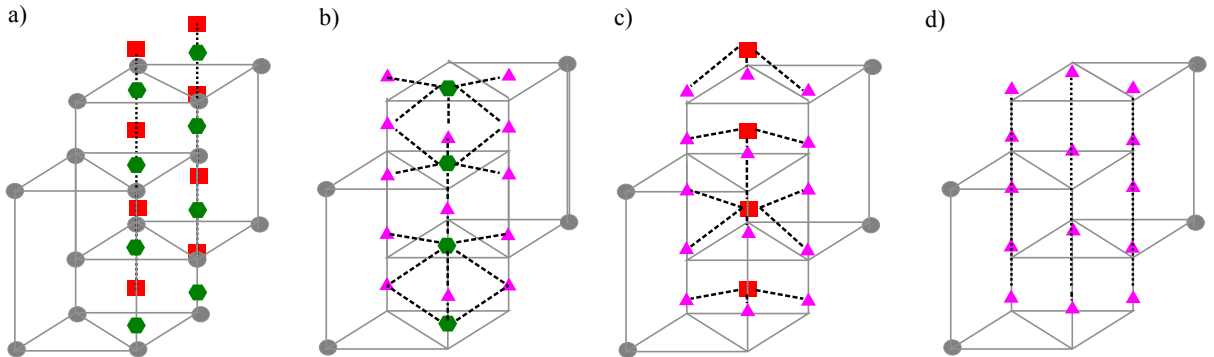
Figure A.2: Schematic representation of transition pathways of self-interstitial jumps in hcp crystal: a) BO↔OC, b) BO↔SP, c) OC↔SP and d) SP↔SP transitions.

adjacent basal planes (SP→BO), or to one of the two SP site along c. These transitions are schematically displayed in Fig. A.2, and their migration energies and effective frequencies are reported in Table A.2.

The bulk diffusivity data at low temperature (20-230 °C) calculated with KMC simulations are displayed in Fig. A.3. The activation energy of self-interstitial results equals to 0.383 eV, smaller than the value reported by Zhang *et al* [191], though of the same order of magnitude. This indicates that Ti can actually diffuse at low temperature by a self-interstitial migration rather than vacancy-mediated mechanism, and affect the mechanical behaviour at these temperatures.
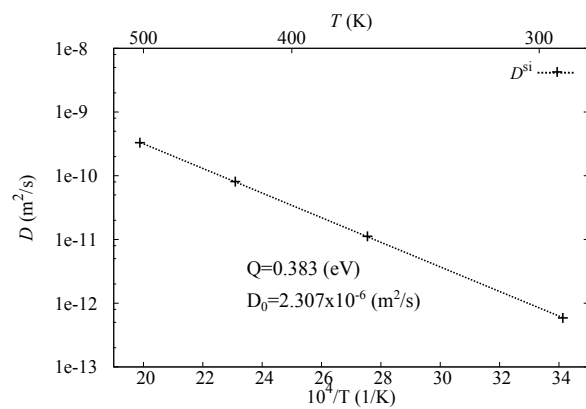
Figure A.3: Self-interstitial diffusion coefficients evaluated between 20-230 °C.

Appendix B

Multi-State Diffusion matrix

B.1 Oxygen

The Laplace transform matrix of waiting time and Fourier transform matrix of displacement of O in Ti were obtained following the procedure in [52, 53]. $\widetilde{\underline{\psi}}(u)$ and $\underline{\tilde{p}^*}\left(\overrightarrow{k}\right)$ are n x n matrices, where n is the number of interstitial sites in the unit cell. The columns and rows represent respectively the initial and final sites of each jump. In the case of O, n is equal 10, and we decided to use the site notation in Fig. B.1 and to denote the jump frequencies as follow,

- w_{oo}: octahedral→octahedral jump frequency;

- w_{oh}: octahedral→hexahedral jump frequency;

- w_{oc}: octahedral→crowdion jump frequency;

- w_{ho}: hexahedral→octahedral jump frequency;

- w_{hc}: hexahedral→crowdion jump frequency;

- w_{co}: crowdion→octahedral jump frequency;

- w_{ch}: crowdion→hexahedral jump frequency.

Considering OC1 site (see Fig. B.1) as initial site, O can jump along $-\overrightarrow{k^3}$ direction to OC2 sites, one in the same unit cell and one in the repeated cell. Additionally, it can jump to three

Figure B.1: Notation of O interstitial sites in the unit cell used to build the Laplace transform matrix of waiting time and Fourier transform matrix of displacement.

different HE1 sites, one in the same unit cell, and the other two in the two repeated cells along $\overrightarrow{k^1}$ and along $\overrightarrow{k^2}$ directions. Similarly, it can reach HE2 in the three repeated cells along $\overrightarrow{k^1}$, along $\overrightarrow{k^2}$ and along $\overrightarrow{k^1} + \overrightarrow{k^2}$ directions. Finally, OC1 site is surrounded by six CR sites: two CR1, one in the same unit cell and one in the repeated cell along $\overrightarrow{k^1}$ direction; two CR2, one in the same unit cell and one in the repeated cell along $\overrightarrow{k^2}$ direction; two CR3 in the repeated cells along $\overrightarrow{k^1}$ and along $\overrightarrow{k^2}$ directions. We can now start to fill the $\underline{\widetilde{\psi}}(u)$ matrix. For example, the jump OC1→OC2 is associated to the element $\underline{\widetilde{\psi}}(u)_{21}$ which is equal to,

$$\underline{\widetilde{\psi}}(u)_{21} = \frac{n_{oo} \mathrm{w}_{oo}}{\Lambda_o + u} \tag{B.1}$$

where n_{oo} is equal 2 and

$$\Lambda_o = 2 \, \mathrm{w}_{oo} + 6 \, \mathrm{w}_{oh} + 6 \, \mathrm{w}_{oc}. \tag{B.2}$$

The rest of the matrix is determined in a similar manner.

The elements of $\underline{\tilde{p}^*}\left(\overrightarrow{k}\right)$ matrix can be expressed by

$$\underline{\tilde{p}^*}\left(\overrightarrow{k}\right)_{gr} = \frac{\sum_h \delta^h_{gr}}{n_{gr}} \tag{B.3}$$

with

$$\delta^h_{gr} = \exp\left[i\left(m^1_g \, (l^1_g - l^1_r) \, \overrightarrow{k^1} + m^2_g \, (l^2_g - l^2_r) \, \overrightarrow{k^2} + m^3_g \, (l^3_g - l^3_r) \, \overrightarrow{k^3}\right)\right] \tag{B.4}$$

153

where i is the imaginary unit, $(l_g - l_r)$ values are the displacements along the three directions $\overrightarrow{k^1}$, $\overrightarrow{k^2}$ and $\overrightarrow{k^3}$, m_g values denote the unit cell containing the final site g, they can be equal ± 1 or 0 depends if the unit cell is repeated or not along that direction. In the case of OC1$\rightarrow$OC2, the element $\underline{\tilde{p}^*}\left(\overrightarrow{k}\right)_{21}$ is obtained by

$$\underline{\tilde{p}^*}\left(\overrightarrow{k}\right)_{21} = \frac{\delta_{21}^1 + \delta_{21}^2}{2} \tag{B.5}$$

where,

$$\delta_{21}^1 = \exp\left(-im_2^3 \frac{c}{4} \overrightarrow{k^3}\right) \tag{B.6}$$

with m_2^3 equal 0 because OC1 and OC2 are in the same unit cell, while

$$\delta_{21}^2 = \exp\left(im_2^3 \frac{c}{4} \overrightarrow{k^3}\right) \tag{B.7}$$

with m_2^3 equal -1 because OC2 is in the repeated cell below. Following these steps for all O interstitial sites in the unit cell, we built $\underline{\tilde{\psi}}(u)$ and $\underline{\tilde{p}^*}\left(\overrightarrow{k}\right)$ for O,

$$
\underline{\tilde{\psi}}(u) =
\begin{array}{c}
\begin{array}{cccccccccc}
\text{OC1} & \text{OC2} & \text{HE1} & \text{HE2} & \text{CR1} & \text{CR2} & \text{CR3} & \text{CR4} & \text{CR5} & \text{CR6}
\end{array} \\
\begin{array}{c}
\text{OC1} \\ \text{OC2} \\ \text{HE1} \\ \text{HE2} \\ \text{CR1} \\ \text{CR2} \\ \text{CR3} \\ \text{CR4} \\ \text{CR5} \\ \text{CR6}
\end{array}
\left(
\begin{array}{cccccccccc}
0 & \frac{2\,\text{w}_{oo}}{\Lambda_o + u} & \frac{3\,\text{w}_{ho}}{\Lambda_h + u} & \frac{3\,\text{w}_{ho}}{\Lambda_h + u} & \frac{2\,\text{w}_{co}}{\Lambda_c + u} & \frac{2\,\text{w}_{co}}{\Lambda_c + u} & \frac{2\,\text{w}_{co}}{\Lambda_c + u} & 0 & 0 & 0 \\[4pt]
\frac{2\,\text{w}_{oo}}{\Lambda_o + u} & 0 & \frac{3\,\text{w}_{ho}}{\Lambda_h + u} & \frac{3\,\text{w}_{ho}}{\Lambda_h + u} & 0 & 0 & 0 & \frac{2\,\text{w}_{co}}{\Lambda_c + u} & \frac{2\,\text{w}_{co}}{\Lambda_c + u} & \frac{2\,\text{w}_{co}}{\Lambda_c + u} \\[4pt]
\frac{3\,\text{w}_{oh}}{\Lambda_o + u} & \frac{3\,\text{w}_{oh}}{\Lambda_o + u} & 0 & 0 & \frac{\text{w}_{ch}}{\Lambda_c + u} & \frac{\text{w}_{ch}}{\Lambda_c + u} & \frac{\text{w}_{ch}}{\Lambda_c + u} & \frac{\text{w}_{ch}}{\Lambda_c + u} & \frac{\text{w}_{ch}}{\Lambda_c + u} & \frac{\text{w}_{ch}}{\Lambda_c + u} \\[4pt]
\frac{3\,\text{w}_{oh}}{\Lambda_o + u} & \frac{3\,\text{w}_{oh}}{\Lambda_o + u} & 0 & 0 & \frac{\text{w}_{ch}}{\Lambda_c + u} & \frac{\text{w}_{ch}}{\Lambda_c + u} & \frac{\text{w}_{ch}}{\Lambda_c + u} & \frac{\text{w}_{ch}}{\Lambda_c + u} & \frac{\text{w}_{ch}}{\Lambda_c + u} & \frac{\text{w}_{ch}}{\Lambda_c + u} \\[4pt]
\frac{2\,\text{w}_{oc}}{\Lambda_o + u} & 0 & \frac{\text{w}_{hc}}{\Lambda_h + u} & \frac{\text{w}_{hc}}{\Lambda_h + u} & 0 & 0 & 0 & 0 & 0 & 0 \\[4pt]
\frac{2\,\text{w}_{oc}}{\Lambda_o + u} & 0 & \frac{\text{w}_{hc}}{\Lambda_h + u} & \frac{\text{w}_{hc}}{\Lambda_h + u} & 0 & 0 & 0 & 0 & 0 & 0 \\[4pt]
\frac{2\,\text{w}_{oc}}{\Lambda_o + u} & 0 & \frac{\text{w}_{hc}}{\Lambda_h + u} & \frac{\text{w}_{hc}}{\Lambda_h + u} & 0 & 0 & 0 & 0 & 0 & 0 \\[4pt]
0 & \frac{2\,\text{w}_{oc}}{\Lambda_o + u} & \frac{\text{w}_{hc}}{\Lambda_h + u} & \frac{\text{w}_{hc}}{\Lambda_h + u} & 0 & 0 & 0 & 0 & 0 & 0 \\[4pt]
0 & \frac{2\,\text{w}_{oc}}{\Lambda_o + u} & \frac{\text{w}_{hc}}{\Lambda_h + u} & \frac{\text{w}_{hc}}{\Lambda_h + u} & 0 & 0 & 0 & 0 & 0 & 0 \\[4pt]
0 & \frac{2\,\text{w}_{oc}}{\Lambda_o + u} & \frac{\text{w}_{hc}}{\Lambda_h + u} & \frac{\text{w}_{hc}}{\Lambda_h + u} & 0 & 0 & 0 & 0 & 0 & 0
\end{array}
\right),
\end{array}
\tag{B.8}
$$

where

$$\Lambda_o = 2\ \mathrm{w}_{oo} + 6\ \mathrm{w}_{oh} + 6\ \mathrm{w}_{oc};$$

$$\Lambda_h = 6\ \mathrm{w}_{ho} + 6\ \mathrm{w}_{hc};$$
(B.9)

$$\Lambda_c = 2\ \mathrm{w}_{co} + 2\ \mathrm{w}_{ch};$$

$$
\underline{\tilde{p}^*}\left(\overrightarrow{k}\right) =
\begin{array}{c}
\begin{array}{cccccccccc}
\ \ \text{OC1} & \text{OC2} & \text{HE1} & \text{HE2} & \text{CR1} & \text{CR2} & \text{CR3} & \text{CR4} & \text{CR5} & \text{CR6}
\end{array} \\
\begin{array}{c}
\text{OC1} \\ \text{OC2} \\ \text{HE1} \\ \text{HE2} \\ \text{CR1} \\ \text{CR2} \\ \text{CR3} \\ \text{CR4} \\ \text{CR5} \\ \text{CR6}
\end{array}
\left(
\begin{array}{cccccccccc}
0 & A & B & C & D & D & E & 0 & 0 & 0 \\
A & 0 & F & C & 0 & 0 & 0 & D & D & E \\
B & F & 0 & 0 & 1 & 1 & 1 & G & G & G \\
C & C & 0 & 0 & H & H & 1 & H & H & 1 \\
D & 0 & 1 & H & 0 & 0 & 0 & 0 & 0 & 0 \\
D & 0 & 1 & H & 0 & 0 & 0 & 0 & 0 & 0 \\
E & 0 & 1 & 1 & 0 & 0 & 0 & 0 & 0 & 0 \\
0 & D & G & H & 0 & 0 & 0 & 0 & 0 & 0 \\
0 & D & G & H & 0 & 0 & 0 & 0 & 0 & 0 \\
0 & E & G & 1 & 0 & 0 & 0 & 0 & 0 & 0
\end{array}
\right),
\end{array}
$$
(B.10)

where

$$A = \frac{1 + \exp\left(-i\frac{c}{2}\overrightarrow{k^3}\right)}{2};$$

$$B = \frac{1 + \exp\left(-i\frac{2a}{3}\overrightarrow{k^1}\right) + \exp\left(-i\frac{2a}{3}\overrightarrow{k^2}\right)}{3};$$

$$C = \frac{\exp\left(-i\frac{a}{3}\overrightarrow{k^1}\right) + \exp\left(-i\frac{a}{3}\overrightarrow{k^2}\right) + \exp\left[-i\frac{a}{3}\left(\overrightarrow{k^1} + \overrightarrow{k^2}\right)\right]}{3};$$

$$D = \frac{1 + \exp\left(-i\frac{a}{2}\overrightarrow{k^1}\right)}{2};$$

$$E = \frac{\exp\left(-i\frac{a}{2}\overrightarrow{k^1}\right) + \exp\left(-i\frac{a}{2}\overrightarrow{k^2}\right)}{2};$$

$$F = \frac{\exp\left(-i\frac{c}{4}\overrightarrow{k^3}\right) + \exp\left[-i\left(\frac{2a}{3}\overrightarrow{k^1} + \frac{c}{4}\overrightarrow{k^3}\right)\right] + \exp\left[-i\left(\frac{2a}{3}\overrightarrow{k^2} + \frac{c}{4}\overrightarrow{k^3}\right)\right]}{3};$$

$$G = \exp\left(-i\frac{c}{4}\overrightarrow{k^3}\right);$$

$$H = \exp\left(-i\frac{a}{3}\overrightarrow{k^2}\right).$$

(B.11)

B.2   Nitrogen

In the case of N, there are sixteen interstitial sites in the unit cell, notating as in Fig. B.2. The jump frequencies involved are,

- w_{oo}: octahedral→octahedral jump frequency;

- w_{oh}: octahedral→hexahedral jump frequency;

- w_{oc}: octahedral→crowdion jump frequency;

- w_{ob}: octahedral→basal crowdion jump frequency;

- w_{ho}: hexahedral→octahedral jump frequency;

- w_{hc}: hexahedral→crowdion jump frequency;
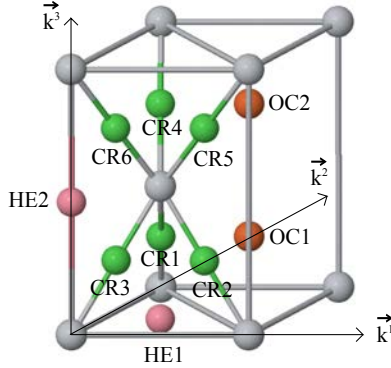
Figure B.2: Notation of N interstitial sites in the unit cell used to build the Laplace transform matrix of waiting time and Fourier transform matrix of displacement.

- w_{co}: crowdion→octahedral jump frequency;

- w_{ch}: crowdion→hexahedral jump frequency;

- w_{cb}: crowdion→basal crowdion jump frequency;

- w_{bo}: basal crowdion→octahedral jump frequency;

- w_{bc}: basal crowdion→crowdion jump frequency.

$\widetilde{\underline{\psi}}(u)$ and $\widetilde{\underline{p^*}}\left(\overrightarrow{k}\right)$ are 16 x 16 matrices and they can be built following the steps explained in case of O.

$$\widetilde{\underline{\psi}}(u) =$$

	OC1	OC2	HE1	HE2	CR1	CR2	CR3	CR4	CR5	CR6	BC1	BC2	BC3	BC4	BC5	BC6
OC1	0	a	b	b	c	c	c	0	0	0	d	d	d	d	d	d
OC2	a	0	b	b	0	0	0	c	c	c	d	d	d	d	d	d
HE1	e	e	0	0	f	f	f	f	f	f	0	0	0	0	0	0
HE2	e	e	0	0	f	f	f	f	f	f	0	0	0	0	0	0
CR1	g	0	i	i	0	0	0	0	0	0	m	0	m	m	0	m
CR2	g	0	i	i	0	0	0	0	0	0	m	m	0	0	m	m
CR3	g	0	i	i	0	0	0	0	0	0	0	m	m	m	m	0
CR4	0	g	i	i	0	0	0	0	0	0	m	0	m	m	0	m
CR5	0	g	i	i	0	0	0	0	0	0	m	m	0	0	m	m
CR6	0	g	i	i	0	0	0	0	0	0	0	m	m	m	m	0
BC1	n	n	0	0	p	p	0	p	p	0	0	0	0	0	0	0
BC2	n	n	0	0	0	p	p	0	p	p	0	0	0	0	0	0
BC3	n	n	0	0	p	0	p	p	0	p	0	0	0	0	0	0
BC4	n	n	0	0	p	0	p	p	0	p	0	0	0	0	0	0
BC5	n	n	0	0	0	p	p	0	p	p	0	0	0	0	0	0
BC6	n	n	0	0	p	p	0	p	p	0	0	0	0	0	0	0

, (B.12)

where

$$a = \frac{2\ \text{w}_{oo}}{\Lambda_o + u};$$

$$b = \frac{3\ \text{w}_{ho}}{\Lambda_h + u};$$

$$c = \frac{2\ \text{w}_{co}}{\Lambda_c + u};$$

$$d = \frac{\text{w}_{bo}}{\Lambda_b + u};$$

$$e = \frac{3\ \text{w}_{oh}}{\Lambda_o + u};$$

$$f = \frac{\text{w}_{ch}}{\Lambda_c + u}; \tag{B.13}$$

$$g = \frac{2\ \text{w}_{oc}}{\Lambda_o + u};$$

$$i = \frac{\text{w}_{hc}}{\Lambda_h + u};$$

$$m = \frac{\text{w}_{bc}}{\Lambda_b + u};$$

$$n = \frac{\text{w}_{ob}}{\Lambda_o + u};$$

$$p = \frac{\text{w}_{bc}}{\Lambda_b + u};$$

with

$$\Lambda_o = 2\ \text{w}_{oo} + 6\ \text{w}_{oh} + 6\ \text{w}_{oc} + 6\ \text{w}_{ob};$$

$$\Lambda_h = 6\ \text{w}_{ho} + 6\ \text{w}_{hc};$$

$$\Lambda_c = 2\ \text{w}_{co} + 2\ \text{w}_{ch} + 4\ \text{w}_{cb}; \tag{B.14}$$

$$\Lambda_b = 2\ \text{w}_{bo} + 4\ \text{w}_{bc}.$$

$$\underline{\tilde{p}^*}\left(\vec{k}\right) = \begin{array}{c} \\ \text{OC1} \\ \text{OC2} \\ \text{HE1} \\ \text{HE2} \\ \text{CR1} \\ \text{CR2} \\ \text{CR3} \\ \text{CR4} \\ \text{CR5} \\ \text{CR6} \\ \text{BC1} \\ \text{BC2} \\ \text{BC3} \\ \text{BC4} \\ \text{BC5} \\ \text{BC6} \end{array}$$

	OC1	OC2	HE1	HE2	CR1	CR2	CR3	CR4	CR5	CR6	BC1	BC2	BC3	BC4	BC5	BC6
OC1	0	A	B	C	D	E	F	0	0	0	1	G	H	1	1	1
OC2	A	0	I	C	0	0	0	D	E	F	1	L	M	1	1	1
HE1	B	I	0	0	1	1	1	N	N	N	0	0	0	0	0	0
HE2	C	C	0	0	H	G	1	H	G	1	0	0	0	0	0	0
CR1	D	0	1	H	0	0	0	0	0	0	1	0	1	1	0	G
CR2	E	0	1	G	0	0	0	0	0	0	1	1	0	0	1	H
CR3	F	0	1	1	0	0	0	0	0	0	0	1	1	H	G	0
CR4	0	D	N	G	0	0	0	0	0	0	N	0	N	1	0	G
CR5	0	E	N	H	0	0	0	0	0	0	N	N	0	0	1	H
CR6	0	F	N	1	0	0	0	0	0	0	0	N	N	H	G	0
BC1	1	1	0	0	1	1	0	N	N	0	0	0	0	0	0	0
BC2	G	L	0	0	0	1	1	0	N	N	0	0	0	0	0	0
BC3	H	M	0	0	1	0	1	N	0	N	0	0	0	0	0	0
BC4	1	1	0	0	1	0	H	1	0	H	0	0	0	0	0	0
BC5	1	1	0	0	0	1	G	0	1	G	0	0	0	0	0	0
BC6	1	1	0	0	G	H	0	G	H	0	0	0	0	0	0	0

$$\text{(B.15)}$$

159

where

$$A = \frac{1 + \exp\left(-i\frac{c}{2}\overrightarrow{k^3}\right)}{2};$$

$$B = \frac{\exp\left(-i\frac{c}{4}\overrightarrow{k^3}\right) + \exp\left[-i\left(\frac{2a}{3}\overrightarrow{k^1} + \frac{c}{4}\overrightarrow{k^3}\right)\right] + \exp\left[-i\left(\frac{2a}{3}\overrightarrow{k^2} + \frac{c}{4}\overrightarrow{k^3}\right)\right]}{3};$$

$$C = \frac{\exp\left(-i\frac{a}{3}\overrightarrow{k^1}\right) + \exp\left(-i\frac{a}{3}\overrightarrow{k^2}\right) + \exp\left[-i\frac{a}{3}\left(\overrightarrow{k^1} + \overrightarrow{k^2}\right)\right]}{3};$$

$$D = \frac{1 + \exp\left(-i\frac{a}{2}\overrightarrow{k^1}\right)}{2};$$

$$E = \frac{1 + \exp\left(-i\frac{a}{2}\overrightarrow{k^2}\right)}{2};$$

$$F = \frac{\exp\left(-i\frac{a}{2}\overrightarrow{k^1}\right) + \exp\left(-i\frac{a}{2}\overrightarrow{k^2}\right)}{2};$$

$$G = \exp\left(-i\frac{a}{3}\overrightarrow{k^1}\right)$$

$$H = \exp\left(-i\frac{a}{3}\overrightarrow{k^2}\right)$$

$$I = \frac{1 + \exp\left(-i\frac{2a}{3}\overrightarrow{k^1}\right) + \exp\left(-i\frac{2a}{3}\overrightarrow{k^2}\right)}{3};$$

$$L = \exp\left[-i\left(\frac{a}{3}\overrightarrow{k^1} + \frac{c}{4}\overrightarrow{k^3}\right)\right]$$

$$M = \exp\left[-i\left(\frac{a}{3}\overrightarrow{k^2} + \frac{c}{4}\overrightarrow{k^3}\right)\right]$$

$$N = \exp\left(-i\frac{c}{4}\overrightarrow{k^3}\right).$$

(B.16)

B.3 Carbon

In the case of C, there are fourteen interstitial sites in the unit cell, notating as in Fig. B.3.
The jump frequencies involved are,

- w_{oo}: octahedral→octahedral jump frequency;

- w_{oc}: octahedral→crowdion jump frequency;

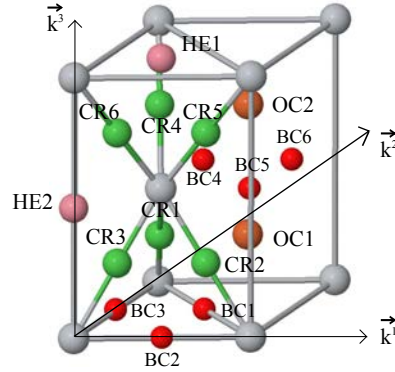- w_{ob}: octahedral→basal crowdion jump frequency;

160
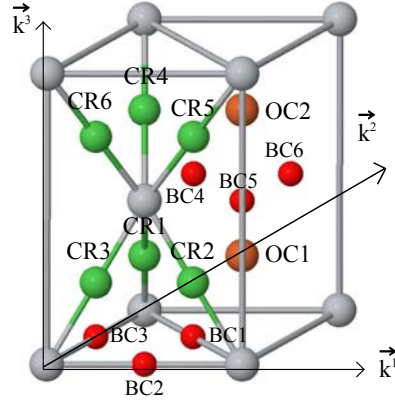
Figure B.3: Notation of C interstitial sites in the unit cell used to build the Laplace transform matrix of waiting time and Fourier transform matrix of displacement.

- w_{co}: crowdion→octahedral jump frequency;

- w_{cb}: crowdion→basal crowdion jump frequency;

- w_{bo}: basal crowdion→octahedral jump frequency;

- w_{bc}: basal crowdion→crowdion jump frequency.

$\underaccent{\tilde}{\underline{\psi}}(u)$ and $\underline{\tilde{p}^*}\left(\vec{k}\right)$ are 14 x 14 matrices and they can be built following the steps explained in case of O.

$$
\underaccent{\tilde}{\underline{\psi}}(u) =
\begin{array}{c|cccccccccccccc}
 & \text{OC1} & \text{OC2} & \text{CR1} & \text{CR2} & \text{CR3} & \text{CR4} & \text{CR5} & \text{CR6} & \text{BC1} & \text{BC2} & \text{BC3} & \text{BC4} & \text{BC5} & \text{BC6} \\
\hline
\text{OC1} & 0 & \frac{2\,w_{oo}}{\Lambda_o+u} & \frac{2\,w_{co}}{\Lambda_c+u} & \frac{2\,w_{co}}{\Lambda_c+u} & \frac{2\,w_{co}}{\Lambda_c+u} & 0 & 0 & 0 & \frac{w_{bo}}{\Lambda_b+u} & \frac{w_{bo}}{\Lambda_b+u} & \frac{w_{bo}}{\Lambda_b+u} & \frac{w_{bo}}{\Lambda_b+u} & \frac{w_{bo}}{\Lambda_b+u} & \frac{w_{bo}}{\Lambda_b+u} \\
\text{OC2} & \frac{2\,w_{oo}}{\Lambda_o+u} & 0 & 0 & 0 & 0 & \frac{2\,w_{co}}{\Lambda_c+u} & \frac{2\,w_{co}}{\Lambda_c+u} & \frac{2\,w_{co}}{\Lambda_c+u} & \frac{w_{bo}}{\Lambda_b+u} & \frac{w_{bo}}{\Lambda_b+u} & \frac{w_{bo}}{\Lambda_b+u} & \frac{w_{bo}}{\Lambda_b+u} & \frac{w_{bo}}{\Lambda_b+u} & \frac{w_{bo}}{\Lambda_b+u} \\
\text{CR1} & \frac{2\,w_{oc}}{\Lambda_o+u} & 0 & 0 & 0 & 0 & 0 & 0 & 0 & \frac{w_{bc}}{\Lambda_b+u} & 0 & \frac{w_{bc}}{\Lambda_b+u} & \frac{w_{bc}}{\Lambda_b+u} & 0 & \frac{w_{bc}}{\Lambda_b+u} \\
\text{CR2} & \frac{2\,w_{oc}}{\Lambda_o+u} & 0 & 0 & 0 & 0 & 0 & 0 & 0 & \frac{w_{bc}}{\Lambda_b+u} & \frac{w_{bc}}{\Lambda_b+u} & 0 & 0 & \frac{w_{bc}}{\Lambda_b+u} & \frac{w_{bc}}{\Lambda_b+u} \\
\text{CR3} & \frac{2\,w_{oc}}{\Lambda_o+u} & 0 & 0 & 0 & 0 & 0 & 0 & 0 & 0 & \frac{w_{bc}}{\Lambda_b+u} & \frac{w_{bc}}{\Lambda_b+u} & \frac{w_{bc}}{\Lambda_b+u} & \frac{w_{bc}}{\Lambda_b+u} & 0 \\
\text{CR4} & 0 & \frac{2\,w_{oc}}{\Lambda_o+u} & 0 & 0 & 0 & 0 & 0 & 0 & \frac{w_{bc}}{\Lambda_b+u} & 0 & \frac{w_{bc}}{\Lambda_b+u} & \frac{w_{bc}}{\Lambda_b+u} & 0 & \frac{w_{bc}}{\Lambda_b+u} \\
\text{CR5} & 0 & \frac{2\,w_{oc}}{\Lambda_o+u} & 0 & 0 & 0 & 0 & 0 & 0 & \frac{w_{bc}}{\Lambda_b+u} & \frac{w_{bc}}{\Lambda_b+u} & 0 & 0 & \frac{w_{bc}}{\Lambda_b+u} & \frac{w_{bc}}{\Lambda_b+u} \\
\text{CR6} & 0 & \frac{2\,w_{oc}}{\Lambda_o+u} & 0 & 0 & 0 & 0 & 0 & 0 & 0 & \frac{w_{bc}}{\Lambda_b+u} & \frac{w_{bc}}{\Lambda_b+u} & \frac{w_{bc}}{\Lambda_b+u} & \frac{w_{bc}}{\Lambda_b+u} & 0 \\
\text{BC1} & \frac{w_{ob}}{\Lambda_o+u} & \frac{w_{ob}}{\Lambda_o+u} & \frac{w_{bc}}{\Lambda_b+u} & \frac{w_{bc}}{\Lambda_b+u} & 0 & \frac{w_{bc}}{\Lambda_b+u} & \frac{w_{bc}}{\Lambda_b+u} & 0 & 0 & 0 & 0 & 0 & 0 & 0 \\
\text{BC2} & \frac{w_{ob}}{\Lambda_o+u} & \frac{w_{ob}}{\Lambda_o+u} & 0 & \frac{w_{bc}}{\Lambda_b+u} & \frac{w_{bc}}{\Lambda_b+u} & 0 & \frac{w_{bc}}{\Lambda_b+u} & \frac{w_{bc}}{\Lambda_b+u} & 0 & 0 & 0 & 0 & 0 & 0 \\
\text{BC3} & \frac{w_{ob}}{\Lambda_o+u} & \frac{w_{ob}}{\Lambda_o+u} & \frac{w_{bc}}{\Lambda_b+u} & 0 & \frac{w_{bc}}{\Lambda_b+u} & \frac{w_{bc}}{\Lambda_b+u} & 0 & \frac{w_{bc}}{\Lambda_b+u} & 0 & 0 & 0 & 0 & 0 & 0 \\
\text{BC4} & \frac{w_{ob}}{\Lambda_o+u} & \frac{w_{ob}}{\Lambda_o+u} & \frac{w_{bc}}{\Lambda_b+u} & 0 & \frac{w_{bc}}{\Lambda_b+u} & \frac{w_{bc}}{\Lambda_b+u} & 0 & \frac{w_{bc}}{\Lambda_b+u} & 0 & 0 & 0 & 0 & 0 & 0 \\
\text{BC5} & \frac{w_{ob}}{\Lambda_o+u} & \frac{w_{ob}}{\Lambda_o+u} & 0 & \frac{w_{bc}}{\Lambda_b+u} & \frac{w_{bc}}{\Lambda_b+u} & 0 & \frac{w_{bc}}{\Lambda_b+u} & \frac{w_{bc}}{\Lambda_b+u} & 0 & 0 & 0 & 0 & 0 & 0 \\
\text{BC6} & \frac{w_{ob}}{\Lambda_o+u} & \frac{w_{ob}}{\Lambda_o+u} & \frac{w_{bc}}{\Lambda_b+u} & \frac{w_{bc}}{\Lambda_b+u} & 0 & \frac{w_{bc}}{\Lambda_b+u} & \frac{w_{bc}}{\Lambda_b+u} & 0 & 0 & 0 & 0 & 0 & 0 & 0 \\
\end{array}
, \tag{B.17}
$$

where

$$\Lambda_o = 2\,\mathrm{w}_{oo} + 6\,\mathrm{w}_{oc} + 6\,\mathrm{w}_{ob};$$
$$\Lambda_c = 2\,\mathrm{w}_{co} + 4\,\mathrm{w}_{cb};$$
$$\Lambda_b = 2\,\mathrm{w}_{bc} + 4\,\mathrm{w}_{bc}. \tag{B.18}$$

$$\underline{\tilde{p}^*}\left(\vec{k}\right) =$$

	OC1	OC2	CR1	CR2	CR3	CR4	CR5	CR6	BC1	BC2	BC3	BC4	BC5	BC6
OC1	0	A	D	E	F	0	0	0	1	G	H	1	1	1
OC2	A	0	0	0	0	D	E	F	1	L	M	1	1	1
CR1	D	0	0	0	0	0	0	0	1	0	1	1	0	G
CR2	E	0	0	0	0	0	0	0	1	1	0	0	1	H
CR3	F	0	0	0	0	0	0	0	0	1	1	H	G	0
CR4	0	D	0	0	0	0	0	0	N	0	N	1	0	G
CR5	0	E	0	0	0	0	0	0	N	N	0	0	1	H
CR6	0	F	0	0	0	0	0	0	0	N	N	H	G	0
BC1	1	1	1	1	0	N	N	0	0	0	0	0	0	0
BC2	G	L	0	1	1	0	N	N	0	0	0	0	0	0
BC3	H	M	1	0	1	N	0	N	0	0	0	0	0	0
BC4	1	1	1	0	H	1	0	H	0	0	0	0	0	0
BC5	1	1	0	1	G	0	1	G	0	0	0	0	0	0
BC6	1	1	G	H	0	G	H	0	0	0	0	0	0	0

$$, \tag{B.19}$$

where

$$A = \frac{1 + \exp\left(-i\frac{c}{2}\overrightarrow{k^3}\right)}{2};$$
$$D = \frac{1 + \exp\left(-i\frac{a}{2}\overrightarrow{k^1}\right)}{2};$$
$$E = \frac{1 + \exp\left(-i\frac{a}{2}\overrightarrow{k^2}\right)}{2};$$
$$F = \frac{\exp\left(-i\frac{a}{2}\overrightarrow{k^1}\right) + \exp\left(-i\frac{a}{2}\overrightarrow{k^2}\right)}{2};$$
$$G = \exp\left(-i\frac{a}{3}\overrightarrow{k^1}\right)$$
$$H = \exp\left(-i\frac{a}{3}\overrightarrow{k^2}\right)$$
$$L = \exp\left[-i\left(\frac{a}{3}\overrightarrow{k^1} + \frac{c}{4}\overrightarrow{k^3}\right)\right]$$
$$M = \exp\left[-i\left(\frac{a}{3}\overrightarrow{k^2} + \frac{c}{4}\overrightarrow{k^3}\right)\right]$$
$$N = \exp\left(-i\frac{c}{4}\overrightarrow{k^3}\right)$$

$$\tag{B.20}$$

Bibliography

[1] C. Leyens and M. Peters. *Titanium and Titanium Alloys*. Wiley Online Library, 2003.

[2] K. E. Thiehsen, M. E. Kassner, D. R. Hiatt, and B. M. Bristow. Some factors affecting the creep properties of Ti 6242. *Titanium'92: Science and Technology*, page 1, 1993.

[3] S. R. Seagle, G. S. Hall, and H. B. Bomberger. High temperature properties of Ti–6Al–2Sn–4Zr–2Mo–0.09 Si. Technical report, RMI Co., Niles, OH, 1975.

[4] A T. K. Assadi, H. M. Flower, and D. R. F. West. Creep resistance of certain alloys of the Ti–AI–Zr–Mo–Si system. *Metals Technology*, 6(1):16–23, 1979.

[5] K. E. Thiehsen, M. E. Kassner, J. Pollard, D. R. Hiatt, and B. M. Bristow. The effect of nickel, chromium, and primary alpha phase on the creep behavior of Ti 6242Si. *Metallurgical Transactions A*, 24(8):1819–1826, 1993.

[6] P. J. Bania and J. A. Hall. Creep studies of Ti-6242-Si alloy. *Titanium: Science and Technology*, pages 2371–2378, 1985.

[7] G. B. Viswanathan, S. Karthikeyan, R. W. Hayes, and M. J. Mills. Creep behaviour of Ti-6Al-2Sn-4Zr-2Mo: II. Mechanisms of deformation. *Acta Materialia*, 50(20):4965–4980, 2002.

[8] M. Bourgeois, X. Feaugas, F. De Mestral, T. Chauveau, and M. Clavel. Creep mechanisms in Ti-6246 alloy at 773 K. *Titanium'95: Science and Technology*, pages 1083–1090, 1996.

[9] M. Köppers, C. Herzig, M. Friesel, and Y. Mishin. Intrinsic self-diffusion and substitutional Al diffusion in α-Ti. *Acta Materialia*, 45(10):4181–4191, 1997.

[10] M. Köppers, D. Derdau, M. Friesel, and C. Herzig. Self-diffusion and group III (Al, Ga, In) solute diffusion in hcp titanium. In *Defect and Diffusion Forum*, volume 143, pages 43–48. Trans Tech Publ, 1997.

[11] T. Noda, M. Okabe, S. Isobe, and M. Sayashi. Silicide precipitation strengthened TiAl. *Materials Science and Engineering: A*, 192:774–779, 1995.

[12] Y. Imbert. Creep resistance and embrittlement of a Ti-6% Al-5% Zr-1% W-0.4% Si alloy. *Journal of the Less Common Metals*, 37(1):71–89, 1974.

[13] M. Döner and H. Conrad. Deformation mechanisms in commercial Ti-5Al-2.5 Sn (0.5 At. pct Oeq) alloy at intermediate and high temperatures (0.3-0.6 tm). *Metallurgical Transactions A*, 6(4):853–861, 1975.

[14] A. K. Nag, K. V. U. Praveen, and V. Singh. Effect of heat treatment on tensile behaviour of Ti–6Al–5Zr–0.5 Mo–0.25 Si alloy. *Bulletin of Materials Science*, 29(2):147–154, 2006.

[15] M. R. Winstone, R. D. Rawlings, and D. R. F. West. Dynamic strain ageing in some titanium-silicon alloys. *Journal of the Less Common Metals*, 31(1):143–150, 1973.

[16] H. Hofmann, G. Frommeyer, and C. Derder. Creep mechanisms in particle strengthened α-titanium–Ti 2 Co alloys. *Materials Science and Engineering: A*, 245(1):127–134, 1998.

[17] N. E. Paton and M. W. Mahoney. Creep of titanium-silicon alloys. *Metallurgical Transactions A*, 7(11):1685–1694, 1976.

[18] H. M. Flower, P. R. Swann, and D. R. F. West. Silicide precipitation in the Ti-Zr-Al-Si system. *Metallurgical and Materials Transactions B*, 2(12):3289–3297, 1971.

[19] N. Singh and V. Singh. Effect of temperature on tensile properties of near-α alloy Timetal 834. *Materials Science and Engineering: A*, 485(1):130–139, 2008.

[20] D. F. Neal and S. P. Fox. The influence of silicon and silicides on the properties of near-alpha titanium alloys. *Titanium'92: Science and technology*, pages 287–294, 1993.

[21] P. Kofstad. High-temperature oxidation of titanium. *Journal of the Less Common Metals*, 12(6):449–464, 1967.

[22] H. Conrad. Effect of interstitial solutes on the strength and ductility of titanium. *Progress in Materials Science*, 26(2):123–403, 1981.

[23] F. L. Bregolin, M. Behar, and F. Dyment. Diffusion study of ^{18}O implanted into α-Ti using the nuclear resonance technique. *Applied Physics A*, 86(4):481–484, 2007.

[24] F. L. Bregolin, M. Behar, and F. Dyment. Diffusion study of ^{15}N implanted into α-Ti using the nuclear resonance technique. *Applied Physics A*, 90(2):347–349, 2008.

[25] M. I. De Barros, D. Rats, L. Vandenbulcke, and G. Farges. Influence of internal diffusion barriers on carbon diffusion in pure titanium and Ti–6Al–4V during diamond deposition. *Diamond and Related Materials*, 8(6):1022–1032, 1999.

[26] C. Minkwitz and C. Herzig. Diffusion of ^{14}C in single and polycrystalline α-titanium. In *Defect and Diffusion Forum*, volume 143, pages 61–66. Trans Tech Publ, 1997.

[27] K. S. Chan, M. Koike, R. L. Mason, and T. Okabe. Fatigue life of titanium alloys fabricated by additive layer manufacturing techniques for dental implants. *Metallurgical and Materials Transactions A*, 44(2):1010–1022, 2013.

[28] R. W. Evans, R. J. Hull, and B. Wilshire. The effects of alpha-case formation on the creep fracture properties of the high-temperature titanium alloy IMI834. *Journal of Materials Processing Technology*, 56(1):492–501, 1996.

[29] A. Fitzner, J. Q. da Fonseca, M. Preuss, and M. Thomas. The effect of Aluminium on deformation by twinning in alpha titanium. *A. Khan, Analytical, Computational, and Experimental Inelasticity in Deformable Solids, NEAT*, page 4, 2013.

[30] P. Kwasniak, M. Muzyk, H. Garbacz, and K. J. Kurzydlowski. Influence of oxygen content on the mechanical properties of hexagonal Ti–First principles calculations. *Materials Science and Engineering: A*, 590:74–79, 2014.

[31] H. R. Ogden and R. I. Jaffee. The effects of carbon, oxygen, and nitrogen on the mechanical properties of titanium and titanium alloys. Technical Report TML-20, Battelle Memorial Inst. Titanium Metallurgical Lab., Columbus, Ohio, 1955.

[32] L. Zhu, Q.-M. Hu, R. Yang, and G. J. Ackland. Atomic-scale modeling of the dynamics of titanium oxidation. *The Journal of Physical Chemistry C*, 116(45):24201–24205, 2012.

[33] H. Mishra, D. V. V. Satyanarayana, T. K. Nandy, and P. K. Sagar. Effect of trace impurities on the creep behavior of a near α titanium alloy. *Scripta Materialia*, 59(6):591–594, 2008.

[34] R. W. Hayes, G. B. Viswanathan, and M. J. Mills. Creep behavior of Ti–6Al–2Sn–4Zr–2Mo: I. The effect of nickel on creep deformation and microstructure. *Acta Materialia*, 50(20):4953–4963, 2002.

[35] H. Mishra, P. Ghosal, T. K. Nandy, and P. K. Sagar. Influence of Fe and Ni on creep of near α-Ti alloy IMI834. *Materials Science and Engineering: A*, 399(1):222–231, 2005.

[36] P. A. Russo, J. R. Wood, R. N. Brosius, S. W. Marcinko, and S. R. Giangiordano. Influence of Ni and Fe on the creep of beta annealed Ti-6242S. *Titanium'95: Science and Technology*, pages 1075–1082, 1996.

[37] J. H. Moon, S. Karthikeyan, B. M. Morrow, S. P. Fox, and M. J. Mills. High-temperature creep behavior and microstructure analysis of binary Ti–6Al alloys with trace amounts of Ni. *Materials Science and Engineering: A*, 510:35–41, 2009.

[38] H. Nakajima and M. Koiwa. Diffusion of iron, cobalt and nickel in alpha-titanium. *Titanium–Science and Technology*, 3:1759–1766, 1984.

[39] H. Nakajima, M. Koiwa, Y. Minonishi, and S. Ono. Diffusion of cobalt in single crystal α-titanium. *Transactions of the Japan Institute of Metals*, 24(10):655–660, 1983.

[40] H. Nakajima, M. Koiwa, and S. Ono. Diffusion of iron in single crystal α-titanium. *Scripta Metallurgica*, 17(12):1431–1434, 1983.

166

[41] R. A. Pérez, F. Dyment, G. G. Bermúdez, D. Abriola, and M. Behar. Diffusion of Ta in α-Ti. *Applied Physics A*, 76(2):247–250, 2003.

[42] F. C. Frank and D. Turnbull. Mechanism of diffusion of copper in germanium. *Physical Review*, 104(3):617, 1956.

[43] G. M. Hood and R. J. Schultz. Tracer diffusion in α-Zr. *Acta Metallurgica*, 22(4):459–464, 1974.

[44] Y. Yoshida, M. Sugimoto, D. Tuppinger, and G. Vogl. Search for Anomalously Fast Diffusion in alpha-Ti and alpha-Zr with Mössbauer Spectroscopy. In *Defect and Diffusion Forum*, volume 66, pages 347–352. Trans Tech Publ, 1991.

[45] M. D. Sturge. A Note on the Theory of Diffusion of Copper in Germanium. *Proceedings of the Physical Society*, 73(2):297–306, 1959.

[46] J. W. Miller. Diffusion of interstitial solute-vacancy pairs in a dilute alloy. *Physical Review*, 188(3):1074, 1969.

[47] R. C. Pasianot, R. A. Pérez, V. P. Ramunni, and M. Weissmann. Ab initio approach to the effect of Fe on the diffusion in hcp Zr II: The energy barriers. *Journal of Nuclear Materials*, 392(1):100–104, 2009.

[48] S. Ganeshan, L. G. Hector, and Z.-K. Liu. First-principles study of self-diffusion in hcp Mg and Zn. *Computational Materials Science*, 50(2):301–307, 2010.

[49] S. Ganeshan, L. G. Hector, and Z.-K. Liu. First-principles calculations of impurity diffusion coefficients in dilute Mg alloys using the 8-frequency model. *Acta Materialia*, 59(8):3214–3228, 2011.

[50] H. H. Wu and D. R. Trinkle. Direct Diffusion through interpenetrating Networks: Oxygen in titanium. *Physical Review Letters*, 107(4):045504, 2011.

[51] P. B. Ghate. Screened Interaction Model for Impurity Diffusion in Zinc. *Physical Review*, 133(4A):A1167–A1175, 1964.

[52] U. Landman and M. Shlesinger. Stochastic theory of multistate diffusion in perfect and defective systems. I. Mathematical formalism. *Physical Review B*, 19(12):6207–6219, June 1979.

[53] U. Landman and M. Shlesinger. Stochastic theory of multistate diffusion in perfect and defective systems. II. Case studies. *Physical Review B*, 19(12):6220–6237, June 1979.

[54] H. Z. Fang, S. L. Shang, Y. Wang, Z.-K. Liu, D. Alfonso, D. E. Alman, Y. K. Shin, C. Y. Zou, A. C. T. van Duin, Y. K. Lei, and G. F. Wang. First-principles studies on vacancy-modified interstitial diffusion mechanism of oxygen in nickel, associated with large-scale atomic simulation techniques. *Journal of Applied Physics*, 115(4):043501, 2014.

[55] W. M. Young and E. W. Elcock. Monte Carlo studies of vacancy migration in binary ordered alloys: I. *Proceedings of the Physical Society*, 89(3):735, 1966.

[56] W. Kohn and L. J. Sham. Self-Consistent Equations Including Exchange and Correlation Effects. *Physical Review*, 140(4A):A1133–A1138, 1965.

[57] P. Hohenberg and W. Kohn. Inhomogeneous Electron Gas. *Physical Review*, 136(3B):B864–B871, 1964.

[58] G. Kresse, M. Marsman, and J. Fürthmuller. VASP the Guide, 2010.

[59] G. Kresse and J. Furhmüller. Software VASP, Vienna (1999); G. Kresse, J. Hafner. *Physical Review B*, 47:R558, 1993.

[60] G. Kresse and J. Furthmüller. Efficiency of ab-initio total energy calculations for metals and semiconductors using a plane-wave basis set. *Computational Materials Science*, 6(1):15 – 50, 1996.

[61] G. Kresse and J. Furthmüller. Efficient iterative schemes for *ab initio* total-energy calculations using a plane-wave basis set. *Physical Review B*, 54:11169–11186, Oct 1996.

[62] H. Jónsson, G. Mills, and K. W. Jacobsen. Nudged elastic band method for finding minimum energy paths of transitions, 1998.

[63] G. Henkelman, B. P. Uberuaga, and H. Jónsson. A climbing image nudged elastic band method for finding saddle points and minimum energy paths. *The Journal of Chemical Physics*, 113(22):9901–9904, 2000.

[64] G. Henkelman and H. Jónsson. Improved tangent estimate in the nudged elastic band method for finding minimum energy paths and saddle points. *The Journal of Chemical Physics*, 113(22):9978–9985, 2000.

[65] W. L. Finlay and J. A. Snyder. Effects of three interstitial solutes (nitrogen, oxygen, and carbon) on the mechanical properties of high-purity, alpha titanium. *Journal of Metals*, 188, 1950.

[66] M. J. Donachie. *Titanium: a technical guide*. ASM international, 2000.

[67] Y. B. Chun, S.-H. Yu, S. L. Semiatin, and S.-K. Hwang. Effect of deformation twinning on microstructure and texture evolution during cold rolling of CP-titanium. *Materials Science and Engineering: A*, 398(1):209–219, 2005.

[68] I. Weiss and S. L. Semiatin. Thermomechanical processing of alpha titanium alloysan overview. *Materials Science and Engineering: A*, 263(2):243–256, 1999.

[69] S. Hardt, H. J. Maier, and H.-J. Christ. High-temperature fatigue damage mechanisms in near-α titanium alloy IMI 834. *International Journal of Fatigue*, 21(8):779–789, 1999.

[70] J. H. Kim, S. L. Semiatin, and C. S. Lee. Constitutive analysis of the high-temperature deformation of Ti6Al4V with a transformed microstructure. *Acta Materialia*, 51(18):5613–5626, 2003.

[71] J. I. Qazi, H. J. Rack, and B. Marquardt. High-strength metastable beta-titanium alloys for biomedical applications. *JOM*, 56(11):49–51, 2004.

[72] C. Hammond and J. Nutting. The physical metallurgy of superalloys and titanium alloys. *Metal Science*, 11(10):474–490, 1977.

[73] Z. X. Guo and T. N. Baker. Microstructural modification and analysis of an IMI 685 titanium alloy. *Titanium'92: Science and Technology*, pages 455–462, 1992.

[74] P. Wanjara, M. Jahazi, H. Monajati, and S. Yue. Influence of thermomechanical processing on microstructural evolution in near-α alloy IMI834. *Materials Science and Engineering: A*, 416(1):300–311, 2006.

[75] J. R. Wood, P. A. Russo, M. F. Welter, and E. M. Crist. Thermomechanical processing and heat treatment of Ti6Al2Sn2Zr2Cr2MoSi for structural applications. *Materials Science and Engineering: A*, 243(1):109–118, 1998.

[76] H. R. Phelps and J. R. Wood. Correlation of mechanical properties and microstructures of Ti-6 Al-2 Sn-2 Zr-2 Mo-2 Cr-0. 25 S titanium alloy. *Titanium'92: Science and Technology*, pages 193–199, 1993.

[77] L. Qi, T. Tsuru, M. Asta, and D. Chrzan. Interactions between Oxygen Interstitial and <a>-Type Screw Dislocations in alpha-Titanium. *arXiv preprint arXiv:1502.05129*, 2015.

[78] M. Es-Souni. Primary, secondary and anelastic creep of a high temperature near α-Ti alloy Ti6242Si. *Materials Characterization*, 45(2):153–164, 2000.

[79] M. Es-Souni. Creep behaviour and creep microstructures of a high-temperature titanium alloy Ti–5.8 Al–4.0 Sn–3.5 Zr–0.7 Nb–0.35 Si–0.06 C (Timetal 834): part I. Primary and steady-state creep. *Materials Characterization*, 46(5):365–379, 2001.

[80] C. Quesne, C. Duong, F. Charpentier, J. F. Friès, and P. Lacombe. A comparative study of creep resistance and thermal stability of titanium alloys 685 and 6242 in air and in vacuum. *Journal of the Less Common Metals*, 68(2):133–142, 1979.

[81] S.-Y. Sung and Y.-J. Kim. Alpha-case formation mechanism on titanium investment castings. *Materials Science and Engineering: A*, 405(1):173–177, 2005.

[82] B. J. Choi, S. Lee, and Y. J. Kim. Influence of TiO2 on alpha case reaction of Al2O3

mould in Ti investment casting. *Materials Science and Technology*, 29(12):1453–1462, 2013.

[83] A. M. Bauristhene, K. Mutombo, and W. E. Stumpf. Alpha case formation mechanism in Ti-6Al-4V alloy investment castings using YFSZ shell moulds. *Journal of the Southern African Institute of Mining and Metallurgy*, 113(4):357–361, 2013.

[84] S. N. Patankar and Y. T. Kwang and T. M. Jen. Alpha casing and superplastic behavior of Ti-6Al-4V. *Journal of Materials Processing Technology*, 112(1):24–28, 2001.

[85] A. H. Cottrell. *Dislocations and plastic flow in crystals.* Clarendon Press, 1965.

[86] A. P. Woodfield and M. H. Loretto. Structural determination of silicides in Ti 5331S. *Scripta Metallurgica*, 21(2):229–232, 1987.

[87] C. L. Hale, W. S. Rollings, and M. L. Weaver. Activation energy calculations for discontinuous yielding in Inconel 718SPF. *Materials Science and Engineering: A*, 300(1):153–164, 2001.

[88] K. Peng, W. Chen, and K. Qian. Study on dynamic strain aging phenomenon of 3004 aluminum alloy. *Materials Science and Engineering: A*, 415(1):53–58, 2006.

[89] Q. M. Hu, D. S. Xu, and D. Li. First-principles investigations of the solute–vacancy interaction energy and its effect on the creep properties of α-titanium. *Philosophical Magazine A*, 81(12):2809–2821, 2001.

[90] S. Zaefferer. A study of active deformation systems in titanium alloys: dependence on alloy composition and correlation with deformation texture. *Materials Science and Engineering: A*, 344(1):20–30, 2003.

[91] Q. Yu, L. Qi, T. Tsuru, R. Traylor, D. Rugg, J. W. Morris, M. Asta, D. C. Chrzan, and A. M. Minor. Origin of dramatic oxygen solute strengthening effect in titanium. *Science*, 347(6222):635–639, 2015.

[92] K. A. Chao and G. S. Ansell. Electronic Effect on the Solubility of Interstitials in Transition Metal Alloys. *Journal of Applied Physics*, 41(1):417–421, 1970.

[93] S. Gollapudi, D. V. V. Satyanarayana, C. Phaniraj, and T. K. Nandy. Transient creep in titanium alloys: Effect of stress, temperature and trace element concentration. *Materials Science and Engineering: A*, pages 510–518, 2012.

[94] W. K. Warburton. Modified Model of Diffusion by Interstitial-Vacancy Pairs. *Physical Review B*, 7(4):1341–1352, 1973.

[95] C. M. Libanati and F. Dyment. Autodifusion de titanio alfa. *Acta Metallurgica*, 11(11):1263–1268, November 1963.

[96] N. E. W. De Reca and C. M. Libanati. Autodifusion de titanio beta y hafnio beta. *Acta Metallurgica*, 16(10):1297–1305, 1968.

[97] F. Dyment and C.M. Libanati. Self-diffusion of Ti, Zr, and Hf in their hcp phases, and diffusion of Nb95 in hcp Zr. *Journal of Materials Science*, 3(4):349–359, 1968.

[98] G. M. Hood, H. Zou, R. J. Schultz, N. Matsuura, J. A. Roy, and J. A. Jackman. Self-and Hf Diffusion in α-Zr and in Dilute, Fe-Free, Zr (Ti) and Zr (Nb) Alloys. In *Defect and Diffusion Forum*, volume 143, pages 49–54. Trans Tech Publ, 1997.

[99] G. Kidson and J. McGurn. Self-diffusion in body-centered cubic zirconium. *Canadian Journal of Physics*, 39(8):1146–1157, 1961.

[100] J. Räisänen, A. Anttila, and J. Keinonen. Diffusion of aluminum in ion-implanted α-Ti. *Journal of Applied Physics*, 57(2):613–614, 1985.

[101] J. Räisänen and J. Keinonen. Annealing behavior of Si in ion-implanted α-Ti. *Applied Physics Letters*, 49(13):773–775, 1986.

[102] M. Behar, J. H. R. dos Santos, F. Bernardi, and F. Dyment. Diffusion of Ga Implanted into α-Ti Studied by Means of the Rutherford Backscattering Technique. In *Defect and Diffusion Forum*, volume 213, pages 1–18. Trans Tech Publ, 2003.

[103] R. A. Pérez, F. Dyment, and M. Behar. Diffusion of Sn in different purity α-Ti. *Materials Letters*, 57(18):2670–2674, 2003.

[104] R. A. Pérez, M. R. F. Soares, M. Behar, and F. Dyment. Indium diffusion study in α-titanium. *Journal of Nuclear Materials*, 249(1):52–57, 1997.

[105] W. K. Warburton. Diffusion of Pb and Hg in Dilute Pb: Hg Alloys. *Physical Review B*, 7(4):1330–1341, 1973.

[106] M. Krčmar, C. L. Fu, A. Janotti, and R. C. Reed. Diffusion rates of 3d transition metal solutes in nickel by first-principles calculations. *Acta Materialia*, 53(8):2369–2376, 2005.

[107] S. Huang, D. L. Worthington, M. Asta, V. Ozolins, G. Ghosh, and P. K. Liaw. Calculation of impurity diffusivities in α-Fe using first-principles methods. *Acta Materialia*, 58(6):1982–1993, 2010.

[108] A. B. Lidiard. CXXXIII. Impurity diffusion in crystals (mainly ionic crystals with the sodium chloride structure). *The London, Edinburgh, and Dublin Philosophical Magazine and Journal of Science*, 46(382):1218–1237, 1955.

[109] J. R. Manning. Correlation Factors for Impurity Diffusion. bcc, Diamond, and fcc Structures. *Physical Review*, 136(6A):A1758–A1766, 1964.

[110] A. O'Hara and A. A. Demkov. Oxygen and nitrogen diffusion in α-hafnium from first principles. *Applied Physics Letters*, 104(21):211909, May 2014.

[111] S. Ulam, R. D. Richtmyer, and J. Von Neumann. Statistical methods in neutron diffusion. *LAMS-551, Los Alamos National Laboratory*, pages 1–22, 1947.

[112] A. Van der Ven, G. Ceder, M. Asta, and P. D. Tepesch. First-principles theory of ionic diffusion with nondilute carriers. *Physical Review B*, 64(18):184307, 2001.

[113] Titanium Metals Corporation. http://www.timet.com/.

[114] ET UK LTD. http://www.etltd.co.uk/titanium-ti.html.

[115] Stainless Steel World. http://www.stainless-steel-world.net/.

[116] R. Boyer, G. Welsch, and E. W. Collings, editors. *Materials properties handbook: titanium alloys*. ASM International, fourth edition, 1994.

[117] J. I. Qazi, B. Marquardt, L. F. Allard, and H. J. Rack. Phase transformations in Ti–35Nb–7Zr–5Ta–(0.06–0.68) O alloys. *Materials Science and Engineering: C*, 25(3):389–397, 2005.

[118] N. Argaman and G. Makov. Density functional theory: An introduction. *American Journal of Physics*, 68(1):69–79, 2000.

[119] J. E. Jaffe, R. Pandey, and M. J. Seel. *Abinitio* high-pressure structural and electronic properties of ZnS. *Physical Review B*, 47(11):6299–6303, 1993.

[120] P. R. Rablen, J. W. Lockman, and W. L. Jorgensen. Ab Initio Study of Hydrogen-Bonded Complexes of Small Organic Molecules with Water. *The Journal of Physical Chemistry A*, 102(21):3782–3797, 1998.

[121] S. L. Shang, L. G. Hector, Y. Wang, and Z.-K. Liu. Anomalous energy pathway of vacancy migration and self-diffusion in hcp Ti. *Physical Review B*, 83(22):224104, 2011.

[122] X. L. Han, Q. Wang, D. L. Sun, and H. X. Zhang. First-principles study of the effect of hydrogen on the Ti self-diffusion characteristics in the alpha Ti–H system. *Scripta Materialia*, 56(1):77–80, 2007.

[123] D. Connétable, É. Andrieu, and D. Monceau. First-principles nickel database: Energetics of impurities and defects. *Computational Materials Science*, 101:77–87, 2015.

[124] D. Connétable, J. Huez, É. Andrieu, and C. Mijoule. First-principles study of diffusion and interactions of vacancies and hydrogen in hcp-titanium. *Journal of Physics: Condensed Matter*, 23(40):405401, 2011.

[125] O. Le Bacq, F. Willaime, and A. Pasturel. Unrelaxed vacancy formation energies in group-IV elements calculated by the full-potential linear muffin-tin orbital method: Invariance with crystal structure. *Physical Review B*, 59(13):8508–8515, 1999.

[126] A. T. Raji, S. Scandolo, R. Mazzarello, S. Nsengiyumva, M. Härting, and D. T. Britton. Ab initio pseudopotential study of vacancies and self-interstitials in hcp titanium. *Philosophical Magazine*, 89(20):1629–1645, 2009.

[127] B. Medasani, M. Haranczyk, A. Canning, and M. Asta. Vacancy formation energies in metals: A comparison of MetaGGA with LDA and GGA exchange–correlation functionals. *Computational Materials Science*, 101:96–107, 2015.

[128] K. Carling, G. Wahnström, T. R. Mattsson, A. E. Mattsson, N. Sandberg, and G. Grimvall. Vacancies in Metals: From First-Principles Calculations to Experimental Data. *Physical Review Letter*, 85:3862–3865, Oct 2000.

[129] R. G. Hennig, D. R. Trinkle, J. Bouchet, S. G. Srinivasan, R. C. Albers, and J. W. Wilkins. Impurities block the α to ω martensitic transformation in titanium. *Nature materials*, 4(2):129–133, 2005.

[130] K. P. McKenna and A. L. Shluger. First-principles calculations of defects near a grain boundary in MgO. *Physical Review B*, 79:224116, Jun 2009.

[131] B. J. Morgan and G. W. Watson. A DFT+U description of oxygen vacancies at the TiO2 rutile (110) surface. *Surface Science*, 601(21):5034–5041, 2007.

[132] M. Marlo and V. Milman. Density-functional study of bulk and surface properties of titanium nitride using different exchange-correlation functionals. *Physical Review B*, 62(4):2899–2907, 2000.

[133] B. Mayer, H. Anton, E. Bott, M. Methfessel, J. Sticht, J. Harris, and P. C. Schmidt. Ab-initio calculation of the elastic constants and thermal expansion coefficients of Laves phases. *Intermetallics*, 11(1):23–32, 2003.

[134] P. Ravindran, L. Fast, P. A. Korzhavyi, B. Johansson, J. Wills, and O. Eriksson. Density functional theory for calculation of elastic properties of orthorhombic crystals: Application to TiSi2. *Journal of Applied Physics*, 84(9):4891–4904, 1998.

[135] C. Li, Z. Wang, and C. Wang. Phase stability, mechanical properties and electronic structure of hexagonal and trigonal Ti5Al2C3: An ab initio study. *Intermetallics*, 33:105–112, 2013.

[136] P. Souvatzis and O. Eriksson. *Ab initio* calculations of the phonon spectra and the thermal expansion coefficients of the $4d$ metals. *Physical Review B*, 77(2):024110, 2008.

[137] D. Raabe, B. Sander, M. Friák, D. Ma, and J. Neugebauer. Theory-guided bottom-up design of β-titanium alloys as biomaterials based on first principles calculations: Theory and experiments. *Acta Materialia*, 55(13):4475–4487, 2007.

[138] P. A. Korzhavyi, L. V. Pourovskii, H. W. Hugosson, A. V. Ruban, and B. Johansson. *Ab Initio* Study of Phase Equilibria in TiC_x. *Physical Review Letters*, 88(1):015505, 2001.

[139] S.-D. Mo and W. Y. Ching. Electronic and optical properties of three phases of titanium dioxide: Rutile, anatase, and brookite. *Physical Review B*, 51(19):13023–13032, 1995.

[140] J.-H. Cho and M. Scheffler. *Ab initio* pseudopotential study of Fe, Co, and Ni employing the spin-polarized LAPW approach. *Physical Review B*, 53(16):10685–10689, 1996.

[141] A. Vittadini, A. Selloni, F. P. Rotzinger, and M. Grätzel. Formic Acid Adsorption on Dry and Hydrated TiO2 Anatase (101) Surfaces by DFT Calculations. *The Journal of Physical Chemistry B*, 104(6):1300–1306, 2000.

[142] G. Kresse and D. Joubert. From ultrasoft pseudopotentials to the projector augmented-wave method. *Physical Review B*, 59(3):1758–1775, 1999.

[143] J. P. Perdew, K. Burke, and M. Ernzerhof. Generalized Gradient Approximation Made Simple. *Physical Review Letters*, 77(18):3865–3868, 1996.

[144] L. Louail, D. Maouche, A. Roumili, and F. A. Sahraoui. Calculation of elastic constants of 4d transition metals. *Materials Letters*, 58(24):2975 – 2978, 2004.

[145] R. Ahuja, J. M. Wills, B. Johansson, and O. Eriksson. Crystal structures of Ti, Zr, and Hf under compression: Theory. *Physical Review B*, 48:16269–16279, Dec 1993.

[146] D. R. Trinkle, R. G. Hennig, S. G. Srinivasan, D. M. Hatch, M. D. Jones, H. T. Stokes, R. C. Albers, and J. W. Wilkins. New Mechanism for the α to ω Martensitic Transformation in Pure Titanium. *Physical Review Letters*, 91:025701, Jul 2003.

[147] B. E. Tegner and G. J. Ackland. Pseudopotential errors in titanium. *Computational Materials Science*, 52(1):2 – 6, 2012. Proceedings of the 20th International Workshop on Computational Mechanics of Materials - {IWCMM} 20.

[148] J. P. Perdew and Y. Wang. Accurate and simple analytic representation of the electron-gas correlation energy. *Physical Review B*, 45(23):13244–13249, 1992.

[149] J. P. Perdew, A. Ruzsinszky, G. I Csonka, O. A. Vydrov, G. E. Scuseria, L. A. Constantin, X. Zhou, and K. Burke. Restoring the Density-Gradient Expansion for Exchange in Solids and Surfaces. *Physical Review Letters*, 100(13):136406, 2008.

[150] K. J. Laidler and M. C. King. Development of transition-state theory. *The Journal of Physical Chemistry*, 87(15):2657–2664, 1983.

[151] H. Eyring. The Activated Complex in Chemical Reaction. *The Journal of Chemical Physics*, 3(2):107–115, 1935.

[152] G. Henkelman and H. Jónsson. A dimer method for finding saddle points on high dimensional potential surfaces using only first derivatives. *The Journal of Chemical Physics*, 111(15):7010–7022, 1999.

[153] G. H. Vineyard. Frequency factors and isotope effects in solid state rate processes. *Journal of Physics and Chemistry of Solids*, 3(1):121–127, 1957.

[154] A. Eichler. CO oxidation on transition metal surfaces: reaction rates from first principles. *Surface Science*, 498(3):314–320, 2002.

[155] S. Zhang and T. N. Truong. Kinetics of Hydrogen Abstraction Reaction Class H + HC(sp3): First-Principles Predictions Using the Reaction Class Transition State Theory. *The Journal of Physical Chemistry A*, 107(8):1138–1147, 2003.

[156] S. Andersson, G. Nyman, A. Arnaldsson, U. Manthe, and H. Jónsson. Comparison of Quantum Dynamics and Quantum Transition State Theory Estimates of the H + CH4 Reaction Rate. *The Journal of Physical Chemistry A*, 113(16):4468–4478, 2009.

[157] G. E. Lienhard. Enzymatic Catalysis and Transition-State Theory. *Science*, 180(4082):149–154, 1973.

[158] V. L. Schramm. Enzymatic Transition State Theory and Transition State Analogue Design. *Journal of Biological Chemistry*, 282(39):28297–28300, 2007.

[159] J. R. Alvarez-Idaboy, N. Mora-Diez, and A. Vivier-Bunge. A Quantum Chemical and Classical Transition State Theory Explanation of Negative Activation Energies in OH Addition To Substituted Ethenes. *Journal of the American Chemical Society*, 122(15):3715–3720, 2000.

[160] S. Petrie and R. C. Dunbar. Radiative Association Reactions of Na+, Mg+, and Al+ with Abundant Interstellar Molecules. Variational Transition State Theory Calculations. *The Journal of Physical Chemistry A*, 104(19):4480–4488, 2000.

[161] D. R. Baker. Chemical interdiffusion of dacite and rhyolite: anhydrous measurements at 1 atm and 10 kbar, application of transition state theory, and diffusion in zoned magma chambers. *Contributions to Mineralogy and Petrology*, 104(4):407–423, 1990.

[162] A. A. Gray-Weale, R. H. Henchman, R. G. Gilbert, M. L. Greenfield, and D. N. Theodorou. Transition-state theory model for the diffusion coefficients of small penetrants in glassy polymers. *Macromolecules*, 30(23):7296–7306, 1997.

[163] D. Dubbeldam, E. Beerdsen, S. Calero, and B. Smit. Dynamically Corrected Transition State Theory Calculations of Self-Diffusion in Anisotropic Nanoporous Materials. *The Journal of Physical Chemistry B*, 110(7):3164–3172, 2006. PMID: 16494324.

[164] D. H. Mathews and D. A. Case. Nudged Elastic Band Calculation of Minimal Energy Paths for the Conformational Change of a {GG} Non-canonical Pair. *Journal of Molecular Biology*, 357(5):1683–1693, 2006.

[165] L. Xie, H. Liu, and W. Yang. Adapting the nudged elastic band method for determining minimum-energy paths of chemical reactions in enzymes. *The Journal of Chemical Physics*, 120(17):8039–8052, 2004.

[166] M. Mantina. *A first-principles methodology for diffusion coefficients in metals and dilute alloys.* PhD thesis, The Pennsylvania State University, 2008.

[167] L. Pizzagalli, P. Beauchamp, and H. Jónsson. Calculations of dislocation mobility using Nudged Elastic Band method and first principles DFT calculations. *Philosophical Magazine*, 88(1):91–100, 2008.

[168] G.-R. Qian, X. Dong, X.-F. Zhou, Y. Tian, A. R. Oganov, and H.-T. Wang. Variable cell nudged elastic band method for studying solid–solid structural phase transitions. *Computer Physics Communications*, 184(9):2111–2118, 2013.

[169] P. Jäckel. *Monte Carlo methods in finance.* J. Wiley, 2002.

[170] H. T. MacGillivray, R. J. Dodd, B. V. McNally, J. F. Lightfoot, H. G. Corwin, and S. R. Heathcote. Monte-Carlo simulations of Galaxy systems. *Astrophysics and Space Science*, 81(1-2):231–250, 1982.

[171] M. Schunack, T. R. Linderoth, F. Rosei, E. Lægsgaard, I. Stensgaard, and F. Besenbacher. Long Jumps in the Surface Diffusion of Large Molecules. *Physical Review Letters*, 88(15):156102, 2002.

[172] T. R. Linderoth, S. Horch, E. Lægsgaard, I. Stensgaard, and F. Besenbacher. Surface diffusion of Pt on Pt (110): Arrhenius behavior of long jumps. *Physical Review Letters*, 78(26):4978–4981, 1997.

[173] P. Ramanarayanan, K. Cho, and B. M. Clemens. Effect of composition on vacancy mediated diffusion in random binary alloys: First principles study of the Si1xGex system. *Journal of Applied Physics*, 94(1):174–185, 2003.

[174] W. Cai, V. V. Bulatov, S. Yip, and A. S. Argon. Kinetic Monte Carlo modeling of dislocation motion in BCC metals. *Materials Science and Engineering: A*, 309:270–273, 2001.

[175] F. Soisson, A. Barbu, and G. Martin. Monte Carlo simulations of copper precipitation in dilute iron-copper alloys during thermal ageing and under electron irradiation. *Acta Materialia*, 44(9):3789–3800, 1996.

[176] P. Kratzer and M. Scheffler. Reaction-Limited Island Nucleation in Molecular Beam Epitaxy of Compound Semiconductors. *Physical Review Letters*, 88(3):036102, 2002.

[177] C. C. Battaile and D. J. Srolovitz. Kinetic Monte Carlo simulation of chemical vapor deposition. *Annual Review of Materials Research*, 32(1):297–319, 2002.

[178] C. Domain, C. S. Becquart, and L. Malerba. Simulation of radiation damage in Fe alloys: an object kinetic Monte Carlo approach. *Journal of Nuclear Materials*, 335(1):121–145, 2004.

[179] M. J. Caturla, N. Soneda, E. Alonso, B. D. Wirth, T. D. De la Rubia, and J. M. Perlado. Comparative study of radiation damage accumulation in Cu and Fe. *Journal of Nuclear Materials*, 276(1):13–21, 2000.

[180] J. Emsley. *The Elements*. Clarendon Press, 1998.

[181] K. Compaan and Y. Haven. Correlation factors for diffusion in solids. *Transactions of the Faraday Society*, 52:786–801, 1956.

[182] J. Bardeen and C. Herring. *Imperfections in nearly perfect crystals.* Wiley, New York, 1952.

[183] J. G. Mullen. Effect of Bardeen-Herring correlation on vacancy diffusion in anisotropic crystals. *Physical Review*, 124(6):1723–1730, 1961.

[184] E. Hashimoto, E. A. Smirnov, and T. Kino. Temperature dependence of the Doppler-broadened lineshape of positron annihilation in α-Ti. *Journal of Physics F: Metal Physics*, 14(10):L215–L217, October 1984.

[185] V. O. Shestopal. Specific heat and vacancy formation in titanium at high temperatures. *Soviet Phys Solid State*, 7(11):2798–2799, 1966.

[186] G. Vérité. *Structure, stabilité et mobilité des défauts ponctuels dans le zirconium hexagonal compact: étude ab initio.* PhD thesis, Université Pierre et Marie Curie-Paris VI, 2007.

[187] G. D. Samolyuk, A. V. Barashev, S. I. Golubov, Y. N. Osetsky, and R. E. Stoller. Analysis of the anisotropy of point defect diffusion in hcp Zr. *Acta Materialia*, 78:173–180, 2014.

[188] G. M. Hood, H. Zou, D. Gupta, and R. J. Schultz. α-Zr self-diffusion anisotropy. *Journal of Nuclear Materials*, 223(2):122–125, 1995.

[189] L. Vitos, B. Johansson, J. Kollár, and H. L. Skriver. Exchange energy in the local Airy gas approximation. *Physical Review B*, 62(15):10046–10050, 2000.

[190] R. Armiento and A. E. Mattsson. Functional designed to include surface effects in self-consistent density functional theory. *Physical Review B*, 72(8):085108, 2005.

[191] Z. Zhang, M. A. Cuddihy, and F. P. E. Dunne. On rate-dependent polycrystal deformation: the temperature sensitivity of cold dwell fatigue. In *Proceedings of the Royal Society of London A*, volume 471, page 20150214. The Royal Society, 2015.

[192] R. A. Swalin. A model for solute diffusion in metals based on elasticity concepts. *Acta Metallurgica*, 5(8):443–448, 1957.

[193] V. B. Vykhodets, S. M. Klotsman, and T. E. Kurennykh. Oxygen Diffusion in alpha-Titanium. I. Anisotropy of Oxygen Diffusion in alpha-Titanium. *Fiz. Met. Metalloved.*, 63(5):974–980, 1987.

[194] Y. A. Bertin, J. Parisot, and J. L. Gacougnolle. Modèle atomique de diffusion de l'oxygène dans le titane α. *Journal of the Less Common Metals*, 69(1):121–138, 1980.

[195] D. Vanderbilt. Soft self-consistent pseudopotentials in a generalized eigenvalue formalism. *Physical Review B*, 41:7892–7895, Apr 1990.

[196] G. Kresse and J. Hafner. Norm-conserving and ultrasoft pseudopotentials for first-row and transition elements. *Journal of Physics: Condensed Matter*, 6(40):8245, 1994.

[197] J. P. Perdew and Y. Wang. Pair-distribution function and its coupling-constant average for the spin-polarized electron gas. *Physical Review B*, 46(20):12947–12954, 1992.

[198] C. Herzig, R. Willecke, and K. Vieregge. Self-diffusion and fast cobalt impurity diffusion in the bulk and in grain boundaries of hexagonal titanium. *Philosophical Magazine A*, 63(5):949–958, 1991.

[199] W. C. Roberts-Austen. Bakerian Lecture: On the Diffusion of Metals. *Proceedings of the Royal Society of London*, 59(353-358):281–285, 1895.

[200] B. F. Dyson, T. Anthony, and D. Turnbull. Interstitial diffusion of copper and silver in lead. *Journal of Applied Physics*, 37(6):2370–2374, 1966.

[201] R. A. Ross, H. B. Vanfleet, and D. L. Decker. Diffusion of zinc in lead. *Physical Review B*, 9(10):4026–4029, 1974.

[202] U. Gösele and F. Morehead. Diffusion of zinc in gallium arsenide: A new model. *Journal of Applied Physics*, 52(7):4617–4619, 1981.

[203] S. Coffa, J. M. Poate, D. C. Jacobson, W. Frank, and W. Gustin. Determination of diffusion mechanisms in amorphous silicon. *Physical Review B*, 45(15):8355–8358, 1992.

[204] N. Bernstein, A. Shabaev, and S. G. Lambrakos. First principles study of normal and fast diffusing metallic impurities in hcp titanium. *Computational Materials Science*, 109:380–387, 2015.

[205] Y. Yoshida, M. Menningen, R. Sielemann, G. Vogl, G. Weyer, and K. Schröder. Local Atomic-Jump Process of Iron in $\alpha - Zr$. *Physical Review Letters*, 61(2):195–198, 1988.

[206] R. C. Pasianot and R. A. Pérez. First-principles appraisal of solute ultra-fast diffusion in hcp Zr and Ti. *Journal of Nuclear Materials*, 434(1):158–161, 2013.

[207] R. A. Pérez and M. Weissmann. Ab-initio approach to the effect of Fe on the diffusion in hcp Zr. *Journal of Nuclear Materials*, 374(1):95–100, 2008.

[208] P. A. Burr, M. R. Wenman, B. Gault, M. P. Moody, M. Ivermark, M. J. D. Rushton, M. Preuss, L. Edwards, and R. W. Grimes. From solid solution to cluster formation of Fe and Cr in α-Zr. *Journal of Nuclear Materials*, 2015.

[209] M. Behar, M. R. F. Soares, F. Dyment, R. A. Pérez, and S. Balart. Diffusion of Pd in α-Ti studied by means of Rutherford back-scattering and channelling techniques. *Philosophical Magazine A*, 80(6):1319–1334, 2000.

[210] J. H. R. dos Santos, P. F. P. Fichtner, M. Behar, R. Pérez, and F. Dyment. Au diffusion in α-Ti. *Applied Physics A*, 58(5):453–457, 1994.

[211] X.-X. Yu and C.-Y. Wang. The effect of alloying elements on the dislocation climbing velocity in Ni: A first-principles study. *Acta Materialia*, 57(19):5914–5920, 2009.

[212] K. N. Goswami and A. Mottura. Can slow-diffusing solute atoms reduce vacancy diffusion in advanced high-temperature alloys? *Materials Science and Engineering: A*, 617:194 – 199, 2014.

[213] A. Van De Walle and G. Ceder. The effect of lattice vibrations on substitutional alloy thermodynamics. *Reviews of Modern Physics*, 74(1):11–45, 2002.

[214] V. L. Moruzzi, J. F. Janak, and K. Schwarz. Calculated thermal properties of metals. *Physical Review B*, 37(2):790–799, 1988.

[215] J. M. Sanchez, F. Ducastelle, and D. Gratias. Generalized cluster description of multicomponent systems. *Physica A: Statistical Mechanics and its Applications*, 128(1):334–350, 1984.

[216] A. Van der Ven, H.-C. Yu, G. Ceder, and K. Thornton. Vacancy mediated substitutional diffusion in binary crystalline solids. *Progress in Materials Science*, 55(2):61–105, 2010.

[217] J. A. Yasi, L. G. Hector, and D. R. Trinkle. First-principles data for solid-solution strengthening of magnesium: From geometry and chemistry to properties. *Acta Materialia*, 58(17):5704–5713, 2010.

[218] P. Kwasniak, H. Garbacz, and K. J. Kurzydlowski. Solid solution strengthening of hexagonal titanium alloys: Restoring forces and stacking faults calculated from first principles. *Acta Materialia*, 102:304–314, 2016.

[219] G. Lucas and R. Schäublin. Vibrational contributions to the stability of point defects in bcc iron: A first-principles study. *Nuclear Instruments and Methods in Physics Research Section B: Beam Interactions with Materials and Atoms*, 267(18):3009–3012, 2009.

[220] R. A. Pérez, M. L. Aguirre, and F. Dyment. Zr diffusion in α-Ti matrices with different Fe content. Application of models developed to α-Zr self-diffusion. *Journal of Nuclear Materials*, 229:15–23, 1996.